2013

Nanostructured carbon electrodes

Dennis Antiohos
University of Wollongong

Nanostructured Carbon Electrodes

A Dissertation Presented to The Academic Faculty

By

Dennis Antiohos
B Sc. Photonics, B. Nanotechnology (Honours)

In Partial Fulfilment

of the Requirements for the Degree

Doctor of Philosophy in the School of Chemistry

From

The University of Wollongong

Supervisors- Prof. Gordon G. Wallace, Asc. Prof. Jun Chen, Asc. Prof. Andrew Minett.

June 2013

“Some men see things as they are and say why, I dream of things that never were and ask why not?”

‘George Bernard Shaw’

“The only thing standing between you and your goal is the bullshit story you keep telling yourself as to why you can’t achieve it.”

‘Greg Legin’

i) Thesis declaration

This is to certify that I am responsible for the work in this thesis, and that the work is my own unless otherwise acknowledged. This thesis and its original work contained within has not been submitted to any other institution for a higher degree. The work was carried out under supervision from Prof. Gordon G. Wallace, Dr. Jun Chen, Assoc. Prof. Andrew Minett at the Intelligent Polymer Research Institute at the University of Wollongong.

Dennis Antiohos Date

ii) Acknowledgements

To my parents, this would not have been possible without your support during my undergraduate years. Thank you for all that you have done, I would not be at this stage without you. To my wife Maria, your love, support and putting up with all of my crazy science talk at home has made the last three and a half years fly by.

I would like to thank Dr. Peter Sherrell and Dr. Weimin Zang for all of their help and guidance in the lab, plus the endless hours of discussions on anything carbon and electrochemistry. A special thank you to Prof. Dennis Tallman for all his help with impedance spectroscopy theory. I would like to thank all of my colleagues and friends at IPRI who have offered help and support.

To Dr. Phil Aitchison and A/Prof Andrew Minett, thank you for the opportunity to work on the ARC Linkage project. I have truly learnt a lot from the both of you.

To A/Prof . Jun Chen, your guidance and encouragement throughout the last three and a half years have been absolutely fantastic. None of this would have been possible without your perseverance and trust in me. Thank you for everything.

Lastly, to Professor Gordon Wallace, words cannot express what a privilege it has been to work under you and be mentored by you. Thank you for the opportunity to work in such a prestigious research environment.

iii) Publications

Dennis Antiohos, Mark Romano, Joe, Razal, Phil Aitchison, Andrew Minett, Gordon Wallace, Jun Chen, 'Single walled carbon nanotube – microwave exfoliated graphene oxide composites for supercapacitor device applications', (Manuscript in preparation, June 2013).

Mark S. Romano, Na Li, **Dennis Antiohos**, Andrew Nattestad, Stephen Beirne, Shaoli Fang, Yongsheng Chen, Rouhollah Jalili, Gordon G. Wallace, Ray Baughman, Joselito M. Razal*, and Jun Chen, 'Carbon Nanotube - Reduced Graphene Oxide Composites for Thermal Energy Harvesting Applications', Advanced Materials (Accepted May 2013).

Sureyya Saricilar, **Dennis Antiohos**, Kewei Shu, Caiyun Wang, Philip G. Whitten, Gordon G. Wallace' *'High strain stretchable solid electrolyte's,* Electrochemistry Communications, *(Accepted March 2013).*

D. Antiohos, K. Pingmuan, M. Romano, S. Beirne, T. Romeo, P. Aitchison, A. Minett, G. Wallace, S. Phanichphant, J. Chen, *Manganese oxide - microwave exfoliated graphene oxide composites for asymmetric supercapacitor device applications.* Electrochimica Acta, *(Accepted September 2012).*

D. Antiohos, M. Romano, J. Razal. J. Chen. '*Recent Progress in Carbon Nanotube Research',* **Book chapter***: Carbon Nanotubes for Energy Applications,* Publisher-Intech. *(Accepted September 2012).*

D. Antiohos, G. Folkes, P. Sherrell, S. Ashraf, G. G. Wallace, P. Aitchison, A. T. Harris, J. Chen and A. I. Minett, *Compositional effects of PEDOT-PSS/single walled carbon nanotube films on supercapacitor device performance.* Journal of Materials Chemistry, 2011, 21, 15987-15994.

D. Antiohos, S. E. Moulton, A. I. Minett, G. G. Wallace and J. Chen, *Electrochemical investigation of carbon nanotube nanoweb architecture in biological media.* Electrochemistry Communications, 2010, 12, 1471-1474.

iv) Abstract

Supercapacitors are promising energy storage and power output technologies due to their improved energy density, rapid charge-discharge cycle, high cycle efficiency and long cycle life. Free standing poly(3,4-ethylenedioxythiophene) poly(styrene sulfonate) / single walled nanotube films have been characterised by scanning electron microscopy, Raman spectroscopy and thermo-gravimetric analysis to understand the physical properties of the films. Films with varying compositions of poly(3,4-ethylenedioxythiophene) / poly(styrene sulfonate) and single walled nanotubes were compared by electrochemical impedance spectroscopy, cyclic voltammetry and galvanostatic charge / discharge to understand their electrochemical properties. A comparison of the results shows that having single walled nanotubes dispersed throughout the polymer matrix increases the capacitance by 65 % and the energy density by a factor of 3 whilst achieving good capacity retention over 1000 cycles.

Graphene is sp^2 hybridised carbon atoms in a honeycomb crystal lattice, which has attracted a lot of interest in materials science and condensed matter physics research due to its favourable electronic properties, abundance and low cost. Exfoliated graphene oxide which has also been partially reduced has been achieved using microwave irradiation through the use of a conventional microwave that has led to rapid expansion and a marked volume increase of the graphene oxide. This has enabled a porous material to be developed that can serve as a conductive scaffold and support for composite electrode materials.

Graphene based materials coupled with transition metal oxides are promising electrode materials in asymmetric supercapacitors owing to their unique properties which include high surface area, good chemical stability, electrical conductivity, abundance, and lower cost profile over time. A composite material consisting of graphene oxide exfoliated with microwave radiation (mw rGO), and manganosite (MnO) is synthesised in order to explore their potential as an electrode material. The composite material was characterised by scanning electron microscopy (SEM), x-ray diffraction (XRD), x-ray photoelectron spectroscopy (XPS), and Raman spectroscopy. Cyclic voltammetry (CV) and electrochemical impedance spectroscopy (EIS) was used to explore the process occurring at the electrode / electrolyte interface. Long term cyclability and stability was investigated using galvanostatic charge / discharge testing. From the resulting analysis, an asymmetric supercapacitor was constructed with the best composite containing 90% MnO- 10% mw rGO (w/w). The device exhibited a capacitance of 0.11 F/cm^2 (51.5 F/g by mass) and excellent capacity retention of 82% after 15 000 cycles at a current density of 0.5 A/g.

Composites containing CNTs and graphene are materials of particular interest in the energy storage and conversion area due to their favourable properties which can result in unique optical, electrical, magnetic and chemical properties which are substantially different than that of the individual components. It has been shown that the combination of both CNTs and graphene allows an expressway of electron transport from the electrode material to the current collector. The ability of the

CNTs to ‘sandwich’ in between the graphene sheets helps to alleviate restacking by acting as a spacer (thus maintaining surface area) while increasing electrical conductivity and mechanical stability.

We describe a facile method to develop electrodes of SWNT and exfoliated graphene oxide (mw rGO) with varying weight ratios via sonication, centrifugation and vacuum filtration. These composites are then optimised with the best performing weight ratio to be used in the fabrication of a supercapacitor. Extensive electrochemical testing revealed that the incorporation of SWNTs with mw rGO yielded an electrode material with large specific capacitances. The specific capacitances in all cases exceeded 125 F/g with the optimised / ideal weight ratio of 90% SWNT – 10% mw rGO exceeding 300 F/g. The thickness of the 90% SWNT – 10% mw rGO was optimised with the maximum attainable current per unit area arising at a thickness of 17 microns. Lastly, a device was fabricated that showed excellent reversibility upon current switching from 0.05 A/g up to 4.0 A/g, with a specific capacitance of 80 mF/cm^2 and 128 F/g respectively at 0.05 A/g. Long term testing showed excellent stability over 10 000 cycles, with the maximum attainable energy and power density being 5.8 W.h/kg and 1.9 MW/kg.

v) List of abbreviations

Å	Angstrom: 1×10^{-10} m
α	Electron transfer coefficient
ΔE_p	Peak voltage
$\varepsilon_{(0)}$	Permittivity of free space
$\varepsilon_{(r)}$	Relative permittivity
η	Overpotential (mV)
$\lambda_{(max)}$	Wavelength maximum from UV-vis spectroscopy
μ	Micron
υ	Scan rate (Usually in mV/s unless otherwise stated)
π	3.142
π	Highest occupied molecular orbital
π*	Lowest unoccupied molecular orbital
τ(s)	Time constant of charging / discharging
ψ	Dimensionless kinetic parameter
2D	2-dimensional
A	Area (usually in cm^2 unless otherwise stated)
C	Concentration of solution in mol/L.
C	Capacitance (F)
C'(ω)	Real part of capacitance (F)
C"(ω)	Imaginary part of capacitance (F)
$C_{(sp)}$	Specific capacitance (F)

CCG	Chemically converted graphene
CDC	Chemically derived graphene
C_{dl}	Double layer capacitance (Equivalent circuit model)
CHP	1-Cyclohexyl-2-pyrrolidone
CNT	Carbon nanotube
CV	Cyclic voltammetry
CVD	Chemical vapour deposition
$\vec{D}$	D field, which corresponds to an electric field that accounts for charge due to polarisation
D	Diffusion coefficient (cm^2/s)
deg	Degree Celsius
DOS	Density of states
$\overrightarrow{ds}$	Vector quantity representing a change in surface area
$\frac{dv}{dt}$	Scan rate in cyclic voltammetry.
E	Potential in volts
$E_{1/2}$	Half wave potential
E_{2g}	C = C stretching mode
EDLC	Electric double layer capacitor
EDOT	Ethylene dioxythiophene
EDS	Energy dispersive X-ray
EIS	Electrochemical impedance spectroscopy
ESR	Equivalent series resistance

F	Farad
$f_{(p)}$	Peak frequency
FC	Functionalised carbon black
GCD	Galvanostatic charge / discharge
GO	Graphene oxide
HiPCO	High pressure carbon monoxide process
HOPG	Highly ordered pyrolytic graphite
I	Intensity (a.u)
i_0	Exchange current
i_a	Current
ICP	Inherently conducting polymer
Re Z’	Real part of impedance
Im Z"	Imaginary part of impedance
iR	Resistance drop (V)
k^0	Electron transfer rate constant
K_α	Electron transition from L to K orbital
m	Mass (generally in grams unless otherwise stated)
min	Minute
Mn_3O_4	Manganese Oxide
MnO	Manganese Oxide (Manganosite)
mw rGO	Microwave exfoliated graphene oxide
MWNT	Multi-walled carbon nanotube
n	Principal quantum number

OCP	Open circuit potential
PANI	Poly(aniline)
PEDOT/PSS	Poly(3,4-ethylenedioxythiophene) poly(styrenesulfonate)
PTFE	Polytetrafluoroethylene
Q	Charge (C)
$R_{(ct)}$	Charge transfer resistance (Ohm.cm^2)
$R_{(p)}$	Polarisation resistance (Ohm.cm^2)
$R_{(s)}$	Series resistance (Ohm.cm^2)
R_1	Resistance 1 in equivalent circuit model
R_2	Resistance 2 in equivalent circuit model
RBM	Radial breathing mode
Scm^{-1}	Conductivity measurement of Siemens per centimetre.
SEM	Scanning electron microscopy
SWNT	Single-walled carbon nanotube
t	Time (usually in seconds unless otherwise stated)
TED	Transmitted electron detection
TGA	Thermo-gravimetric analysis
UV-vis	Ultra violet – visible spectroscopy
V	Volume fraction
V	Voltage
W	Work done in moving a point charge in an electric field
w/w	Weight for weight percent
XPS	X-ray photo fluorescence spectroscopy

XRD	X-ray diffraction

vi) Table of contents

vii) List of figures

viii) List of tables

Chapter 1: Introduction.

1. Introduction.

1.1. The Energy Problem.

The energy crisis during the 1970s sparked the development of renewable energy sources and energy conservations measures. As supply eventually met demand, these programs were scaled back. Ten years later, the hazards of pollution led to work on minimisation and reversal of the environmental impact of fossil fuel extraction, transport and consumption [1].The United States Department of Energy predicts that 20 years from now, the world's energy consumption will increase by 20% (Figure 1. 1). The growing concerns over the constant use of fossil fuels and its effect on climate change [2], has once again spurred research on sustainable energy development and on enhancement in renewable energy systems. Advances in energy storage and conversion systems that will make our energy usage more efficient are essential if we are to meet the challenge of global warming and the finite nature of fossil fuels [2, 3].

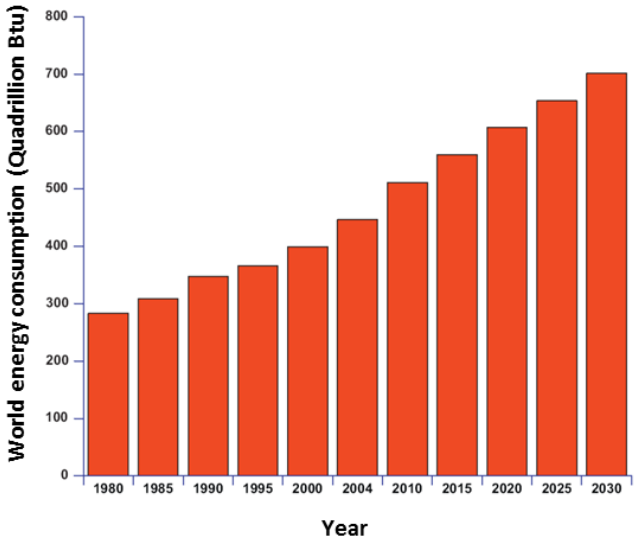

Figure 1. 1: The United States Department of Energy values and forecasts for energy utilisation in the period from 1980 to 2030 [4].

Currently, there are a variety of electricity generating technologies that have been implemented (and are still under development) in order to reduce the dependence on the use of coal in electricity generation. These include (and not limited to) nuclear energy, wind, solar, geothermal, landfill gas, sewage gas, wood waste, biomass, tidal/wave, hydro, and solar thermal [5]. The main issues with these current renewable energy generation systems is that the electricity generated must be used immediately; and often as is the case electricity production is in peaks and troughs due to environmental conditions meaning that the load levelling capability is poor and power disruptions result [6].

The need for the development of efficient energy storage systems is paramount in meeting the world's future energy targets, especially when energy costs are on the increase and more people need access to electricity [4, 6]. Energy storage technologies can improve efficiencies in supply systems by storing the energy when it is in excess, and then release it at a time of high demand [6]. Supercapacitor technologies can help with the development of smarter and more efficient systems through the use of materials chemistry and materials engineering which specifically targets and enhances the nanostructured properties of electrode materials which improves the electrochemical response at the electrode / electrolyte interface. Further material progression in research and development fundamentals, as well as engineering improvements need to be continued in order to create energy storage systems that will help alleviate humanities energy storage and conversion dilemmas.

1.2. Double layer electrochemistry.

In electrochemistry, voltage or current signals are applied to a system immersed in a conductive electrolyte in order to gauge the systems response. Briefly, a standard potentiostat used for electrochemical measurements will contain a working electrode, counter electrode and a reference electrode. In the electronics of the potentiostat, a control amplifier inputs the voltage signal while the current follower measures the current at that given input signal [7]. A voltage follower / summing amplifier will regulate the potential between the reference and working electrode such that there is no current flow [7]. A simplified schematic of a typical electrochemical set-up is shown in Figure 1. 2.

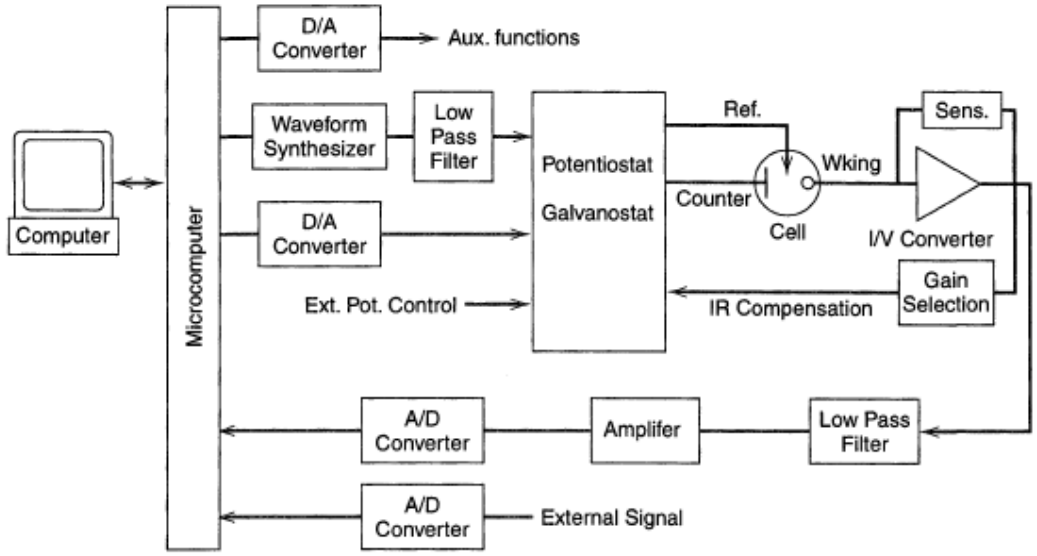

Figure 1. 2: Simplified sketch of a typical computer-controlled electrochemical instrument. The waveform synthesiser produces the signal required. The D/A converter generates the DC bias signal. These two signals are fed into the adder potentiostat. The analogue output creates various operational signals. Printed from John Wiley & Sons [7].

When there is an applied potential between a working electrode and counter electrode, there will be an orientation of dipoles from the electrolyte relative to the polarity of the working electrode. The orientation of these dipoles leads to adsorption / desorption of ions giving rise to electrical phenomena [8]. The ions, electrons, and dipoles will induce an electric field an electric field in this region termed that is termed 'electrical double layer' as shown in Figure 1. 3. The electrode has an associated charge (Q) that is uniformly distributed over the interface with respect to the electrolyte. The majority of the charge is located at the electrode / electrolyte interface with the electrode / air portion (part of electrode not immersed in solution) containing a negligible amount of charge [8]. The thickness of a typical electrical double layer is 5Å-10Å and is dependent on the size and concentration of the ions in solution. The systems can be considered as a parallel plate capacitor as represented by H. L. F. Helmholtz with the larger the electrical double layer, then the greater the generated capacitance [8]. It must be noted that conservation of charge holds true at the interface such that; $Q_{electrode} + Q_{electrolyte} = 0$.

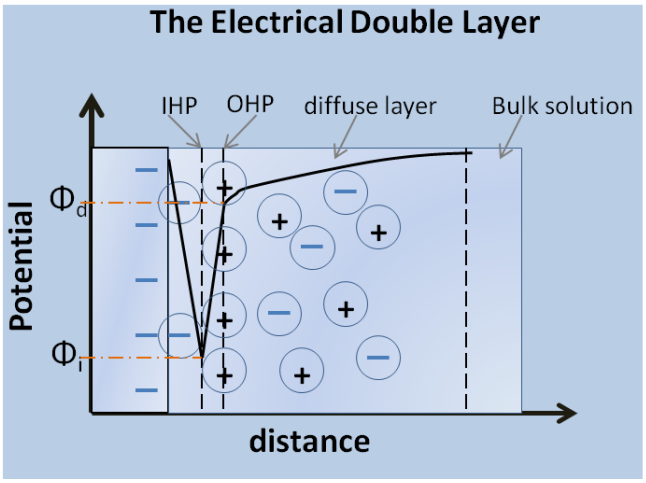

Figure 1. 3: Representation of the electric double layer with the negative region depicting the electrode and positive region representing the electrolyte. IHP represents the inner Helmholtz plane, while OHP is the outer Helmholtz plane.

1.3. Supercapacitors.

1.3.1. Background Information.

Electrical energy can be stored in two different forms and can best be described when considering a battery and a capacitor. In a battery, it is the available chemical energy through the release of charges that performs work when two electroactive species undergo oxidation and reduction [7]; this is termed a Faradaic reaction. In a capacitor, electrostatic forces between two oppositely charged plates will separate charge. The generated potential is due to an excess and deficiency of electron charges between the two plates without charge transfer taking place [7]. The current that is observed can be considered as a displacement current due to the rearrangement of charges [2]; this effect is termed as non-Faradaic in nature.

1.3.2. Supercapacitor operation and types.

There are two types of electrochemical capacitors that are referred to as electric double layer capacitors (EDLC) and pseudocapacitors. The construction of these devices can vary, with electrodes being fabricated from porous carbon materials including activated carbons, graphene, carbon nanotubes, templated carbons, metal oxides and conducting polymers [9, 10]. EDLC or supercapacitors have two electrodes immersed in an electrolyte solution, separated by a semi-permeable dielectric that allows the movement of ions to complete the circuit but prevents a short circuit from being formed. They are advantageous as they are able to provide large power densities, relatively larger energy densities than conventional capacitors, and long life cycles compared to that of a battery and ordinary capacitor [11]. The performance of supercapacitors is affected by the power density requirements, high electrochemical stability, fast charge/discharge phenomena, and low self-discharging [12]. Table 1. 1 below shows a comparison between capacitors, supercapacitors and batteries.

Energy storage is achieved by the build-up and separation of electrical charge that is accumulated on two oppositely charged electrodes as shown in Figure 1. 4 [13]. As stated previously, no charge transfer takes place across the electrode-electrolyte interface and the current that is measured is due to a rearrangement of charges. The electrons involved in the non-Faradaic electrical double layer charging are the conduction band electrons of the electrode.

Table 1. 1: Comparison of key parameters for a capacitor, supercapacitor and battery [14].

Parameters	Capacitor	Supercapacitor	Battery
Charge time	10^{-6} – 10^{-3} sec	1- 30 sec	0.3 – 3 hrs
Discharge time	10^{-6} – 10^{-3} sec	1 – 30 sec	1 – 5 hrs
Energy Density (Wh/kg)	<0.1	1 - 10	20 - 100
Power Density (W/kg)	>10 000	1000 - 2000	50 - 200
Cycle life	> 500 000	> 100 000	500 - 2000
Charge/discharge efficiency.	≈ 1	0.90 – 0.95	0.7 – 0.85

These electrons leave or enter the conduction band state depending on the energy of the least tightly bound electrons or the Fermi level of the system [2]. Supercapacitors exhibit very high energy storage efficiencies exceeding 95 %, and are relatively stable for up to10^4-10^5 cycles [4, 6]. The energy given by the equation, $E = 0.5\ CV^2$, means that the operating voltage (V) is the key in determining the energy characteristics of a supercapacitor. The choice of electrolyte when designing and fabricating a supercapacitor device dictates the operating voltage [15]. Operating voltages are approximately 1.2 V, 2.7 V, and 3.5 V respectively for aqueous, organic and ionic liquid with all of them having associated advantages and disadvantages [4, 6].

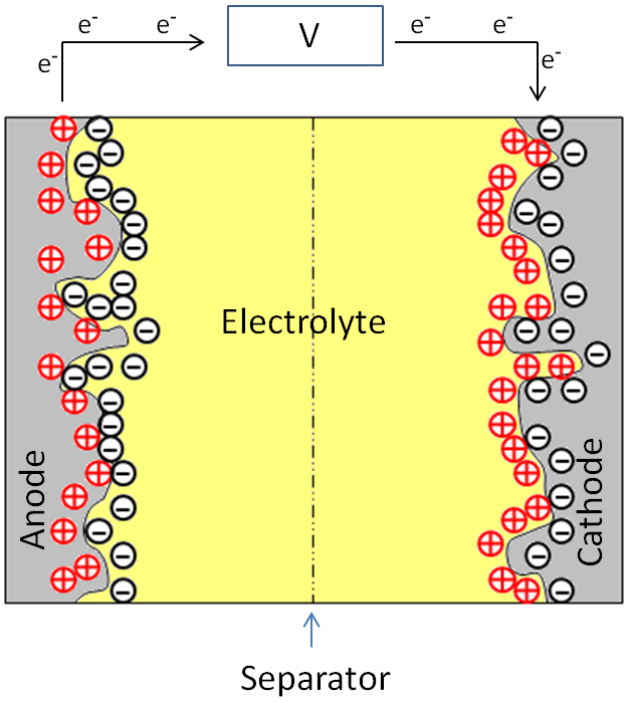

Figure 1. 4: Schematic diagram of an EDLC supercapacitor with a positive and negative electrode, separator and porous carbon.

Like EDLC, a pseudocapacitor consists of two porous electrodes with a separator between them all immersed in an electrolyte solution [16]. However the difference is that the charge is accumulated during Faradaic reactions near to, or at the surface of the electrodes [9], hence non-Faradaic double-layer charging and Faradaic surface processes occur simultaneously [17]. The pseudocapacitance arises from a Faradaic reaction when some of the charge (q) passed in an electrode process is related to the electrode potential V via thermodynamical considerations [18]. The two principal cases are adsorption pseudocapacitance arising in underpotential deposition processes [18], and homogeneous redox pseudocapacitance where the reaction is reversible [18, 19]. Pseudocapacitors thus combine features of both capacitors and batteries [9, 20]. A comparison of energy

density and power density for various electrical energy storage systems is depicted in Figure 1. 5. Current commercial uses of supercapacitors include personnel electronics, mobile telecommunications, back-up power storage, and industrial power and energy management [21, 22]. A recent application is the use of supercapacitors in emergency doors on the Airbus A380, highlighting their safe and reliable performance [22].

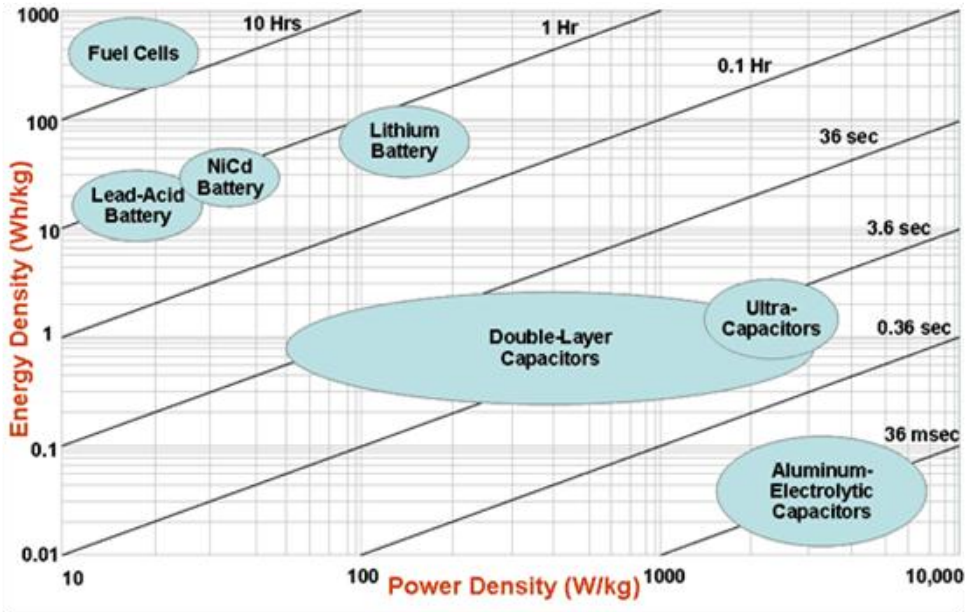

Figure 1. 5: Ragone plot showing specific power against specific energy for various electrical energy storage systems. The times shown are the time constants of the device, which are obtained by dividing the energy density and power density [23].

1.4. Derivation of capacitance.

For a full understanding of the key parameters important in selecting materials for supercapacitors, and more broadly energy storage applications, it is important to grasp an understanding of the mathematics involved in determining such key

parameters. The capacitance which is by definition the ratio of the charge (*q)* to the voltage *(V)* is a constant of proportionality that is determined by the geometry, separation, type of electrode and also the type of electrolyte [24]. When determining the capacitance, it is assumed that the charge is uniform over both of the surfaces provided, and that the area is relatively large with the separation distance is small. Also, capacitor systems are not in a direct vacuum, but often contain a dielectric medium. When this is the case, the total charge generated is comprised of two parts; namely the free charge and the polarisation charge [24].

Gauss law for elementary electrostatics can now be used where if we enclose a net volume with an imaginary surface (Gaussian surface); the net charge (*q*) will be given as an integral of the electric field (*E*) over the surface (*A)*, as governed by Equation 1.1 [24];

$$\int \vec{D}.\overrightarrow{ds} = q \qquad \textit{Equation 1.1}$$

The flux of D (Electric field due to free and polarisation charge) is orthogonal to the surface. Where $D = \varepsilon_0\varepsilon_r E$ where ε_r is the dielectric constant of the material. From the assumptions provided above the left hand side of the equation simplifies down to;

$$DA = q \qquad \textit{Equation 1.2}$$

$$E = \frac{D}{\varepsilon_0 \varepsilon_r} \qquad \textit{Equation 1.3}$$

And the voltage (V) is given by;

$$V = -\int_{d}^{0} \vec{E}.\overrightarrow{dl} \qquad \textit{Equation 1.4}$$

Again the electric field is parallel to the length *d,* therefore the integral expression simplifies to,

$$E = \frac{V}{d} \qquad \textit{Equation 1.5}$$

Therefore we can substitute Equation 1.3 into Equation 1.4 to obtain an expression for the capacitance in Farads.

$$\frac{q}{V} = C = \frac{A\varepsilon_0\varepsilon_r}{d} \qquad \textit{Equation 1.6}$$

During charging of a supercapacitor, a re-arrangement of charges occurs between the electrode and electrolyte interface [2]. In doing so, the moving charges fight against the electric field which is pulling them back meaning that work is required to charge a capacitor to its final amount Q [24]. The work that must be done to transport a piece of charge is given by;

$$\int dW = \int_{0}^{q} \frac{q}{c}\, dq \qquad \textit{Equation 1.7}$$

Simply by integrating the left and right hand sides of equation 8, an expression for the total work done, or maximum energy density is;

$$W = \frac{1}{2}\frac{q^2}{C} \qquad \textit{Equation 1.8}$$

Which simplifies down to;

$$W = \frac{1}{2}CV^2 = Energy \qquad \textit{Equation 1.9}$$

Where C is the specific capacitance and V is the voltage. The power is then just simply the energy density per unit time;

$$P = \frac{W}{t} \qquad \textit{Equation 1.10}$$

It can be seen that from the derivations, it is important that materials have not only large surface area, but surface area that is accessible by electrolyte ions such that ion diffusion is fast. This enables a large energy density and power density which is needed in modern day applications. With these considerations, the materials chosen must also be stable and robust so the performance does not degrade over time. These are the characteristics needed for potential commercial applications.

1.5. Different electrolytes used and their advantages and disadvantages.

The choice in electrolyte is extremely important for supercapacitor design as it influences the performance for energy storage and delivery. The extremely large surface area can allow for enhanced energy and power density as long as the micro porosity and meso porosity is tailored to suit the type of electrolyte being used. The electrolyte can be designed to enhance the cyclability, to sustain target power densities during operation, and to have an excellent rate capability (i.e. excellent charge/ discharge behaviour) [25].

1.5.1. Aqueous Electrolytes.

For aqueous electrolytes, the maximum operating voltage is theoretically limited by the reduction potential of water (1.23 V at 25^{o}C, 1 atm, and 1 molar concentration) [25]. Most aqueous electrolyte systems tend to have an electrochemical window of

approximately 1 V [25]. Electrolyte conductivity has a significant effect on the equivalent series resistance (ESR) of the cell, which determines the power output [6]. Concentrated electrolytes are required to minimise the ESR and maximise power capability [25]. In general, strong solutions of acidic electrolytes are much more corrosive than strong basic electrolytes meaning that the electrolyte has to be carefully selected for the particular electrode material as the pH plays an important role in the electrochemical performance.

1.5.2. Organic Electrolytes.

The use of non-aqueous electrolytes in supercapacitors has the main advantage of higher operating voltages compared to aqueous systems. Voltage windows can range up to 2.5 V and since the stored energy increases as V^2, it is possible to attain large energy and power densities [25, 26]. It must be noted that to operate at these higher voltages, non-aqueous electrolytes must be free of water and oxygen which will ensure no evolution of O_2 and/or H_2O at potential differences above 1.23 V [27]. Salts are added to the system to provide mobile ion movement at the electrode/electrolyte interface. The most common salt used generally consists of lithium ions (eg. $LiClO_4$, $LiPF_6$) as these ions move very well under an electric field, and the effective ion diameter is very small [7, 28, 29].

1.5.3. Advantages, limitations and comparison for use in supercapacitors.

Aqueous electrolytes tend to have very good kinetic behaviour of the electrolyte ions leading to very efficient charge/discharge rates. This behaviour is due to the relatively high conductivity and low viscosity of the concentrated solutions [6, 30]. For example, the conductivity of 1M H_2SO_4 is 730 mS cm^{-1} compared to the much lower value of 10-20 mS cm^{-1} for organic solutions of lithium salts [26]. Time constants of symmetrical carbon supercapacitors using H_2SO_4 were reported to be 0.1s by Lewandowski et. al. [26]. Other advantages include the purification and drying processes are less stringent during production which minimises cost [27]. The major disadvantage of aqueous electrolytes is the smaller operating voltage that is able to be obtained, which can lead to a reduced power capability.

The advantage of an organic electrolyte is the larger potential window that can be achieved which is typically in the order of 2 V. This value of 2 V is limited by any residual water and oxygen content in the electrolyte. Current commercial research is revolving around the potential to achieve a larger voltage exceeding 3 V, using extreme purification processes as well as a corrosion inhibition of the carbon electrode. This is advantageous as the energy and power density may be significantly enhanced [27].

The major disadvantages of non-aqueous systems are the lower conductivity and the higher viscosity resulting in higher equivalent series resistance (ESR) and

reduced wettability if the electrode is hydrophilic. A decrease in wettability will effectively reduce the surface area used by the electrolyte, reducing the energy and power density. Most commercial systems that use organic electrolytes are manufactured in inert atmospheres and are costly to be produced [6].

1.6. Carbon materials.

There are a variety of carbon materials that have been suggested for the use in supercapacitors. In particular these include activated carbons, carbon nanotubes, and graphene / graphene oxide variations [31, 32]

1.6.1. Carbon nanotubes.

Carbon nanotubes (CNTs) were first discovered in 1953 through research in the Soviet Union, but the first accessible results were by Sumio Iijima [33], in 1991 as a result of research into buckminster fullerenes. CNTs have a cylindrical shape that can be considered as a graphene sheet rolled up; either individually as a single-walled carbon nanotube (SWNT), or concentrically as a multi-walled carbon nanotube (MWNT) as depicted in Figure 1. 6 and Figure 1. 7. However, these sheets can have varying degrees of twist along its length that can lead to the nanotubes to be either metallic or semi-conducting as the change in chiralities induces different orbital overlaps [34]. They exhibit remarkable electrical transport and mechanical properties [35], which is why interest and research into this material has increased over the last two decades. CNT powders have the potential to be tailored to specific energy storage and conversion applications with their being an added advantage

that they can be used in all electrolyte environments that encompass aqueous, organic and ionic liquids [36].

1.6.1.1 CNT brief synthesis overview.

There are a variety of different methods for making SWNTs and MWNTs that have been developed since CNTs were first discovered. These include laser ablation, arc discharge, chemical vapour deposition (CVD), and high pressure carbon monoxide disproportionation (HiPCO). Recently, work by Harris et. al. has successfully scaled-up the synthesis of CNT using a fluidised bed reactor [37]. All growing conditions for synthesising CNTs require a catalyst to achieve high yields, where the size of the catalyst nanoparticles will determine the diameter and chirality of the CNT [38]. The CNTs that are formed are generally in a mixture with other carbonaceous product including amorphous carbon and graphitic nanoparticles.

1.6.1.2 Single walled nanotubes.

SWNT have been studied extensively as a supercapacitor and hybrid energy material [6, 39, 40]. The structure of a SWNT is illustrated in Figure 1. 6 with a cylindrical nature apparent. Its advantage is that it has very good thermal and conductive properties where the thermal conductivity can exceed 6000 $Wm^{-1}K^{-1}$ and a potential current carrying capacity of 10^9 A/cm^2 [41, 42].

The maximum reported capacitance for SWNT fabricated electrodes (PVA / PVC binder; pressed into pellet) is 180 F/g with an energy density of 7 Wh/kg and a

power density of 20 kW/kg using KOH electrolyte [43, 44]. Hu et. al. have recently reported a solid state paper based SWNT supercapacitor, which has a specific capacitance of 115 F/g, energy density of 48 Wh/kg and a large operating voltage of 3V. The electrode preparation involved pre-processing where cotton sheets were immersed in the SWNT dispersion, annealed then immersed in an PVA/ H_3PO_4 electrolyte [45].

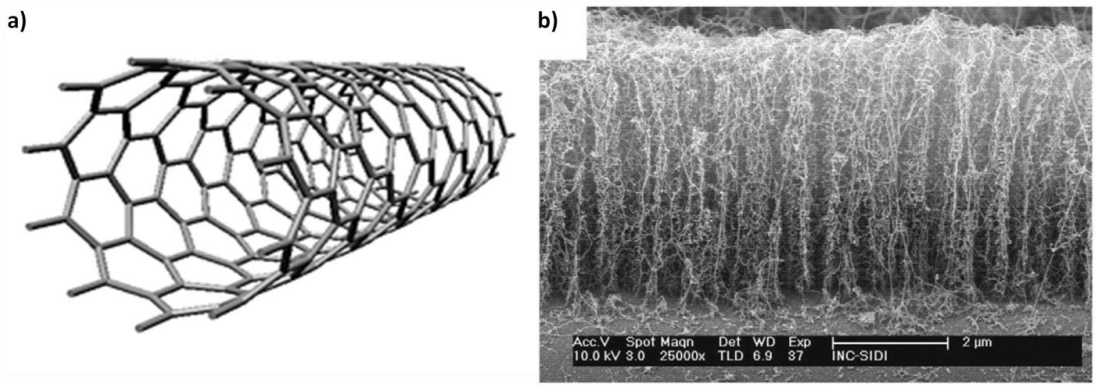

Figure 1. 6: (a) Schematic representation of a SWNT [46]. (b) FESEM of SWNTs grown onto a Si wafer substrate [47].

1.6.1.3 Multi-walled nanotubes.

Like their SWNT counter parts, MWNT have also been studied extensively as electrode materials for supercapacitors [6, 39, 40]. The advantages over SWNTs are their ability to be more easily synthesised on much larger scales, making them more suitable for commercial application. The concentric nature of these nanotubes can be observed in the SEM image of Figure 1. 7. The maximum capacitance attained for electrodes constructed from MWNTs range between 4-140 F/g with the best available commercial result at 130 F/g from Maxwell's Boost capacitor [48]. Wang et. al. have recently reported partially exfoliated MWNTs on carbon cloth that gave

a specific capacitance in the range of 130-165 F/g with a coulombic efficiency of 98% [39].

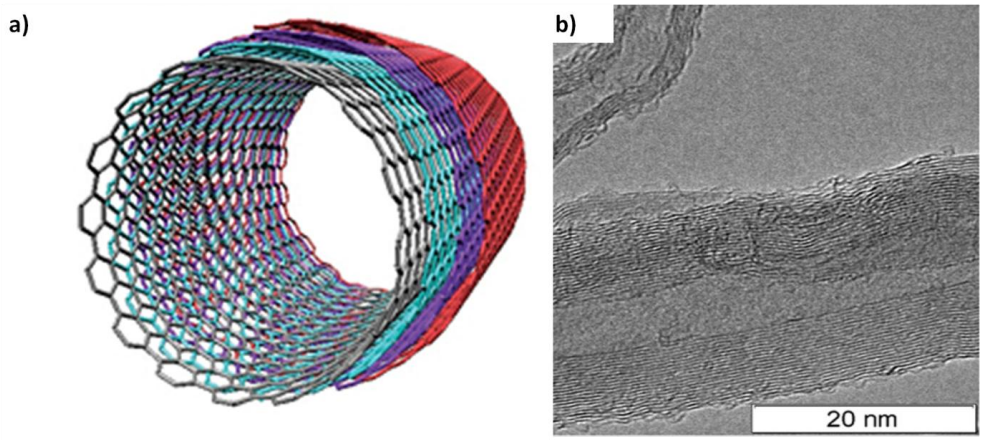

Figure 1. 7: (a) Schematic representation of a MWNT [46]. (b) TEM images of pristine MWNTs [48].

1.6.1.4 Graphene and graphene oxide.

The discovery of monolayer graphene was observed by chemist and surface scientists that can be traced back to the 1960s and 1970s [49]. Graphene is an atomically thin layer of sp^2 hybridised carbon arranged in a honeycomb lattice (as can be seen in Figure 1. 8) with the exfoliation of graphite into individual graphene sheets by a simple scotch tape method being reported in 2004 [49].

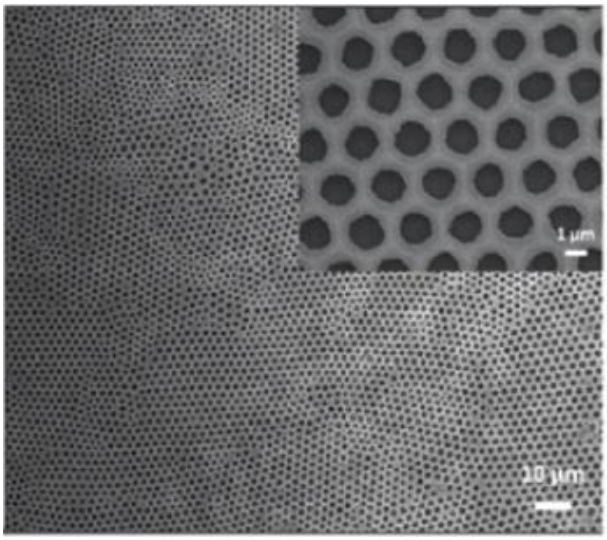

Figure 1. 8: SEM image of a honeycomb structured film based in graphene oxide [48].

Exfoliation is necessary as a very small amount of the bulk material translates into atomically thin films with extremely large surface areas. The synthesis of graphene has developed rapidly, with exfoliation occurring by mechanical techniques, chemical vapour deposition, solid state carbon source deposition, solution exfoliation, and nanotube splitting / unzipping [49, 50]. Alternatively, graphene can be synthesised by the forming graphene oxide (GO) through chemical techniques such as the Hummer's method (and its variations) and is termed chemically concerted graphene (CCD) [51, 52]. CCG is generally in the form of GO with the degree of functionality being able to be tailored depending on the properties required. A major advantage of CCG is its straight forward processing and scalability which makes it suitable for potential commercial applications in film and device manufacturing [53]. Reduced graphene oxide is advantageous for energy storage applications due to its giant carrier mobility, quantum Hall effect, crystallinity, and

semi-metal electronic properties [49, 53]. Other potential uses for reduced GO could be in the form of gas capture and storage, electrodes for water splitting, and fuel cells [54-56]. An SEM image of GO is shown in Figure 1. 9. Here the exfoliation of GO enables more porosity (hence larger surface area) to be formed with minimal restacking. However, re-stacking of sheets can occur through π-π interactions that result in an inter-layer distance of ≈ 0.34 nm which is too small for electrolyte ion accessibility [53]. To date, one of the largest reported surface areas has been obtained by Srinivas et.al. at 1900 m^2/g [54]. S. Bose et. al. in their critical review have reported specific capacitances of between 101 F/g and 347 F/g for reduced GO and exfoliated GO supercapacitor devices [12, 57, 58]. While J. Miller et. al. developed at graphene capacitor with an RC time constant of 200 microseconds [59].

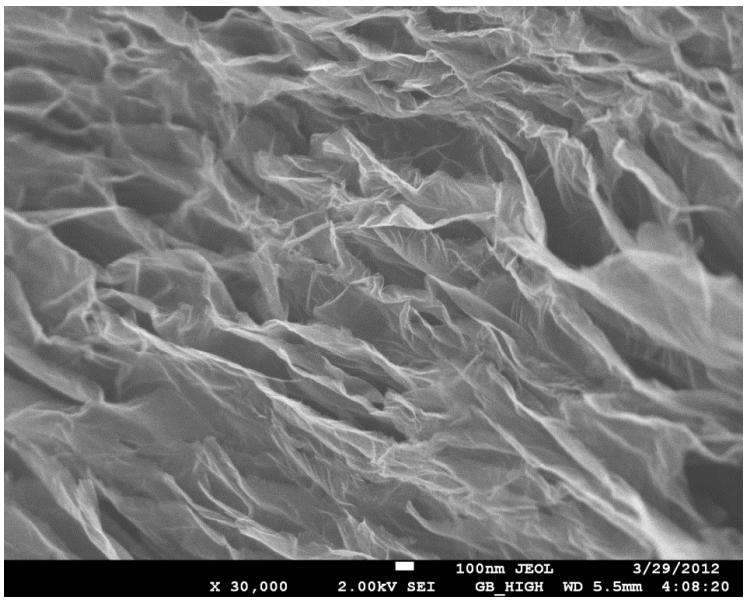

Figure 1. 9: SEM of exfoliated GO sheets.

1.6.1.5 How and why carbon materials can address the issues of energy storage and conversion.

Nanostructured materials are of great interest in the energy storage and conversion field due to their favourable mechanical, and electrical properties [3, 35]. Carbon nanotubes (CNTs) and graphene are types of nanostructured materials that possess favourable electrical and mechanical properties due to the confinement of one dimension, combined with the surface properties that contribute to the enhanced overall behaviour. The potential of nanostructured materials is not only limited to energy storage and conversion devices; but also to nanotransistors [34, 60], actuators [34, 60], electron field emission [34, 60], and biological sensing devices [61, 62].

The use of carbon-based nanomaterials as electrode materials is practical and economically viable because cheap carbon pre-cursor materials are abundant [13]. As the research into carbon nanotubes (CNTs) has increased over the last 20 years, the cost of these materials has significantly reduced alongside improvements in processability and scalability [63].

The advantage of incorporating carbon materials and specifically CNTs and graphene as part of the electrode material is the excellent mechanical and electrical properties. They provide mechanical support to the substrate while enhancing the conductive and electrochemical properties. The low cost of the carbon precursor material used to synthesise CNTs makes device fabrication scalable and economically viable [64]. CNT and graphene assemblies can have extremely high

specific surface areas, which are extremely important in capacitor design. These carbon electrode materials can be confined to a smaller areas increasing the electrode-electrolyte contact and decreasing the weight of the device therefore maximising the overall gravimetric performance of the device [65]. Conductive carbons are also chemically stable, which enhances the resistance to degradation of the electrode surface [66].

1.7. Surface Functionalities.

The presence of surface functionalities such as oxygen, nitrogen, hydrogen, boron and catalyst nanoparticles (dependent on the synthesis environment and pre-cursor materials) can affect the capacitive behaviour of the electrode through the introduction of Faradaic reactions [67], changes in electric and ionic conductivity [15], and influencing wettability [68]. A schematic representation of a sp^2 hybridised carbon lattice with various dopants is show in Figure 1. 10.

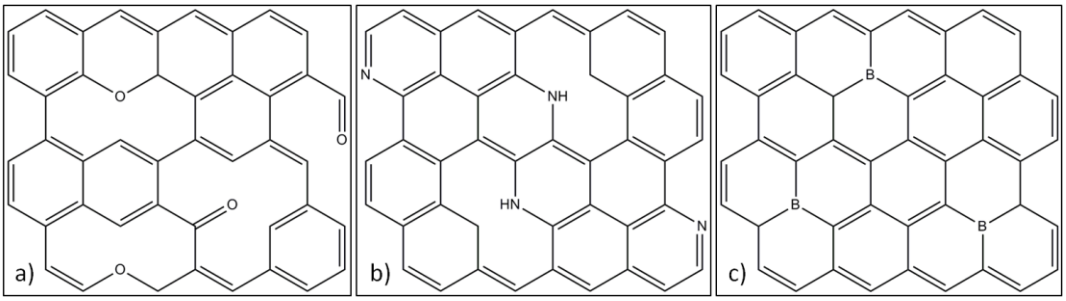

Figure 1. 10: Schematic representation of a sp^2 hybridised carbon lattice that has been doped with; (a) oxygen functional groups, (b) nitrogen functional groups, (c) boron.

1.7.1. Oxygen.

Carbon materials will have functional groups present on their surface as a result of the precursors and preparation conditions [15]. Most of these functional groups are in the form of carboxyl (–COOH), Carbonyl (C=O) as well as others such as phenol, quinone and lactone groups [6, 15]. Activation procedures such as post treatment with H_2SO_4 and / or HNO_3 will lead to acid oxygen functionalities [6]

Most of these groups are bonded with carbon atoms at the edge of hexagonal carbon layers where Faradaic reactions via interactions with the electrolyte lead to pseudocapacitance such as those developed with transition metal oxides RuO_2 and MnO_2 [15, 69]. These functional groups can also be purposely added onto the surface of carbons via oxidation with O_2 or acid treatment with HNO_3 or H_2SO_4 [70]. In aqueous systems, the presence of oxygen containing functional groups can lead to an enhanced wettability as well as pseudocapacitance as mentioned above, which maximises the electroactive surface area leading to larger energy densities [15, 60]. The following reactions occur [71]:

$>C\text{-}OH < -- > C=O + H^+ + e^-$

$>C=O + e^- < -- > C - O^-$

In non-aqueous systems, however, oxygen functionalities are detrimental to device performance. Parasitic redox reactions can lead to a degradation of the electrode, as well as adverse effects relating to voltage proofing and increased leakage current

[6, 72]. These redox reactions will reduce the cycle life of a device, as well as lowering the operating voltage.

Shen et. al. reported in 2011 the effects of changing the carboxylic group concentration on SWNTs. The specific capacitance, power density and energy density 0.5 M H_2SO_4 electrolyte increased with carboxylic group density reaching a maximum of 149.1 F/g, 304.8 kW/kg, and 20.71 Wh/kg, respectively. The 10 µm film electrodes were fabricated using vacuum filtration to create "bucky papers" onto a mixed cellulose estate membrane [73].

1.7.2. Nitrogen.

Nitrogen containing carbons have recently attracted interest due to its n-type behaviour that promotes large pseudocapacitance, which can be obtained even if the surface area of the material is decreased [74]. In some instances, up to 3-fold increase in capacitance have been reported [75]. Typical examples of redox reactions involving nitrogen are described below [76]:

$$>C+NH + 2e^- + 2H^+ \leftrightarrow CH_2\text{-}NH_2$$

$$>CH\text{-}NHOH + 2e^- + 2H^+ \leftrightarrow CH_2\text{-}NH_2 + H_2O$$

The chosen precursor material affects the types of functionalities that are attached to the carbon backbone. Nitrogen containing groups (such as amino functionalities, tertiary and quaternary nitrogens) may be added via various methods with

compounds containing nitrogen including treatment with urea, melamine, aldehyde resins and polyacrylonitrile [6, 77-81]. Surface areas for nitrogen doped carbon materials are thought to be in excess of 400 m^2/g [15]. This is much lower than pure SWNTs and pure MWNTs that have been reported to attain a surface area greater than 1315 m^2/g and 830 m^2/g respectively; suggesting that pseudocapacitance makes up a substantial portion of the total capacitance [82, 83]. Y. Zhang et. al. have showed that N-doped MWNTs synthesised via CVD growth exhibited a capacitance of 44.3 F/g, which was more than twice the value obtained than that of the un-doped MWNTs in a 6M KOH electrolyte [84]. K. Lee et. al. have shown that the nitrogen content on vertically aligned CNTs increases the capacitance until a certain point due to an increased donation of an electron by the N (N acts as an n-type dopant) and an enhanced wettability in aqueous systems [85]. Excessive N-doping significantly reduced the conductivity and inhibited charge storage and delivery [85]. The doped and un-doped CNTs were directly grown onto a stainless steel substrate using CVD [85].

1.7.3. Boron.

Boron is another interesting material for doping CNTs due to its p-type nature which promotes CNT growth and increases the oxidation temperature of the nanotubes [86]. However the development of boron doped CNTs for the use as electrodes in supercapacitor devices is not well established [15]. Work by Shiraishi et. al. showed that boron doping MWNTs, increased the capacitance per surface area from 6.5 $\mu F/cm^2$ to 6.8 $\mu F/cm^2$ in 0.5M LiBF4/PC [87]. These electrodes were

once again synthesised using CVD[87]. Wang et. al. reported in 2008 that interfacial capacitance was increased by 1.5-1.6 times in boron-doped carbon than that in boron-free carbon with alkaline electrolyte (6 M KOH) and/or acid electrolyte (1 M H_2SO_4) [88]. The carbon material was made into a slurry using carbon black and PTFE binder and pasted onto a Ni mesh current collector [88].

1.7.4. Advantages, limitations and comparison.

It can be seen that CNTs can be tailored different ways in order to tune (to a degree) the performance of the electrode material. This control has been demonstrated by firstly, varying the chirality of the nanotube to produce the single-walled or the multi-walled variety. Both CNT types have associated advantages and disadvantages with SWNTs being able to be synthesised with a high degree of purity; while MWNTs can be synthesised on a larger scale. CNTs can also have functionalities (through addition of oxygen or nitrogen containing groups) added to their structure through treatment in order to change the surface properties and hence wettability of the material. These functionalities enable enhanced compatibility to an electrolyte to maximise electroactive surface area usage and hence performance. Further doping with specific elements such boron and nitrogen can introduce a p-type/n-type behaviour where electrons contribute a Faradaic response to the system and enhance capacitance and energy density. However, it must be noted that when Faradaic processes occur at the electrode/electrolyte interface, irreversible processes increase degradation of the electrode over time. Specific capacitance of CNTs is in the order of 5 – 165 F/g with an increase

thereafter as a result of doping (i.e due to Faradaic contribution). When considering graphene and GO, the degree of crystallinity and functionality can also be varied depending on the synthesis method and extent of exfoliation. Reported capacitances for graphene based devices have a wide range exceeding 100 F/g, while extremely fast time constants have been reported due to the flat nature and mesoporosity of the graphene surface. Exfoliation of the graphene structure is extremely important as it minimises the effects of restacking, hence allowing maximum utilisation of the surface area. It must be pointed out that with electrical energy devices, there is always a trade-off between energy and power density. Therefore the electrode material has to be tailored to meet the requirements of the specific application.

1.8. Composite electrode materials.

Typical carbonaceous electrode materials (activated carbon, CNTs, graphene, CDC) with high surface areas used in supercapacitors have somewhat reached a limit when it comes energy storage capacity, thus restricting their possible applications [89]. Pseudocapacitor materials such as conducting polymers and metal oxides that are able to meet the needs of higher energy density are currently being developed and combined with carbonaceous materials in order to create composites that when designed into hybrid supercapacitors have advantages of fast rate capability, high storage capacity, and long cyclability [31, 89, 90]. Figure 1. 11 depict two processes at the electrode / electrolyte interface where EDLC and a reversible redox reaction leads to pseudocapacitance.

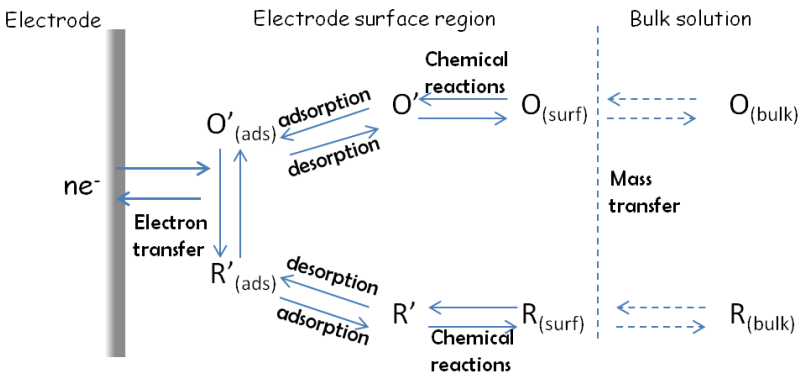

Figure 1. 11: Schematic diagram of a reversible redox reaction, as well as EDLC occurring at the electrode/electrolyte interface leading to pseudocapacitance.

1.8.1. Carbon / polymer.

The advent of researching supercapacitor composites comprised of inherently conducting polymers (ICPs) and CNTs is an area of research as the conductive polymer matrix, combined with the network like structure of the CNTs provides an enhanced electronic and ionic conductivity that can considerably improve charge storage and delivery [91-93].

H. Lee et. al. reported a polypyrrole / CNT composite electrode material that was fabricated into a device which had a specific capacitance of 153 F/g (1 M $LiClO_4$ / PC), coupled with an excellent stability (≈85% capacity retention) over 5000 cycles using galvanostatic charge / discharge [94]. The polypyrrole / CNT composite is depicted in Figure 1. 12 where SWNTs are thoroughly dispersed throughout the polypyrrole fibre matrix. Kim et. al. recently fabricated a ternary composite material consisting of MWNTs, graphene, and PANI where a specific capacitance of 1118 F/g

was achieved. The stability of this electrode was on the order of 85% capacity retention after 500 cycles using galvanostatic charge / discharge [95]. Hu et. al. have recently reported a composite electrode materials containing MWNTs coated with polypyrrole that achieved a high capacitance of 587 F/g in a 0.1 M $NaClO_4$ / acetonitrile electrolyte.

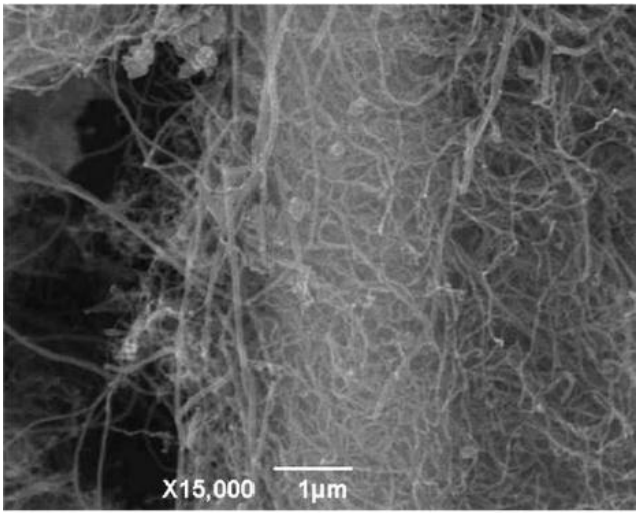

Figure 1. 12: SEM image of polypyrrole/SWNT composite showing coating of the polypyrrole fibre by CNTs [96].

1.8.2. Carbon / metal oxide.

Metal oxides exhibit pseudocapacitive behaviour over small rages of potentials, through redox processes which contribute electron transfer between the electrode / electrolyte interface (Figure 1. 11). Common materials used in the construction of such devices are oxides of manganese (Mn), ruthenium (Ru), iridium (Ir), platinum (Pt), Rhodium (Rh), palladium (Pd), gold (Au), cobalt (Co) and tungsten (W) [14, 18]. By combining metal oxides with CNTs, composites can be formed that combine both Faradaic and non-faradic effects enabling a larger energy density to be

obtained, while still holding reasonable power density. Figure 1. 13 shows MnO_2 particles that have been formed (insitu) in the presence of MWNTs.

Very recent work on carbon / metal oxide composites can be found in the review by Wang et. al. [39]. Myoungki et. al. reported recently in their a RuO_2 / MWNT electrode material which achieved a specific capacitance of 628 F/g [97]. The electrode was fabricated by dispersing the mixture in ethanol and casting onto carbon paper [97]. Li et. al. reported that when MWNT were coated with MnO_2 (Figure 1. 13), a capacitance of 350 F/g was achieved [98]. More novel materials have been created by incorporating MWNTs and Co_3O_4 yielded specific capacitances of 200 F/g [99] (acetylene black / PVDF slurry on Ni gauze); while Jayalakshmi et. al. reported in 2007 $V_2O_5.xH_2O$ / CNT film with a specific capacitance of 910 F/g with the material bring ground into a paste with paraffin and spread onto a graphite electrode, and tested in 0.1 M KCl [100].

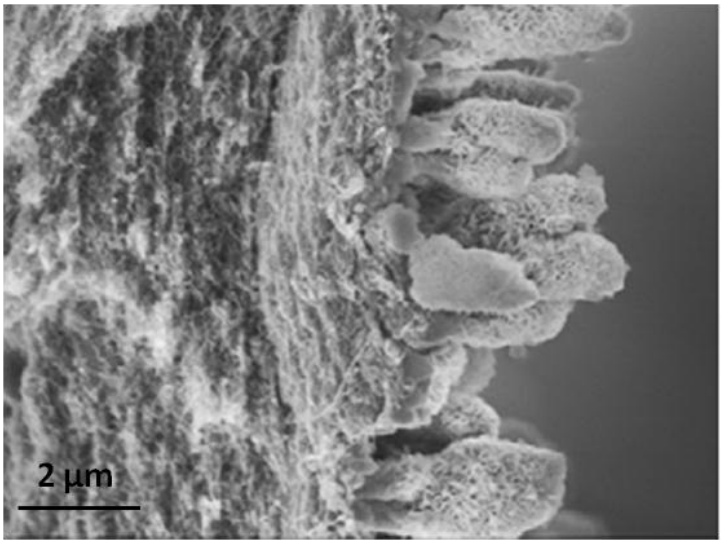

Figure 1. 13: Surface cross-section morphology of MnO_2 particles being grown (insitu) onto MWNTs [101].

1.8.3. Polymer / metal oxide.

As stated in section 1.8.2 above; metal oxides exhibit pseudocapacitive effects which contributes Faradaic charge transfer into the system. The combination of metal oxides with conductive polymers has been of particular interest due to the face that this polymer can act as a conductive binder which can supress degradation of the electrode surface and thus maintain good charge storage and delivery capability.

Work compiled by Z. Dong et. al. on polypyrrole / manganese oxide composite electrodes (Figure 1. 14) yielded specific capacitances of 376 F/g in 0.5 M Na_2SO_4 / H_2O [102].

J. Shaikh et. al. reported CuO / poly(acrylic acid) composites that yielded specific capacitances of 65 F/g in 1 M H_2SO_4; while most recently S. Mujawar et. al. showed that composites comprised of polyaniline and TiO_2 yielded a specific capacitance of 740 F/g at a discharge rate of 3 A/g in 0.5 M H_2SO_4 [103, 104].

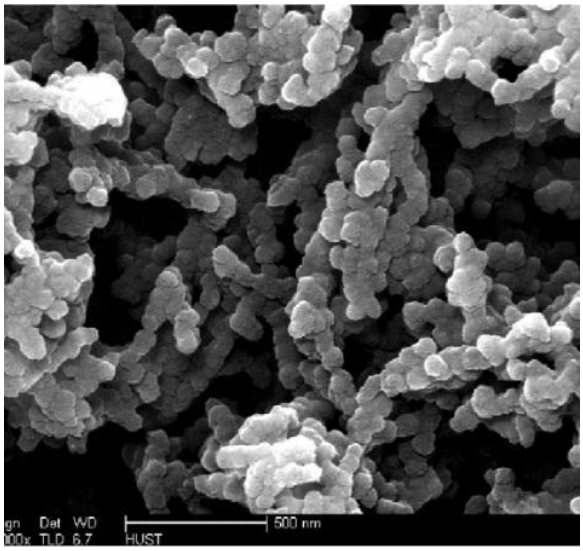

Figure 1. 14: Doped polypyrrole / manganese oxide nanocomposite developed by Z. Dong et.al for the use in supercapacitor device applications [102].

1.8.4. Composite carbon architectures.

Creating composite materials utilising CNTs and graphene / graphene oxides can be advantages due to the fact that the CNTs will provide microporosity (large surface area to maximise capacitance and hence energy density); while graphene / graphene oxide can be used to tailor the mesoporosity which improve ions kinetics, enhancing the power density [12]. In Figure 1. 15 composite of graphene oxide coated with SWNTs are depicted that has been formed into a porous film. The edges of the graphene oxide protrude out with a uniform coating of SWNTs. Recently, Li et. al. fabricated different mass loadings of graphene and CNT composite electrodes by solution casting onto glass, annealing then peeling off [105] They reported capacitance ranges of 70-110 F/g at a scan rate of 1 mV/s in 1M H_2SO_4 [105]. Xiangjun Lu have reported a CNT / graphene composite which was bound together with polypyrrole (through a filtration process) that achieved a

specific capacitance of 361 F/g at a current density of 0.2 A/g in 1 M KCl. The electrode exhibited excellent stability with only a 4% capacity loss over 2000 cycles [105]. Dong et. al. have shown that is it possible to form SWNT/graphene oxide core shell structures and spray coat the subsequent material onto a current collector [106]. The performance of these core structures yielded a material with a specific capacitance of 194 F/g using galvanostatic charge / discharge at a high current density of 0.8 A/g in 1 M KOH [106].

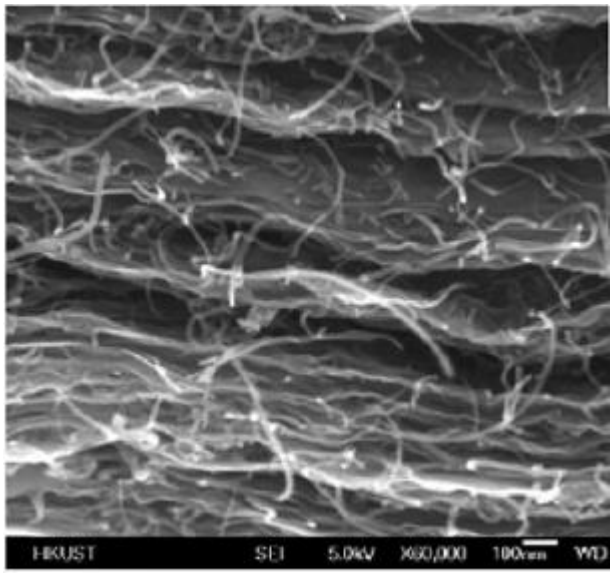

Figure 1. 15: SEM image of a reduced graphene oxide / SWNT composite formed into a film produced by Z. Huang et. al. [107].

1.9. Conclusions.

It can be seen that there has been extensive research and development in the use of CNT as electrode materials for energy storage applications. Currently they provide an excellent platform for devices that require high power density due to the very high surface areas and fast rate capability. Further studies need to be

implemented in order to better understand the relationship between electrode porosity and electrolyte. This is an enhanced understanding of the role of micro and mesoporosity and its effect on system performance. Electrolyte selection is also critical to device performance as it is proportional to the square of the voltage. The main classes of electrolytes are aqueous based, organic based and room temperature ionic liquids. Evolving work has focused on using CNT materials in conjunction with doping of various functional groups such as carboxyl's, amine's and elements such as boron and nitrogen in order to enhance the electrode performance through increased usage of electrode surface area and / or Faradaic contributions. The most recent work has focused on the creation of composite materials via the combination of CNTs with conducting polymers or metal oxides. This has amassed into a prevalent area of research through the search for the discovery of hybrid energy storage devices that are able to have high energy and high power density which are beneficial for creating more energy efficient systems and providing a greater range of applications.

1.10. Thesis objectives.

Research in the area of energy storage and conversion over the last decade has indicated that carbon materials in the form of nanotubes and graphene have great potential as electrode materials for supercapacitors. These materials can act as conductive supports and are advantageous due to their electronic properties, abundance and low cost. The purpose of this study is to improve the electrochemical performance of electrode materials for energy storage

applications. This is to be achieved by utilising appropriate materials, and combining them into composites in order to improve performance through the optimisation of key functional parameters that include; (i) surface area, (ii) conductivity, (iii) porosity, and (iv) kinetic mobility. In this thesis, nanostructured carbon additives in the form of CNTs and / or GO are combined with other conductive materials to form these composite electrodes. The reason for doing this is to develop electrode materials that have the right balance of microporosity and mesoporosity which enables utilisation of all the electroactive surface area and maximises the kinetics of the electrolyte ions. Optimum ratios of the composite materials are based on varying the weight ratios and studying the physical and electrochemical effects of these systems. The first approach is combining SWNTs with conducting polymer poly(3,4-ethylenedioxythiophene) poly(styrenesulfonate) or (PEDOT:PSS) whereby the PEDOR:PSS acts a conductive binder, thus enhancing conductivity. The second approach is a dedicated to developing exfoliated GO. This GO is used in the third and fourth approach to combine exfoliated GO and SWNTs. In the third approach, exfoliated and reduced GO is combined with the metal oxide manganosite (MnO) to enhance the non-Faradaic charge storage and delivery with Faradaic processes. Lastly, exfoliated and reduced GO is combined with SWNTs in order to develop an electrode platform whereby the GO sheets are separated by SWNTs thus tailoring the micro and mesoporosity.

1.11. References.

1. Turner, J. A., *A Realizable Renewable Energy Future.* Science, 1999. 285(5428): p. 687-689.
2. A. K. Shukla, S. S., K. Vijayamohanan, *Electrochemical supercapacitors: Energy storage beyond batteries.* Current Science, 2000. 79.
3. Arico, A. S., P. Bruce, B. Scrosati, J.-M. Tarascon, and W. van Schalkwijk, *Nanostructured materials for advanced energy conversion and storage devices.* Nat Mater, 2005. 4(5): p. 366-377.
4. Hall, P. J. and E. J. Bain, *Energy-storage technologies and electricity generation.* Energy Policy, 2008. 36(12): p. 4352-4355.
5. *About CEC*. 2012 [cited 30/12/12]; Available from: www.cleanenergycouncil.org.
6. Hall, P. J., M. Mirzaeian, S. I. Fletcher, F. B. Sillars, A. J. R. Rennie, G. O. Shitta-Bey, G. Wilson, A. Cruden, and R. Carter, *Energy storage in electrochemical capacitors: designing functional materials to improve performance.* Energy & Environmental Science, 2010.
7. A. J. Bard and L. R. Faulkner, *Electrochemical Methods: Fundamentals and Applications* 2001: John Wiley & Sons, Inc.
8. J. Koryta, J. D., L. Kavan, *Principles of Electrochemistry 2nd Edition* 1993: John Wiley & Sons Inc.
9. Yoon, S., C. Lee, S. M. Oh, Y.-K. Park, and W. Choon Choi, *Preparation of mesoporous carbon/manganese oxide materials and its application to*

supercapacitor electrodes. Journal of Non-Crystalline Solids, 2009. 355(4-5): p. 252-256.

10. Snook, G. A., P. Kao, and A. S. Best, *Conducting-polymer-based supercapacitor devices and electrodes.* Journal of Power Sources, 2011. 196(1): p. 1-12.

11. Qu Q. T., W. B., Yang L. C., Shi Y., Tian S., Wu Y. P., *Study on electrochemical performance of activated carbon in aqueous Li2SO4, Na2SO4 and K2SO4 electrolytes.* Electrochemistry Communications, 2008. 10(10): p. 1652-1655.

12. Bose, S., T. Kuila, A. K. Mishra, R. Rajasekar, N. H. Kim, and J. H. Lee, *Carbon-based nanostructured materials and their composites as supercapacitor electrodes.* Journal of Materials Chemistry, 2012. 22(3): p. 767-784.

13. Aaron Davies and A. Yu, *Material Advancements in Supercapacitors: From Activated Carbon to Carbon Nanotube and Graphene.* The Canadian Journal of Chemical Engineering, 2011. 89: p. 1342-1357.

14. Zhou, C., *PhD thesis*, Carbon Nanotube Based Electrochemical Supercapacitors, 2006. School of Polymer, Textile and Fiber Engineering, Georgia Institute of Technology

15. Inagaki, M., H. Konno, and O. Tanaike, *Carbon materials for electrochemical capacitors.* Journal of Power Sources, 2010. 195(24): p. 7880-7903.

16. Subramanian, V. R., S. Devan, and R. E. White, *An approximate solution for a pseudocapacitor.* Journal of Power Sources, 2004. 135(1-2): p. 361-367.

17. Delahay, P. and K. Holub, *Coupling of charging and Faradaic processes: Electrode admittance for reversible processes.* Journal of Electroanalytical Chemistry, 1968. 16(2): p. 131-136.

18. Liu, T. C., W. G. Pell, and B. E. Conway, *Stages in the development of thick cobalt oxide films exhibiting reversible redox behavior and pseudocapacitance.* Electrochimica Acta, 1999. 44(17): p. 2829-2842.

19. Pollak, E., G. Salitra, and D. Aurbach, *Can conductivity measurements serve as a tool for assessing pseudocapacitance processes occurring on carbon electrodes?* Journal of Electroanalytical Chemistry, 2007. 602(2): p. 195-202.

20. Bradley, D., *Ordered energy storage: Energy.* Materials Today, 2010. 13(1-2): p. 9-9.

21. Presser, V., M. Heon, and Y. Gogotsi, *Carbide-Derived Carbons – From Porous Networks to Nanotubes and Graphene.* Advanced Functional Materials, 2011. 21(5): p. 810-833.

22. Zhang, L. L. and X. S. Zhao, *Carbon-based materials as supercapacitor electrodes.* Chemical Society Reviews, 2009. 38(9): p. 2520-2531.

23. *Battery and Energy Technologies*. 2012 [cited 14/06/12]; Available from: http://www.mpoweruk.com/performance.htm.

24. Griffiths, D. J., *Introduction to Electrodynamics*. Third ed 1999, New Jersey: Prentice Hall.

25. Conway, B. E., *Electrochemical Supercapacitors: Scientific Fundamentals and Technological Applications.* 1999, New York: Kluwer Acedemic / Plenum Publishers.

26. Lewandowski, A., A. Olejniczak, M. Galinski, and I. Stepniak, *Performance of carbon-carbon supercapacitors based on organic, aqueous and ionic liquid electrolytes.* Journal of Power Sources, 2010. 195(17): p. 5814-5819.

27. Kötz, R. and M. Carlen, *Principles and applications of electrochemical capacitors.* Electrochimica Acta, 2000. 45(15-16): p. 2483-2498.

28. Zhang, F., T. Zhang, X. Yang, L. Zhang, K. Leng, Y. Huang, and Y. Chen, *A high-performance supercapacitor-battery hybrid energy storage device based on graphene-enhanced electrode materials with ultrahigh energy density.* Energy & Environmental Science, 2013. 6(5): p. 1623-1632.

29. Sudhakar, Y. N. and M. Selvakumar, *Lithium perchlorate doped plasticized chitosan and starch blend as biodegradable polymer electrolyte for supercapacitors.* Electrochimica Acta, 2012. 78(0): p. 398-405.

30. Jong, H. J., K. Akiko, M. Kenji, and N. Katsuhiko, *Supercapacitor Performance of Hydrous Ruthenium Oxide Electrodes Prepared by Electrophoretic Deposition.* Journal of The Electrochemical Society, 2006. 153(2): p. A321-A328.

31. Patel, D., *PhD thesis*, Carbon Nanofibres for Use in Supercapacitors, 2006. Loughborough University

32. Yoo, J. J., K. Balakrishnan, J. Huang, V. Meunier, B. G. Sumpter, A. Srivastava, M. Conway, A. L. Mohana Reddy, J. Yu, R. Vajtai, and P. M. Ajayan, *Ultrathin Planar Graphene Supercapacitors.* Nano Letters, 2011. 11(4): p. 1423-1427.

33. Iijima, S., *Helical microtubules of graphitic carbon.* Nature, 1991. 354(6348): p. 56-58.

34. Anantram, M. P. and F. Léonard, *Physics of carbon nanotube electronic devices* Rep. Prog. Phys. , 2006. 69

35. Chung, J., K.-H. Lee, J. Lee, and R. S. Ruoff, *Toward Large-Scale Integration of Carbon Nanotubes.* Langmuir, 2004. 20(8): p. 3011-3017.

36. Yu, B., F. Zhou, G. Liu, Y. Liang, W. T. S. Huck, and W. Liu, *The electrolyte switchable solubility of multi-walled carbon nanotube/ionic liquid (MWCNT/IL) hybrids.* Chemical Communications, 2006(22): p. 2356-2358.

37. Liu, J., O. M. Dunens, K. J. Mackenzie, C. H. See, and A. T. Harris, *Postsynthesis microwave treatment to give high-purity multiwalled carbon nanotubes.* AIChE Journal, 2008. 54(12): p. 3303-3307.

38. Che, G., B. B. Lakshmi, C. R. Martin, and E. R. Fisher, *Metal-Nanocluster-Filled Carbon Nanotubes:â€‰ Catalytic Properties and Possible Applications in Electrochemical Energy Storage and Production.* Langmuir, 1999. 15(3): p. 750-758.

39. Wang, G., L. Zhang, and J. Zhang, *A review of electrode materials for electrochemical supercapacitors.* Chemical Society Reviews, 2012. 41(2): p. 797-828.

40. Huang, C. W., C. T. Hsieh, P. L. Kuo, and H. Teng, *Electric double layer capacitors based on a composite electrode of activated mesophase pitch and carbon nanotubes.* Journal of Materials Chemistry, 2012. 22(15): p. 7314-7322.

41. Dai, L., *Carbon Nanotechnology* 2006, Amsterdam: Elsevier.

42. Deng, F. and Q. Zheng, *Interaction models for effective thermal and electric conductivities of carbon nanotube composites.* Acta Mechanica Solida Sinica, 2009. 22(1): p. 1-17.

43. Obreja, V. V. N., *On the performance of supercapacitors with electrodes based on carbon nanotubes and carbon activated material--A review.* Physica E: Low-dimensional Systems and Nanostructures, 2008. 40(7): p. 2596-2605.

44. Kay Hyeok An, Kwan Koo Jeon, Won Seok Kim, Young Soo Park, Seong Chu Lim, Dong Jae Bae, and Y. H. Lee, *Characterization of Supercapacitors Using Singlewalled Carbon Nanotube Electrodes.* Journal of the Korean Physical Society, 2001. 39: p. S511-S517.

45. Hu, S., R. Rajamani, and X. Yu, *Flexible solid-state paper based carbon nanotube supercapacitor.* Applied Physics Letters, 2012. 100(10).

46. *School of Pharmacy, Research Program: University of Waterloo.* [cited 20/16/12]; Available from: http://science.uwaterloo.ca/~foldvari/images/SWNT-MWNT.jpg.

47. Morant, C., T. Campo, F. Marquez, C. Domingo, J. M. Sanz, and E. Elizalde, *Mo-Co catalyst nanoparticles: Comparative study between TiN and Si surfaces for single-walled carbon nanotube growth.* Thin Solid Films, 2012. 520(16): p. 5232-5238.

48. Candelaria, S. L., Y. Shao, W. Zhou, X. Li, J. Xiao, J. G. Zhang, Y. Wang, J. Liu, J. Li, and G. Cao, *Nanostructured carbon for energy storage and conversion.* Nano Energy, 2012. 1(2): p. 195-220.

49. Y. Zhu, D. K. James, and J. M. Tour, *New routes to grapheen, graphene oxide and their related applications.* Advanced Materials, 2012. 24: p. 4924-4955.

50. Chen, S., J. Zhu, and X. Wang, *From Graphene to Metal Oxide Nanolamellas: A Phenomenon of Morphology Transmission.* ACS Nano, 2010. 4(10): p. 6212-6218.

51. Ravindra Kempaiah, Alfred Chung, and V. Maheshwari, *Graphene as Cellular Interface: Electromechanical Coupling with Cells.* ACS Nano, 2011. 5(7): p. 6025-6031.

52. Marcano, D. C., D. V. Kosynkin, J. M. Berlin, A. Sinitskii, Z. Sun, A. Slesarev, L. B. Alemany, W. Lu, and J. M. Tour, *Improved Synthesis of Graphene Oxide.* ACS Nano, 2010. 4(8): p. 4806-4814.

53. Eda, G. and M. Chhowalla, *Chemically Derived Graphene Oxide: Towards Large-Area Thin-Film Electronics and Optoelectronics.* Advanced Materials, 2010. 22(22): p. 2392-2415.

54. Srinivas, G., J. Burress, and T. Yildirim, *Graphene oxide derived carbons (GODCs): Synthesis and gas adsorption properties.* Energy and Environmental Science, 2012. 5(4): p. 6453-6459.

55. Jae Young Kim, Ji-Wook Jang, Duck Hyun Youn, Jae Yul Kim, Eun Sun Kim, and J. S. Lee, *Graphene–carbon nanotube composite as an effective conducting scaffold to enhance the photoelectrochemical water oxidation activity of a hematite film.* The Royal Society of Chemistry, 2012.

56. Qian, W., R. Hao, J. Zhou, M. Eastman, B. A. Manhat, Q. Sun, A. M. Goforth, and J. Jiao, *Exfoliated graphene-supported Pt and Pt-based alloys as*

electrocatalysts for direct methanol fuel cells. Carbon, 2013. 52(0): p. 595-604.

57. Stoller, M. D., S. Park, Y. Zhu, J. An, and R. S. Ruoff, *Graphene-Based Ultracapacitors.* Nano Letters, 2008. 8(10): p. 3498-3502.

58. Chen, Y., X. Zhang, D. Zhang, P. Yu, and Y. Ma, *High performance supercapacitors based on reduced graphene oxide in aqueous and ionic liquid electrolytes.* Carbon, 2011. 49(2): p. 573-580.

59. J. R. Miller, R. A. Outlaw, and B. C. Holloway, *Graphene DLC with ac line filtering performance.* Science, 2010. 329(1637).

60. Frackowiak, E., K. Metenier, V. Bertagna, and F. Beguin, *Supercapacitor electrodes from multiwalled carbon nanotubes.* Applied Physics Letters, 2000. 77(15): p. 2421.

61. Pauliukaite, R., M. E. Ghica, O. Fatibello-Filho, and C. M. A. Brett, *Electrochemical impedance studies of chitosan-modified electrodes for application in electrochemical sensors and biosensors.* Electrochimica Acta, 2010. 55(21): p. 6239.

62. Dolatshahi-Pirouz, A., K. Rechendorff, M. B. Hovgaard, M. Foss, J. Chevallier, and F. Besenbacher, *Bovine serum albumin adsorption on nano-rough platinum surfaces studied by QCM-D.* Colloids and Surfaces B: Biointerfaces, 2008. 66(1): p. 53.

63. Sherman, L. M. *Carbon Nanotubes Lots of Potential--If the Price is Right*. 2007 [cited 01/05/12]; Available from: www.ptonline.com/articles/carbon-nanotubes-lots-of-potentialif-the-price-is-right.

64. Kierzek, K., E. Frackowiak, G. Lota, G. Gryglewicz, and J. Machnikowski, *Electrochemical capacitors based on highly porous carbons prepared by KOH activation.* Electrochimica Acta, 2004. 49(4): p. 515-523.

65. Izadi-Najafabadi, A., S. Yasuda, K. Kobashi, T. Yamada, D. N. Futaba, H. Hatori, M. Yumura, S. Iijima, and K. Hata, *Extracting the Full Potential of Single-Walled Carbon Nanotubes as Durable Supercapacitor Electrodes Operable at 4 V with High Power and Energy Density.* Advanced Materials: p. n/a-n/a.

66. Kim, B. C., G. G. Wallace, Y. I. Yoon, J. M. Ko, and C. O. Too, *Capacitive properties of RuO2 and Ru-Co mixed oxide deposited on single-walled carbon nanotubes for high-performance supercapacitors.* Synthetic Metals, 2009. 159(13): p. 1389-1392.

67. P. Chen, J. C., J. Qiu, C. Zhou, Nano Research, 2010. 3: p. 594-603.

68. Chau, T. T., W. J. Bruckard, P. T. L. Koh, and A. V. Nguyen, *A review of factors that affect contact angle and implications for flotation practice.* Advances in Colloid and Interface Science, 2009. 150(2): p. 106-115.

69. K. Kuratani, T. K., N. Kuriyama, Journal of Power Sources, 2009. 189: p. 1284-1291.

70. B.P. Bakhmatyuk, B. Y. V., I.I. Grygorchak, M.M. Micov, Journal of Power Sources, 2008. 180: p. 890-895.

71. Pan, H., J. Li, and Y. Feng, *Carbon Nanotubes for Supercapacitor.* Nanoscale Research Letters, 2010. 5(3): p. 654-668.

72. Fuertes, A. B., G. Lota, T. A. Centeno, and E. Frackowiak, *Templated mesoporous carbons for supercapacitor application.* Electrochimica Acta, 2005. 50(14): p. 2799-2805.

73. Shen, J., A. Liu, Y. Tu, G. Foo, C. Yeo, M. B. Chan-Park, R. Jiang, and Y. Chen, *How carboxylic groups improve the performance of single-walled carbon nanotube electrochemical capacitors?* Energy & Environmental Science, 2011. 4(10): p. 4220-4229.

74. Wu, Z.-S., W. Ren, L. Xu, F. Li, and H.-M. Cheng, *Doped Graphene Sheets as Anode Materials with Superhigh Rate and Large Capacity for Lithium Ion Batteries.* ACS Nano, 2011: p. 5463–5471.

75. Babel, K. and K. Jurewicz, *Electrical capacitance of fibrous carbon composites in supercapacitors.* Fuel Processing Technology, 2002. 77-78: p. 181-189.

76. Béguin, F., K. Szostak, G. Lota, and E. Frackowiak, *A Self-Supporting Electrode for Supercapacitors Prepared by One-Step Pyrolysis of Carbon Nanotube/Polyacrylonitrile Blends.* Advanced Materials, 2005. 17(19): p. 2380-2384.

77. Drage, T. C., A. Arenillas, K. M. Smith, C. Pevida, S. Piippo, and C. E. Snape, *Preparation of carbon dioxide adsorbents from the chemical activation of urea-formaldehyde and melamine-formaldehyde resins.* Fuel, 2007. 86(1-2): p. 22-31.

78. Inagaki, N., K. Narushima, H. Hashimoto, and K. Tamura, *Implantation of amino functionality into amorphous carbon sheet surfaces by NH3 plasma.* Carbon, 2007. 45(4): p. 797-804.

79. Li, W., D. Chen, Z. Li, Y. Shi, Y. Wan, J. Huang, J. Yang, D. Zhao, and Z. Jiang, *Nitrogen enriched mesoporous carbon spheres obtained by a facile method and its application for electrochemical capacitor.* Electrochemistry Communications, 2007. 9(4): p. 569-573.

80. Stein, A., Z. Wang, and M. A. Fierke, *Functionalization of Porous Carbon Materials with Designed Pore Architecture.* Advanced Materials, 2009. 21(3): p. 265-293.

81. Wei, J., D. Zhou, Z. Sun, Y. Deng, Y. Xia, and D. Zhao, *A Controllable Synthesis of Rich Nitrogen-Doped Ordered Mesoporous Carbon for CO2 Capture and Supercapacitors.* Advanced Functional Materials, 2013. 23(18): p. 2322-2328.

82. Peigney, A., C. Laurent, E. Flahaut, R. R. Bacsa, and A. Rousset, *Specific surface area of carbon nanotubes and bundles of carbon nanotubes.* Carbon, 2001. 39(4): p. 507-514.

83. Niu, J. J., J. N. Wang, Y. Jiang, L. F. Su, and J. Ma, *An approach to carbon nanotubes with high surface area and large pore volume.* Microporous and Mesoporous Materials, 2007. 100(1-3): p. 1-5.

84. Zhang, Y., C. Liu, B. Wen, X. Song, and T. Li, *Preparation and electrochemical properties of nitrogen-doped multi-walled carbon nanotubes.* Materials Letters, 2011. 65(1): p. 49-52.

85. Lee, K.-Y., Y.-S. Lin, Y.-M. Chen, and Y.-S. Huang, *Influence of the nitrogen content on the electrochemical capacitor characteristics of vertically aligned*

carbon nanotubes. Physica E: Low-dimensional Systems and Nanostructures, 2010. 42(10): p. 2799-2803.

86. Antal A. Koósa, E. A. Obraztsova, A. Crossley, and N. Grobert, *Comparison of structural changes in nitrogen and boron-doped multi-walled carbon nanotubes.* Carbon, 2010. 48(11): p. 3033-3041.

87. Shiraishi, S., M. Kibe, T. Yokoyama, H. Kurihara, N. Patel, A. Oya, Y. Kaburagi, and Y. Hishiyama, *Electric double layer capacitance of multi-walled carbon nanotubes and B-doping effect.* Applied Physics A: Materials Science and Processing, 2006. 82(4 SPEC. ISS.): p. 585-591.

88. Wang, D.-W., F. Li, Z.-G. Chen, G. Q. Lu, and H.-M. Cheng, *Synthesis and Electrochemical Property of Boron-Doped Mesoporous Carbon in Supercapacitor.* Chemistry of Materials, 2008. 20(22): p. 7195-7200.

89. Fu, C., H. Zhou, R. Liu, Z. Huang, J. Chen, and Y. Kuang, *Supercapacitor based on electropolymerized polythiophene and multi-walled carbon nanotubes composites.* Materials Chemistry and Physics, 2011. 132(2): p. 596-600.

90. Wu, Z. S., G. Zhou, L. C. Yin, W. Ren, F. Li, and H. M. Cheng, *Graphene/metal oxide composite electrode materials for energy storage.* Nano Energy, 2012. 1(1): p. 107-131.

91. S. Bhandari, M. Deepa, A. K. Srivastava, A. G. Joshi, and R. Kant, *PEDOT-MWNTs commposite films.* J. Phys. Chem B, 2009. 113: p. 9416-9428.

92. Zhang, X., J. Liu, B. Xu, Y. Su, and Y. Luo, *Ultralight conducting polymer/carbon nanotube composite aerogels.* Carbon, 2011. 49(6): p. 1884-1893.

93. Crispin, X., F. L. E. Jakobsson, A. Crispin, P. C. M. Grim, P. Andersson, A. Volodin, C. van Haesendonck, M. Van der Auweraer, W. R. Salaneck, and M. Berggren, *The Origin of the High Conductivity of Poly(3,4-ethylenedioxythiophene) Poly(styrenesulfonate) (PEDOT/PSS) Plastic Electrodes.* Chemistry of Materials, 2006. 18(18): p. 4354-4360.

94. Antiohos, D., G. Folkes, P. Sherrell, S. Ashraf, G. G. Wallace, P. Aitchison, A. T. Harris, J. Chen, and A. I. Minett, *Compositional effects of PEDOT-PSS/single walled carbon nanotube films on supercapacitor device performance.* Journal of Materials Chemistry, 2011. 21(40): p. 15987-15994.

95. Kim, K.-S. and S.-J. Park, *Influence of multi-walled carbon nanotubes on the electrochemical performance of graphene nanocomposites for supercapacitor electrodes.* Electrochimica Acta, 2011. 56(3): p. 1629-1635.

96. Lee, H., H. Kim, M. S. Cho, J. Choi, and Y. Lee, *Fabrication of polypyrrole (PPy)/carbon nanotube (CNT) composite electrode on ceramic fabric for supercapacitor applications.* Electrochimica Acta, 2011. 56(22): p. 7460-7466.

97. Myoungki, M., M. Kenji, J. Jong Hyun, and N. Katsuhiko, *Hydrous RuO2/Carbon Black Nanocomposites with 3D Porous Structure by Novel Incipient Wetness Method for Supercapacitors.* Journal of The Electrochemical Society, 2006. 153(2): p. A334-A338.

98. Zhai, Y., Y. Dou, D. Zhao, P. F. Fulvio, R. T. Mayes, and S. Dai, *Carbon materials for chemical capacitive energy storage.* Advanced Materials, 2011. 23(42): p. 4828-4850.

99. Shan, Y. and L. Gao, *Formation and characterization of multi-walled carbon nanotubes/Co3O4 nanocomposites for supercapacitors.* Materials Chemistry and Physics, 2007. 103: p. 206-210.

100. Jayalakshmi, M., M. M. Rao, N. Venugopal, and K.-B. Kim, *Hydrothermal synthesis of SnO2-V2O5 mixed oxide and electrochemical screening of carbon nano-tubes (CNT), V2O5, V2O5-CNT, and SnO2-V2O5-CNT electrodes for supercapacitor applications.* Journal of Power Sources, 2007. 166(2): p. 578-583.

101. Li, Q., J. M. Anderson, Y. Chen, and L. Zhai, *Structural evolution of multi-walled carbon nanotube/MnO2 composites as supercapacitor electrodes.* Electrochimica Acta, 2011. 59(0): p. 548-557.

102. Dong, Z. H., Y. L. Wei, W. Shi, and G. A. Zhang, *Characterisation of doped polypyrrole/manganese oxide nanocomposite for supercapacitor electrodes.* Materials Chemistry and Physics, 2011. 131(1–2): p. 529-534.

103. Shaikh, J. S., R. C. Pawar, N. L. Tarwal, D. S. Patil, and P. S. Patil, *Supercapacitor behavior of CuO–PAA hybrid films: Effect of PAA concentration.* Journal of Alloys and Compounds, 2011. 509(25): p. 7168-7174.

104. Mujawar, S. H., S. B. Ambade, T. Battumur, R. B. Ambade, and S.-H. Lee, *Electropolymerization of polyaniline on titanium oxide nanotubes for supercapacitor application.* Electrochimica Acta, 2011. 56(12): p. 4462-4466.

105. Li, J. J., Y. W. Ma, X. Jiang, X. M. Feng, Q. L. Fan, and W. Huang, *Graphene/carbon nanotube films prepared by solution casting for*

electrochemical energy storage. IEEE Transactions on Nanotechnology, 2012. 11(1): p. 3-7.

106. Dong, X., G. Xing, M. B. Chan-Park, W. Shi, N. Xiao, J. Wang, Q. Yan, T. C. Sum, W. Huang, and P. Chen, *The formation of a carbon nanotube-graphene oxide core-shell structure and its possible applications.* Carbon, 2011. 49(15): p. 5071-5078.

107. Huang, Z.-D., B. Zhang, R. Liang, Q.-B. Zheng, S. W. Oh, X.-Y. Lin, N. Yousefi, and J.-K. Kim, *Effects of reduction process and carbon nanotube content on the supercapacitive performance of flexible graphene oxide papers.* Carbon, 2012. 50(11): p. 4239-4251.

Chapter 2: Experimental.

2. Experimental.

2.1. Chemicals and reagents used.

All chemicals and reagents are listed and were used as received unless otherwise stated.

Table 2. 1: Chemicals and reagents used.

Reagent Name	**Grade / batch**	**Company**
Acetonitrile	Analytical reagent	Ajax Finechem
Commercial Poly(3,4-ethylenedioxythiophene) poly(styrenesulfonate)	batch# A65 00000 AC	AGFA
Carbon black	Vulcan XC72R	CABOT
Carbon nanotubes; single walled	HiPCO variety, batch# P0900. Individual diameter 0.8 – 1.2 nm. Length 100 – 1000 nm.	Unidym Carbon Nanotubes
Ethanol	Analytical reagent, 96% (v/v)	Ajax Finechem
Graphite powder		Bay Carbon Inc.
H_2SO_4	Analytical reagent, 98 (w/v)	Univar

H_2O_2	Analytical reagent, 30% (w/v)	Univar
HCl	Analytical reagent, 36% (w/v)	Univar
$KMNO_4$	Analytical reagent	Sigma-Aldrich
$K_3Fe(CN)_6$	Analytical reagent	Ajax
Polytetrafluoroethylene 60 wt% dispersed in water		Sigma-Aldrich
UV cure glue		Dynman Light Weld

2.2. Physical characterisation techniques.

Physical characterisation of synthesised materials was achieved by scanning electron microscopy (SEM), energy dispersive x-ray (EDS), Raman spectroscopy, x-ray diffraction (XRD), UV-visible spectroscopy (UV-vis), x-ray photo-electron spectroscopy (XPS), thermo-gravimetric analysis (TGA), ultra sonication, and sputter coating. Here, SEM was able to show the morphology of the various studied materials. EDS was employed to observe qualitatively different compositions throughout a material. Raman spectroscopy used to assess the vibrational properties of the various materials fabricated. XRD was employed in order to understand the crystallinity of the structure and what type of compounds were present. XPS was used to quantify the O and C component before and after exfoliation. TGA was able to show the thermal stability of materials. UV-vis was

employed to observe any changes in conjugation and also monitor absorbance for concentration calculations. Probe sonication and centrifugation was used to obtain uniform dispersions of SWNTs, GO, mw rGO and the various composites formed.

2.2.1. Scanning electron microscopy.

In scanning electron microscopy (SEM), a small bias voltage is applied between a conducting specimen and the tip of a probe. The bias voltage applied causes electrons to tunnel through the barrier separating the two surfaces due to the small proximity of the probe tip and specimen surface. As the probe scans the specimen, a constant tunnelling current is maintained through a feedback system [1]. The probe tip electrons interact with electrons in the sample leading to the generation of various signals that are detected (see inset of Figure 2. 1). Their detection, coupled with the two dimensional motion of the electron beam (raster scan pattern) forms an image of the specimen that contains information on its topography and composition [1].

SEM and transmitted electron detection (TED) images were obtained from a JEOL JSM-7500FA field emission SEM as is seen in Figure 2. 1. For SEM and TED imaging the accelerating voltage was 5.0 kV and 30 kV respectively with the emission current being set at 10 μA and 20 μA . Samples for TED imaging were drop cast onto 200 rest copper grids coated with a uniform carbon-layer (EMS, USA).

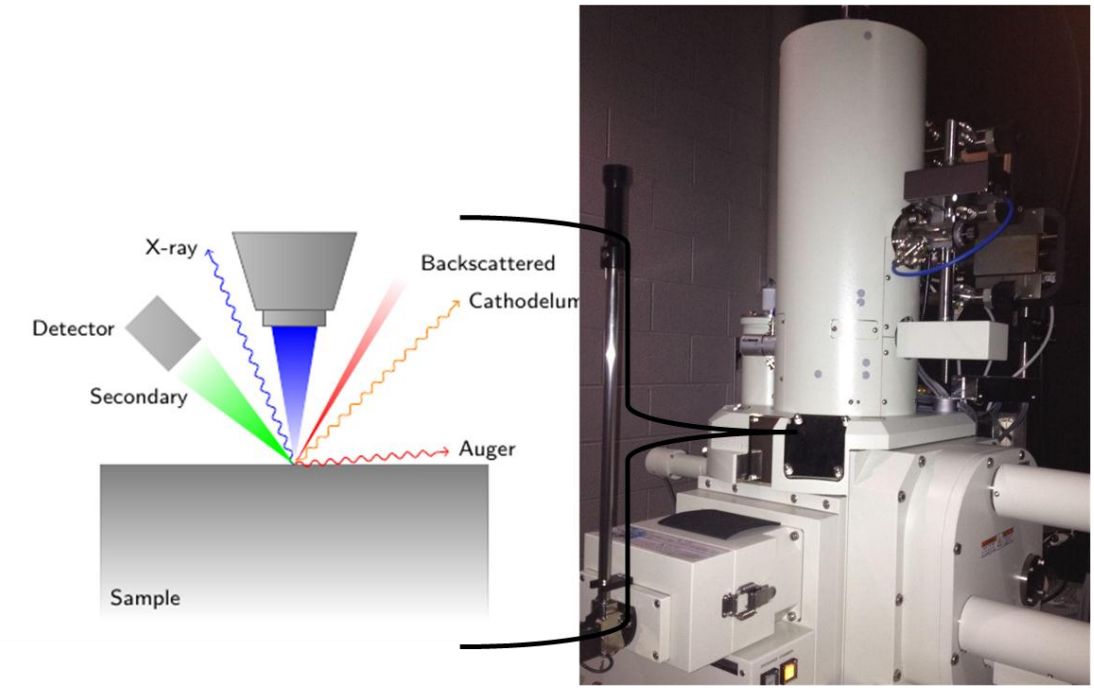

Figure 2. 1: Photograph of JEOL-7500FA field emission gun scanning electron microscope. (Inset); mechanism of scanning electron microscopy [2].

2.2.2. Energy dispersive X-ray spectroscopy.

Energy dispersive x-ray (EDS) are characteristic x-ray signals that are detected after electrons from the probe tip have interacted with the specimen as is depicted in the inset of Figure 2. 1.

EDS spectra were taken on a JEOL JSM-6490LA, where the accelerating voltage was 15kV and the emission current was 19.5µA.

2.2.3. Raman spectroscopy.

A majority of compounds, whether organic or inorganic that have covalent bonding adsorb various frequencies of electromagnetic radiation in the infrared region

portion of the electromagnetic spectrum. This region lies in between the visible and microwave spectrum where the vibrational infrared frequencies lie at wavelengths between 4000 cm^{-1} to 650 cm^{-1} [3]. When light of these wavelengths are absorbed, it induces different types of vibrations within molecules, with the absorbance spectra being characteristic to each molecule.

The reason for this is due to the fact that every type of bond has a different natural frequency of vibration, and since two of the same type of bond in different compounds are in slightly varying environments, no two different molecules can have the same infrared adsorption pattern [3].

Raman spectroscopy was carried out on a Jobin-Yvon Horbia 800 using a 632.81 nm laser. The data analysis was carried out using Labspec V.5.45.09 software.

Figure 2. 2: Photograph of Raman spectroscopy apparatus, Jobin-Yvon Horbia 800.

2.2.4. *X-ray diffraction.*

X-rays are electromagnetic waves with wavelengths ranging from 0.01 nm to a few nanometres. This wavelength size is comparable to that of inter-planar spacing in crystals, thus meaning the use of X-rays are useful in structure determination [4]. In X-ray diffraction (XRD) the X-ray beam is incident on a surface of a material, interacting with the planes of atoms in the crystal. Here, a portion of the X-ray beam will become scattered / diffracted due to interaction with the crystal structure. This diffracted beam is at a well-defined angle 2θ to the incident beam as can be seen from Figure 2. 3 [4]. Every diffraction pattern for an element or compound is unique, thus allowing the structure of different materials to be assessed. XRD was carried out on a GBC MMA XRD (λ = 1.54 Å) with the voltage and current kept at -40 kV and 25 mA respectively.

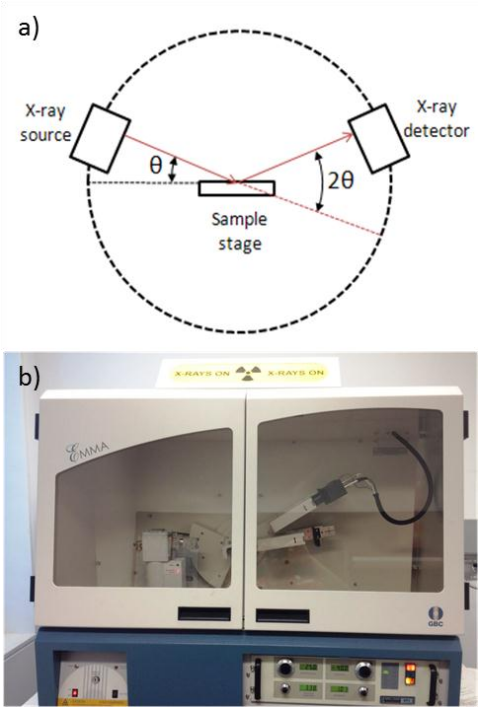

Figure 2. 3: (a) A schematic illustration of X-ray diffraction by a crystal [5]. (b) Photograph of GBC MMA XRD machine used for XRD experiments.

2.2.5. *UV-visible spectroscopy.*

In some cases, useful information can be obtained in the UV-visible (vis) portion of the electromagnetic spectrum which varies between 190 nm and 800 nm. In this type of spectroscopy, a portion of the incident radiation is adsorbed where electrons in the material undergo a transition from a low energy state to a high energy state where the electromagnetic radiation is equal to the energy difference between the excited and ground state [3]. Since there are many possible electronic transitions each differing only very slightly (see Figure 2. 4), the spectrum will consist of a broad band adsorption centred about a major wavelength of the transition.

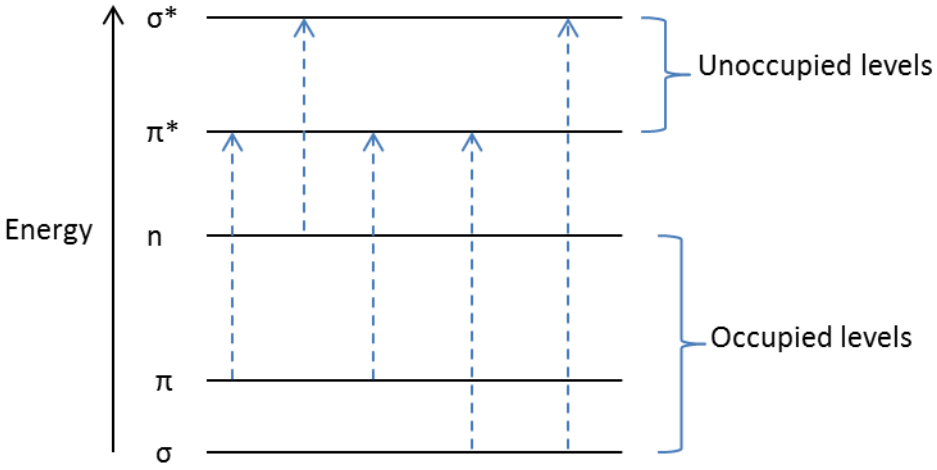

Figure 2. 4: Electronic energy levels and transitions of the excitation process.

Changes in position of this wavelength occur for different molecules / compounds and when combined with other techniques leads to valuable structural insights [3]. UV-visible spectroscopy was recorded using a UV 3600 Shimadzu UV-Vis-NIR spectrophotometer to monitor the changes (if any) in the degree of conjugation

between graphene oxide (GO) before and after irradiation microwave irradiation. The wavelength range was performed between 700 nm and 250 nm.

UV-vis was also used to calculate the concentration of GO dissolved in solution based on the linearity of the absorbance responses for known concentrations at 550 nm. This was used to determine any concentrations of GO after centrifugation where larger agglomerates are removed from a dispersion.

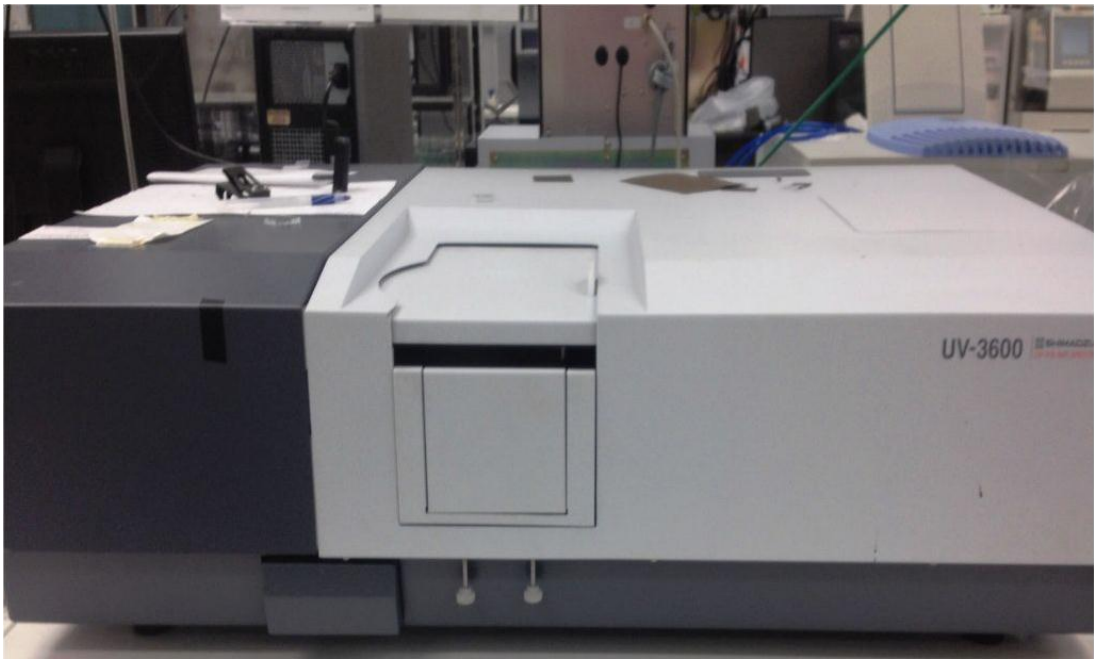

Figure 2. 5: Photograph of Shimadzu UV-Vis-NIR spectrophotometer.

2.2.6. X-ray photoelectron spectroscopy.

X-ray photoelectron spectroscopy (XPS) is a type of spectroscopic technique used for elemental quantitative analysis of samples. The spectra is obtained by irradiation of the sample in question with a beam of x-rays which knocks out electrons from the 1s, 2s, 2p, 3s, etc. orbitals of the material as is shown by Figure

2. 6 [6]. A detector records the kinetic energy and number of electrons that have been emitted through this interaction. The energy of the emitted electron is characteristic of that material and the resulting spectra are thus unique. This technique can describe any change in surface chemistry between different materials [6].

XPS was performed on a PHOIBOS 100 hemispherical energy analyser from SPECS, using Al, Kα radiation (1486.6 eV) in fixed analyser transmission mode.

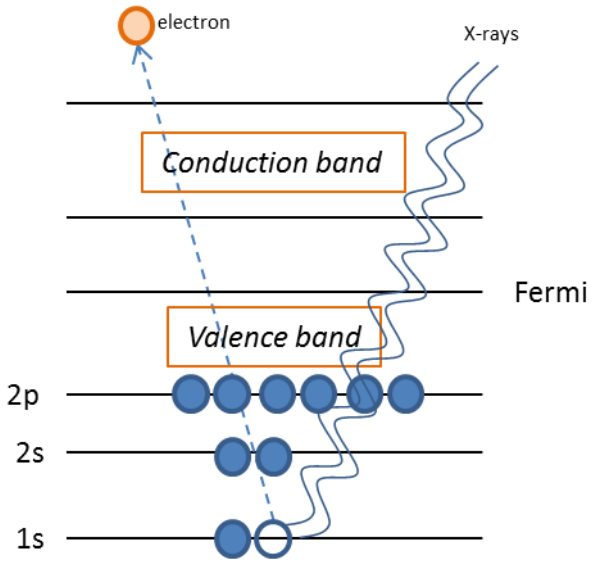

Figure 2. 6: Representation of the processes involved in XPS.

2.2.7. Thermo-gravimetric analysis.

TGA was performed using a Q500 (TA Instruments) with the data analysis carried out using the Q Series software V. 2.5.0.255 (TA Instruments). Temperature range is between 100^0C to 900^0C at a ramp rate of 10 deg/min with a combined gas flow of 10 ml/min Ar and 90 ml/min air.

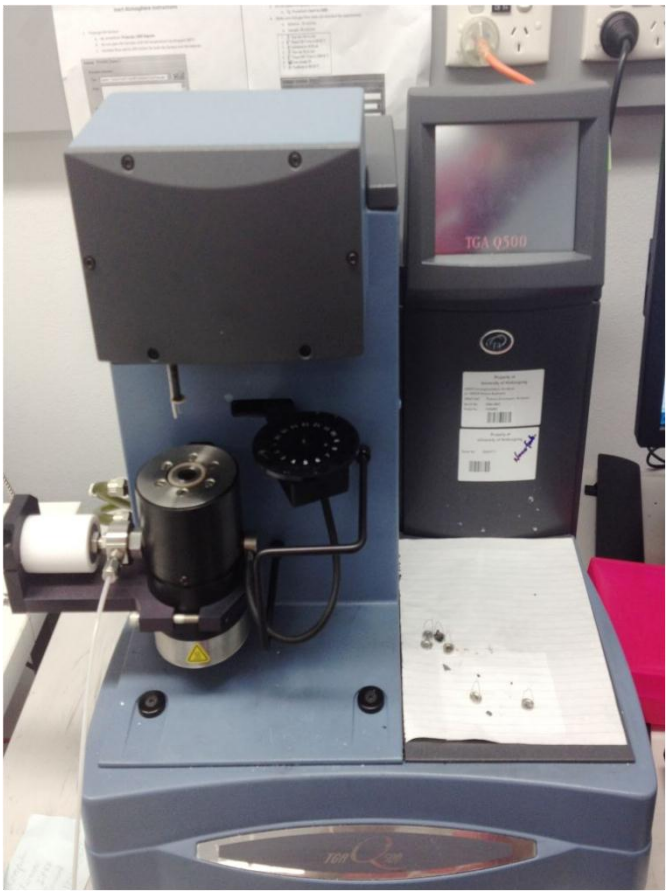

Figure 2. 7: Photograph of the TGA Q500 system.

2.2.8. Ultra-sonication.

The dispersion of carbon containing composites was carried out using a Branson Digital Sonifier Model 102C at 450 W, 20 Hz in a pulsed method (2 seconds on, 1 second). Different composites had varying sonication times and amplitude which are outlined in the specific chapter.

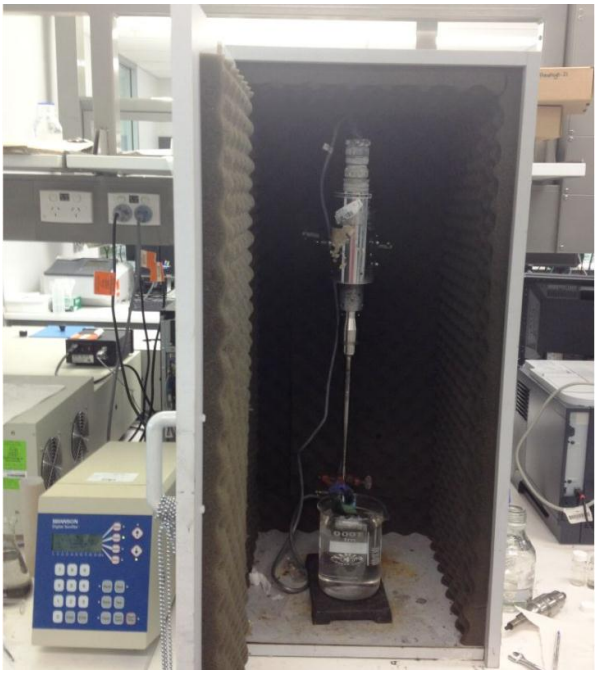

Figure 2. 8: Photograph of Branson Digital Sonifier.

2.2.9. Centrifugation.

Centrifugation of carbon materials and their composites dispersed in various solvents was performed using an eppendorf centrifuge 5702.

Figure 2. 9: Eppendorf centrifuge used to remove agglomerates from solution.

2.2.10. Contact angle measurements.

Contact angle measurements were performed using a Contact Angle System OCA, Data physics instruments with software SCA202 V. 3.11.6.

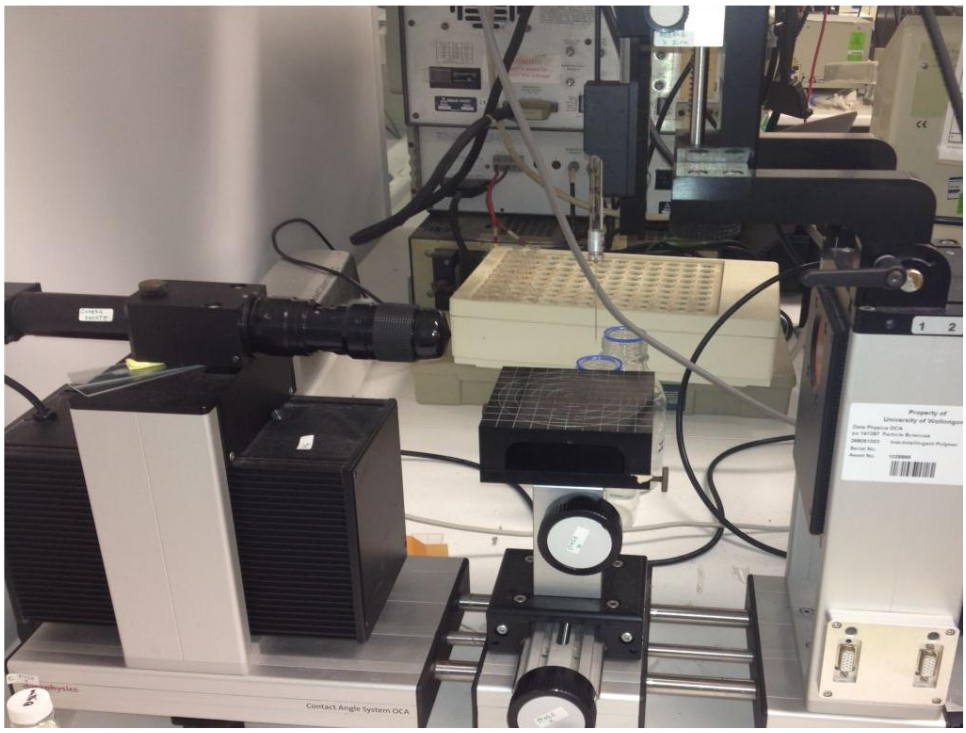

Figure 2. 10: Photograph of Dataphyics contact angle instrumentation.

2.2.11. Sputter coating.

Sputter coating was performed using a EDWARDS FTM6 Auto 306. The sputter coating of Pt onto substrates such as polyvinyidene fluoride and indium tin oxide (ITO) was performed in order to improve the current collecting capabilities of fabricated electrode which helped to improve charge storage and delivery, while minimising and equivalent series resistance (ESR) loss.

Figure 2. 11: Photograph of EDWARDS FTM6 sputter coater.

2.2.12. Conductivity.

Conductivity measurements on composite materials were performed after using a Jandel Model RM3 conductivity tester.

2.3. Electrochemical analysis techniques.

2.3.1. Introduction.

Electrochemistry is used to study and probe non-Faradaic and Faradaic effects at the electrode / electrolyte interface. The main electrochemical techniques used are cyclic voltammetry (CV), electrochemical impedance spectroscopy (EIS). Galvanostatic charge / discharge (GCD) was employed for device testing in order to replicate the performance of the synthesised materials under real world conditions.

2.3.2. Cyclic voltammetry.

The CV response of the various electrode materials were performed in either a two or three-electrode set-up using an EDAQ Australia™ system with EChem V 2 software (ADI Instruments Pty. Ltd). Initial material electrochemical characterisations were performed in the three electrode configuration with a Ag/AgCl reference electrode for aqueous systems, and 1M $NaNO_3$ electrolyte. All organic electrolyte tests were completed with an Ag/Ag^+ reference and a commercially provided electrolyte (Cap-XX Ltd.) in acetonitrile. The counter electrode was Pt mesh with an area of approximately 1.7 cm^2.

For three electrode systems, the capacitance is calculated as follows: InEquation 2.1, I is equal to $(I_a-I_c)/2$, where I_a and I_c are anodic and cathodic current, respectively (A), dv/dt is the scan rate (V/s). In Equation 2.2, the potential V is integrated with respect to time to obtain the capacitance. I is the response current density (A). The limits of the integral are the potential window. In Equation 2.3, the specific capacitance is calculated by dividing the capacitance by the mass where m is the weight of the active material and binder of one electrode. To obtain the capacitance per area (see Equation 2.4), then the capacitance is simply divided by the area A in cm^2.

$$C = \frac{I}{\frac{dv}{dt}} \qquad \textit{Equation 2.1}$$

$$C = \frac{1}{\mathrm{Vm}} \int \mathrm{I}\,\mathrm{dt} \qquad \textit{Equation 2.2}$$

$$C_{sp} = \frac{C}{m}$$ *Equation 2.3*

$$C_{sp} = \frac{C}{A}$$ *Equation 2.4*

In two electrode systems, the specific capacitance per electrode is calculated as per Equation 2.5 where once again *I* is equal to the integral under the CV curve with respect to time, *dv/dt* is the scan rate (V/s), and *m* is the weight (g) of one electrode (active material plus binder). The energy density (E_{CV}) is a function of capacitance (C) multiplied by the square of the voltage (V); while the power density is the energy density multiplied by the scan rate ($\frac{dv}{dt}$) and divided by the voltage (V). See Equation 2.6 and Equation 2.7.

$$C_{sp} = \frac{2C}{m}$$ *Equation 2.5*

$$E_{CV} = \frac{1}{8}\, C_{sp} \mathrm{V}^2$$ *Equation 2.6*

$$P_{CV} = E_{sp}\, X\, \frac{\Delta dv/dt}{V}$$ *Equation 2.7*

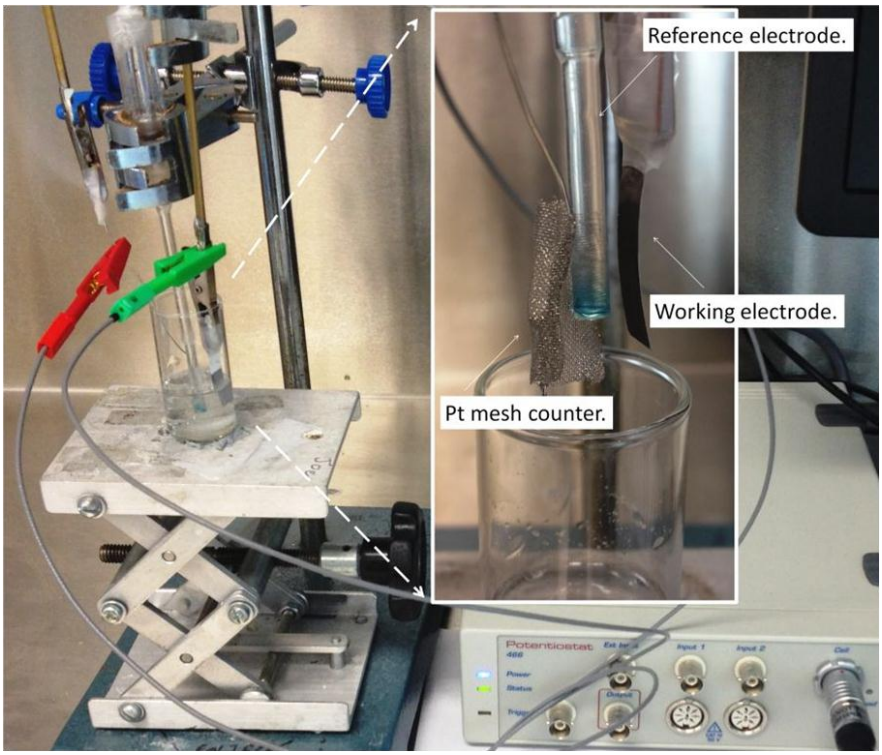

Figure 2. 12: Photograph of EDAQ potentiostat with three-electrode cell.

2.3.3. Electrochemical impedance spectroscopy.

All EIS measurements were performed at room temperature where the frequency range spanned 100 kHz to 0.1 Hz with an AC amplitude of 10 mV (rms) using a Gamry EIS 3000™ system. Each sample is immersed in the electrolyte for 5 minutes prior to the measurement (with the open circuit potential being monitored) to ensure that the working electrode is stable. Initial material electrochemical characterisations were performed in the three electrode configuration with a Ag/AgCl reference electrode for aqueous systems, and 1M $NaNO_3$ electrolyte. All organic electrolyte tests were completed with an Ag/Ag^+ reference and a commercially provided electrolyte (Cap-XX Ltd.) in acetonitrile. The counter electrode was Pt mesh with an area of approximately 1.7 cm^2. Equivalent circuit

modelling and values for R_s, R_p, R_{ct}, C_{dl}, C_f, f_p were obtained using ZView™ V 3.2, Scribner Associates.

The capacitance (C) from impedance for a three electrode system can be calculated according to Equation 2.8 where C that is a complex number is comprised of a real part (*C'*) Equation 2.9), and an imaginary part (*C"*) (see Equation 2.10). Where *Z'* is the real part of impedance (Ω), *Z"* is the imaginary part of impedance (Ω), *f* is the frequency (Hz), and $|Z|$ is the modulus of the impedance (Ω). Values can be either divided by the mass of the electrode (active material plus binder) or the geometric area (cm^2). The time constant τ(s) of charging / discharging is calculated by is multiplying the reciprocal of the peak frequency f_p by 2π which is depicted by Equation 2.11 [7].

$$C = \mathrm{C}' - i\mathrm{C}'' \qquad \textit{Equation 2.8}$$

$$Re\ C' = -\frac{Z"}{2\pi \mathrm{f}\,|\mathrm{Z}|^2} \qquad \textit{Equation 2.9}$$

$$Im\ C" = \frac{Z'}{2\pi \mathrm{f}\,|\mathrm{Z}|^2} \qquad \textit{Equation 2.10}$$

$$\tau(s) = \frac{1}{2\pi \mathrm{f}_{(p)}} \qquad \textit{Equation 2.11}$$

The specific capacitance per electrode for a two electrode system is outlined by Equation 2.12 and Equation 2.13; where *m* is the mass of one electrode (active material plus binder).

$$\mathrm{Re}\ C_{sp} = \frac{2C'}{m} \qquad \textit{Equation 2.12}$$

$$\mathrm{Im}\ C_{sp} = \frac{2C''}{m} \qquad \textit{Equation 2.13}$$

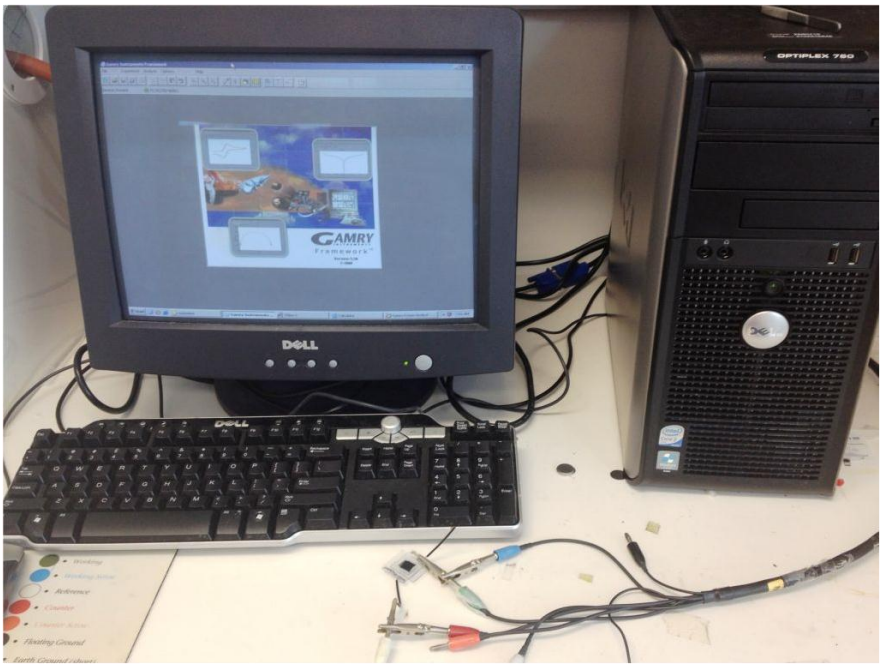

Figure 2. 13: Photograph of the Gamry EIS software and system.

2.3.4. Galvanostatic charge / discharge.

For long-term cyclability of the device, Galvanostatic cycling tests were carried out with a Neware potentiostat, Test Control V.5.0 software, able to record a point every 1s. The potential window studied was between either 0 V and 1.0 V or 0 V and 1.1 V depending on the chapter in question. Calculations for specific capacitance per electrode, energy density and power density can be obtained by Equation 2.14,Equation 2.15, and Equation 2.16 below, where I_d is the discharge current, ΔT_d is the discharge time, V is the potential difference during discharge excluding the portion of the *iR* drop, and m is the mass of one electrode (active

material plus binder) [8, 9]. The term ESR represents 'equivalent series resistance' and is calculated by dividing either the voltage drop at the beginning of the discharge cycle by the total current; or conversely can be obtained from EIS where the ESR is the intercept of the plot of the on the real axis [8-10]. The calculation of ESR was used in some cases for the calculation of maximum power density as is shown by Equation 2.17. The reason for this is due to the fact that when testing a supercapacitor test cell, all resistances (leads, current collectors, electrodes, electrolyte and separator) must be taken into account as only a portion of the measured resistance can be attributed to the electrode material [11].

$$C_{sp} = \frac{2\, I_d \Delta T_d}{Vm} \qquad \textit{Equation 2.14}$$

$$E = \frac{1}{4}\frac{CV^2}{m} \qquad \textit{Equation 2.15}$$

$$P = \frac{1}{2}\frac{I_d V}{m} \qquad \textit{Equation 2.16}$$

$$P = \frac{1}{4}\frac{V^2}{(ESR)m} \qquad \textit{Equation 2.17}$$

Figure 2. 14: Photograph of Neware cell tester.

2.4. Electrode fabrication.

Specific to each chapter.

2.5. Device fabrication.

Specific to each chapter.

2.6. References.

1. Tipler, P. A. and R. Llewellyn, *Modern Physics* 2002: W.H. Freeman.
2. Jensen, E. *Example: Mechanism of Scanning electron microscopy*. 2012 [cited 2012 08/01/13]; Available from: http://www.texample.net/tikz/examples/scanning-electron-microscopy/.
3. D. L. Pavia, G. M. Lampman, and G. S. Kriz, *Introduction to Spectroscopy*. 3rd ed 2001: Brooks/Cole : Thomson Learning.
4. Kasap, S. O., *Principles of Electronic Materials and Devices*. 3rd ed 2006, New York: McGraw-HIll.
5. Grebenkemper, J. *Powder X-ray diffraction*. 2010 [cited 2013 05/01/13]; Available from: http://chemwiki.ucdavis.edu/Analytical_Chemistry/Instrumental_Analysis/Diffraction/Powder_X-ray_Diffraction.
6. Heide, P. v. d., *X-ray photoelectron spectroscopy. An introduction to principles and practices.* 2011, New Jersey: Wiley.
7. H. Kurig, A. Janes, and E. Lust, *Electrochemical Characteristics of Carbide-Derived Carbon|1-Ethyl-3-methylimidazolium Tetrafluoroborate*

Supercapacitor Cells. Journal of The Electrochemical Society, 2010. 157(3): p. A272-A279.

8. Prabaharan, S. R. S., R. Vimala, and Z. Zainal, *Nanostructured mesoporous carbon as electrodes for supercapacitors.* Journal of Power Sources, 2006. 161(1): p. 730-736.

9. Taberna, P. L., P. Simon, and J. F. Fauvarque, *Electrochemical Characteristics and Impedance Spectroscopy Studies of Carbon-Carbon Supercapacitors.* Journal of The Electrochemical Society, 2003. 150(3): p. A292-A300.

10. El-Kady, M. F. and R. B. Kaner, *Scalable fabrication of high-power graphene micro-supercapacitors for flexible and on-chip energy storage.* Nat Commun, 2013. 4: p. 1475.

11. Stoller, M. D. and R. S. Ruoff, *Best practice methods for determining an electrode material's performance for ultracapacitors.* Energy & Environmental Science, 2010. 3(9): p. 1294-1301.

Chapter 3: Poly(3,4-ethylenedioxythiophene) poly(styrenesulfonate) : single walled carbon nanotube composite electrodes for supercapacitor device applications.

3. Poly(3,4-ethylenedioxythiophene) poly(styrenesulfonate) : single walled carbon nanotube composite electrodes for supercapacitor device applications.

3.1. Introduction.

Nanostructured materials, particularly carbon nanotubes (CNTs) are potentially useful in energy storage and conversion devices due to their favourable mechanical, and electrical properties.[1, 2] which when combined with their surface properties contribute to an enhanced overall behaviour. The potential of nanostructured materials in energy storage systems includes batteries, fuel cells, renewable energy storage, devices for load levelling, and uninterrupted power supply [3-6].

The development of composites for use in supercapacitor electrodes comprising inherently conducting polymers (ICPs) and CNTs is an area of research as the conductive polymer matrix, combined with the network-like structure of the CNTs provides enhanced electronic and ionic conductivity that can considerably improve charge storage and delivery.[7-9] The use of poly(3,4-ethylenedioxythiophene) poly(styrene sulfonate), (PEDOT/PSS) has been reported in the literature due to its high stability with respect to repeated cycling, which makes it very suitable as a potential electrode material in supercapacitor device applications [10, 11]. Recent research has focused on improving the mass transport of counter ions into and out of the film during charging / discharging by preparing nanostructured and high surface area electrodes which limits the distance over which ion diffusion can

occur, thus improving power and energy density [10, 12]. However the development of flexible stand-alone composites for device components remains of high interest due to PEDOTs potential as a viable electrode material due to its conjugated backbone and processability [7, 9, 10, 13]. PEDOT/PSS has a conjugated backbone that allows easy transportation of de-localised electrons through the π orbital system [14]. It is interesting as a charge storage material because of the oxygen atoms that have unfilled valence shells leading to higher doping levels.[14, 15] The challenge in fabricating a composite material containing ICPs and CNTs is achieving the correct ratio of the two materials. Pristine CNTs can agglomerate due to strong van der Waals interactions between adjacent tubes reducing electroactive surface area; while the incorrect amount of ICPs can alter the porosity in such a way as to hinder electrolyte ion movement into the pores of the electrode [16].

To address this, we describe a facile method to develop free standing films of PEDOT/PSS-SWNT via vacuum filtration and their subsequent use in a novel supercapacitor. Physical characterisation of the PEDOT/PSS-SWNT films have shown SWNTs to be well dispersed throughout the polymer giving rise to uniform films that can support their own weight. Extensive electrochemical testing revealed that the incorporation of SWNTs with PEDOT/PSS yielded an electrode material that had an increased energy density coupled with excellent capacity retention and long term stability.

3.2. Experimental specific to chapter 3.

3.2.1. Synthesis of poly(3,4-ethylenedioxythiophene) poly(styrene sulfonate).

Polymerization of 3,4-ethylenedioxythiophene (EDOT) in the presence of polystyrenesulfonate (PSS) was carried out by dissolving the PSS (13.14g) in 200mL water by vigorous stirring, followed by degassing for 3-5 minutes. EDOT (distilled) 5.3g was added drop wise to this solution while stirring. The stirring was continued for 2hr followed by ultrasonication for 30min. Ammonium persulfate 11.8g dissolved in 200mL water was then added slowly while stirring. Ferrous ammonium sulphate 5 mg dissolved in 5 mL water was added drop wise to the reaction mixture and left to stir overnight. The resultant dark blue/black polymer solution was dialysed (tubing) in water for 24hr. A film was then made to measure the conductivity (four point probe) six times measurement gave a conductivity approximately to 0.5 S/cm.

3.2.2. Composite film fabrication.

The composite film that was used as the electrode material was made using single walled nanotubes (SWNTs, HiPCO, Unidym Carbon Nanotubes, batch P0900) and poly (3,4-ethylenedioxythiophene) poly(styrene sulfonate) (PEDOT/PSS) mixed in 40% w/w in H_2O. The PEDOT/PSS and SWNTs were mixed and sonicated for one hour (Sonics Vibracell ultrasonic processor, 500 watt, 30% amplitude), with a pulse of one second on and one second off, total time two hours. It was then vacuum filtered using a hydrophilic 0.22µm filter, and washed once with ethanol to remove

water. The films are described as 20% SWNT, 30% SWNT, 40% SWNT, and 50% SWNT. For example, the 20% SWNT refers to a composition of 30 mg SWNT, 120 mg PEDOT/PSS in H_2O. Each composite film was subsequently annealed at 90^0C for 90 minutes. The film referred to as SWNT only was made using vacuum filtration as stated above with the SWNTs dispersed in a 1% triton X-100/H_2O solution.

3.2.3. Capacitor fabrication.

The PEDOT/PSS-SWNT supercapacitor was made by sputter coating 2 pieces of the PEDOT/PSS-SWNT film with Pt (approximately a 10 nm coating each film) and pressing in between ITO glass with the two films with an approximate loading of 8 mg/cm^2, being separated by a Millipore© - Durapore® PVDF hydrophilic separator of thickness 110 microns and a 0.22 micron pore size. A clamp was used to hold the system in place while UV cure glue (Dynman Light Weld) and UV light source (Dynmax Blue Wave 50) was used to seal the 0.25 cm^2 cell. Lastly, a small hole was left where 1M $NaNO_3$ in H_2O was added as the electrolyte via vacuum filling, with the hole being sealed thereafter.

3.3. Discussion of Results.

3.3.1. Physical characterisation of PEDOT:PSS-SWNT film.

3.3.1.1 Scanning electron microscopy.

SEM images of the PEDOT/PSS-SWNT composites are shown in Figure 3. 1. The morphology of the system depicts a very rough surface where the PEDOT/PSS polymer has encased bundles of SWNTs, with a highly porous structure apparent.

This porous network is very desirable as it maximises surface area, potentially allowing large capacitances to be obtained [17]. In Figure 3. 1 the morphology changes as the ratio of PEDOT/PSS to SWNTs is varied. In Figure 3. 1a (20% SWNT) and Figure 3. 1b (30% SWNT), the bundles of SWNTs are smallest with the SWNTs uniformly distributed throughout the polymer matrix, where large spacing is apparent between adjacent nanotube bundles. In Figure 3. 1c (40% SWNT) and Figure 3. 1d (50% SWNT), the bundles of SWNTs are larger with the 40% SWNT composition still maintaining a fine structure and a randomly distributed nanotube network. The larger apparent agglomerates of the 50% SWNT composition are to be expected as the SWNT concentration is the largest and hence much harder for uniform distribution to occur.

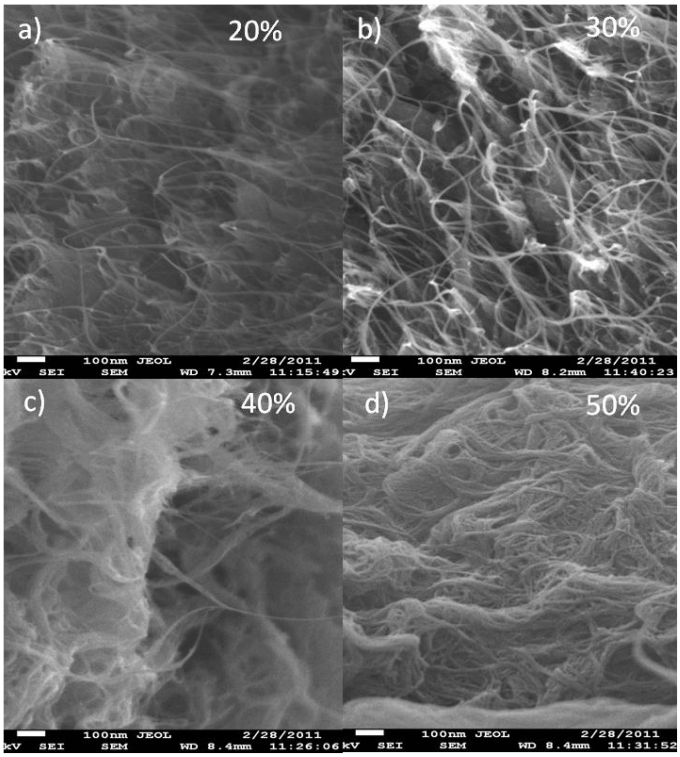

Figure 3. 1 : SEM image of PEDOT/PSS-SWNT composite showing PEDOT/PSS polymer to be integrated with the SWNT. (a) 20% SWNT, (b) 30% SWNT, (c) 40% SWNT, (d) 50% SWNT.

3.3.1.2 Raman Spectroscopy.

Figure 3. 2a and Figure 3. 2b show the Raman spectra of all PEDOT/PSS-SWNT composite films, as well as pure PEDOT/PSS and pure SWNT. The spectra is characteristic of single walled nanotubes with the radial breathing mode (RBM) between 120 cm^{-1} and 305 cm^{-1} that represents the coherent vibration of the C atoms in the radial direction [18]. The ratio of the G/D band (D band is the disorder induced band arising from defects in the walls of the nanotubes; the G band is a result of phonon wave confinement along the circumferential direction of the nanotube that leads to tangential C-C stretching transitions) is 24.52 indicating a high degree of purity for the SWNTs [18, 19]. When comparing the composite films to PEDOT/PSS only, it can be seen that the peaks located at 1146 cm^{-1} (S-O stretching vibration), and between 1400-1580 cm^{-1} (assigned to PEDOT stretching) for the PEDOT/PSS only, disappear as SWNT are added into the system [20]. The use of the 632.81 nm excitation wavelength results in scattering from PSS that is very weak compared to PEDOT as stated by Stavytkska-Barba et. al. [20]. It is thought that SWNTs at this 632.81 nm line produce more intense scattering phenomena meaning the PEDOT/PSS signal is somewhat suppressed and not visible in the spectra of the composite material.

The diameter of the SWNTs can be estimated by evaluating the peaks of the RBM using Equation 3.1 [21], where d is the diameter in nanometres and ω is the wavenumber in cm^{-1}.

$$d = \frac{248}{\omega}$$ *Equation 3.1*

For pure SWNTs, there are four distinct peaks in this RBM region at 170 cm^{-1}, 232 cm^{-1}, 264 cm^{-1}, and 302 cm^{-1}; which correspond to a mixture of diameters ranging from 1.46 nm, 1.07 nm, 0.94 nm and 0.82 nm respectively. From Figure 3. 2b it can be seen that there is a marginal shift in the 170 cm^{-1} 232 cm^{-1}, 264 cm^{-1} and 302 cm^{-1} RBM bands towards slightly smaller wavenumbers as the amount of PEDOT/PSS is increased.

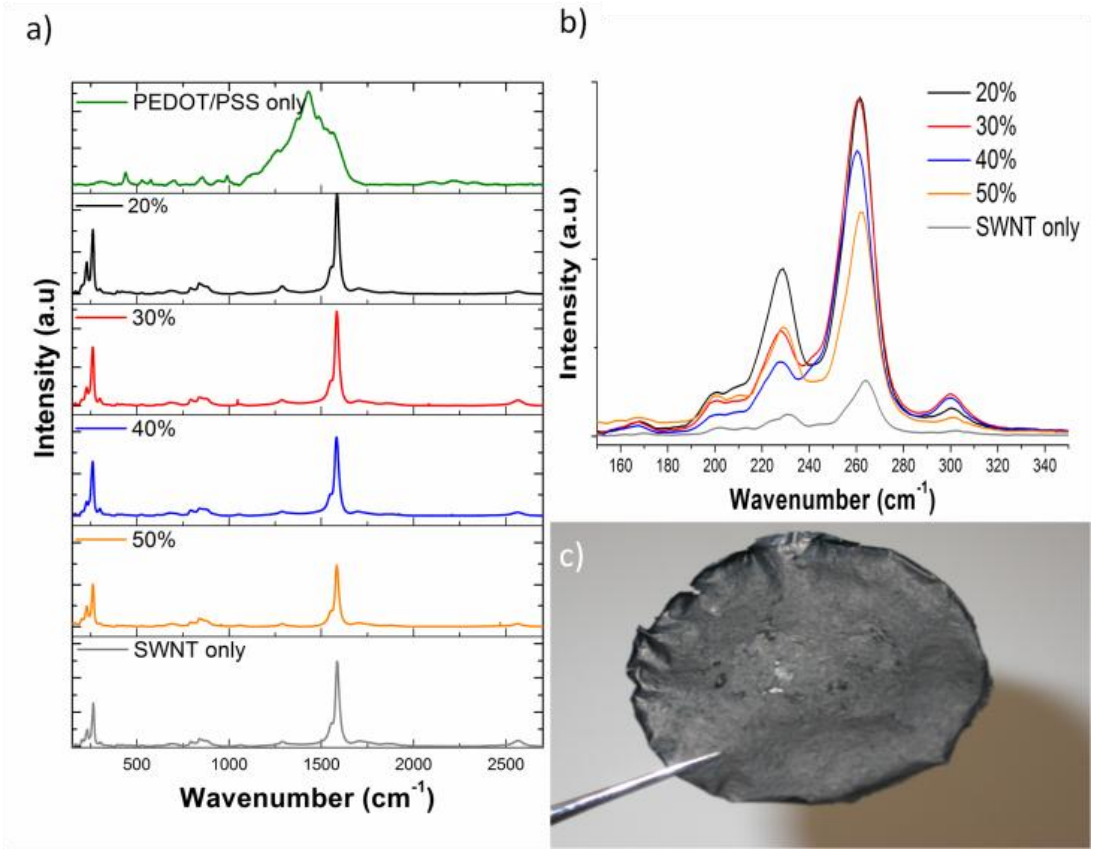

Figure 3. 2: (a) Stack of Raman spectra depicting PEDOT/PSS only, 20% SWNT, 30% SWNT, 40% SWNT, 50% SWNT and SWNT only, (b) RBM bands for, 20% SWNT, 30% SWNT, 40% SWNT, 50% SWNT and SWNT only composite films, (c) Image of 50% SWNT sample after filtering and drying.

In Table 3. 1 below, the SWNT bundle diameters have increased only very marginally indicating that a uniform and very well exfoliated dispersion between SWNTs and PEDOT/PSS has still occurred. Qualitatively speaking, the PEDOT/PSS-SWNT RBM intensity is also much larger than pure SWNT which is caused by the more pronounced radial expansion / contraction of the SWNTs in the PEDOT/PSS matrix. Figure 3. 2c is a 50% SWNT film prepared after filtering and drying. The sample is relatively strong and able to support its own weight.

Table 3. 1: SWNT bundle diameter as PEDOT/PSS is added to the system. Laser line was at 785 nm excitation.

% SWNT	**d(nm)** [1st peak]	**d(nm)** [2nd peak]	**d(nm)** [3rd peak]	**d(nm)** [4tht peak]
100	1.456	1.071	0.939	0.821
50	1.478	1.083	0.944	0.825
40	1.478	1.089	0.953	0.825
30	1.478	1.083	0.944	0.825
20	1.478	1.083	0.948	0.825

[a] diameter calculated from RBM values using Equation 3.1.

3.3.1.3 Thermo-Gravimetric Analysis.

The thermal stability of the PEDOT/PSS-SWNT composite was examined by TGA. Figure 3. 3 shows the weight loss of the composite material upon heating in an air / Ar mixture. The first weight loss up to 180^0C can be ascribed to the loss of water [8]. The degradation peak at 320 ^{0}C is due to the decomposition of PSS where the PSS

degrades via rupture of the sulfonate group from styrene [8, 22] .The steepest weight loss is due to the oxidation of the SWNTs at 420 ^{0}C followed by another decomposition of PEDOT/PSS at 505 ^{0}C which is thought to occur due to the polymer backbone rupturing [8, 22]. The residual amount of material left over at 850 degrees for the SWNT are the metal catalyst particles consistent with compositional content of the batch number. For PEDOT/PSS, the residual amount is likely to be salt associated with the dopant. From the TGA, it was deduced that any annealing of the PEDOT/PSS-SWNT composite film prior to electrochemical analysis could safely be conducted at 90^{0}C under vacuum.

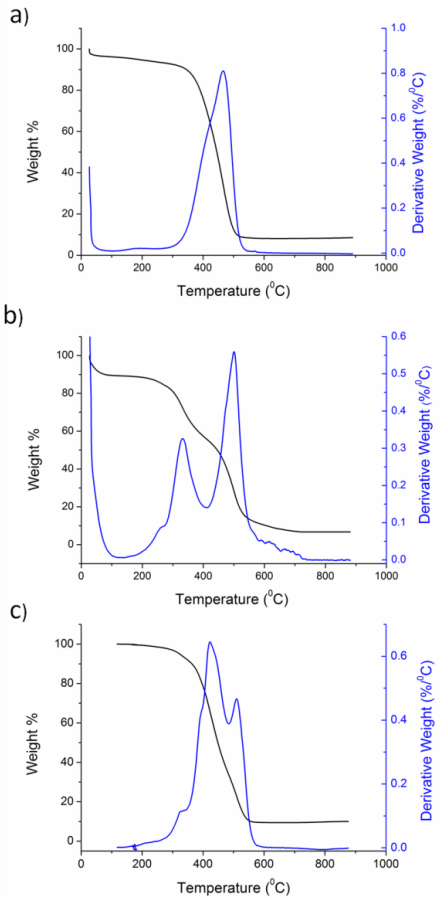

Figure 3. 3: TGA curves of (a) SWNT only, (b) PEDOT / PSS only, (c) PEDOT / PSS-SWNT composite material (30% SWNT). Temperature range is between 100^{0}C to 900^{0}C at a ramp rate of 10 deg/min.

3.3.2. Electrochemical properties of PEDOT/PSS-SWNT films

3.3.2.1 Three electrode tests.

Electrochemical impedance spectroscopy (EIS) and cyclic voltammetry (CV) was used to determine the electrochemical properties of the PEDOT/PSS-SWNT films in which the ratios of PEDOT/PSS to SWNTs had been varied as outlined in the experimental section.

The Nyquist plot of Figure 3. 4a is characteristic of capacitive type behaviour [23]. In the high frequency domain (inset), a small semi-circle is observed (bulk RC response) that can be attributed to a contact impedance generated between the SWNTs and PEDOT/PSS as well as electrolyte resistance within the pores of the composite material [24, 25]. In the middle frequency regime, an extremely small 45^0 degree inclination can be seen (Warburg response) which arises as a result of distributed capacitance / impedance in a porous material [26]. The fact that this region is extremely small is important as it signifies fast ion re-arrangement / kinetics [26].

In the low frequency portion of the spectrum, the plot tends towards a vertical line where the imaginary part of impedance rapidly increases which is characteristic of capacitive behaviour [27, 28]. When comparing the polarisation resistance (R_{ct}) of Figure 3. 4a inset, it can be seen that the size of the semi-circle at high frequencies decreases when the composition of PEDOT/PSS-SWNT increases from 20% SWNT to 50% SWNT.

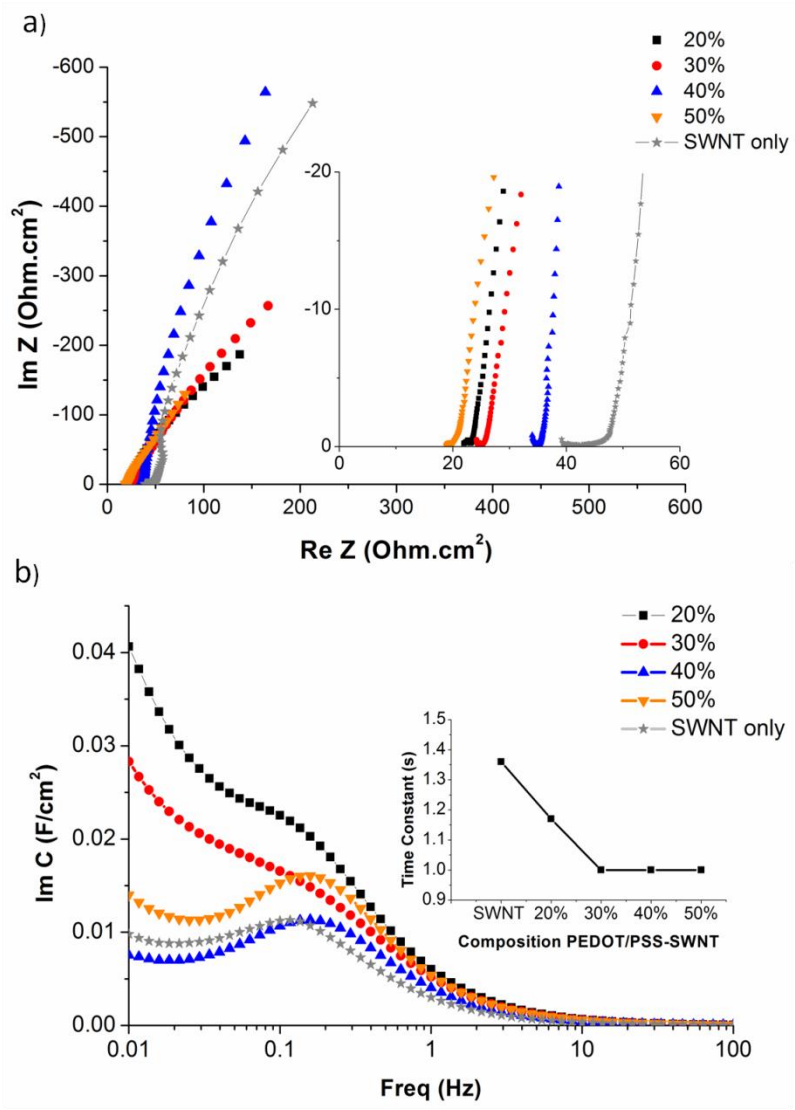

Figure 3. 4: (a) Nyquist plot (with inset) for PEDOT/PSS-SWNT film with varied composition, (b) imaginary part of capacitance verses frequency. All composite films were annealed for 90 minutes at 90 ^{0}C. Electrolyte used is 1M $NaNO_3$, with a Pt mesh counter of 1.7 cm^2 and Ag/AgCl reference electrode.

The imaginary part of capacitance (Figure 3. 4b) represents the energy dissipation of the complex part of the capacitance, characteristic of an irreversible process, which can lead to the hysteresis of the electrochemical process [25, 26, 29]. The relaxation time constant *τ(s)* can be evaluated from Figure 3. 4b by finding the peak frequency f_p of $C''(\omega)$, multiplying f_p by 2π and inverting. When comparing the

PEDOT/PSS-SWNT films of varied composition, there is a shift in f_p towards higher frequency (hence lower time constant) from 20% SWNT to 50% SWNT. The higher frequency indicates better rate capability and hence faster charging of the electric double layer [30]. The values of *τ(s)* for the PEDOT/PSS-SWNT films can be seen in the inset of Figure 3. 4b where the smallest *τ(s)* was calculated to be 1.0 s. The values for the imaginary part of capacitance $C"(\omega)$ have been calculated according to H. Kurig et. al. (see Chapter 2, section 2.2) [25].

The PEDOT/PSS-SWNT film displays a highly rectangular CV curve at 5 mV/s, as is observed in Figure 3. 5a. These results indicate that the charge – discharge responses of the electric double layer are highly reversible and kinetically facile [24]. However, the CV above scan rates of 10 mV/s (not shown) did not keep its rectangular shape. This can be attributed to the time constant of the system where the transient response falls off exponentially with the RC time constant [31]. This means that as the scan rate increases, the concentration gradient at the electrode / electrolyte interface increases and the time constant becomes larger. The transient response is pronounced leading to a lag between charging and discharging of the capacitor causing distortion of the CV [32]. The specific capacitance was calculated from CV using the attained current density of 0.67 A/g at a scan rate of 5 mV/s, (which can be seen in Figure 3. 5a using equations obtained from Chapter 2, section 2.2 [25], with the maximum value being 133 F/g. A general trend can be seen in Figure 3. 5b with the specific capacitance reaching the maximum at approximately

30% SWNT composition of PEDOT/PSS-SWNT with the capacitance falling off either side.

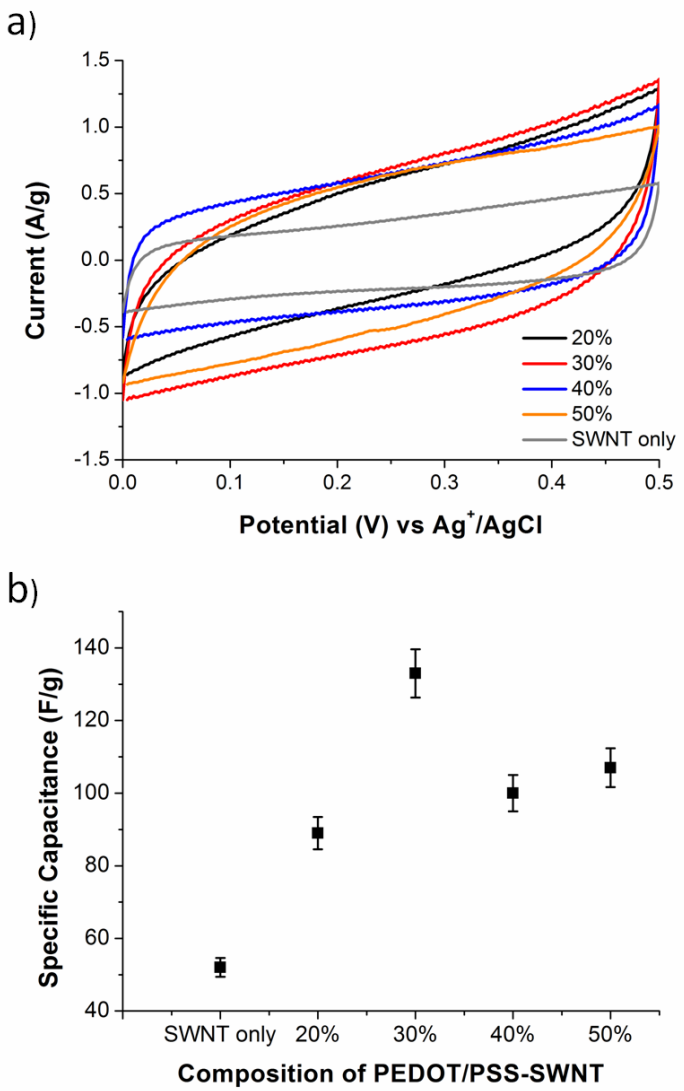

Figure 3. 5: CV of PEDOT/PSS-SWNT films where the composition of PEDOT/PSS and SWNT has been varied, (d) specific capacitance for PEDOT/PSS-SWNT calculated at a scan rate of 5 mV/s and average current of 0.67 A/g. All composite films were annealed for 90 minutes at 90 ^{0}C. Electrolyte used is 1M $NaNO_3$, with a Pt mesh counter of 1.7 cm^2 and Ag/AgCl reference electrode.

The distribution of capacitance in this way suggest that at 30% SWNT and 40% SWNT composition the ideal amount of PEDOT/PSS and SWNTs is ascertained allowing the right balance between porosity size, connectiveness of nanotubes and amount of conductive polymer matrix. This result is also in agreement with conductivity values obtained for each of the different films with the conductivity increasing from 10 S/cm for the 20% SWNT film to 15 S/cm for the 30% SWNT, 20 S/cm for the 40% SWNT film, and a decrease back to 17 S/cm for the 50% SWNT film.

3.3.2.2 Supercapacitor devices with varying PEDOT/PSS-SWNT compositions.

Supercapacitor cells were fabricated using varying compositions of PEDOT/PSS and SWNTs.. The Nyquist plot of Figure 3. 6a are characteristic of capacitive type behaviour as has been explained previously [23]. As observed for the three electrode system, all composite supercapacitor devices exhibit an extremely small 45^0 degree Warburg region signifying fast ion re-arrangement / kinetics of the electrolyte ions in the device [26]. The PEDOT/PSS-SWNT film displays a highly rectangular CV curve at 50 mV/s, as is observed in Figure 3. 6b with the largest average current density of 1.55 A/g arising from the 30% SWNT film. These results indicate that there is a minimal lag time between the charge – discharge responses of the electric double layer, signifying a highly reversible and kinetically facile behaviour [24]. However, the CV above scan rates of 50 mV/s (not shown) did not keep its rectangular shape and thus the specific capacitance decreased. Compared

to the three electrode system, the devices were able to have highly rectangular curves at faster scan rates due to much better connection of the active material with the current collector. The specific capacitance per electrode was calculated at 50 mV/s using equations available in chapter 2, section 2.2.2 [33], with the maximum value being 66 F/g for the 30% SWNT device and 75 F/g for the 40% SWNT device.

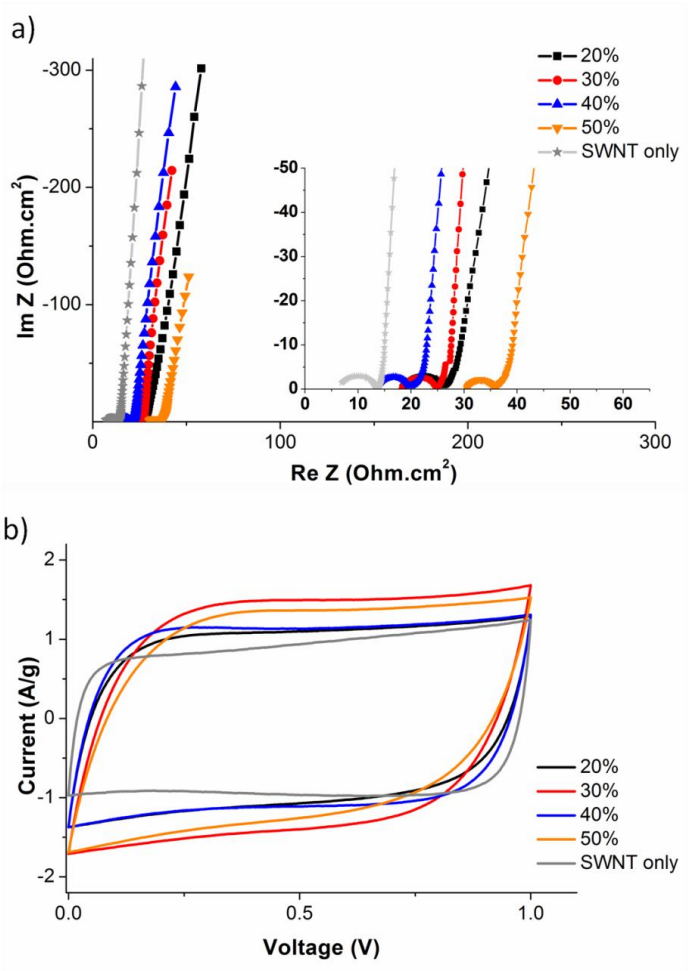

Figure 3. 6: Nyquist plot (with inset) for PEDOT/PSS-SWNT device with varied composition of PEDOT/PSS and SWNTs. (b) CV of PEDOT/PSS-SWNT films where the composition of PEDOT/PSS and SWNT has been varied. Scan rate at 50 mV/s. Electrolyte used was aqueous 1M $NaNO_3$. All composite films were annealed for 90 minutes at 90 ^{0}C. EIS was conducted at OCP.

The symmetry of the charge / discharge curves (Figure 3. 7) signifies excellent capacitive characteristics, with the discharge time decreasing significantly as the applied current is increased leading to a decrease in specific capacitance as can be seen by Figure 3. 7 [34, 35]. A very small potential drop (*iR* drop) at the very beginning of the constant current discharge is observed for all PEDOT/PSS-SWNT devices. The *iR* drop is attributed to a couple of factors including; (i) the contact resistance between PEDOT/PSS and SWNT, and (ii) contact resistance between the electrode material and current collector [36, 37].

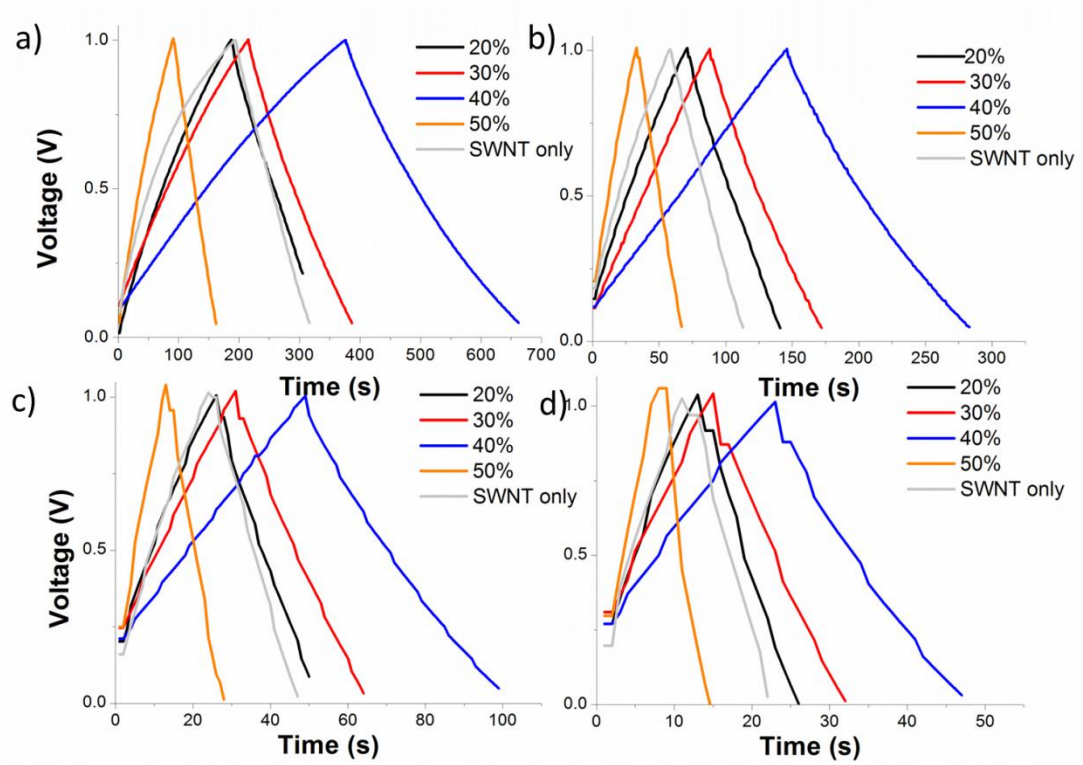

Figure 3. 7: Galvanostatic charge / discharge of PEDOT/PSS-SWNT device with varying SWNTs concentrations. (a) 0.2 A/g, (b) 0.4 A/g (c) 1 A/g, (d) 2 A/g. The cycle that is shown is cycle 2.

From Figure 3. 8, it can be seen that the largest specific capacitance is obtained for the 40% SWNT device and reaches 104 F/g at a current density of 0.2 A/g. Its corresponding highest energy density and highest power density was calculated to be 7 Wh/kg and 825 W/kg respectively. The next best performing device is the 30% SWNT device (85 F/g at 0.2 A/g with a highest energy density and power density of 6 Wh/kg and 1110 W/kg respectively) then followed by the 20% SWNT and SWNT only devices. Calculations for specific capacitance per electrode, energy density and power density can be obtained from Chapter 2, section 2.2.

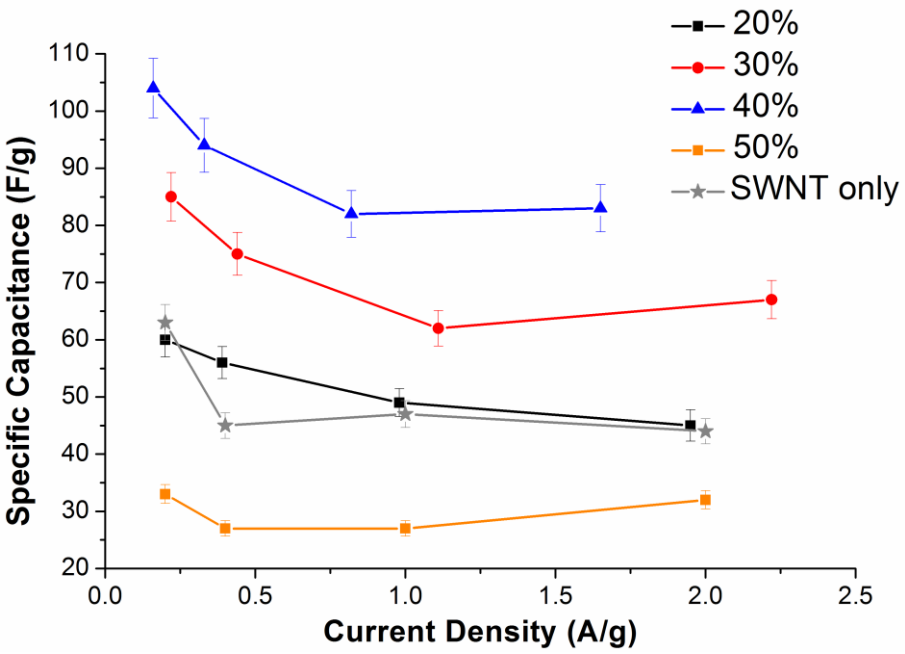

Figure 3. 8: Influence of the constant current density on capacitance for varying compositions of PEDOT/PSS-SWNT supercapacitor devices.

The galvanostatic charge / discharge curves of Figure 3. 9a and Figure 3. 9b show excellent symmetry and overlay of cycles 2, 500 and 1000 signifying good capacity behaviour. The 30% SWNT and 40% SWNT device displayed excellent capacity

retention (Figure 3. 9c with less than 10% decrease over 1000 cycles. The decrease can be attributed to some film swelling as the electrolyte ions intercalate in and out of the pores of the film, as well as some energy loss to irreversible processes that lead to hysteresis [26, 38].The specific capacitance values are well maintained, even at a high current density of 1 A/g meaning that the rate capability of the device is good [39]. The superior rate capability of the 40 SWNT device can be attributed to the reduced short diffusion paths of ions leading to faster kinetics (ion insertion / extraction) in the electrode film [39, 40]

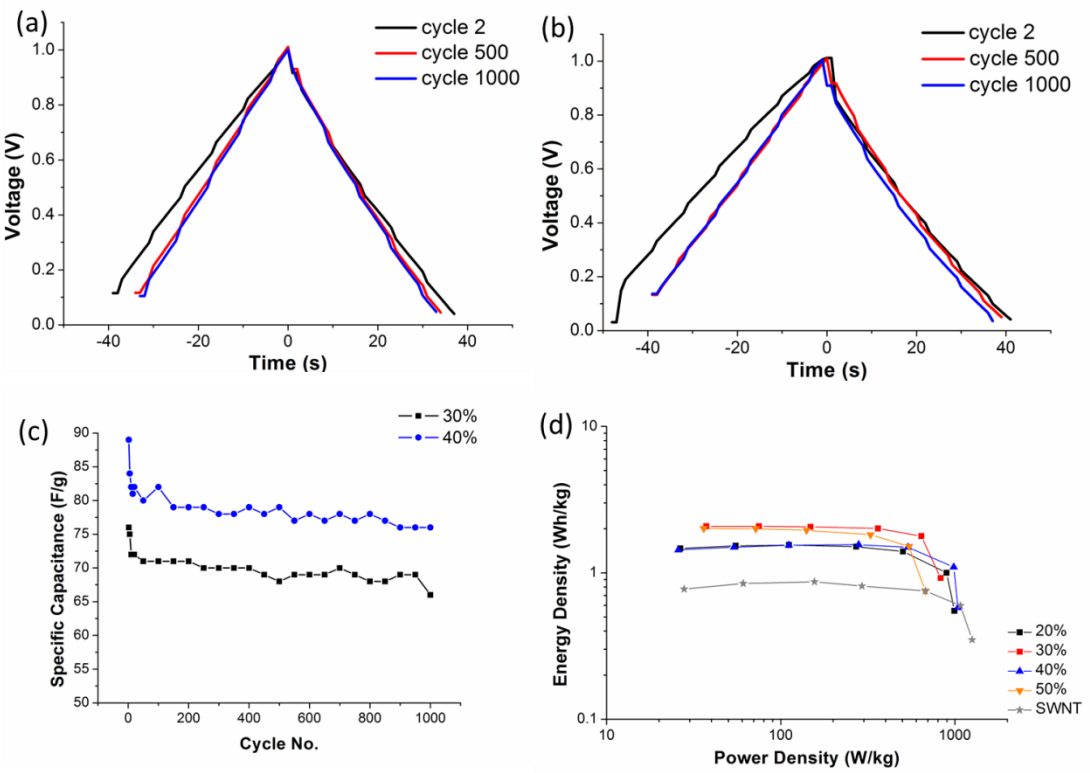

Figure 3. 9: Galvanostatic charge / discharge of (a) 30% SWNT; (b) 40% SWNT at a current density of 1 A/g, (c) Galvanostatic charge / discharge test over 1000 cycles at 1 A/g, (d) Plots of utilisable specific energy density verses specific power density (Ragone plot) for varying PEDOT/PSS-SWNT supercapacitor devices. The values are calculated from CV using equations given in Chapter 2, section 2.2).

There is also a marketable difference in the energy density which can be observed in the Ragone plot of Figure 3. 9d. In all devices, the power density either approaches or exceeds 1000 W/kg; however the addition of the PEDOT/PSS significantly increases the energy density. It can clearly be established that the maximum energy and power density occur when the ratio of PEDOT/PSS to SWNTs is 30% SWNTs and 40% SWNTs; while there is a decrease either side of these ratios. Equations for the calculation of maximum energy and power density for the 30% SWNT and 40% SWNT were are outlined in Chapter 2, section 2.2. The values for the 30% SWNT device were 2.80 Wh/kg and 1105 W/kg, while the 40% SWNT device was 1.56 Wh/kg and 1042 W/kg respectively. At this 30% and 40% ratio of PEDOT/PSS to SWNT it is thought that the kinetics of the electrolyte ions and availability of electroactive surface area is maximised, leading to improved charge storage and delivery [41].

Comparatively, Snook et. al have reported composites containing PEDOT/PSS and carbon nanotubes that can reach specific capacitances ranging from 85 F/g to a 150 F/g; while the energy density can exceed 0.92 Wh/kg and power density can range from 100 W/kg to 3000 W/kg [16]. Frackowiak et. al reported PEDOT/PSS and multi walled nanotube composites that achieved capacitance values of 100 F/g with excellent stability [42].

Recent work published by Lei et.al. Involving electrochemical capacitors made from PEDOT mixed with activated carbon in an ethylene based organic electrolyte

yielded energy densities and power densities approaching 200 Wh/kg and 10000 W/kg respectively [43]. Lastly, Zhu et. al. have reported extremely large specific capacitances exceeding 500 F/g for a composites of polyaniline nanorods and sulfonated mulit-walled carbon nanotubes [44].

Overall, the increase in energy density, while power density is still maintained makes it possible for the use of this PEDOT/PSS-SWNT electrode material as an effective electrode in the use of supercapacitor design and fabrication. Coupled to this, it may be plausible to use a PEDOT/PSS conducting polymer / CNT composite as the cathode in an asymmetric supercapacitor where enhanced energy density is required.

3.4. Conclusions.

In summary, a supercapacitor device containing free standing PEDOT/PSS-SWNT composite material was constructed and tested successfully in order to evaluate its performance. The first part of the paper presents physical characteristics of the PEDOT/PSS, SWNTs and the composite material formed with the PEDOT/PSS and SWNT. The SEM images show uniformly dispersed bundles of SWNTs in a PEDOT/PSS polymer matrix. The SWNT diameter in the polymer matrix is on average less than 1.5 nm in diameter, while the Raman spectra shows a large D/G band ratio, with a slight shift of the RBM mode toward smaller wavenumbers as PEDOT:PSS is added. The TGA clearly shows defined peaks for the decomposition of

PEDOT/PSS and SWNTs arising from the rupture of the polymer backbone and oxidation of the nanotubes.

The second part of this chapter compares the electrochemical properties of the varied compositions of PEDOT/PSS-SWNT films using a three electrode system. The 30% SWNT composition had the smallest time constant of 1.0 s and the largest specific capacitance of 133 F/g

The third part of this chaper compares supercapacitor devices made from the four compositions studied. The PEDOT/PSS-SWNT device with the 40% SWNT composition was the best performing in terms of capacitance, energy density and maintained power density as compared to the 20% SWNT, 30% SWNT and 50% SWNT compositions. In all instances the impedance spectra showed Nyquist plots that were characteristic of capacitive behaviour, with all the CV plots displaying highly rectangular curves and the galvanostatic charge / discharge exhibiting very triangular cycles and a lengthy discharge time. The 40% SWNT device displayed the largest specific capacitance and energy density with the power density being around the same order of magnitude as all other devices. Using galvanostatic charge / discharge at a current rate of 1 A/g, the specific capacitance was calculated to be 104 F/g, while the maximum energy and power density were 7 Wh/kg and 825 W/kg respectively. The stability of the 40% SWNT device was very good with the capacity retention over 1000 cycles being greater than 90% of the initial value at cycle 2.

3.5. References.

1. Arico, A. S., P. Bruce, B. Scrosati, J.-M. Tarascon, and W. van Schalkwijk, *Nanostructured materials for advanced energy conversion and storage devices.* Nat Mater, 2005. 4(5): p. 366-377.
2. Chung, J., K.-H. Lee, J. Lee, and R. S. Ruoff, *Toward Large-Scale Integration of Carbon Nanotubes.* Langmuir, 2004. 20(8): p. 3011-3017.
3. Simon, P. and Y. Gogotsi, *Materials for electrochemical capacitors.* Nature Materials, 2008. 7(11): p. 845-854.
4. Zhao, X., B. M. Sanchez, P. J. Dobson, and P. S. Grant, *The role of nanomaterials in redox-based supercapacitors for next generation energy storage devices.* Nanoscale, 2011. 3(3): p. 839-855.
5. Roberts, M. E., D. R. Wheeler, B. B. McKenzie, and B. C. Bunker, *High specific capacitance conducting polymer supercapacitor electrodes based on poly(tris(thiophenylphenyl)amine).* Journal of Materials Chemistry, 2009. 19(38): p. 6977-6979.
6. Zhao, X., C. Johnston, and P. S. Grant, *A novel hybrid supercapacitor with a carbon nanotube cathode and an iron oxide/carbon nanotube composite anode.* Journal of Materials Chemistry, 2009. 19(46): p. 8755-8760.
7. S. Bhandari, M. Deepa, A. K. Srivastava, A. G. Joshi, and R. Kant, *PEDOT-MWNTs commposite films.* J. Phys. Chem B, 2009. 113: p. 9416-9428.
8. Zhang, X., J. Liu, B. Xu, Y. Su, and Y. Luo, *Ultralight conducting polymer/carbon nanotube composite aerogels.* Carbon, 2011. 49(6): p. 1884-1893.

9. Crispin, X., F. L. E. Jakobsson, A. Crispin, P. C. M. Grim, P. Andersson, A. Volodin, C. van Haesendonck, M. Van der Auweraer, W. R. Salaneck, and M. Berggren, *The Origin of the High Conductivity of Poly(3,4-ethylenedioxythiophene) Poly(styrenesulfonate) (PEDOT/PSS) Plastic Electrodes.* Chemistry of Materials, 2006. 18(18): p. 4354-4360.

10. Kelly, T. L., K. Yano, and M. O. Wolf, *Supercapacitive Properties of PEDOT and Carbon Colloidal Microspheres.* ACS Applied Materials & Interfaces, 2009. 1(11): p. 2536-2543.

11. J. Chen, Y. L., A. I. Minett, C. Lynam, J. Wang, G. G. Wallace, *Flexible, Aligned Carbon Nanotube/Conducting Polymer Electrodes for a Lithium-Ion Battery.* Chem. Mater. , 2007. 19: p. 3595.

12. Byrne, M. T. and Y. K. Gun'ko, *Recent Advances in Research on Carbon Nanotube–Polymer Composites.* Advanced Materials. 22(15): p. 1672-1688.

13. Peng, C., J. Jin, and G. Z. Chen, *A comparative study on electrochemical co-deposition and capacitance of composite films of conducting polymers and carbon nanotubes.* Electrochimica Acta, 2007. 53(2): p. 525-537.

14. T. A. Skotheim and J. R. Reynolds, *Conjugated Polymers: Theory, Synthesis, Proerties and Characterisation* 2007, Boca Raton: CRC Press.

15. Chandrasekhar, P., *Conducting Polymers: Fundamentals and Applications* 1999, Boston: Kluwer Acedemic Publishers.

16. Snook, G. A., P. Kao, and A. S. Best, *Conducting-polymer-based supercapacitor devices and electrodes.* Journal of Power Sources, 2011. 196(1): p. 1-12.

17. Naoi, K. and P. Simon, *New Materials and New Configurations for Advanced Electrochemical Capacitors.* Journal of The Electrochemical Society 2008. 17(1): p. 34-37.

18. Dresselhaus, M. S., G. Dresselhaus, R. Saito, and A. Jorio, *Raman spectroscopy of carbon nanotubes.* Physics Reports, 2005. 409(2): p. 47-99.

19. Salzmann, C. G., S. A. Llewellyn, G. Tobias, M. A. H. Ward, Y. Huh, and M. L. H. Green, *The Role of Carboxylated Carbonaceous Fragments in the Functionalization and Spectroscopy of a Single-Walled Carbon-Nanotube Material.* Advanced Materials, 2007. 19(6): p. 883-887.

20. Stavytska-Barba, M. and A. M. Kelley, *Surface-Enhanced Raman Study of the Interaction of PEDOT:PSS with Plasmonically Active Nanoparticles.* The Journal of Physical Chemistry C, 2010. 114(14): p. 6822-6830.

21. S H Shiau, C W Liu, C Gau, and B. T. Dai, *Growth of a single-wall carbon nanotube film and its patterning as an n-type field effect transistor device using an integrated circuit compatible process.* Nanotechnology, 2008. 19(10): p. 105303.

22. Friedel, B., P. E. Keivanidis, T. J. K. Brenner, A. Abrusci, C. R. McNeill, R. H. Friend, and N. C. Greenham, *Effects of Layer Thickness and Annealing of PEDOT:PSS Layers in Organic Photodetectors.* Macromolecules, 2009. 42(17): p. 6741-6747.

23. Segalini, J., B. Daffos, P. L. Taberna, Y. Gogotsi, and P. Simon, *Qualitative Electrochemical Impedance Spectroscopy study of ion transport into sub-*

nanometer carbon pores in Electrochemical Double Layer Capacitor electrodes. Electrochimica Acta, 2010. 55(25): p. 7489-7494.

24. Prabaharan, S. R. S., R. Vimala, and Z. Zainal, *Nanostructured mesoporous carbon as electrodes for supercapacitors.* Journal of Power Sources, 2006. 161(1): p. 730-736.

25. H. Kurig, A. Janes, and E. Lust, *Electrochemical Characteristics of Carbide-Derived Carbon|1-Ethyl-3-methylimidazolium Tetrafluoroborate Supercapacitor Cells.* Journal of The Electrochemical Society, 2010. 157(3): p. A272-A279.

26. Taberna, P. L., P. Simon, and J. F. Fauvarque, *Electrochemical Characteristics and Impedance Spectroscopy Studies of Carbon-Carbon Supercapacitors.* Journal of The Electrochemical Society, 2003. 150(3): p. A292-A300.

27. Li, L., E. Liu, J. Li, Y. Yang, H. Shen, Z. Huang, X. Xiang, and W. Li, *A doped activated carbon prepared from polyaniline for high performance supercapacitors.* Journal of Power Sources, 2010. 195(5): p. 1516-1521.

28. Liu, C., Z. Yu, D. Neff, A. Zhamu, and B. Z. Jang, *Graphene-Based Supercapacitor with an Ultrahigh Energy Density.* Nano Letters, 2010. 10(12): p. 4863-4868.

29. Arulepp, M., J. Leis, M. Lätt, F. Miller, K. Rumma, E. Lust, and A. F. Burke, *The advanced carbide-derived carbon based supercapacitor.* Journal of Power Sources, 2006. 162(2): p. 1460-1466.

30. Jong, H. J., K. Akiko, M. Kenji, and N. Katsuhiko, *Supercapacitor Performance of Hydrous Ruthenium Oxide Electrodes Prepared by Electrophoretic*

Deposition. Journal of The Electrochemical Society, 2006. 153(2): p. A321-A328.

31. Kötz, R., M. Hahn, and R. Gallay, *Temperature behavior and impedance fundamentals of supercapacitors.* Journal of Power Sources, 2006. 154(2): p. 550-555.

32. Lu, W., L. Qu, K. Henry, and L. Dai, *High performance electrochemical capacitors from aligned carbon nanotube electrodes and ionic liquid electrolytes.* Journal of Power Sources, 2009. 189(2): p. 1270-1277.

33. Portet, C., J. Chmiola, Y. Gogotsi, S. Park, and K. Lian, *Electrochemical characterizations of carbon nanomaterials by the cavity microelectrode technique.* Electrochimica Acta, 2008. 53(26): p. 7675-7680.

34. Ye, J.-S., X. Liu, H. F. Cui, W.-D. Zhang, F.-S. Sheu, and T. M. Lim, *Electrochemical oxidation of multi-walled carbon nanotubes and its application to electrochemical double layer capacitors.* Electrochemistry Communications, 2005. 7(3): p. 249-255.

35. Malak-Polaczyk, A., C. Vix-Guterl, and E. Frackowiak, *Carbon/Layered Double Hydroxide (LDH) Composites for Supercapacitor Application* Energy & Fuels, 2010. 24(6): p. 3346-3351.

36. Hsieh, C.-T., W.-Y. Chen, and J.-H. Lin, *Synthesis of carbon nanotubes on carbon fabric for use as electrochemical capacitor.* Microporous and Mesoporous Materials, 2009. 122(1-3): p. 155-159.

37. Kaempgen, M., C. K. Chan, J. Ma, Y. Cui, and G. Gruner, *Printable Thin Film Supercapacitors Using Single-Walled Carbon Nanotubes.* Nano Letters, 2009. 9(5): p. 1872-1876.

38. Hantel, M. M., T. Kaspar, R. Nesper, A. Wokaun, and R. Kötz, *Partially reduced graphite oxide for supercapacitor electrodes: Effect of graphene layer spacing and huge specific capacitance.* Electrochemistry Communications, 2010. 13(1): p. 90-92.

39. Hou, Y., Y. Cheng, T. Hobson, and J. Liu, *Design and Synthesis of Hierarchical MnO2 Nanospheres/Carbon Nanotubes/Conducting Polymer Ternary Composite for High Performance Electrochemical Electrodes.* Nano Letters, 2010. 10(7): p. 2727-2733.

40. Wu, Q., Y. Xu, Z. Yao, A. Liu, and G. Shi, *Supercapacitors Based on Flexible Graphene/Polyaniline Nanofiber Composite Films.* ACS Nano, 2010. 4(4): p. 1963-1970.

41. Lewandowski, A., A. Olejniczak, M. Galinski, and I. Stepniak, *Performance of carbon-carbon supercapacitors based on organic, aqueous and ionic liquid electrolytes.* Journal of Power Sources, 2010. 195(17): p. 5814-5819.

42. Frackowiak, E., V. Khomenko, K. Jurewicz, K. Lota, and F. Béguin, *Supercapacitors based on conducting polymers/nanotubes composites.* Journal of Power Sources, 2006. 153(2): p. 413-418.

43. Lei, C., P. Wilson, and C. Lekakou, *Effect of poly(3,4-ethylenedioxythiophene) (PEDOT) in carbon-based composite electrodes for electrochemical supercapacitors.* Journal of Power Sources, 2011. 196(18): p. 7823-7827.

44. Zhu, Z. Z., G. C. Wang, M. Q. Sun, X. W. Li, and C. Z. Li, *Fabrication and electrochemical characterization of polyaniline nanorods modified with sulfonated carbon nanotubes for supercapacitor applications.* Electrochimica Acta, 2011. 56(3): p. 1366-1372.

Chapter 4: Synthesis of Graphene Oxide.

4. Synthesis of graphene oxide.

4.1. Introduction.

Graphene is a one-atom thick, two-dimensional (2D) material composed of sp^2 hybridised carbon which is a good candidate for energy storage materials due to its superior electrical conductivity, mechanical properties, thermal conductivity, high surface area, and its minimal cytotoxicity [1, 2]. Graphene nano-sheets were first obtained by mechanical exfoliation ("scotch tape" method) of bulk graphite and by epitaxial CVD [3]. Further developments have led to graphene, and more generally graphene oxide (GO) to be synthesised by several methods such as chemical vapour deposition (CVD), micro mechanical exfoliation, epitaxial growth, the creation of colloidal suspensions, and inorganic reactions [3, 4]. Chemical means of creating graphene / GO are more viable as these methods are straight forward to synthesise, and thus more effective for large-scale manufacturing, which can lead to the development of devices on a commercial scale [5, 6]. Coupled to this has been the further improvement in creating dispersions of graphene / GO that are more uniform in terms of lateral thickness, lateral area, and size through the selection and use of good dispersion solvents and post treatment [6, 7].

The exfoliation of GO using microwave irradiation is of particular interest as the process can be performed at room temperature, using a conventional microwave leading to a marked volume increase of the GO, forming an extremely porous powder [8]. Coupled to this, microwave irradiation of GO can be considered a "green approach" to exfoliation to graphene oxide as no harmful and toxic

chemicals are used. The benefit of exfoliation is that it provides a porous material that can serve as a conductive scaffold and support for the formation of stable and robust composite materials.

4.2. Experimental specific to chapter 4.

4.2.1. Synthesis of graphene oxide.

Graphene oxide was synthesised using a modified Hummers method as outlined by Marcano et. al. [3]. In detail, 1 g of graphite powder (Bay Carbon Inc.) was added to 60 ml of concentrated (98% w/v) H_2SO_4 (Univar) and mixed thoroughly for a few minutes. Then 3.5 g of $KMNO_4$ (Sigma-Aldrich) was added in small aliquots so as the temperature did not exceed 100^0C. This mixture was left stirring overnight for 18 hours. At this point of the synthesis, the following reaction has taken place [9];

$$5C_{24} + KMNO_4 + 17H_2SO_4 \rightarrow 5C_{24}HSO_4^- . 2HSO_4 . 2H_2SO_4 + MnSO_4 + KHSO_4 + H_2O$$

At this point some rapid bubbling occurs due to the release of carbon dioxide following the reaction scheme [9];

$$5C + 4KMNO_4 + 8H_2SO_4 \rightarrow 5CO_2 + 4MnSO_4 + 4KHSO_4 + 6H_2O$$

300 ml to 500 ml of distilled H_2O is added (ice bath condition) to hydrolyse the intercalation compound that forms graphite oxide. Lastly, 30% aqueous H_2O_2 (Univar) (drop wise, approximately 3 ml) is added until a complete colour change is observed. The H_2O_2 is added after hydrolysis to decompose permanganate ions into

manganese (IV) ions where after the manganese (IV) ions are removed by vacuum filtration (PVDF membrane, 0.22 micron pour size) by washing twice each with concentrated (36% w/v) HCl (Univar), water, and ethanol. The HCl ensures no undesirable manganese hydroxides form, which can get trapped in between the graphene / graphite layers [10]. After vacuum filtration the slurry is dried in a vacuum oven overnight at 50^0C.The

EDX spectra of Figure 4. 1 confirms that no $Mn(OH)_2$ has precipitated as no Mn peak is apparent. The C and O peaks are from the GO while the F peak is ascribed to the PVDF membrane and Na from residual NaCl due to the ocean.

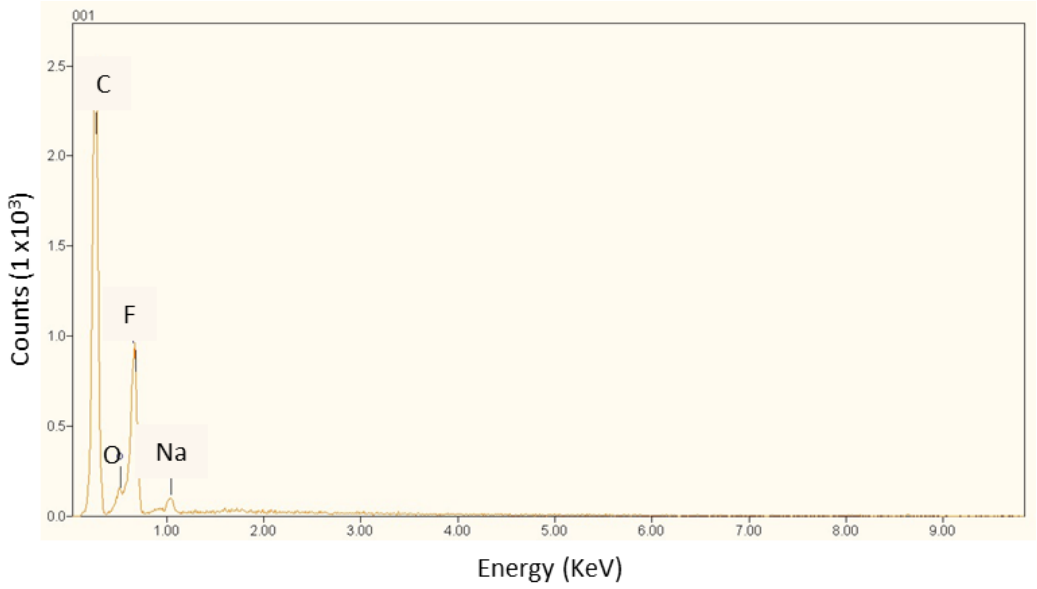

Figure 4. 1: EDX spectra of the GO oxide film that was made via vacuum filtration onto a hydrophilic PVDF membrane.

4.2.2. *Preparation of exfoliated graphene oxide.*

Exfoliated GO (mw rGO) was formed by using a conventional microwave oven (1200 W) as can be seen by the schematic diagram of Figure 4. 2.. After irradiation, the GO glowed red-hot accompanied by fuming and sparking, leading to a remarkable volume expansion caused by the violent expulsion of the volatile species from the interlayer spaces of the graphene intercalation compound (see Figure 4. 2) [8, 11]. There was a visibly observable difference between graphite, GO and mw rGO as a result of chemical treatment that changed the colour of graphite from grey to black, and microwave irradiation which produced a powder that was very lightweight in nature. It is important for exfoliation that the synthesised material remains moist so that the irradiation can rapidly release moisture from the GO sheets. If the sample is dried out too much, then little if any exfoliation occurs.

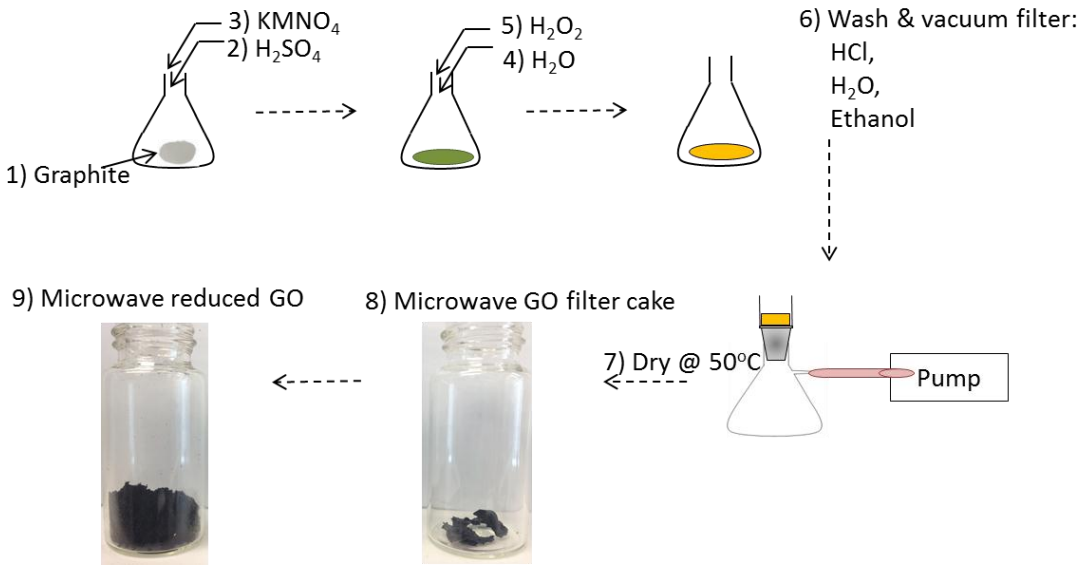

Figure 4. 2: Schematic representation of the synthesis of GO and exfoliation by microwave irradiation.

4.2.3. Electrode fabrication for organic and aqueous electrolyte testing.

Organic electrode fabricated via a drop cast method onto a heated Al substrate. Mw rGO was first dispersed in cyclohexyl pyrrolidone (CHP) and probe sonicated in an ice bath for 60 minutes at 30% amplitude. After this, the dispersion was centrifuged to remove any larger agglomerates. Following this, the dispersion was placed into a sonicator bath overnight with electrodes being made thereafter. CHP was selected based on the fact that there is extremely good matching between solvent and graphene surface energy which leads to the large scale exfoliation of graphene and GO [7]. The electrodes were then placed into a vacuum oven over night with the electrode being washed in acetonitrile prior to entering the oven. The initial temperature was 100^{o}C, and after 3 hours the electrode was washed once more with acetonitrile. The temperature was then increased to 175^{o}C and left for 12 hours. The approximate loading of mw rGO was 0.5 mg/cm^{2}.

The electrodes for electrochemical testing in aqueous media were fabricated by dispersing the mw rGO in ethanol and adding 10% PTFE binder. The suspension was probe sonicated for 30 minutes to ensure good mixing of the binder and mw rGO. After this, the vial containing the suspension was placed onto a hot plate at 65^{0}C and constantly mixed using a magnetic stirrer until all a majority of the ethanol evaporated, leaving a binded slurry. A spatula was used to spread the slurry onto a stainless steel mesh current collector, which was then placed into a vacuum oven at

100^{o}C and dried for 12 hours to remove any excess moisture. The approximate loading of mw rGO plus PTFE after drying was 0.8 mg/cm^{2}.

4.2.4. Brunauer-Emmett-Teller Measuremnets.

Brunauer-Emmett-Teller (BET) measurements are gas adsorption experiments on a solid surface that are able to deduce the specific surface area of that material. Here, the pores are filled with liquid N_2 at a relative pressure of P/P_0 close to unity [12]. When the relative pressure is lowered, a liquid volume will desorb from the surface of the material that is being studied which removes the condensate from the largest pores and reduces the thickness of the layer that is physically adsorbed. Further reduction in the relative pressure subsequently removes more condensate from the next largest pore size and so on [12]. The volume of N_2 used can be correlated to the volume of the material being studied [13, 14]. BET measurements were performed using a Autosorb IQ gas adsorption system from Quantachrome Instruments ™ with ASiQWin V.1.11 software.

Figure 4. 3: Photograph of BET system used for surface area determination of GO and mw rGO.

4.3. Discussion of Results.

4.3.1. Physical characterisation of as synthesised and microwave exfoliated graphene oxide.

The need for a quick and rapid method to exfoliate GO is paramount in order to have a fast and cost effective method that allows scaling for industrial scale production of graphene and graphene oxide [6]. Having well exfoliated GO is important as is allows the GO to be much more easily dispersed and stabilised, hence reducing aggregation and paving the way for better processability of carbon materials [7, 15].

4.3.1.1 Scanning electron microscopy.

In Figure 4. 4 below, SEM images are shown that depict the change of graphite into GO and further into mw rGO. In Figure 4. 4a, large graphite platelets can be observed where a large amount of stacking is apparent. Figure 4. 4b, the GO produced shows large stacked sheets which have a wave and crumpled like nature with some other carbonaceous agglomerates also apparent. In Figure 4. 4c after microwave irradiation has occurred, the GO expands and forms an accordion type structure that is highly porous [11]. Figure 4. 4d is a zoomed in region of Figure 4. 4c where the individual crumpled GO sheets form an interconnected network with minimal re-stacking.

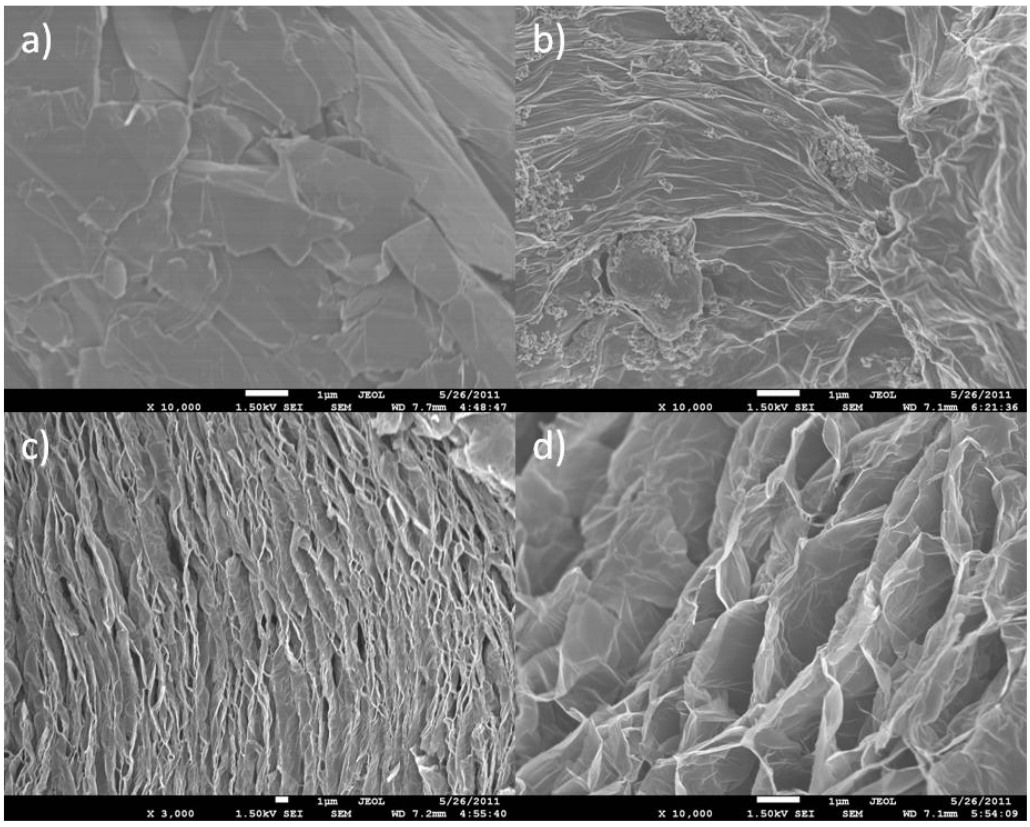

Figure 4. 4: SEM image of (a) As-received graphite (Bay Carbon Inc[(c)]); (b) GO after wash treatment, (c) mw rGO after microwave irradiation (3 x 10s bursts); (d) zoomed in image of the mw rGO.

4.3.1.2 X-ray diffraction.

Microwave irradiation of the GO led to exfoliation through the removal of volatile species from the interlayer spaces of the graphene intercalation compound [8, 11]. The XRD spectra of Figure 4. 5 shows the two distinct peaks for GO at 2θ = 10.2^{o} and 22.0^{o}, and one distinct peak for mw rGO at 2θ = 22^{o}. The sharp peak at 10.2^{o} is characteristic of GO powder that corresponds to an interlayer distance of 0.87 nm [15, 16]. The broader peak at 2θ = 22^{o} corresponds to the (002) crystal plane of graphite and amorphous carbon [17]. It is clear that after exfoliation using microwave irradiation, the sharp peak at 2θ = 10.2^{o} is much more suppressed as a result of the rapid expansion of the GO layers. Conductivity measurements show an order of magnitude change for GO from 167 ± 14 kΩ/square to 21 ± 4 kΩ/square for mw rGO.

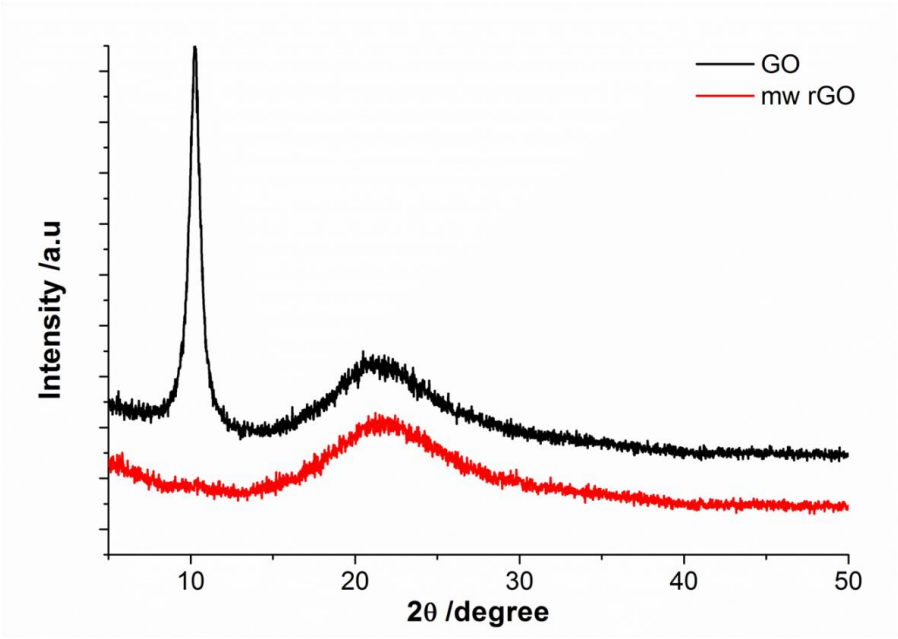

Figure 4. 5: XRD spectra of GO and mw rGO powder before and after microwave irradiation.

4.3.1.3 X-ray photoelectron spectroscopy.

The X-ray photoelectron spectra (XPS) of the graphene oxide before and after exfoliation (Figure 4. 6a and Figure 4. 6b) supports the conclusion that some reduction of the GO has occurred after the microwave irradiation. Each of the C1s spectra for GO and mw rGO can be deconvoluted into three peaks corresponding to certain functional groups. For GO, sp^3 carbon at 285.1eV, epoxy at 286.6 eV and ester at 288.3 eV. For mw rGO, sp^2 carbon at 284.4 eV, sp^3 C at 285.3, and an π-π* shake up at 289.1 eV [3, 15, 18].

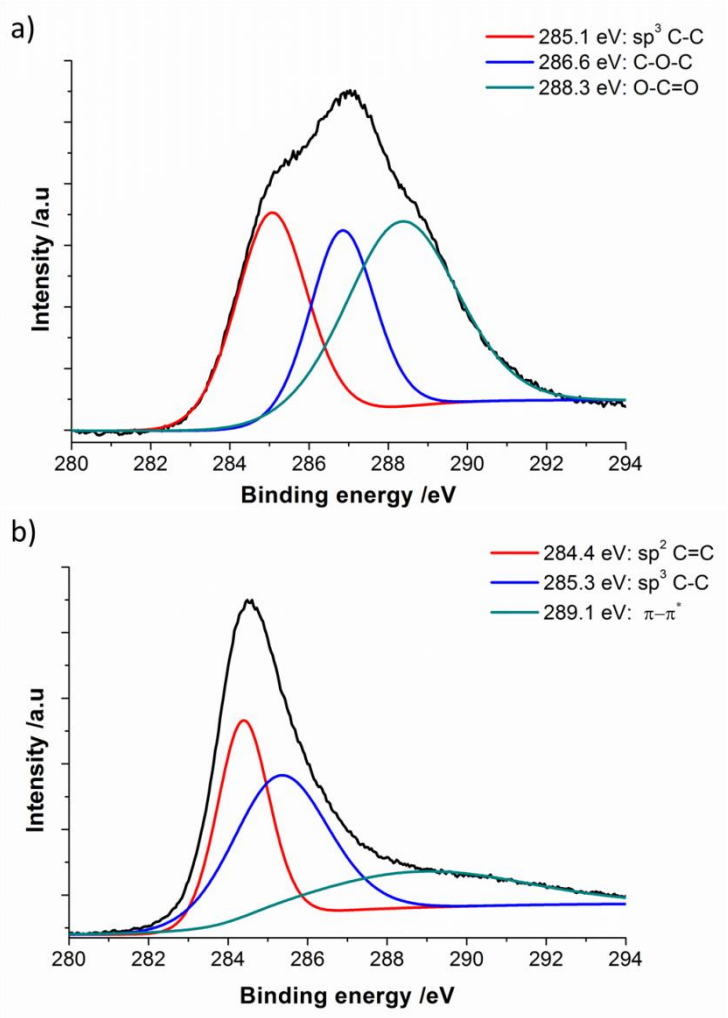

Figure 4. 6: Comparison of the C1s spectra for of (a) GO powder before microwave irradiation. (b) mw rGO after microwave irradiation.

The relative abundance of C and O for GO was 71.85% and 26.49% with similar sized peaks corresponding to a C/O ratio of 3:1. While for mw rGO the relative abundance of C and O was 92.22% and 7.53% with the epoxy / hydroxyl / carbonyl and carboxylate peaks much more depressed than the carbon peak corresponding to a C/O ratio of 12:1. It must also be noted that the slight shift of the deconvoluted peaks for mw rGO is due to the enhanced regular structure as compared to the GO [3].

4.3.1.4 Raman spectroscopy.

The Raman spectra of GO shown in Figure 4. 7a is characteristic of a sp^2 hybridised material that contains defects on the graphene / graphite basal planes. The D band peak of GO is associated with the disorder degree of graphene occurring at 1328 cm^{-1}; while the G band peak associated with first order scattering of the stretching vibration mode E_{2g} observed for sp^2 carbon domains occurs at 1586 cm^{-1} [1]. After microwave irradiation, there is a slight shift in both D and G band peaks from 1326 cm^{-1} and 1588 $cm^{-1}$to 1343 cm^{-1} and 1591 cm^{-1} respectively. The shift in both the D band and G band is due to the modification of the hexagonal network of carbon atoms with defects [19]. The ratio of the G/D band increased from 0.8 to 0.9, suggesting a slight reduction of the GO and a decrease in the quantity of structural defects [20]. A very weak 2D peak is present at 2616 cm^{-1} which is characteristic of chemically converted graphene oxide as full conversion to pure graphene does not occur [1].

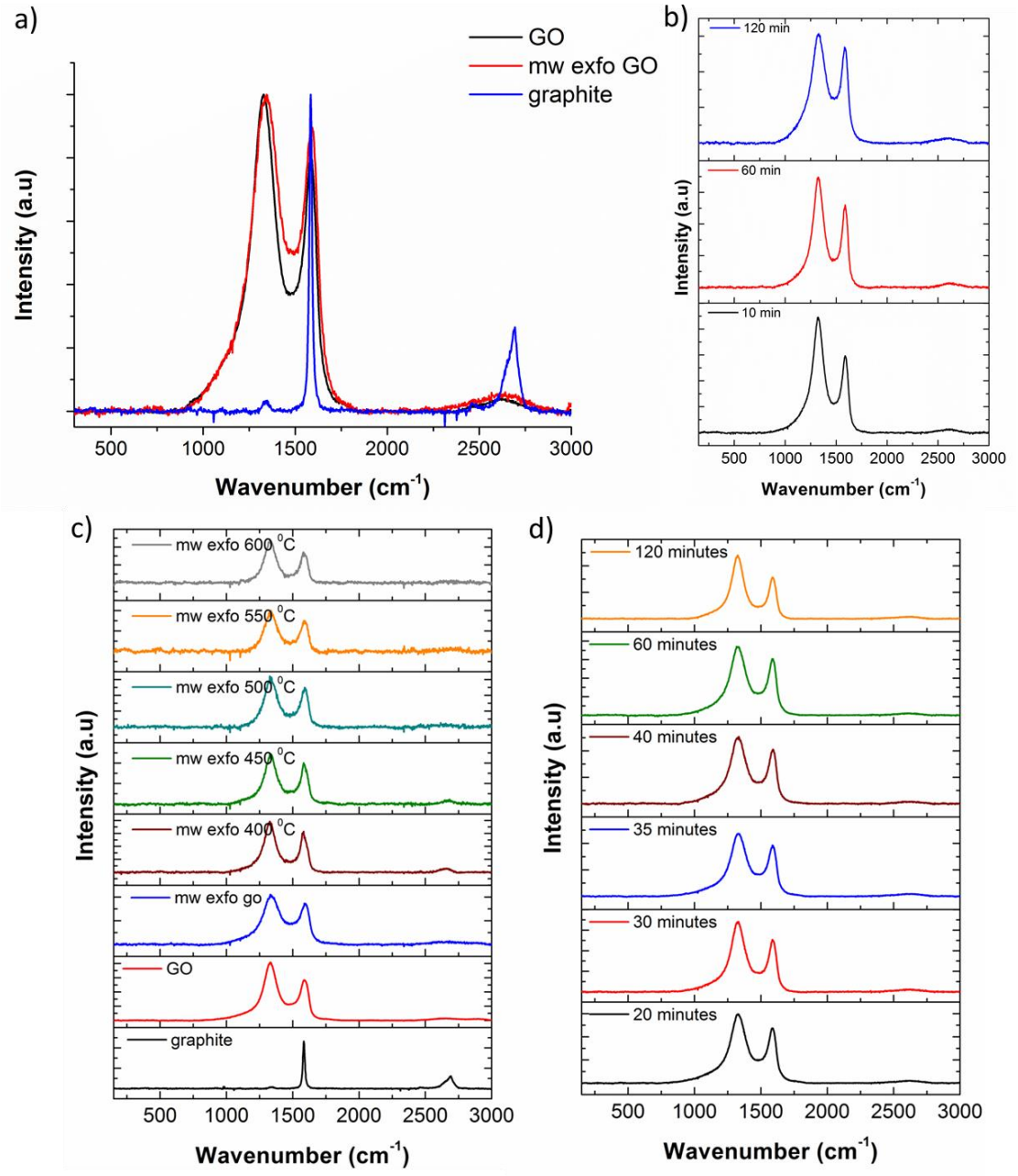

Figure 4. 7: (a) Raman spectra of GO, mw rGO and graphite powder before and after microwave irradiation. (b) Raman spectra of mw rGO powders that have been annealed in a H_2 / Ar atmosphere (1:4 v:v) at a flow rate of 250 mL min^{-1} for 10, 60, and 120 minutes. (c) Raman spectra of (b) graphite, GO, and mw rGO that has been annealed at different temperatures in air for 10 minutes. (d) mw rGO annealed at 400^{0}C for different times in air.

As a comparison, samples of mw rGO were annealed at 400^0C for 10, 60 and 120 minutes in a H_2 / Ar atmosphere (1:4 v:v) at a flow rate of 250 mL min^{-1}, as by Z. Wu et.al (Figure 4. 7b). when reducing graphene sheets [1]. The presence of H_2 gas is used as it is a good reducing agent. There is an improvement in the G/D band ratio when the mw rGO is annealed in a H_2 / Ar atmosphere (see Table 4. 1). The G/D ratio increased for an increased annealing time of 120 minutes reaching 0.87 after 120 minutes. In Figure 4. 7c, mw rGO powders were annealed at varying temperatures ranging from 400^oC to 600^oC in air with the best G/D ratio being 0.8 for an annealing temperature of 400^oC. In Figure 4. 7d, the temperature was kept constant at 400^oC and the time of annealing increased form 10 minutes to 120 minutes. The G/D ratio was maximum at 0.82 after 40 minutes. A detailed analysis of the G/D band ratio for all annealing treatments is outlined in Table 4. 1.

Table 4. 1 G/D band ratio for mw rGO powders at different annealing rates, times and atmospheres.

Material	**G/D**	**Annealing temp (^{0}C)**	**G/D**	**Annealing time (min) @ 400^0C**	**G/D**	**Annealing in H_2/Ar**	**G/D**
GO	0.69	400	0.8	10	0.8	10	0.66
mw rGO	0.8	450	0.79	20	0.79	60	0.74
		500	0.77	30	0.79	120	0.87
		550	0.75	35	0.8		
		600	0.69	40	0.82		
				60	0.82		
				120	0.64		

4.3.1.5 Brunauer-Emmett-Teller measurements.

The porosity characteristics of GO and mw rGO were investigated using N_2 adsorption-desorption isotherms (BET measurements) at 77K. In Figure 4. 8, it can be seen that both GO and mw rGO show N_2 adsorption. At low to middle relative pressures (0-0.8) the isotherms are of a type 4 nature where linearity and hysteresis effects (>0.4) are observed indicating a mesoporous structure [12]. In the high relative pressure regime (0.8-1) there is an abrupt increase in N_2 adsorption which is due to some macroporosity also being apparent [18]. The fact the adsorption / desorption is slightly shifted towards larger values for mw rGO indicates a higher surface area [21]. Surface area and total pore volume is compared in Table 4. 2 with the S_{BET} and total pore volume increasing from 814 m^2/g and 2.59 cm^3/g to 893 m^2/g and 2.71 cm^3/g respectively. In the inset of Figure 4. 8, it can be seen that the pore sizes are not significantly changed before and after microwave irradiation. The pore range distribution ranges from 20 Å to 800 Å indicating that this material is highly mesoporous and contains suitable dimensions for effective electrolyte ion interaction. As a comparison, Srinivas et. al. in 2012 synthesised various GO derived carbons and studied their gas adsorption properties. They found that the specific surface area could be varied from 600 m^2/g to 1900 m^2/g [21].

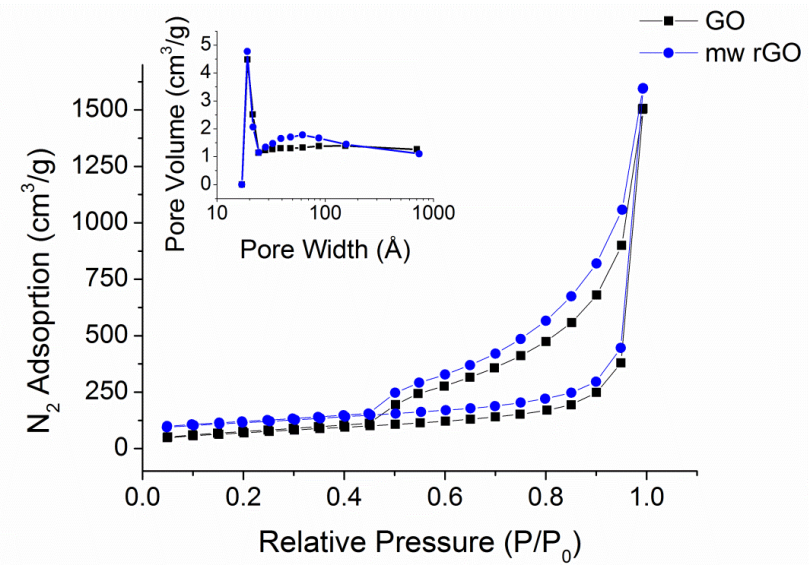

Figure 4. 8: Adsorption-desorption isotherms for GO and mw rGO. The inset represents pore size distributions.

Table 4. 2: Surface characteristics of GO and mw rGO.

Material	S_{BET} (m^2/g)	Total Pore Volume (cm^3/g)	Average Pore Size (Å)
GO	814	2.59	19.15
mw rGO	893	2.71	19.11

4.3.1.6 Thermo-gravimetric analysis of graphite, GO and mw rGO.

A comparison of results from thermo-gravimetric analysis (TGA) under a N_2:air flow at a heating rate of 2^0C/min are shown in Figure 4. 9. Three significant weight loss events are apparent for the GO after washing treatment. Below 100^0C is the weight loss of intercalated water that was not removed during drying, with the weight loss between 120 – 300^0C as a result of CO, CO_2 and H_2O from the most labile functional

groups [3, 11, 15]. Between 400^{o}C and 600^{0}C is the majority of the weight loss due to sample burning, where the carbon starts to decompose with O_2 forming CO_2 [11]. The TGA of the mw rGO does not show the peaks between 120 – 300^{0}C attributed to CO, CO_2 and H_2O, only two decomposition peaks at approximately 578^{0}C and 636^{0}C respectively. The 578^{0}C peak is due to sample burning once more, while the remaining material that decomposes at 636^{0}C corresponds to domains that did not undergo any intercalation and functionalisation that was removed during irradiation [11, 22]. As mentioned above, microwave irradiation of the GO led to exfoliation through the removal of volatile species from the interlayer spaces of the graphene intercalation compound [8, 11]. The pure graphite has the largest decomposition temperature at 800^{o}C which is to be expected due to its highly graphitic nature [11].

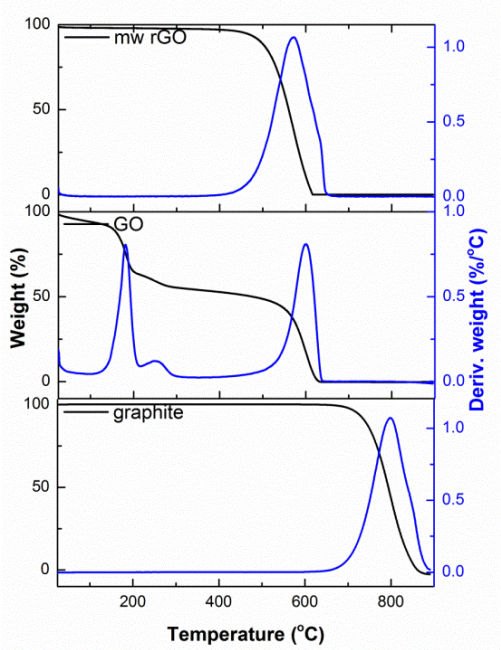

Figure 4. 9: Thermogravimetric analysis of graphite, graphene oxide as synthesised and after microwave irradiation. (Blue lines are first derivative peaks, which specify the temperature at weight loss events).

4.3.1.7 Comparison of mw rGO powders annealed in air at different and in a H_2 / Ar atmosphere..

In Figure 4. 10, a comparison of the TGA's for the mw rGO powders annealed at different temperatures ranging from 400 ^{0}C to 600 ^{0}C showed that the decomposition temperature is maximum at 621^{o}C at an annealing temperature of 400^{o}C, indicating that 400 ^{0}C is a suitable temperature for post treatment of the powders. The increase is mass of the 500^{o}C plot is due to some trapped residue in the heating chamber which dissociated onto the Pt pan during heating.

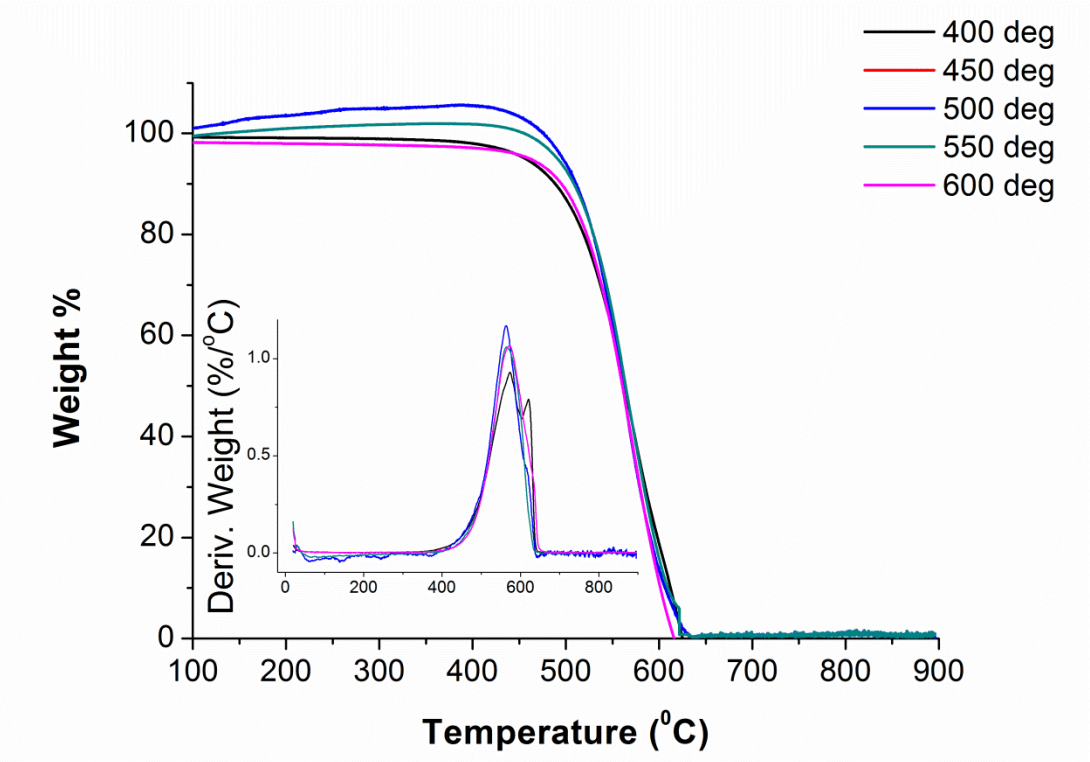

Figure 4. 10: Thermogravimetric analysis of mw rGO powders after annealing at 400 ^{0}C, 450 ^{0}C, 500 ^{0}C, 550 ^{0}C, and 600 ^{0}Cin air for 10 minutes. (Inset is first derivative peaks, which specify the temperature at weight loss events).

From Figure 4. 11, it can be seen that there is a slight shift towards higher decomposition temperatures after the treatment of the mw rGO powders in the H_2 / Ar atmosphere. After 10 and 60 minutes treatment the decomposition temperature was approximately 560^0C; while after 120 minutes the decomposition temperature reached 580^0C. The increased decomposition temperature indicates a higher degree of thermal stability and enhanced sp^2 hybridisation [11, 23]. The residue left over (approximately 6%-9% weight (%)) is most likely due to some contamination where residual material from the chamber wall has impacted on the Pt pan.

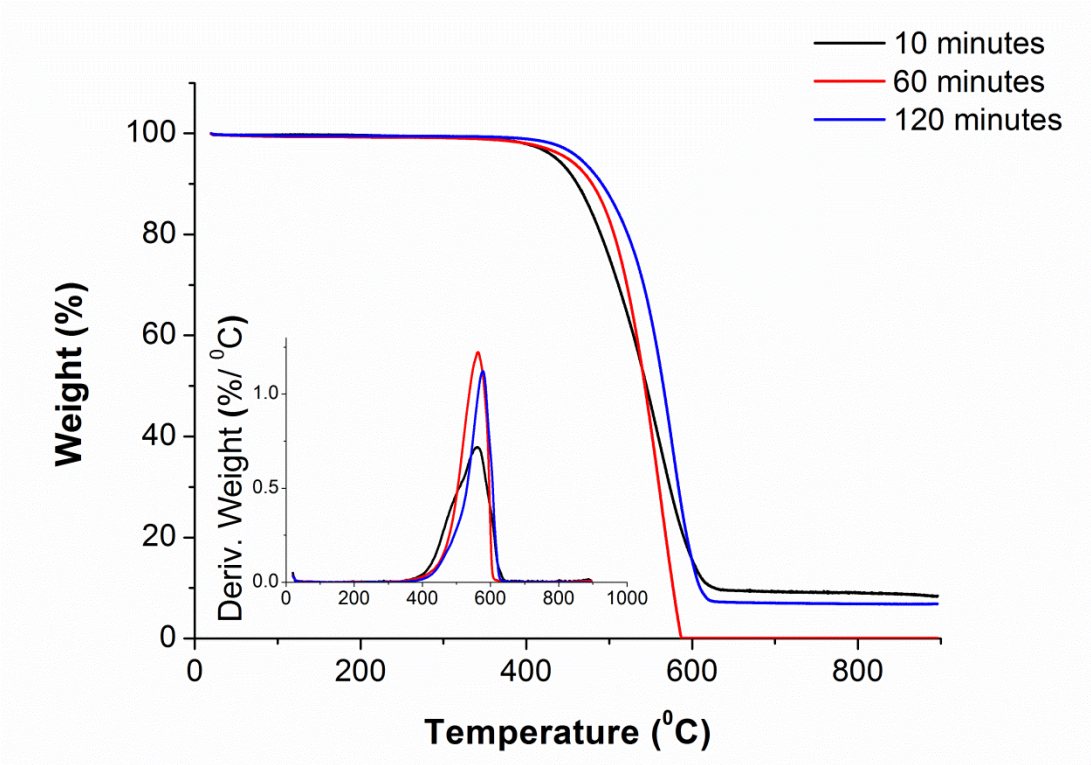

Figure 4. 11: Thermogravimetric analysis of mw rGO powders after annealing at 400 ^{0}C in an atmosphere of H_2 / Ar (1:4 v/v) for 10, 60, and 120 minutes.

4.3.2. *UV-visible spectroscopy of mw rGO powders.*

4.3.2.1 Mw rGO powders annealed in air and 1:4 ratio of H_2 / Ar.

The UV-Vis spectra of the GO, mw rGO and mw rGO annealed in air at 400^{0}C are shown in Figure 4. 12. The degree of conjugation can be determined by the λ_{max} of each UV-Vis spectrum. The more $\pi \rightarrow \pi^*$ transitions (conjugations), the less energy that is required for the electronic transition, resulting in a higher λ_{max} [3]. It can be seen that the GO material as synthesised has a λ_{max} = 263 nm. The mw rGO along with the annealed mw rGO at 400^{0}C have a λ_{max} in the range of 268-271 nm. In all materials, the shoulder peak around 300 nm can be attributed to $n \rightarrow \pi^*$ transitions of the carbonyl groups [3]. These results indicate that annealing at 400 ^{0}C slightly improves the conjugation of the GO material.

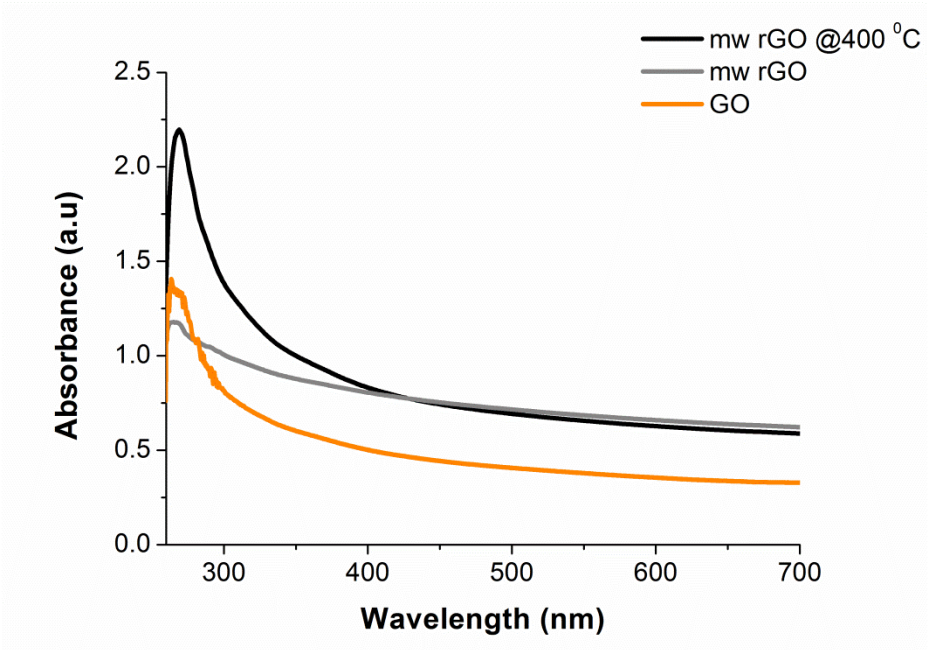

Figure 4. 12: UV-Vis spectra recorded for GO and mw rGO dispersed in organic solvent, N-Cyclohexyl-2-pyrrolidone at different annealing temperatures in air. Concentrations of the solutions varied between 0.02-0.06 mg/ml.

The UV-Vis spectra of the H_2 / Ar treated sample (Figure 4. 13) treated for 60 and 120 minutes shows a slight increase in the λ_{max} to approximately 273 nm and 276 nm respectively, indicating better conjugation [3]. After 10 minutes, λ_{max} was equal to 270 nm and is in the same range as the mw rGO powders treated in air.

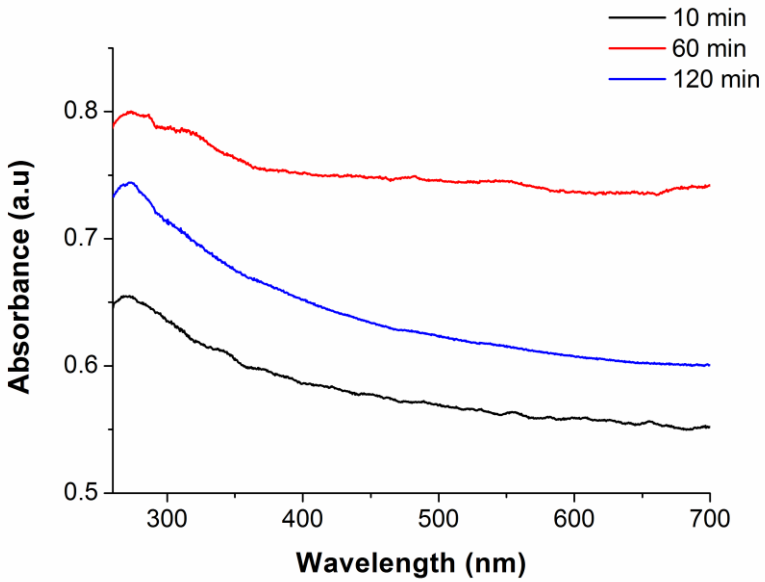

Figure 4. 13: UV-Vis spectra recorded for mw rGO annealed in a H_2 / Ar atmosphere (1:4 v/v) at a flow rate of 250 mL min^{-1} for 10, 60, and 120 minutes. Powders were dispersed in ethanol where the concentrations of the solutions varied between 0.02-0.06 mg/ml.

4.3.3. Kinetic studies of graphene oxide and microwave exfoliated graphene oxide.

4.3.3.1 Activity of carbon electrodes.

Imperfections that disrupt the sp^2 conjugation of graphene can alter its electrical, chemical, and mechanical properties [24]. Early studies by McCreery and co-

workers show that defects can alter the electrochemical activity of highly orientated pyrolytic graphite (HOPG) electrodes [25, 26]. A further extension of this in the role of such defects on the heterogeneous rate constant on the surface of graphene and graphene oxide. Recent literature on graphene and its derivatives has shown that edges and defects are more reactive than the basal plane due to an increase in the density of states (DOS) near the Fermi level [26, 27].

For enhanced electron transfer, the density of the defects needs to be high, while still maintaining conductivity that results in larger carrier densities and higher interfacial capacitance [25, 26]. In addition to the redox mechanism and the DOS, edge plane defects are significant and will alter the electrochemical reactivity toward a particular redox process and apparent k^0 will be controlled by these defects [24, 26, 27]. The redox couple potassium ferricyanide ($K_3Fe(CN)_6$) was used due to the fact that $K_3Fe(CN)_6$ is not a truly outer sphere electron transfer species and its electron transfer kinetics will be influenced by its adsorption the carbon surface and the chemical nature of the carbon.

4.3.3.1 Cyclic Voltammnetry.

It is useful to compare the electron transfer behaviour at the electrode / electrolyte interface of GO and mw rGO using the redox couple $K_3Fe(CN)_6$.

The CV of is of GO that has been cycled in a potassium ferricyanide electrolyte at varied scan rates. It can be seen that as the scan rate increase, the peak anodic

current increases which is indicative of the oxidation reaction; $Fe(CN)_6^{4-} \rightarrow Fe(CN)_6^{3-} + e^-$. As can be seen on the reverse sweep, there is little if any presence of a reversible reduction reaction; $Fe(CN)_6^{3-} + e^- \rightarrow Fe(CN)_6^{4-}$. The decrease in current between -0.2 V and – 0.4V is due to the reduction of any residual dissolved oxygen in the electrolyte that was not removed by N_2 bubbling [28, 29]. The inset of a shows the peak as a function of the square root of the scan rate. The trend is linear indicating an electrochemical behaviour that is controlled by the electron transfer process [30].

The reason for non-reversible behaviour may be due to large interactions between the GO functional groups and $Fe(CN)_6^{3-}$ as well as the larger amount of GO stacking which hinders diffusion and does not allow reduction. The standard heterogeneous rate constant k^0 for an oxidation of a non-reversible reaction can be calculated using [31].

$$E_p = E_{1/2} + \frac{RT}{(1-\alpha)nF}\left[0.780 + ln\left\{\frac{1}{k^0}\sqrt{\frac{(1-\alpha)nFDv}{RT}}\right\}\right] \quad \textit{Equation 4.1}$$

Where ΔE_p is the peak voltage (mV), $E_{1/2}$ is the half wave potential (mV), k^0 is the heterogeneous electron transfer rate constant (*cm/s*), D is the diffusion coefficient (cm^2/s), and v is the scan rate (*V/s*), α is the transfer coefficient, R, T, *n* and F have their usual meaning.

In an ideal reversible reaction, satisfying the Butler-Volmer theory, the transfer coefficient α which represents ideal symmetry of the electron energy barrier is 0.5. Deviation from this occurs for non-ideal systems and it manifests itself as distortion and significant disappearance of the non-reversible redox couple. α of GO was calculated using the slope in the linear portion of the Tafel plot of b and . From the Tafel plot, α was calculated to be 0.98. α was then used in conjunction with Equation 4.3 to calculate k^0. It can also be seen that in the Tafel plot, there is deviation away from the linear segment as the overpotential (η) approaches 0.2 V. The reason for this is due to the fact that back reactions arising from dissolved oxygen can no longer be neglected. At higher overpotentials, the negative deviations come from mass transfer limitations [31].

$$\eta = \frac{2.3RT}{(1-\alpha)nF}\ log\frac{i_a}{i_0} \qquad \textit{Equation 4.2}$$

Where η is the overpotential (mV), α is the transfer coefficient, *i* is the current (A), and i_0 is the exchange current (A), R, T, n, and F have their usual meaning.

The electron transfer rate constant k^0 was calculated to be 3.77 x 10^{-8} ± 1.99 x 10^{-9} cm/s. To confirm these results, the heterogeneous rate constant can be calculated from impedance spectroscopy using Equation 4.4 and Equation 4.5. Here, i_0 corresponds to the exchange current, A is the electrochemical surface area calculated from voltammetry, C is the bulk concentration and R_{ct} is the charge

transfer resistance [30, 31]. The calculation yields k^0 = 8.86 x 10^{-7} ± 4.21 x 10^{-8} cm/s which confirms non-reversible kinetics as obtained from the Nicholson method.

$$i_0 = \frac{RT}{nFR_{ct}} \qquad \textit{Equation 4.3}$$

$$i_0 = FAk^0C \qquad \textit{Equation 4.4}$$

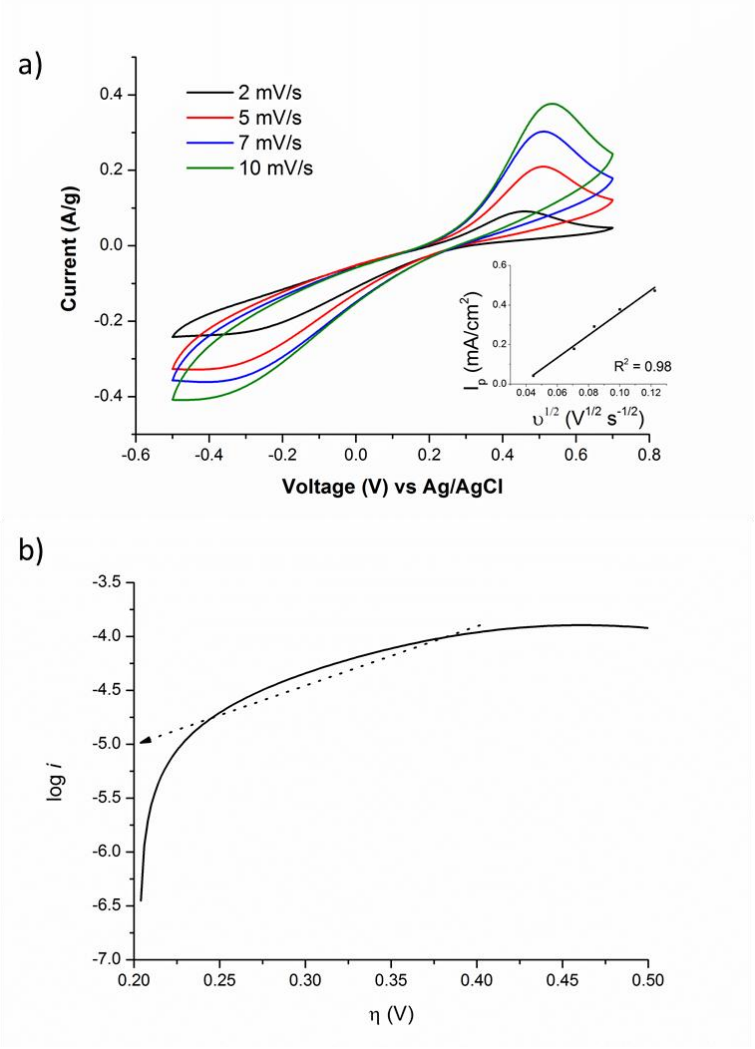

Figure 4. 14: Electrochemistry at the GO electrode. (a) CV of 0.01 M $K_3Fe(CN)_6$ containing 0.1 M $NaNO_3$ at varied scan rates. Inset; Peak anodic current $I_{(p)}$ versus the square root of the scan rate obtained from the CV. (b) Tafel plot of the anodic branch current-overpotential curve at a scan rate of 2 mV/s. Material slurry was cast onto stainless steel mesh using a thin spatula.

In the CV of Figure 4. 15a, the scan rate of the mw rGO electrode is increased from 2 mV/s to 10 mV/s. Here it can be seen that as the scan rate increases, the peak separation (ΔE_p) increases. ΔE_p is much greater than the 59 mV of ideal Nerstian behaviour reflecting an electrochemical behaviour that is controlled by a slow electron transfer process [30]. The electron transfer being quasi reversible signifies that the rate of electron transfer is too slow to keep the redox couple in equilibrium when the potential is changed rapidly. The inset of Figure 4. 15a shows the peak anodic current verses the square root of the potential scan rate obtained from the forward sweep of the ferricyanide redox couple. The plot once again shows good linearity signifying an electrochemical behaviour that is controlled by the electron transfer process and is diffusion controlled [30, 32].

In Figure 4. 15b, the dimensionless kinetic parameter Ψ, that is determined from the potential peak separation, is related to the electron transfer rate constant k^0 from Nicholson's working curve and is given by [32, 33].

$$\Psi = k^0 sqrt\left(\frac{RT}{\pi nFD}\right)v^{-1/2} \qquad \textit{Equation 4.5}$$

Where k^0 is the heterogeneous electron transfer rate constant (*cm/s*), D is the diffusion coefficient (cm^2/s), and v is the scan rate (*V/s*), R, T, *n* and F have their usual meaning. The standard heterogeneous rate constant k^0can be determined by calculating the slope of Ψ verses $\upsilon^{-1/2}$, leading to a value of $1.05 \times 10^{-5} \pm 1.83 \times 10^{-9}$

cm/s. EIS k^0 yielded values of 4.96 x 10^{-5} ± 2.04 x 10^{-7} cm/s which suggests quasi-reversible kinetics as confirmed by the results obtained from the Nicholson method.

Overall it can be seen that mw rGO has a much faster electron transfer rate constant than GO with the values being 1.05 x 10^{-5} ± 1.83 x 10^{-9} cm/s and 8.86 x 10^{-7} ± 4.21 x 10^{-8} cm/s respectively. This is due to the reduced nature of the GO sheets as well as the porosity attained during microwave exfoliation. As a comparison, M. Pacios et. al. calculated the rate constants (using the Nicholson method) of graphite, HOPG basal and edge with the values reported being 3.5 x10^{-4} cm/s, 2.5 x 10^{-5} cm/s, and 7.0 x 10^{-3} cm/s respectively.

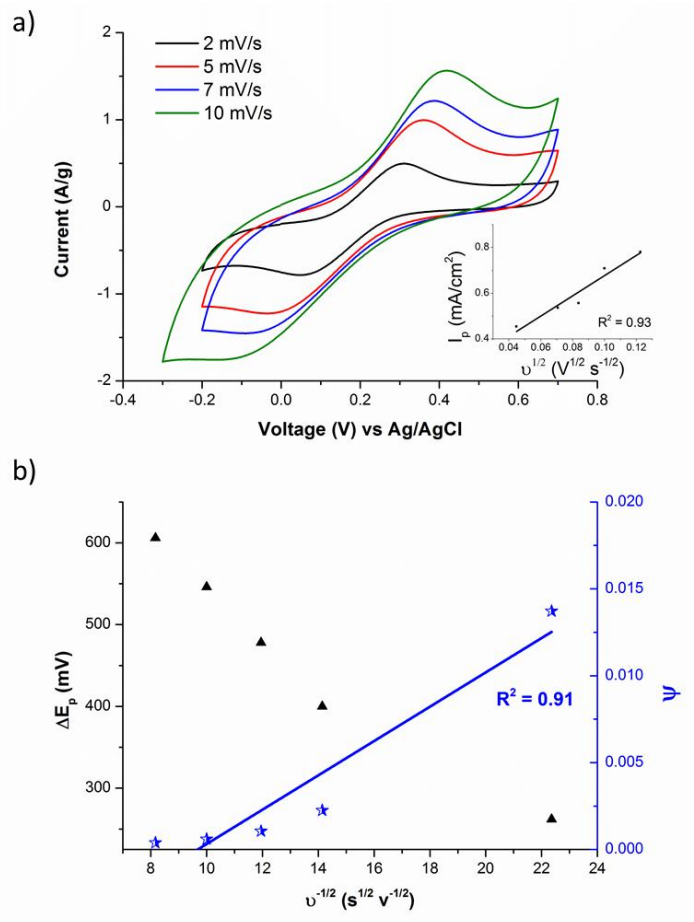

Figure 4. 15: Electrochemistry at the mw rGO electrode. (a) CV of 0.01 M $K_3Fe(CN)_6$ containing 0.1 M $NaNO_3$ at varied scan rates. Inset; Peak anodic current $I_{(p)}$ versus the square root of the scan rate obtained from the CV. (b) Peak separation ΔE_p and Nicholson's kinetic parameter Ψ versus the reciprocal of the square root of the scan rate. Material slurry was cast onto stainless steel mesh using a thin spatula.

4.3.3.2 Electrochemical impedance spectroscopy and cyclic voltammetry in commercially provided organic electrolyte.

In Figure 4. 16, the effects of thee annealing treatments on the electrochemistry is compared. A comparison of the CV in Figure 4. 16a shows that the air and H_2 /Ar annealed mw rGO electrodes obtain a larger current density with a more square behaviour apparent that is indicative of double layer capacitance with better

reversibility if the charging-discharging process [34]. The capacitance was calculated at 5mV/s and the values were 14 F/g (mw rGO); 27 F/g (Air annealed at 400^0C), and 25 F/g (H_2 / Ar annealed at 400^0C). From the Nyquist plot of Figure 4. 16b, it can be seen that the mw rGO has an extended Warburg diffusion (45^0) region indicating slow ion transport at the electrode / electrolyte interface [35]. Both annealed samples show a reduced Warburg region that indicates faster kinetics. The polarisation resistance (the approximate semi-circle that intercepts the x-axis at high frequencies) is also severely reduced after annealing. The value for the mw rGO electrode decreases from approximately 384.9 Ω.cm^2 to 30. Ω.cm^2 and 93.7 Ω.cm^2 for the for the air annealed and H_2 / Ar annealed, indicating that the resistance of the electrolyte ions within the smallest macro and meso-pores of the material is reduced [36]. Figure 4. 16c compares the rate capability of the electric double layer (speed of charge / discharge) with the annealed mw rGO in air showing the fastest time constant.

It was expected that the mw rGO powder treated in the H_2 /Ar atmosphere would give the best performance in terms of capacitance due to the fact the material displayed a greater degree of sp^2 hybridisation leading to an enhanced wettability in the organic electrolyte. This was not the case however; but it was observed that when testing the electrode treated in the H_2 / Ar atmosphere at 400^0C, the electrode showed degradation and peeling off from the ITO. The mw rGO that was not treated, and the air treated mw rGO showed little / or no degradation over the course of the electrochemical measurements.

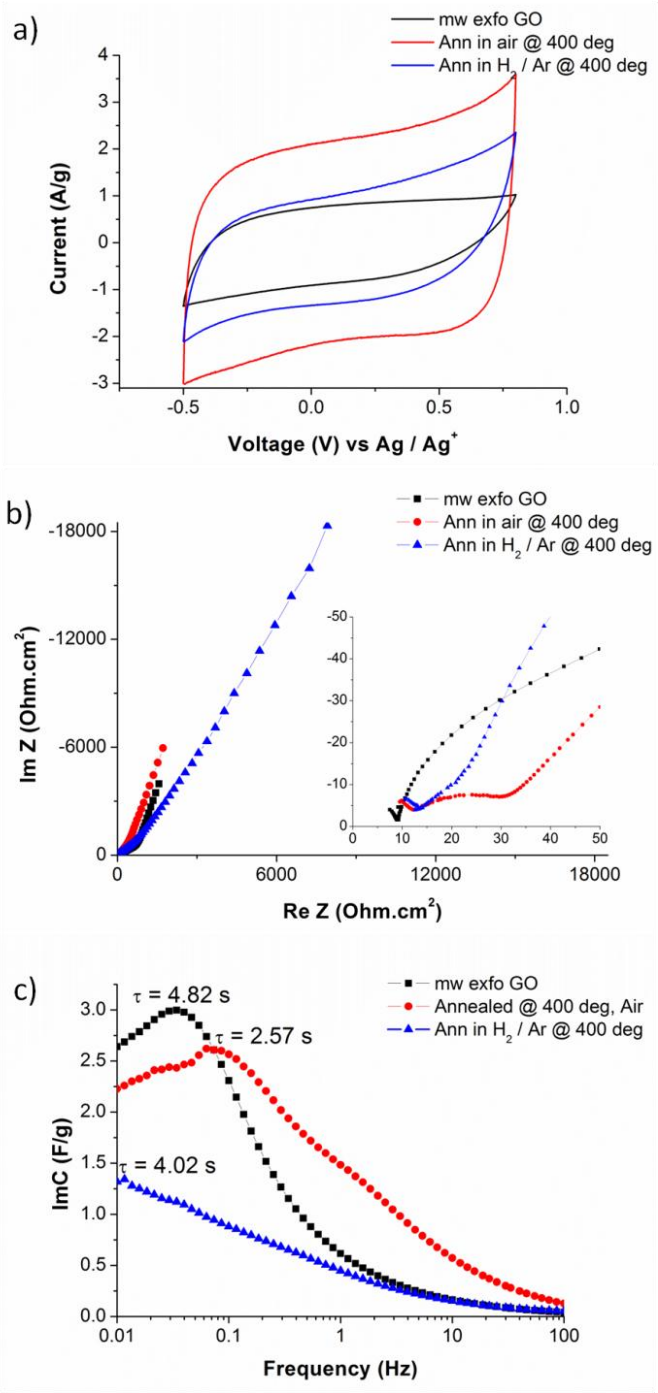

Figure 4. 16: mw rGO, powder annealed in air at 400^{0}C for 40 minutes, and powder annealed in a H_2 / Ar atmosphere (1:4 v/v) at 400^{0}C for 120 minutes. (a) CV comparison at 100 mV/s, (b) Nyquist comparison, (c) Imaginary part of capacitance verses frequency. System is three electrode with a Pt mesh counter, electrolyte supplied by Cap-XX[(c)], and a Ag/Ag$^+$ reference electrode. Material slurry was cast onto stainless steel mesh using a thin spatula.

4.3.3.3 Electrochemical impedance spectroscopy and cyclic voltammetry in 1M $NaNO_3$ / H_2O.

In Figure 4. 17 the effects of thee annealing treatments on the electrochemistry is compared. A comparison of the CV in Figure 4. 17a shows that the air and H_2 /Ar annealed mw rGO electrodes obtain a larger current density with a more elliptical / square behaviour that is indicative of double layer capacitance that is sluggish [34]. The capacitance was calculated at 5mV/s and the values were 9 F/g (mw rGO); 33 F/g (Air annealed at 400^0C), and 13 F/g (H_2 / Ar annealed at 400^0C). From the Nyquist plot of Figure 4. 17b, it can be seen that the H_2 / Ar annealed mw rGO has an extended Warburg diffusion (45^0) region indicating slow ion transport at the electrode / electrolyte interface [35]. Both annealed samples show a larger Warburg region that indicates slower kinetics. The time constants that relate to the rate of charging / discharging have been calculated using the peak of the imaginary capacitance (Figure 4. 17c). The samples that have been annealed show a shift to the left of imaginary part of C indicating a larger time constant. The polarisation resistance (the approximate semi-circle that intercepts the x-axis at high frequencies) is also increased after annealing. The value increases from approximately 100.4 Ω for the mw rGO electrode to 192.7 Ω.cm^2 and 589.3 Ω.cm^2 for the air annealed and H_2 / Ar annealed, indicating that the resistance of the electrolyte ions within the smallest macro and meso-pores of the material is increased [36].

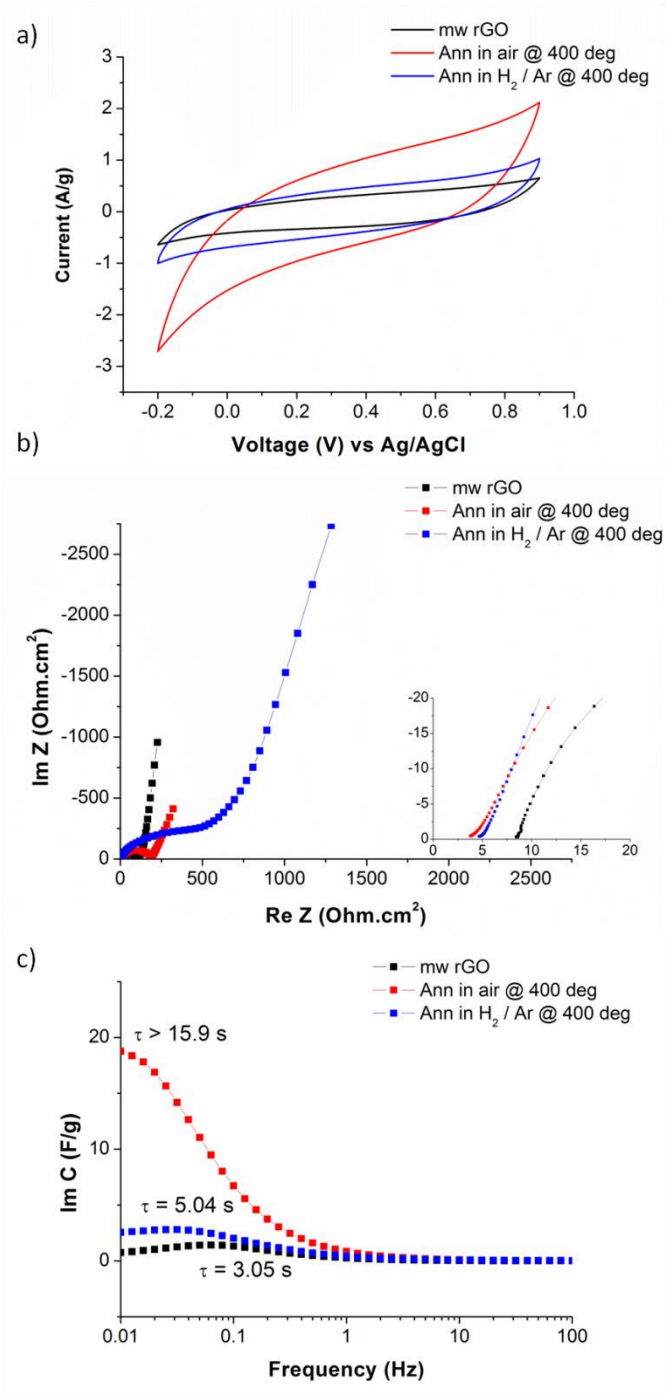

Figure 4. 17: mw rGO, powder annealed in air at 400^{0}C for 40 minutes, and powder annealed in a H_2 / Ar atmosphere (1:4 v/v) at 400^{0}C for 120 minutes. (a) CV comparison at 100 mV/s, (b) Nyquist comparison, (c) Imaginary part of capacitance verses frequency. System is three electrode with a Pt mesh counter, electrolyte is 1M $NaNO_3$ in H_2O, and a Ag/ AgCl reference electrode. Material slurry was cast onto stainless steel mesh using a thin spatula.

It can be seen that the air annealed mw rGO powder gave the best performance in terms of capacitance due to the fact the material displayed an enhanced wettability in the aqueous electrolyte meaning that more of the electroactive surface area was utilised. When the solution resistance values are compared for the three electrodes it can be seen that the air annealed is 4.0 $\Omega.cm^2$, followed by the H_2/ Ar treated and mw rGO electrode at 4.8 $\Omega.cm^2$ and 8.4 $\Omega.cm^2$ respectively.

4.4. Conclusions.

In summary, graphene oxide has been synthesised from commercially available graphite which has then been exfoliated used microwave irradiation. The benefit of synthesising and exfoliating GO in this manner is that it provides a porous and conductive scaffold which can be used in the development of composite materials.

The synthesis involved chemical reactions with H_2SO_4, $KMnO_4$, and H_2O which introduced functional groups on the graphene sheets. Washing treatments with HCL, and ethanol ensured that no $Mn(OH)_2$ precipitates formed throughout the graphene oxide which was confirmed by EDS.

SEM images showed before and after microwave irradiation showed a flat and stacked structure was converted into an porous / accordion type structure where. XRD showed that after microwave irradiation the sharp peak at $2\theta = 10.2^o$ is much more suppressed as a result of the rapid expansion of the GO layers. XPS confirmed that after irradiation the relative abundance of C increased, and O decreased from 71.85% and 26.49% to 92.22% and 7.53%. The FTIR spectra was not as clear but

C=C and C=O stretching vibrations were observed at 1524 cm^{-1},1511 $cm^{-1}$and 1685 cm^{-1},1699 cm^{-1} indicating the presence of functional groups. Raman spectroscopy showed the typical D and G bands and a very weak 2D band that is characteristic of chemically converted graphene. Thermo-gravimetric analysis showed significant weight loss events for GO due to the rapid expansion and release of H_2O, CO and CO_2 with the decomposition of carbon occurring at 600^0C. The mw rGO showed a decomposition temperature of 450^oC.

Raman spectra showed that varying the annealing times and atmospheres resulted in slight alteration of the G/D band ration. The optimum temperature for annealing was found to be at 400^oC. For annealing in air, the optimum temperature was 400^oC for 40 minutes. For annealing in an atmosphere of H_2 / Ar, the optimum temperature was 400^oC for 120 minutes. UV-Vis showed that after microwave exfoliation, λ_{max} increased from 263 nm to between 268-271 nm indicating a higher degree of conjugation.

Lastly, three electrode electrochemical measurements were performed in organic and aqueous conditions. In the organic system the capacitance (calculated at 5mV/s) were 14 F/g (mw rGO); 27 F/g (Air annealed at 400^0C), and 25 F/g (H_2 / Ar annealed at 400^0C). While for the aqueous system, the capacitance (calculated at 5mV/s) were 9 F/g (mw rGO); 33 F/g (Air annealed at 400^0C), and 13 F/g (H_2 / Ar annealed at 400^0C). In both instances the mw rGO powder that was annealed in air had the best performance in terms of capacitance but the organic system displayed a more rectangular behaviour indicating faster charge / discharge effects.

The mw rGO that had been synthesised and optimised will be used in the ensuing chapters for further investigation into composite electrode materials for supercapacitor device applications. The mw rGO will act as a mesoporous high surface area conductive scaffold aiding charge storage and delivery mechanisms.

4.5. References.

1. Wu, Z.-S., W. Ren, L. Xu, F. Li, and H.-M. Cheng, *Doped Graphene Sheets as Anode Materials with Superhigh Rate and Large Capacity for Lithium Ion Batteries.* ACS Nano, 2011: p. 5463–5471.
2. Akhavan, O. and E. Ghaderi, *Toxicity of Graphene and Graphene Oxide Nanowalls Against Bacteria.* ACS Nano, 2010. **4**(10): p. 5731-5736.
3. Marcano, D.C., D.V. Kosynkin, J.M. Berlin, A. Sinitskii, Z. Sun, A. Slesarev, L.B. Alemany, W. Lu, and J.M. Tour, *Improved Synthesis of Graphene Oxide.* ACS Nano, 2010. **4**(8): p. 4806-4814.
4. Hou, C., Q. Zhang, M. Zhu, Y. Li, and H. Wang, *One-step synthesis of magnetically-functionalized reduced graphite sheets and their use in hydrogels.* Carbon, 2011. **49**(1): p. 47-53.
5. Eda, G. and M. Chhowalla, *Chemically Derived Graphene Oxide: Towards Large-Area Thin-Film Electronics and Optoelectronics.* Advanced Materials, 2010. **22**(22): p. 2392-2415.
6. Green, A.A. and M.C. Hersam, *Emerging methods for producing monodisperse graphene dispersions.* Journal of Physical Chemistry Letters, 2010. **1**(2): p. 544-549.

7. Coleman, J.N., *Liquid-Phase Exfoliation of Nanotubes and Graphene.* Advanced Functional Materials, 2009. **19**(23): p. 3680-3695.

8. Tryba, B., A.W. Morawski, and M. Inagaki, *Preparation of exfoliated graphite by microwave irradiation.* Carbon, 2005. **43**(11): p. 2417-2419.

9. N. E. Sorokina, M. A. Khaskov, V. V. Avdeev, and I.V. Nikol'skaya, *reaction of graphite with sulfuric acid.* Russian Journal of General Chem., 2005. **75**(2): p. 162-168.

10. Hirata, *US Patent 6 596 396, 2003*.

11. Falcao, E.H.L., R.G. Blair, J.J. Mack, L.M. Viculis, C.-W. Kwon, M. Bendikov, R.B. Kaner, B.S. Dunn, and F. Wudl, *Microwave exfoliation of a graphite intercalation compound.* Carbon, 2007. **45**(6): p. 1367-1369.

12. Dias, A. and V.S.T. Ciminelli, *Analysis of nitrogen adsorption-desorption isotherms for the estimation of pore-network dimensions and structure of ferroelectric powders.* Ferroelectrics, 2000. **241**(1): p. 9-16.

13. Naono, H., M. Hakuman, and T. Shiono, *Analysis of nitrogen adsorption isotherms for a series of porous silicas with uniform and cylindrical pores: A new method of calculating pore size distribution of pore radius 1-2 nm.* Journal of Colloid and Interface Science, 1997. **186**(2): p. 360-368.

14. Brunauer, S., P.H. Emmett, and E. Teller, *Adsorption of Gases in Multimolecular Layers.* Journal of the American Chemical Society, 1938. **60**(2): p. 309-319.

15. Zhu, Y., M.D. Stoller, W. Cai, A. Velamakanni, R.D. Piner, D. Chen, and R.S. Ruoff, *Exfoliation of Graphite Oxide in Propylene Carbonate and Thermal*

Reduction of the Resulting Graphene Oxide Platelets. ACS Nano, 2010. **4**(2): p. 1227-1233.

16. Li, Z., J. Wang, S. Liu, X. Liu, and S. Yang, *Synthesis of hydrothermally reduced graphene/MnO2 composites and their electrochemical properties as supercapacitors.* Journal of Power Sources, 2011. **196**(19): p. 8160-8165.

17. Chen, Y., Y. Zhang, D. Geng, R. Li, H. Hong, J. Chen, and X. Sun, *One-pot synthesis of MnO2/graphene/carbon nanotube hybrid by chemical method.* Carbon, 2011. **49**(13): p. 4434-4442.

18. Yang, S.-Y., K.-H. Chang, H.-W. Tien, Y.-F. Lee, S.-M. Li, Y.-S. Wang, J.-Y. Wang, C.-C.M. Ma, and C.-C. Hu, *Design and tailoring of a hierarchical graphene-carbon nanotube architecture for supercapacitors.* Journal of Materials Chemistry, 2011. **21**(7): p. 2374-2380.

19. Krishnamoorthy, K., M. Veerapandian, R. Mohan, and S.J. Kim, *Investigation of Raman and photoluminescence studies of reduced graphene oxide sheets.* Applied Physics A: Materials Science and Processing, 2012. **106**(3): p. 501-506.

20. Moon, I.K., J. Lee, R.S. Ruoff, and H. Lee, *Reduced graphene oxide by chemical graphitization.* Nature Communications, 2010. **1**(6).

21. Srinivas, G., J. Burress, and T. Yildirim, *Graphene oxide derived carbons (GODCs): Synthesis and gas adsorption properties.* Energy and Environmental Science, 2012. **5**(4): p. 6453-6459.

22. Stankovich, S., D.A. Dikin, R.D. Piner, K.A. Kohlhaas, A. Kleinhammes, Y. Jia, Y. Wu, S.T. Nguyen, and R.S. Ruoff, *Synthesis of graphene-based nanosheets*

via chemical reduction of exfoliated graphite oxide. Carbon, 2007. **45**(7): p. 1558-1565.

23. Viculis, L.M., J.J. Mack, O.M. Mayer, H.T. Hahn, and R.B. Kaner, *Intercalation and exfoliation routes to graphite nanoplatelets.* Journal of Materials Chemistry, 2005. **15**(9): p. 974-978.

24. Tan, C., J. Rodríguez-López, J.J. Parks, N.L. Ritzert, D.C. Ralph, and H.D. Abruña, *Reactivity of Monolayer Chemical Vapor Deposited Graphene Imperfections Studied Using Scanning Electrochemical Microscopy.* ACS Nano, 2012. **6**(4): p. 3070-3079.

25. Cline, K.K., M.T. McDermott, and R.L. McCreery, *Anomalously Slow Electron Transfer at Ordered Graphite Electrodes: Influence of Electronic Factors and Reactive Sites.* The Journal of Physical Chemistry, 1994. **98**(20): p. 5314-5319.

26. McCreery, R.L. and M.T. McDermott, *Comment on Electrochemical Kinetics at Ordered Graphite Electrodes.* Analytical Chemistry, 2012. **84**(5): p. 2602-2605.

27. Zhang, B., L. Fan, H. Zhong, Y. Liu, and S. Chen, *Graphene Nanoelectrodes: Fabrication and Size-Dependent Electrochemistry.* Journal of the American Chemical Society, 2013. **135**(27): p. 10073-10080.

28. Moulton, S.E., J.N. Barisci, A. Bath, R. Stella, and G.G. Wallace, *Investigation of protein adsorption and electrochemical behavior at a gold electrode.* Journal of Colloid and Interface Science, 2003. **261**(2): p. 312.

29. Moulton, S.E., J.N. Barisci, A. Bath, R. Stella, and G.G. Wallace, *Studies of double layer capacitance and electron transfer at a gold electrode exposed to protein solutions.* Electrochimica Acta, 2004. **49**(24): p. 4223.

30. Pacios, M., M. del Valle, J. Bartroli, and M.J. Esplandiu, *Electrochemical behavior of rigid carbon nanotube composite electrodes.* Journal of Electroanalytical Chemistry, 2008. **619-620**: p. 117-124.

31. A. J. Bard and L.R. Faulkner, *Electrochemical Methods: Fundamentals and Applications*. 2001: John Wiley & Sons, Inc.

32. Li, W., C. Tan, M.A. Lowe, H.c.D. Abrunìfa, and D.C. Ralph, *Electrochemistry of Individual Monolayer Graphene Sheets.* ACS Nano, 2011: p. 2264–2270.

33. Nicholson, R.S., *Theory and Application of Cyclic Voltammetry for Measurement of Electrode Reaction Kinetics.* Analytical Chemistry, 1965. **37**(11): p. 1351-1355.

34. Prabaharan, S.R.S., R. Vimala, and Z. Zainal, *Nanostructured mesoporous carbon as electrodes for supercapacitors.* Journal of Power Sources, 2006. **161**(1): p. 730-736.

35. Lu, W., L. Qu, K. Henry, and L. Dai, *High performance electrochemical capacitors from aligned carbon nanotube electrodes and ionic liquid electrolytes.* Journal of Power Sources, 2009. **189**(2): p. 1270-1277.

36. H. Kurig, A. Janes, and E. Lust, *Electrochemical Characteristics of Carbide-Derived Carbon|1-Ethyl-3-methylimidazolium Tetrafluoroborate Supercapacitor Cells.* Journal of The Electrochemical Society, 2010. **157**(3): p. A272-A279.

Chapter 5: Single walled carbon nanotube – microwave reduced graphene oxide composite electrodes.

5. Single walled carbon nanotube - microwave reduced graphene oxide composite electrodes.

5.1. Introduction

An ideal graphene sheet is a single-atom thick nanostructured sheet arranged in a two dimensional honeycomb lattice with a theoretical surface area of 2630 m^2/g (BET surface area measurements of graphene oxide outlined in Chapter 4), and high electrical conductivity giving it the potential for the use in electrochemical energy storage devices [1, 2]. Economically speaking, graphitic forms of carbon are widely available, while large scale synthesis of graphene (and its derivatives such as graphene oxide) is relatively simple to perform [2, 3]. The advantage of graphene is its ability to be used as a high surface area conducting scaffold in a given electrode system, which provides good electrical properties but a robust and support of the structure [3]. Its disadvantage is that the conductivity of polycrystalline graphene is limited by the high resistance of the grain boundaries [4]. Carbon nanotubes (CNTs) are materials of great interest in the area of energy storage and conversion due to their favourable electrical and mechanical properties; as well as low cost and abundance compared to rare earth elements such as ruthenium oxides that are used in supercapacitors [5, 6]. The theoretical amount of current a CNT can carry within its length is 10^9 A/cm^2 while Young's modulus ranges from 1054 – 1200 GPa [7, 8].

Composites containing CNTs and graphene are materials of particular interest in the areas of energy storage and conversion area due to their physical properties which can result in unique optical, electrical, magnetic and chemical properties which are substantially different than that of the individual components [1, 9]. It has been shown that the combination CNTs and graphene allows an expressway of electron transport from the electrode material to the current collector. The ability of the CNTs to 'sandwich' in between the graphene sheets helps to alleviate restacking by acting as a spacer (thus maintaining surface area) while increasing electrical conductivity and mechanical stability [1, 10]. Thus, the integration of graphene and CNTs into a hybrid electrode material allows the formed composite to utilise the properties of both materials, creating new properties that could not be attained by either material alone [11, 12]. This enables a highly efficient nano-structured system that is highly desirable for electrochemical applications [13].

In this chapter, we describe a facile method to develop electrodes of single walled nanotubes (SWNTs) and microwave exfoliated graphene oxide (mw rGO) with varying weight ratios via sonication, centrifugation and vacuum filtration. These composites are then optimised with the best performing weight ratio to be used in the fabrication of a supercapacitor. Physical characterisation of the SWNT – mw rGO films have shown SWNTs to be well dispersed on the mw rGO sheets. Extensive electrochemical testing revealed that the incorporation of SWNTs with mw rGO yielded an electrode material with large specific capacitances. Further enhancement was made by plasma treating these samples which added functional

groups that provided greater access of the aqueous electrolyte. The specific capacitances in all cases exceeded 125 F/g with the optimised / ideal weight ratio of 90% SWNT – 10% mw rGO exceeding 300 F/g. The thickness of the 90% SWNT – 10% mw rGO was optimised with the maximum attainable current per unit area arising at a thickness of 17 microns (mass loading of 1.57 mg/cm^2). Lastly, a device was fabricated with an electrode thickness of 17 microns that showed excellent reversibility upon current switching from 0.05 A/g up to 4.0 A/g, with a specific capacitance of 80 mF/cm^2 and 128 F/g respectively at 0.05 A/g. Long term testing showed excellent stability over 10 000 cycles, with the maximum attainable energy and power density of the SWNT-mw rGO active material being 5.8 W.h/kg and 1900 kW/kg.

5.2. Experimental specific to chapter 5.

5.2.1. Synthesis and fabrication of SWNT- microwave exfoliated graphene oxide films.

SWNTs and mw rGO were dispersed using 1-cyclohexyl-2-pyrrolidone (CHP) at a concentration of 1 mg/ml using a combination of probe sonication at 30% amplitude for 90 minutes (2s on, 1s off pulse), (Branson probe sonifier) and bath (Branson B1500R-MT) for 90 minutes. The dispersion was left overnight for reaggregation to occur after which centrifugation (Eppendorf Centrifuge 5415 D) was done for 90 minutes at 2500 rcf [14]. The concentration of the supernatant solution was determined via Ultra Violet-Visible Spectroscopy (UV-VIS) using a Shimadzu UV-1800. The sample was then diluted to a concentration of 0.4 mg/ml.

The full description of the synthesis of microwave exfoliated graphene oxide is outlined in Chapter 4.

Dispersions of SWNT and mw rGO were mixed via a combination of probe sonication for 30 minutes at 30% amplitude (330W, 1s on / 1s off pulse), followed by bath sonication for 90 minutes. SWNT-mw rGO composites were prepared by having varied weight ratios of SWNT (Unidym Carbon Nanotubes, batch# P0900) which were used as received, and mw rGO. The weight ratios were:

- 100% SWNT, 95% SWNT-5% mw rGO;
- 90% SWNT-10% mw rGO;
- 85% SWNT-15% mw rGO;
- 80% SWNT-20% mw rGO;
- 50% SWNT-50% mw rGO;
- 40% SWNT- 60% mw rGO;
- 100% mw rGO.

Films of SWNT-mw rGO at different compositions were made using vacuum filtration onto platinum sputter coated (100 nm thickness) hydrophilic Millipore PVDF membrane (VVP) with a pore size of 0.1 um. All electrodes prior to testing were washed with acetonitrile (to remove excess CHP), dried overnight in a vacuum oven at 80^{o}C and plasma treated for 20 minutes to enhance the wettability of the electrode in aqueous environments. The film thickness was 1 µm which

corresponded to a mass loading of 0.049 mg/cm^2. The films were then characterised by three electrode experiments (section 5.2.2).

At the optimum SWNT-mw rGO weight ratio, films were fabricated via the vacuum filtration method described previously to increase the film thickness. Film thickness was increased by increasing the volume of SWNT-mw rGO dispersion during vacuum filtration. The thicknesses and corresponding mass loadings were:

- 1 µm, 0.049 mg/cm^2;
- 1.5 µm, 0.098 mg/cm^2;
- 2.5 µm, 0.196 mg/cm^2;
- 4.5 µm, 0.393 mg/cm^2;
- 6.5 µm, 0.589 mg/cm^2;
- 10.5 µm, 0.982 mg/cm^2;
- 17 µm, 1.571 mg/cm^2;
- 21.5 µm, 1.965 mg/cm^2.

5.2.2. Three electrode electrochemical measurements.

Electrochemical studies of the fabricated electrodes with varied weight ratios were performed using a three electrode set up in order to determine the optimum electrode composition. Subsequently, after the optimum electrode composition of 90%SWNT-10% mw rGO was determined, the thickness of the electrode (at this weight ratio) was varied in order to analyse the electrochemical response / kinetic

response as a function of thickness. Three electrode measurements and device studies were employed to study the varied thicknesses. Once the optimum electrode composition and thickness was deduced, long term supercapacitor device testing took place. The three electrode set-up comprised of 1 M $NaNO_3$ /H_2O, a Pt mesh counter electrode (1.75 cm^2) and the SWNT- mw rGO as the working electrode.

5.2.3. Plasma treatment of single walled – microwave exfoliated graphene oxide films.

Plasma treatment was performed using a Harrick Plasma Cleaner PDC-32G-2 and Plasmaflo PDC-FMG. Air flow was kept at 1100 mTorr with exposure being varied for 10 minutes, 20 minutes, 30 minutes, and 40 minutes.

5.2.4. Profilometry measurements.

The SWNT-mw rGO composite films had their thickness varied by adding more of the dispersion during vacuum filtration. The thickness was measured using a Veeco Wyko NT9100 profilometer. The purpose of this was to determine the thickness of the best performing SWNT-mw rGO ratios, then subsequently use this for device fabrication.

5.2.5. Fabrication of supercapacitor.

Supercapacitor device fabrication and testing occurred for the 90% SWNT-10% mw rGO at a thickness of 17 microns (see section 5.2.1). The test cell developed was

using a Swagelok® system where a nylon union tube fitting was modified to house two stainless steel plates as can be seen by Figure 5. 1 .This type of cell is commonly used in supercapacitor device testing as shown by Demarconnay et. al. and Malak-Polaczyk et.al. [15, 16]. The as-prepared electrode material to be studied was sandwiched between these two plates, with the PVDF membranes acting as a separator. The 1 M H_2SO_4 electrolyte was added through the top nut. The fasteners on either end of the stainless steel rods were used to strongly attach wires for electrical connection to the potentiostat. The Swagelok® test cell and electrodes used are shown in Figure 5. 1. The optimum drying regime for the composite electrode was at 155^0C in a vacuum oven for 8 hours, and then followed by annealing at 310^oC on a hot plate (fume hood) for a further 8 hours to ensure the removal of residual CHP.

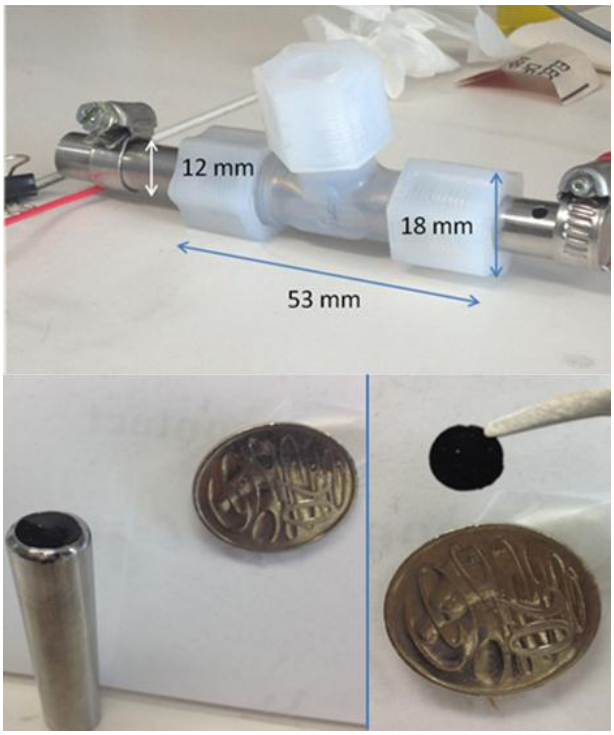

Figure 5. 1: Swagelok test cell comprising a nylon fitting and two stainless steel plates inserted either side. Bottom is SWNT- mw rGO composite material.

5.3. Discussion of Results.

5.3.1. Physical characterisation of single walled carbon nanotubes – microwave reduced graphene oxide films.

5.3.1.1 Scanning electron microscopy, Raman Spectroscopy, x-ray diffraction and x-ray photoelectron spectroscopy of mw rGO.

Please refer to Chapter 4, section 4.3 for physical characterisation of GO and mw rGO using Raman spectroscopy, XRD, and XPS.

5.3.1.2 Scanning electron microscopy.

In Figure 5. 2, a cross- section of SWNT – mw rGO composite electrodes on platinised PVDF membrane with varying weight ratios is shown. The 100% mw rGO shows reduced GO sheets that have some porosity to them, but re-stacking is apparent as some flat sections of the GO sheets will tend to re-stack. When the SWNT- mw rGO composites are considered, it appears that there is a layering effect due to π-π stacking interactions where mw rGO sheets are covered with SWNTs and hence are separated [17]. Physically, the mw rGO acts as a spacer and scaffold that enhances the dispersibility of the SWNTs. This effect is thought to better tailor the micro-porosity and mesoporosity of the system which maximises the utilisable surface area.

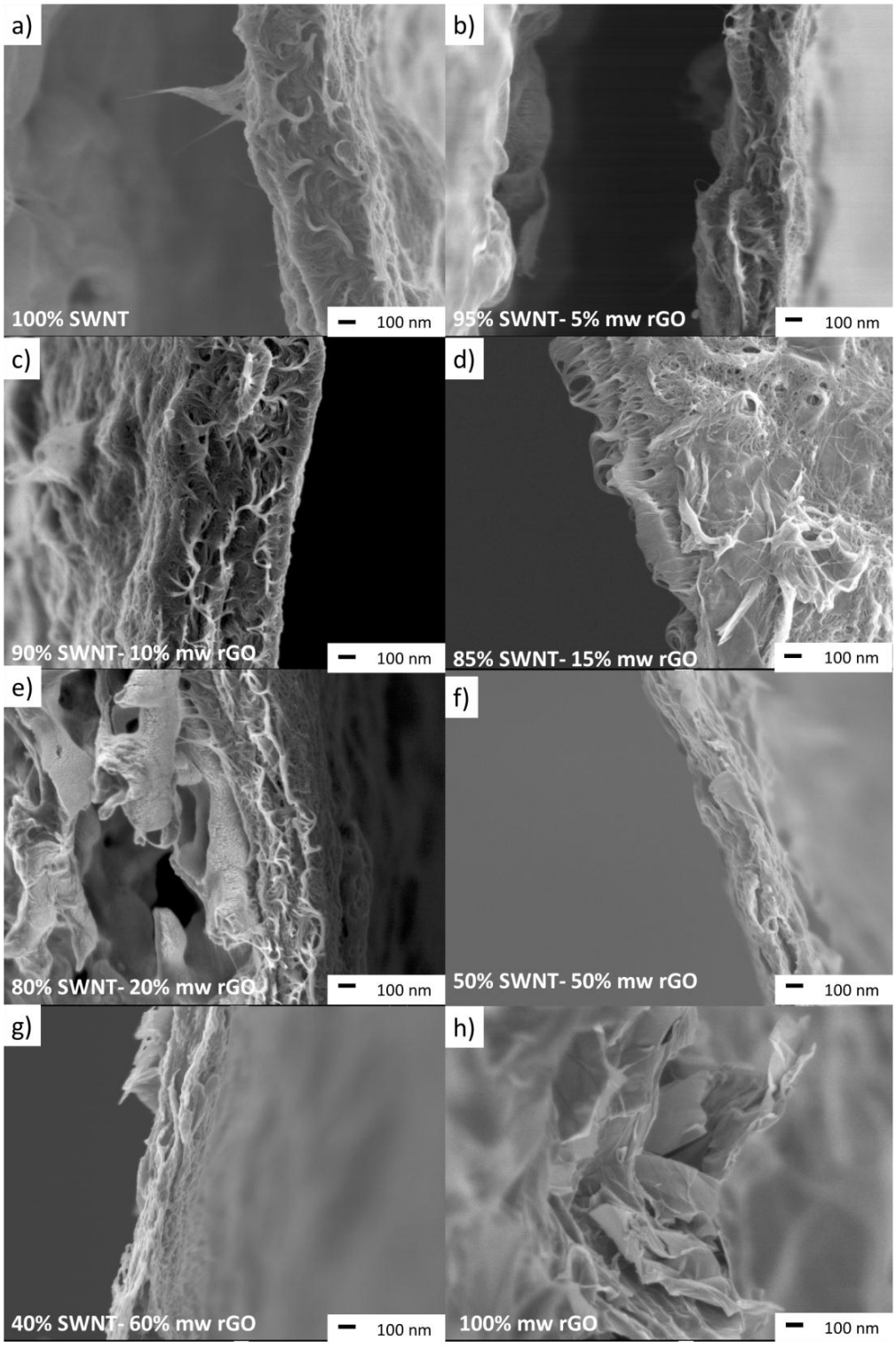

Figure 5. 2: SEM cross-sectional images of SWNT – mw rGO composite with varying weight ratios. (a) 100% SWNT, (b) 95% SWNT- 5% mw rGO, (c) 90% SWNT- 10% mw rGO, (d) 85% SWNT- 15% mw rGO, (e) 80% SWNT- 20% mw rGO, (f) 50% SWNT- 50% mw rGO, (g) 40% SWNT- 60% mw rGO, (h) 100% mw rGO.

In Figure 5. 3, there is significant disparity between the surface images of 100% SWNT, 90% SWNT-10% mw rGO, and 100% mw rGO. When considering the 100% SWNT film (Figure 5. 3a Figure 5. 3b), the SWNTs are distributed in a non-uniform manner with varying bundle sizes and some agglomeration being apparent. For 90% SWNT-10% mw rGO (Figure 5. 3c and Figure 5. 3d), mw rGO islands / platelets are uniformly dispersed throughout the SWNT matrix. Conversely, these GO platelets help to better disperse the SWNTs In Figure 5. 3d, the boundary between two sheets is shown. Here, the GO sheets are joined with SWNTs. It is most likely that the high surface energy of the GO edges attracts the ends of the SWNTs and forms a connection. The 100% mw rGO film (Figure 5. 3e and Figure 5. 3f) contains a random distribution of sheets that are crumpled in nature and absent in large restacking effects.

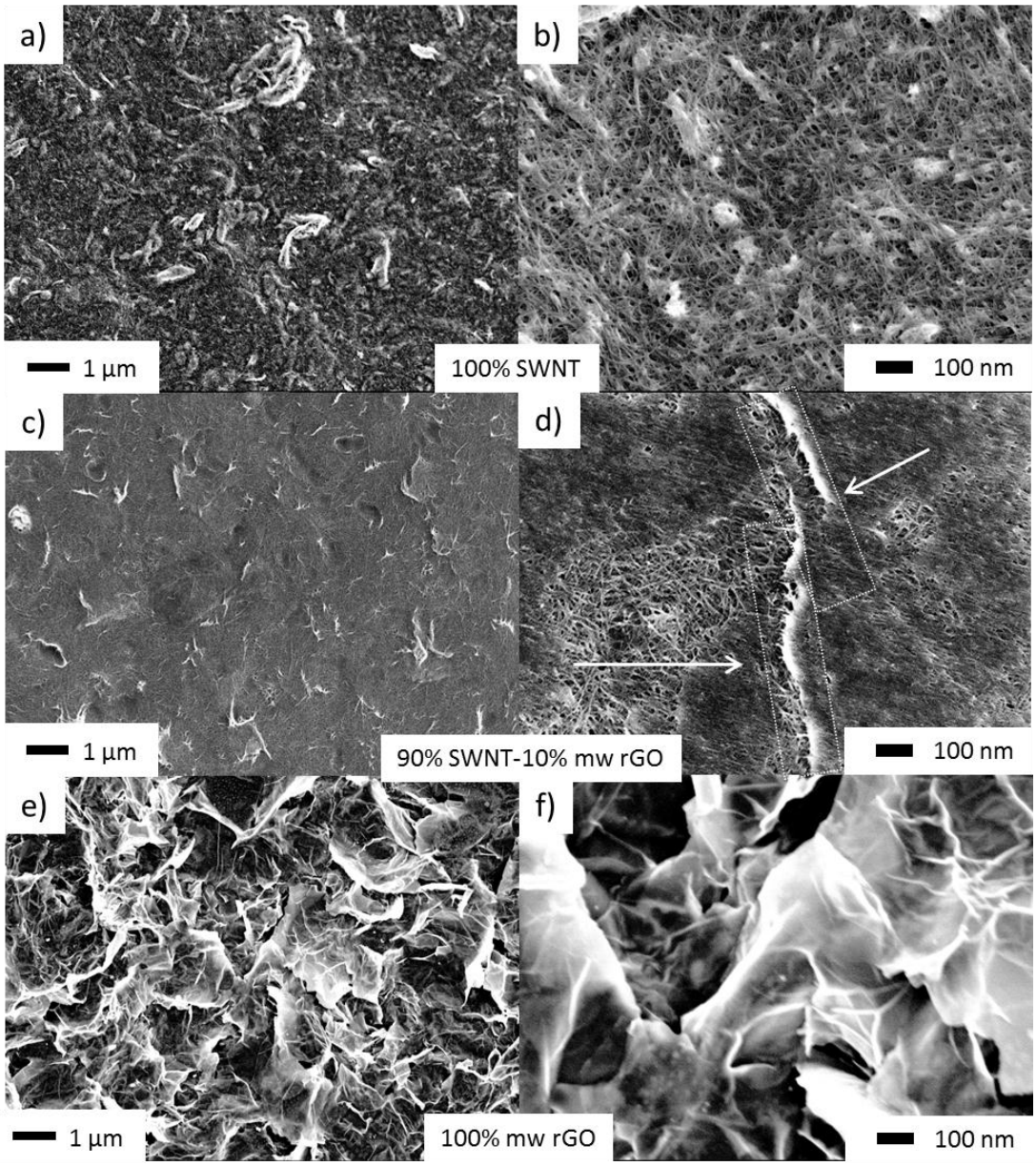

Figure 5. 3: SEM surface images. (a) 100% SWNT (low magnification). (b) 100% SWNT (high magnification). (c) 90% SWNT – 10% mw rGO (low magnification). (d) 90% SWNT – 10% mw rGO (high magnification). (e) 100% mw rGO (low magnification). (f) 100% mw rGO (high magnification).

5.3.1.3 Raman spectroscopy and X-ray diffraction.

The Raman spectra observed in Figure 5. 4 of SWNTs and mw rGO composite electrodes are characteristic of single walled nanotubes where the 632.81 nm line has been used. The radial breathing modes are located between 150 cm^{-1} and 305 cm^{-1} that represent the coherent vibration of the C atoms in the radial direction [18]. The ratio of the D/G band (D band at 1304 cm^{-1} is the disorder induced band arising from defects in the walls of the nanotubes; the G band at 1591 cm^{-1} is a result of phonon wave confinement along the circumferential direction of the nanotube that leads to tangential C-C stretching transitions) is slightly increased after plasma treatment for all electrodes due to the addition of some functional groups. Further in the chapter (section 5.3.1.5), the effects of plasma treatment can be seen by an increase in wettability of the electrode. However the fact that before and after plasma treatment the D/G ratio of SWNT is 0.116 and 0.150 respectively indicates a high degree of purity for the SWNTs [18, 19]. The shoulder peak (1553 cm^{-1}) to the left of the G band (1591 cm^{--1}) is most likely from the effect of functional groups on the sp^2 breathing mode [18].

As the ratio of SWNT is decreased (and subsequently mw rGO is increased) it can be seen that the D band of the composite broadens. This broadening is thought to be two D band peaks associated with SWNT and mw rGO with the D band of the mw rGO becoming stronger as its weight ratio is increased. It can be seen from Figure 5. 4 that there is an extremely small difference in the D/G band ratio of the Raman spectra for the samples prior to and after plasma treatment. This may suggest that

the plasma treatment is sufficient enough to provide an enhanced wettability of the electrode surface, but the there are no significant alteration to the materials structure [20]. It can be seen that the 100% SWNT shows smalls bundles of SWNTs that form the film, with calculation of the SWNT bundle size estimated in Table 5. 1 for all composites [21]. The SWNT bundle diameters have only increased very marginally indicating a uniform and very well formed suspension between SWNT and mw rGO has still occurred. Calculation of average bundle size is obtained from Equation 5.1 where *d* is the diameter in nanometres and ω is the wavenumber in cm^{-1} [21].

$$d = \frac{248}{\omega} \qquad \textit{Equation 5.1}$$

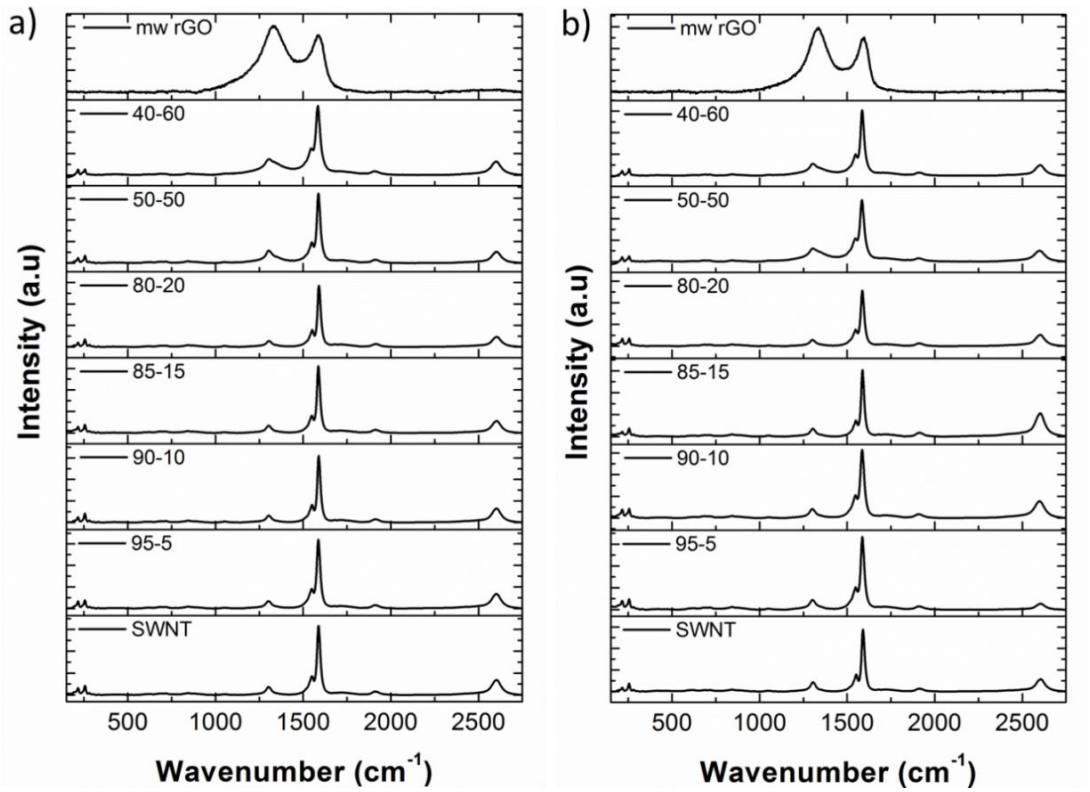

Figure 5. 4: Raman spectroscopy of SWNT-mw rGO composite electrodes at 632.81 nm laser line. (a) As synthesised. (b) After 20 minutes plasma treatment.

Table 5. 1: Comparison of radial breathing modes and D/G band ratio for SWNT – mw rGO composite electrodes before and after 20 minutes plasma treatment.

%Composition of SWNT:mw rGO (w/w)	Before treatment d^{1st} peak (nm)	Before treatment d^{2st} peak (nm)	Plasma treated d^{1st} peak (nm)	Plasma treated d^{2st} peak (nm)	D/G Before	D/G plasma treated
100:0	1.149	0.969	1.153	0.974	*0.116*	*0.150*
95:5	1.147	0.970	1.151	0.974	*0.109*	*0.138*
90:10	1.149	0.973	1.152	0.973	*0.106*	*0.133*
85:15	1.151	0.972	1.152	0.974	*0.111*	*0.118*
80:20	1.147	0.970	1.149	0.973	*0.096*	*0.114*
50:50	1.149	0.970	1.152	0.974	*0.186*	*0.212*
40:60	1.147	0.971	1.154	0.974	*0.182*	*0.229*
0:100	-	-	-	-	*1.168*	*1.240*

5.3.1.4 X-Ray Diffraction.

In the XRD of Figure 5. 5, 100% mw rGO, 90% SWNT-10%mw rGO and 100% SWNT is compared. It can be seen that the broad peak centered between 21^{o} and 22^{o} due to (002) graphitic plane [22]. The broadness of the XRD peak from all samples is most probably due to either an increase in disorder of the through-plane direction and/or structural defects induced by probe sonication [23]. The (002) plane for 90% SWNT – 10% mw rGO composite is slightly shifted to the left to $2\theta = 21^{o}$ due to the increase in interplanar spacing of the GO sheets caused by the insertion of the SWNTs (4.04 Å compared to 4.43 Å). For the 100% SWNT and 90% SWNT-10% mw

rGO samples, it can be seen that there is a sharp peak at 40° coresponding to the (100) plane with an interplanar spacing of 2.2 Å, which is expected for highly pure SWNTs as described by Zhou et. al. [24].

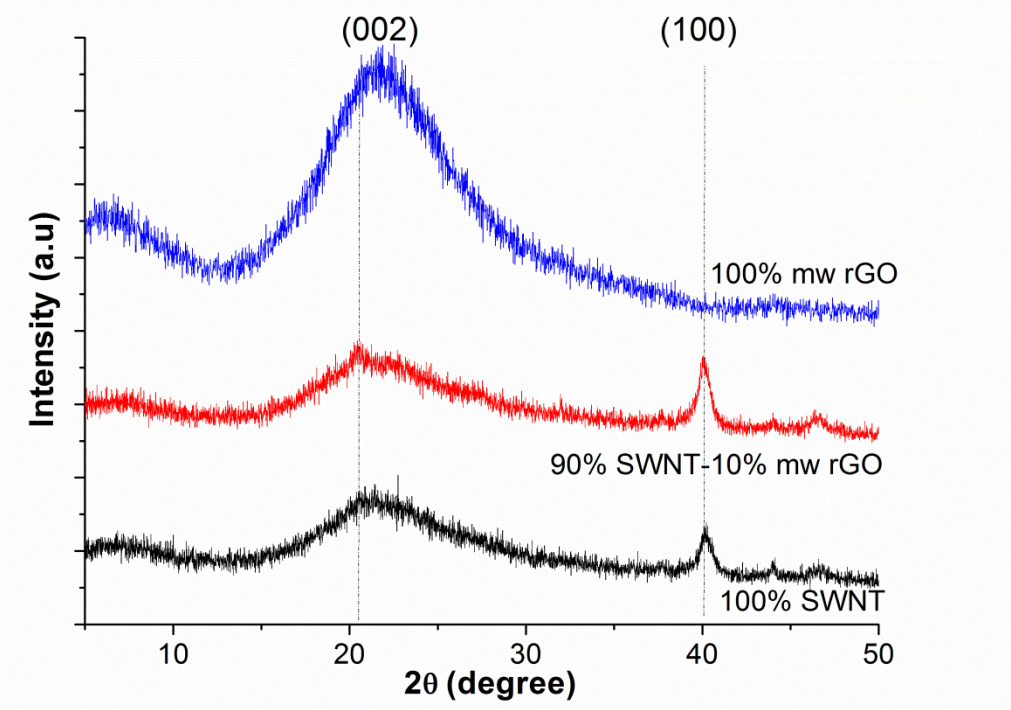

Figure 5. 5: XRD comparison of pure SWNT, 90% SWNT-10% mw rGO, and pure mw rGO.

5.3.1.5 Contact angle comparison prior to and after plasma treatment.

Contact angle comparison of mw rGO-SWNT electrodes prior to, and after plasma treatment clearly shows an enhancement in the wettability of the electrodes towards water as there is a significant decrease in the contact angle of the water droplet which can be seen in Figure 5. 6. Contact angle ranges from 46.3° to 79.1° (see Figure 5. 6a -Figure 5. 6h) indicating normal wetting behaviour [25]. After plasma treatment (see Figure 5. 6i), the contact angle is less than 1° for all

composites indicating an ideal wetting behaviour [25]. It can be seen that there is not a systematic change in the contact angle and this is due to the fact these composites are three-dimensional systems with no spatial symmetry / non-uniform roughness meaning that the contact angle can vary from point to point along the surface [25, 26]. A comparison of contact angle measurements before and after plasma treatment is outlined in Table 5. 2.

Table 5. 2: Contact angle before and after 20 minutes plasma treatment.

% Composition of SWNT-mw rGO (w/w)	**Contact angle before(degrees)**	**Contact angle after(degrees)**
100:0	46.3	<1
95:5	52.1	<1
90:10	54.5	<1
85:15	50.0	<1
80:20	47.0	<1
50:50	75.8	<1
40:60	79.1	<1
0:100	74.9	<1

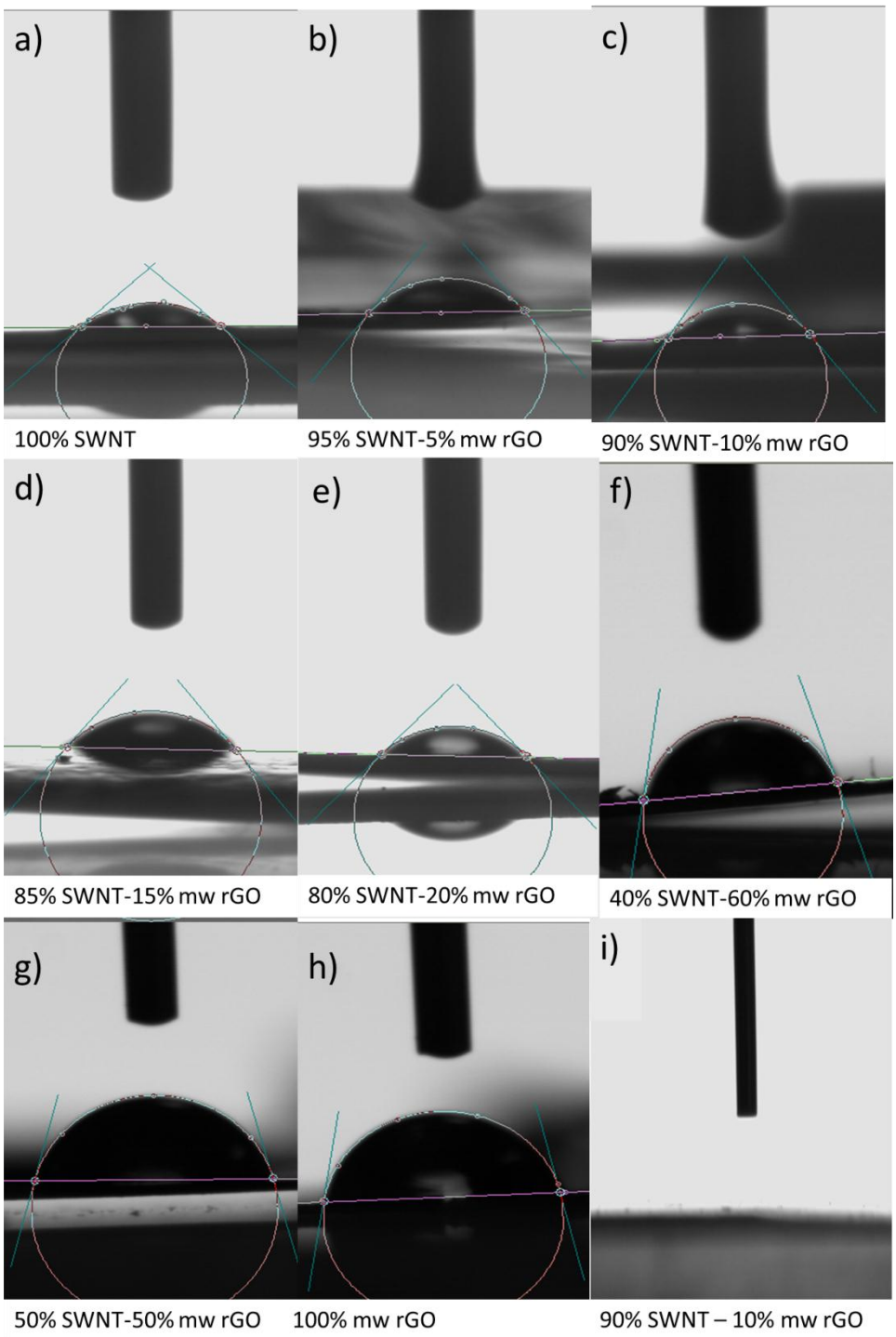

Figure 5. 6: Contact angle measurements. (a) 100% SWNT, (b) 95% SWNT- 5% mw rGO, (c) 90% SWNT- 10% mw rGO, (d) 85% SWNT- 15% mw rGO, (e) 80% SWNT- 20% mw rGO, (f) 50% SWNT- 50% mw rGO, (g) 40% SWNT- 60% mw rGO, (h) 100% mw rGO. (i) 90% SWNT – 10% mw rGO after plasma treatment.

5.3.2. Electrochemical characterisation of single walled carbon nanotubes – microwave reduced graphene oxide films.

5.3.2.1 Three electrode testes with varying weight compositions.

5.3.2.1.1. Three electrode measurements of single walled carbon nanotube- microwave reduced graphene electrodes as synthesised.

The CVs observed in Figure 5. 7a display a highly rectangular nature indicative of electric double layer capacitance [9]. The largest observed current response (w/w) at 500 mV/s was for the 100% SWNT, 95% SWNT: 5% mw rGO, 90% SWNT: 10% mw rGO, 85% SWNT: 15% mw rGO composite electrodes. In Figure 5. 7b, the 90% SWNT-10% mwrGO electrode had its scan rate varied from 20 mV/s to 500 mV/s. It can be seen that the square nature of the CV is maintained throughout these multiple scan rates as a result of a fast charging / discharging process and hence fast electrochemical response [27]. The capacitance is calculated at 20 mV/s and 500 mV/s and compared in Figure 5. 7c. The 95% SWNT: 5% mw rGO, 90% SWNT: 10% mw rGO, and 85% SWNT: 15% mw rGO obtained the highest specific capacitance exceeding 200 F/g (mass of active materials). Ratios either side of these decreased in specific capacitance. The capacitance for the composites at high scan rates of 500 mV/s was also still relatively high exceeding 50 F/g.

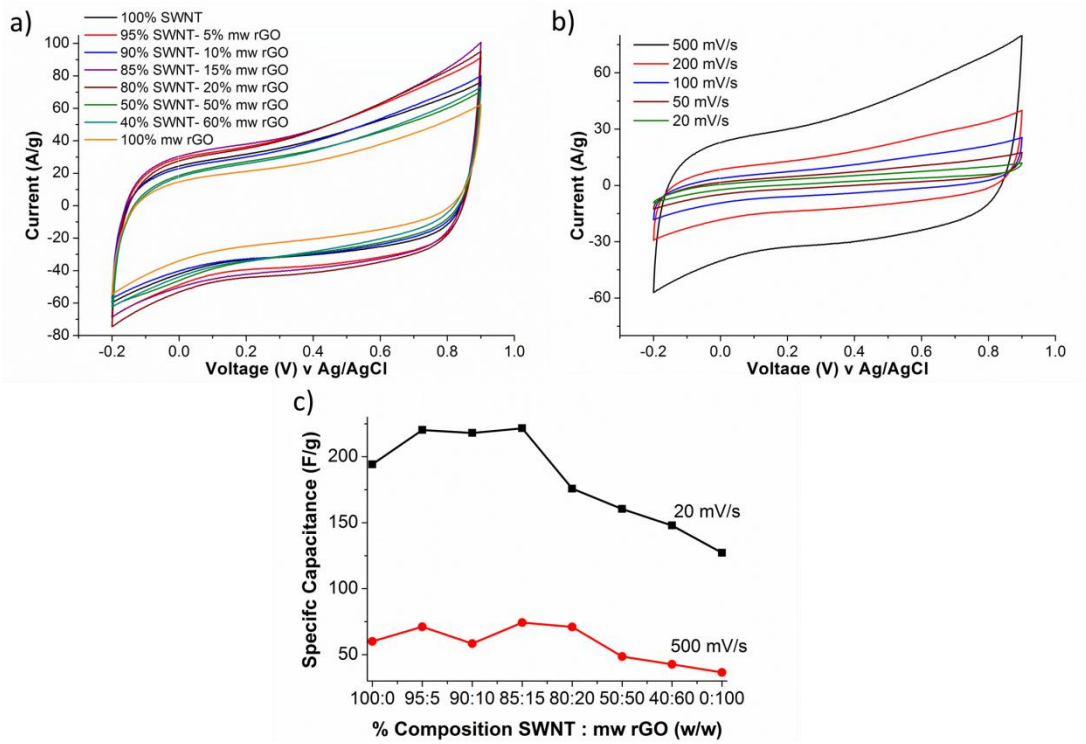

Figure 5. 7: (a) Cyclic voltammetry at 500 mV/s of SWNT : mw rGO composite electrodes with varying weight ratios on a Pt sputter coated (100 nm) PVDF membrane. (b) Cyclic voltammetry at 20 mV/s of 90%SWNT : 10%mw rGO composite electrode. (c) Specific capacitance comparison at 20 mV/s and 500 mV/s. System is three electrode with a Pt mesh counter (1.75 cm^2), Ag/AgCl reference electrode and 1 M $NaNO_3$ / H_2O electrolyte.

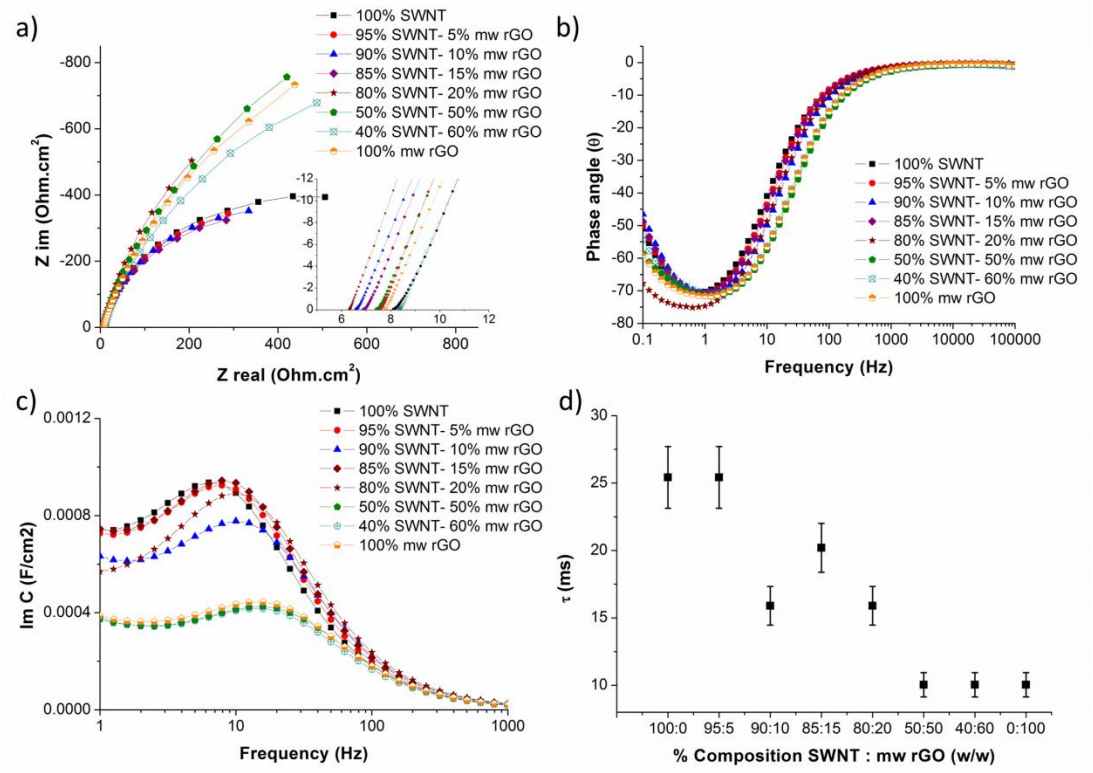

Figure 5. 8: SWNT : mw rGO composite electrodes with varying weight ratios on a Pt sputter coated (100 nm) PVDF membrane. (a) Nyquist plot comparison. (b) Phase angle comparison. (c) Imaginary part of impedance verses capacitance. (d) Time constant as a function of SWNT : mw rGO composition. System is three electrode with a Pt mesh counter (1.75 cm^2), Ag/AgCl reference electrode and 1 M $NaNO_3$ / H_2O electrolyte.

Figure 5. 8a depicts a Nyquist plot comparison of the SWNT: mw rGO composite electrodes and electrodes of pure SWNT and pure mw rGO. It can be seen that in the high to middle frequency regime (see inset of Figure 5. 8) the imaginary part of impedance rapidly rises with the usually observed semi-circle nearly indistinguishable from the graph indicating double layer capacitance and fast ion migration during charging / discharging of the electric double layer [9, 28]. In the inset of Figure 5. 8 the pure SWNT and pure mw rGO have the largest series

resistance (R_s) of 8.2 Ω 7.8 Ω respectively with this significantly reducing when composites are made. The addition of SWNT and mw rGO increases the wettability which is likely to be caused by an enhanced tailoring of the mesoporosity that allows easier access of water molecules. In the low frequency portion of the spectrum, the imaginary part of impedance starts to curve with the real part of impedance also increasing, and is extremely prevalent for the SWNT electrode and electrodes with 85% or greater weight loading of SWNTs. The reason for this is most likely as a result of Faradaic reactions that take place due to the presence of carboxyl and hydroxyl functional groups. To further investigate this low frequency portion of the spectrum, the phase angle verses frequency can be compared (Figure 5. 8b) and it shows a deviation in the phase angle at low frequencies (≈ <0.5 Hz) which suggest ion diffusion processes connected with Faradaic reactions [29].

The imaginary part of capacitance plotted against frequency Figure 5. 8c can be used to evaluate the frequency response of all composites by comparing the position of the peak frequency *(f_p)*. It can be seen that the composite SWNT : mw rGO electrodes and pure mw rGO have peak frequencies slightly shifted to the right (towards higher frequencies) indicating an enhanced rate capability as compared to pure SWNTs [30]. The time constant (τ*(s)*) of the system can be evaluated by multiplying the peak frequency by 2π and inverting. τ*(s)* can describe the speed at which the double layer charges and discharges as shown in Figure 5. 8d. The SWNT : mw rGO composites with ratios (w/w) of 90%: SWNT: 10% mw rGO, 85% SWNT:15% mw rGO, and 80% SWNT:20% mw rGO had τ*(s)* of approximately 17 ms [31]. The 50%: SWNT: 50% mw rGO, 40% SWNT:50% mw rGO, 100% mw rGO has

the smallest τ*(s)* approaching 10 ms due to lower capacitance. This is to be expected due to the flatter nature and re-stacking effects of the GO surface, and that the SWNTs are less well dispersed. It can be seen that by adding mw rGO to SWNT we can create a system that has the balance of micro and mesoporosity which allows the best utilisation of electroactive surface area and fast charging / discharging effects.

5.3.2.1.2. Microwave reduced graphene oxide – single walled carbon nanotube composite electrodes with 20 minutes plasma treatment prior to electrochemical testing.

Plasma treatment of the elctrode materials prior to electrchemical testing has taken place in order to improve the wettability of the electrode surface (without changing the properties of the bulk) through the addition of functional groups [32]. This is achieved through oxygen radicals interacting chemically with the surface atoms leading to the formation of oxygen-rich functional groups [32].

The CVs on the plasma treated electrodes observed in Figure 5. 9a once more display a rectangular nature indicative of electric double layer capacitance at a scan rate 500 mV/s once more [9]. In Figure 5. 9b, multiple scan rate ranges retain their rectangular nature due to fast charging / discharging over the potential range of 1.1 V [11]. The largest observed current was clearly for the 90% SWNT- 10% mw rGO composite electrodes with the specfic capacitance calculated at 20 mV/s and 500 mV/s compared in Figure 5. 7c. The 100% SWNT, 95%:5%, 90%:10%, 85%:15%, and

80% SWNT: 20% mw rGO ratios of SWNT: mw rGO (w/w) obtained the highest specific capacitance ranging between 250 F/g and 306 F/g (mass of active materials). The mw rGO is helping to access the capacitance of the SWNTs. Ratios with a greater weight percent of mw rGO decreased in specific capacitance. The capacitance for the composites at high scan rates of 500 mV/s (Figure 5. 9c) was again relatively high for ratios 100% SWNT, 95% SWNT: 5% mw rGO, and 90% SWNT: 10% mw rGO ranging between 80 F/g and 120 F/g respectively. Ratios 85% SWNT: 15% mw rGO, 80% SWNT: 20% mw rGO, 50% SWNT: 50% mw rGO, 40% SWNT: 60% mw rGO, and 100% mw rGO were all significantly lower in specfic capacitance at 500 mV/s at approxiamtely 40 F/g.

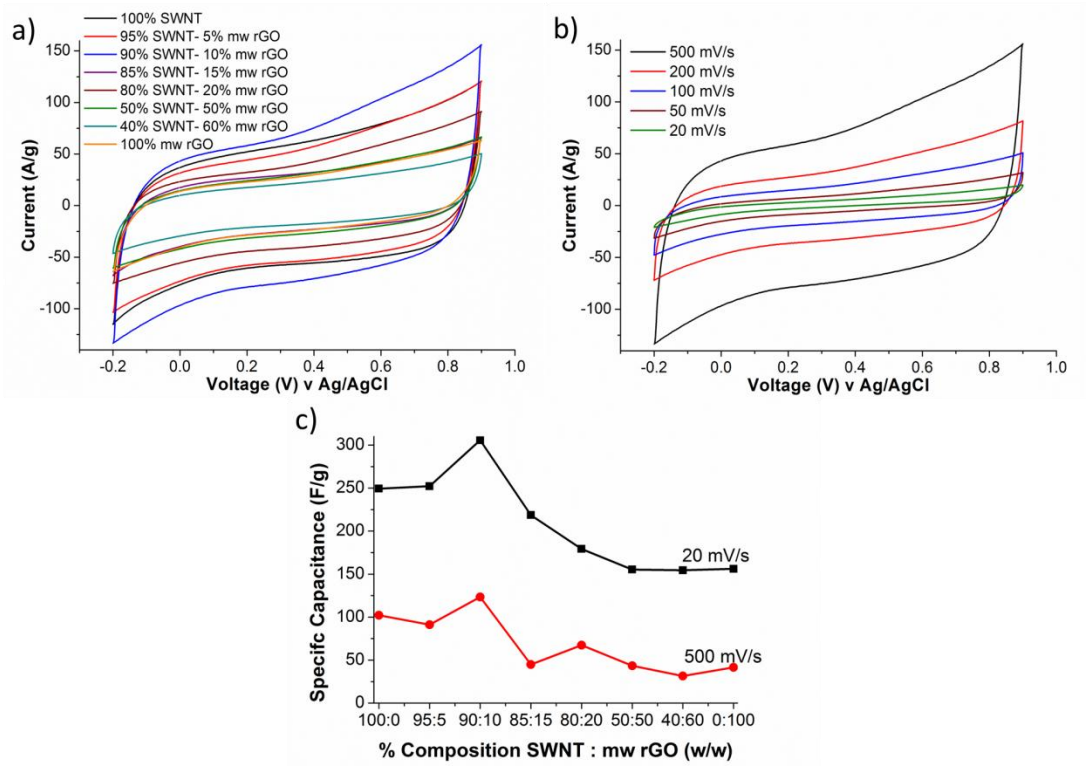

Figure 5. 9: (a) Cyclic voltammetry at 500 mV/s of SWNT : mw rGO composite electrodes with varying weight ratios on a Pt sputter coated (100 nm) PVDF membrane. (b) Cyclic voltammetry at 20 mV/s of 90%SWNT : 10%mw rGO composite electrode. (c) Specific capacitance comparison at 20 mV/s and 500 mV/s. All electrodes have been plasma treated for 20 minutes prior to electrochemical testing. System is three electrode with a Pt mesh counter (1.75 cm^2), Ag/AgCl reference electrode and 1 M $NaNO_3$ / H_2O electrolyte.

Figure 5. 10 depicts a Nyquist plot comparison of the SWNT: mw rGO composite electrodes and electrodes of pure SWNT and pure mw rGO. It can be seen that in the high to middle frequency regime (see inset of Figure 5. 10) the imaginary part of the impedance rapidly rises (near vertical behaviour) with the usually observed semi-circle nearly indistinguishable from the graph indicating double layer capacitance and fast ion migration during charging / discharging of the electric double layer [9, 28]. In the inset of Figure 5. 10 the pure mw rGO electrode has the

largest series resistance (R_s) of 12.1 $\Omega.cm^2$, with this significantly reduced when composites are made. As previously stated, the addition of SWNT and mw rGO increases the wettability which is likely to be caused by an enhanced tailoring of the mesoporosity that allows easier access of water molecules. In the low frequency portion of the spectrum, the imaginary part of impedance starts to curve with the real part of impedance also increasing, and is extremely prevalent for the SWNT electrode and electrodes with 85% or greater weight loading of SWNTs. The reason for this occurrence is due to Faradaic reactions that probably take place due to the presence of carboxyl and hydroxyl functional groups. This non-ideal behaviour is highlighted in the low frequency portion of the phase angle verses frequency plot (Figure 5. 10b) which shows a deviation in the phase angle at low frequencies (≈ <0.5 Hz) which suggests ion diffusion connected with Faradaic reactions [29].

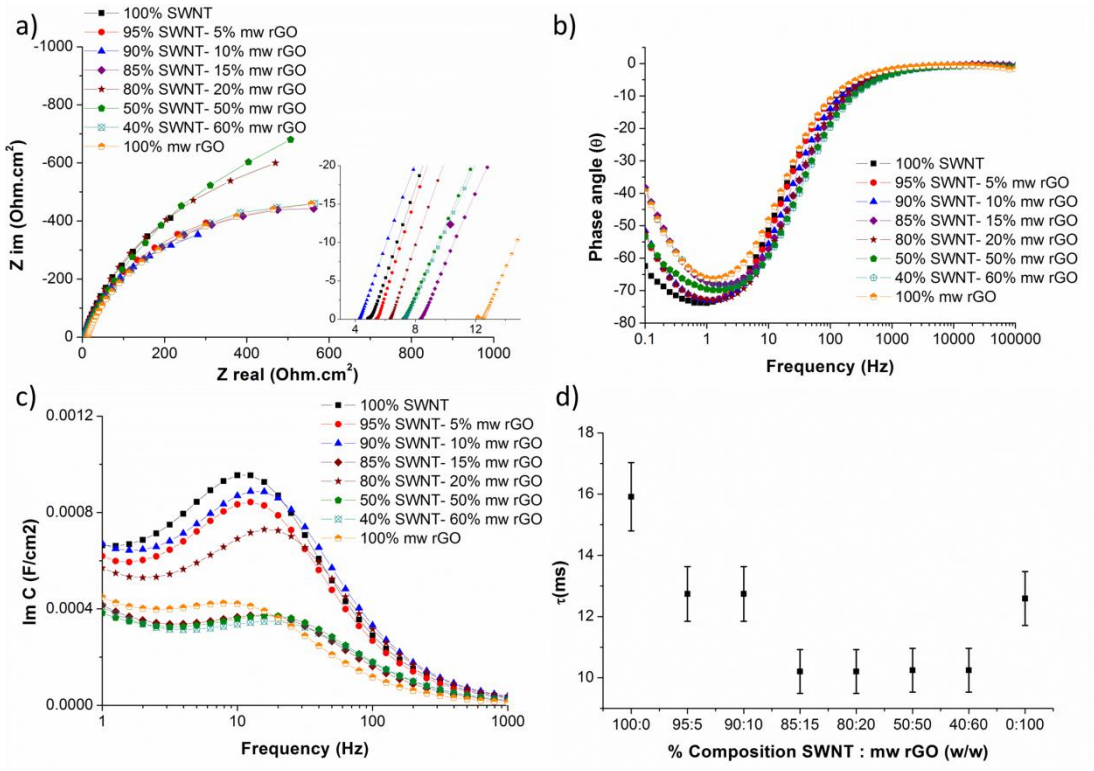

Figure 5. 10: (a) Nyquist plot comparison. (b) Phase angle comparison. (c) Imaginary part of impedance verses capacitance. (b) Time constant as a function of SWNT : mw rGO composition. System is three electrode with a Pt mesh counter (1.75 cm^2), Ag/AgCl reference electrode and 1 M $NaNO_3$ / H_2O electrolyte. All electrodes have been plasma treated for 20 minutes prior to electrochemical testing. SWNT : mw rGO composite electrodes with varying weight ratios on a Pt sputter coated (100 nm) PVDF membrane.

In Figure 5. 10c the imaginary part of capacitance shows that the composite SWNT : mw rGO electrodes and pure mw rGO have peak frequencies slightly shifted to the right (towards higher frequencies) indicating an enhanced rate capability as compared to pure SWNTs [30]. The time constant (τ*(s)*) for the SWNT : mw rGO composites with ratios (w/w) of 85%: SWNT: 15% mw rGO, 80% SWNT: 20% mw rGO, 50% SWNT: 50% mw rGO, and 40% SWNT: 60% mw rGO had the smallest τ*(s)*

of approximately 10 ms [31]. The mw rGO has a slightly increased τ*(s)* (as compared to the composites) at 13 ms which may be due to surface effects of the plasma treatment on the pure mw rGO. It can be seen that by adding mw rGO to SWNT and plasma treating we can create a system that now has an increased utilisable surface electroactive surface area. Coupled to this is a micro and meso porosity benefit that enables fast charging / discharging effects.

5.3.2.2 Comparison of as fabricated and plasma treated composite electrodes.

It can be seen in Figure 5. 11 that there is a difference in specific capacitance at both 20 mV/s and 500 mV/s prior to and after 20 minutes plasma treatment. The largest observed capacitance was for the 90% SWNT – 10% mw rGO (w/w) electrode at 306 F/g and 124 F/g respectively. From Figure 5. 11c, the time constant for the different weight ratios is plotted prior to and after plasma treatment. It can be seen that at high weight ratios of SWNT (exceeding 80% SWNT) the time constant is significantly reduced with the plasma treatment of the films. The plasma treatment adds some carboxyl functional groups which enhances wettability (see Table 5. 2) and increases the available electrode surface area [32].

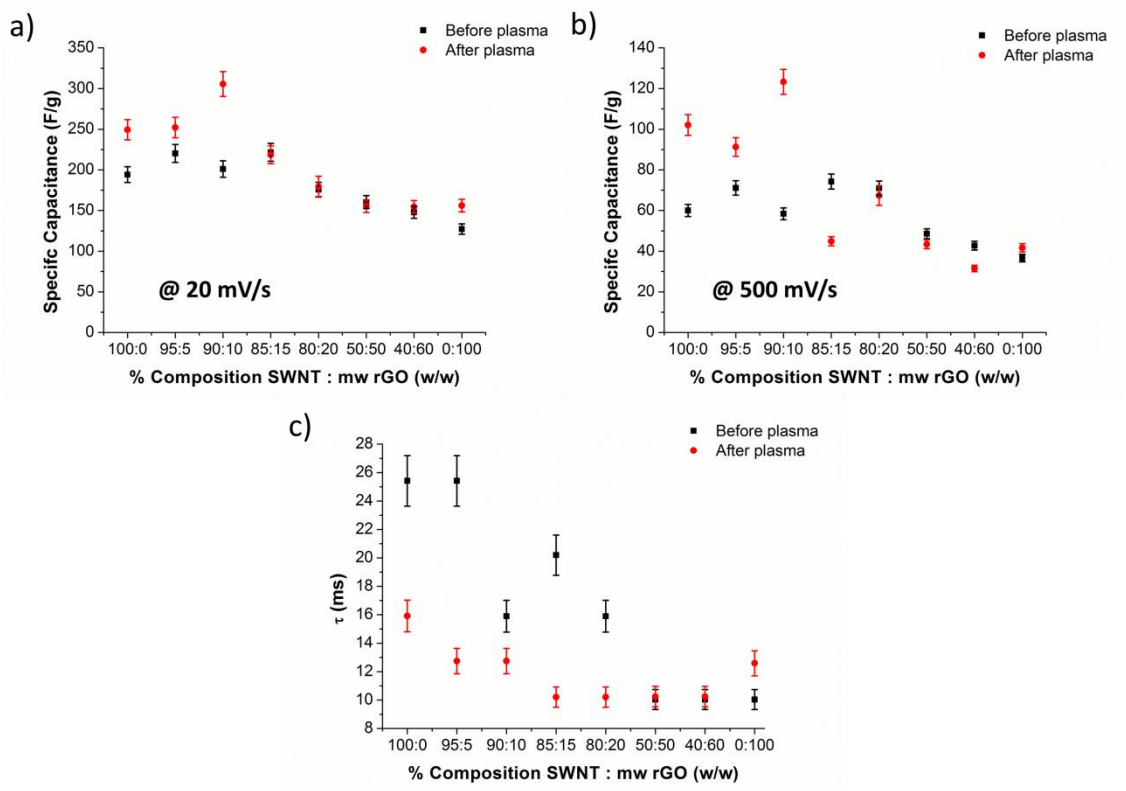

Figure 5. 11: A comparison of electrodes before and after plasma treatment for 20 minutes prior to electrochemical testing. System is three electrode with a Pt mesh counter (1.75 cm^2), Ag/AgCl reference electrode and 1 M $NaNO_3$ / H_2O electrolyte. (a) Specific capacitance of the electrode calculated at 20 mV/s. (b) Specific capacitance of the electrode calculated at 500 mV/s. (c) Time constant calculated by finding the peak frequency from the imaginary capacitance versus frequency plot.

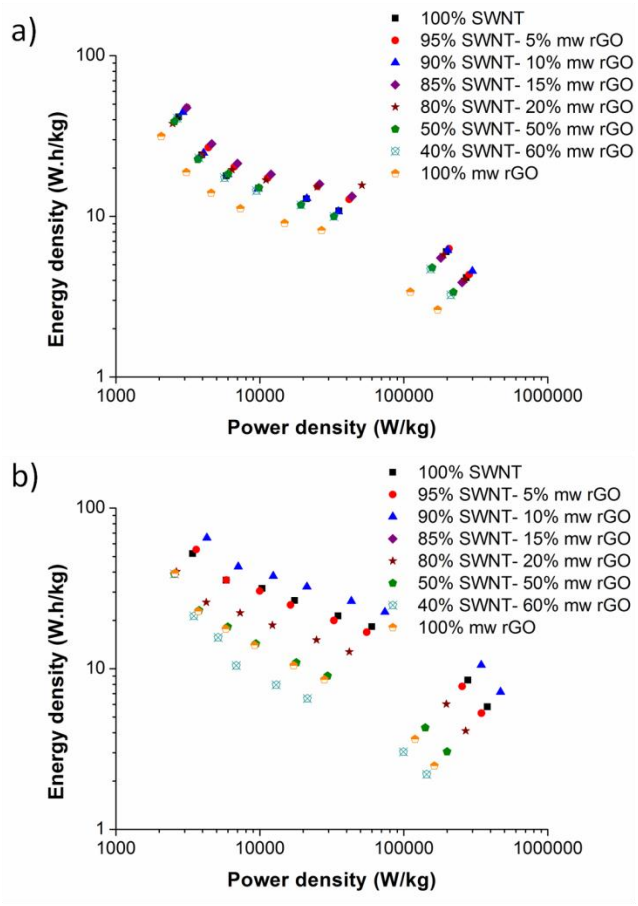

Figure 5. 12: Ragone plot comparison (calculated from CV) showing power density versus energy density for SWNT : mw rGO composite electrodes with varying weight ratios. (a) Before, and (b) Plasma treated for 20 minutes prior to fabrication.

In Figure 5. 12a the energy density verses power density is plotted (Ragone plot) and it can be seen the by creating composites of SWNT and mw rGO the energy and power density can be enhanced. The best performing composites prior to plasma treatment were the 95% SWNT : 5% mw rGO, and 90% SWNT : 10% mw rGO with the energy density and power density reaching 45 W.h/kg and slightly below 300 kW/kg respectively.

After 20 minutes plasma treatment of the electrode surface (see Figure 5. 9b) the energy and power density is increased as compared to the untreated samples. The best performing composite was the 90% SWNT : 10% mw rGO with the energy density and power density exceeding 65 W.h/kg and 470 kW/kg respectively.

5.3.2.3 Varying plasma treatment times of 90% SWNT – 10% mw rGO films.

To optimise the 90% SWNT -10% mw rGO, the plasma treatment time was varied in order increase the amount of functional groups resulting so that the capacitance and utilisable electrode surface area could be maximised. From Figure 5. 13a and Figure 5. 13b it can be seen that 20 minutes plasma treatment times attains the highest result the CV at 500 mV/s obtain the largest capacitive current. When the plasma treatment is less than 20 minutes, it is thought that the degree of functionalisation is not enough which hampers the electrolyte wetting. When the plasma treatment time is greater than 20 minutes, the current is reduced once more meaning the capacitance is less. The excessive plasma treatment starts to degrade the electrode, which was visible after 40 minutes for the composite films started to peel off from the platinised PVDF membrane.

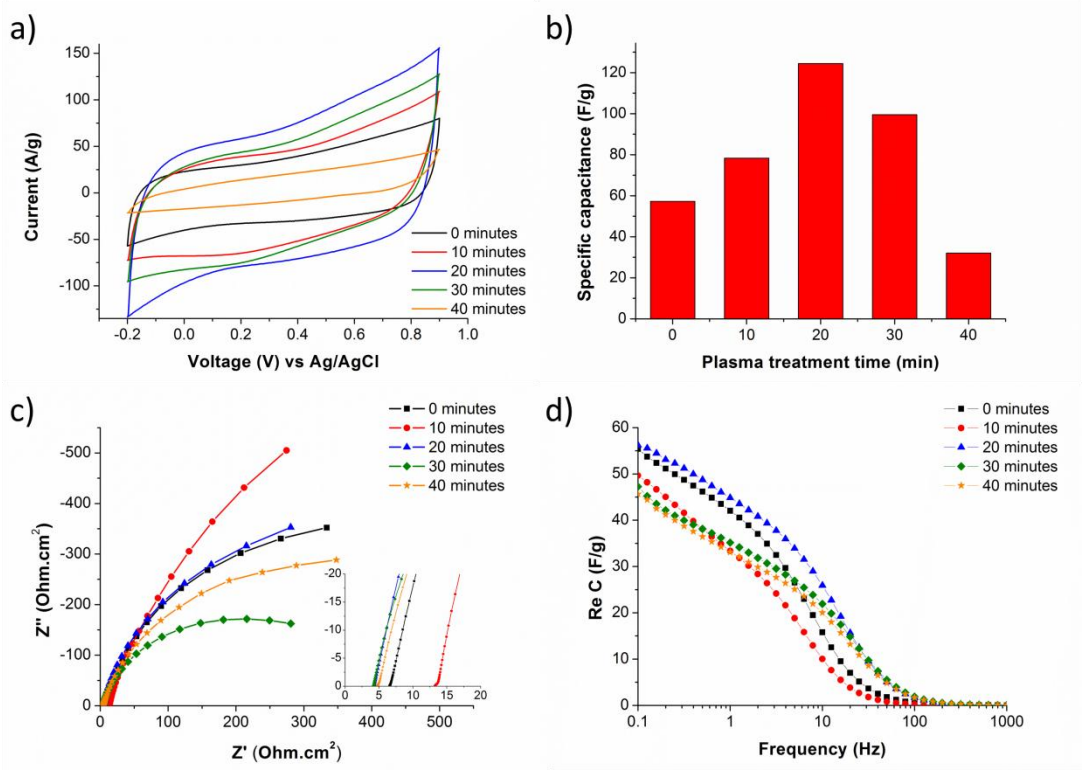

Figure 5. 13: Various plasma treatment times for 90% SWNT – 10% mw rGO a composite electrode. (a) CV at 500 mV/s. (b) Specific capacitance values calculated at 500 mV/s. (c) Nyquist plot. (d) Real part of capacitance versus frequency.

Electrochemical impedance spectroscopy also supports the optimum plasma treatment time being 20 minutes. Firstly the Nyquist plot of Figure 5. 13c shows that for the 0, 10, and 20 minute plasma treated samples, the imaginary part of the impedance is more vertical than the 30 and 40 minute samples indicating more ideal capacitive behaviour [33]. In Figure 5. 13d, the real part of capacitance is largest for the 20 minute plasma treated sample.

5.3.2.4 90% SWNT- 10% mw rGO electrodes with varied thickness.

At 20 mV/s the CVs of Figure 5. 14a display a rectangular shape indicative of capacitive behaviour [34]. As the thickness of the film increases from 1 micron to 21.5 micron, the capacitive current per unit area increases as there is more material that interacts with the electrolyte. The limiting amount is for the 17 micron and 21.5 micron electrode as the CVs overlap, indicating maximum usage of surface area. In Figure 5. 14b, the 17 micron film has its scan rate increased from 5 mV/s to 500 mV/s. It can be seen that at high scan rates of 500 mV/s a large capacitive current is still apparent indicating the electrode can respond quickly. The distortion of the CVs (elliptical appearance) is a result of a hindered kinetic process as the diffusion pathways in / out of the electrode material are slower resulting in a lag between charging and discharging [35, 36].

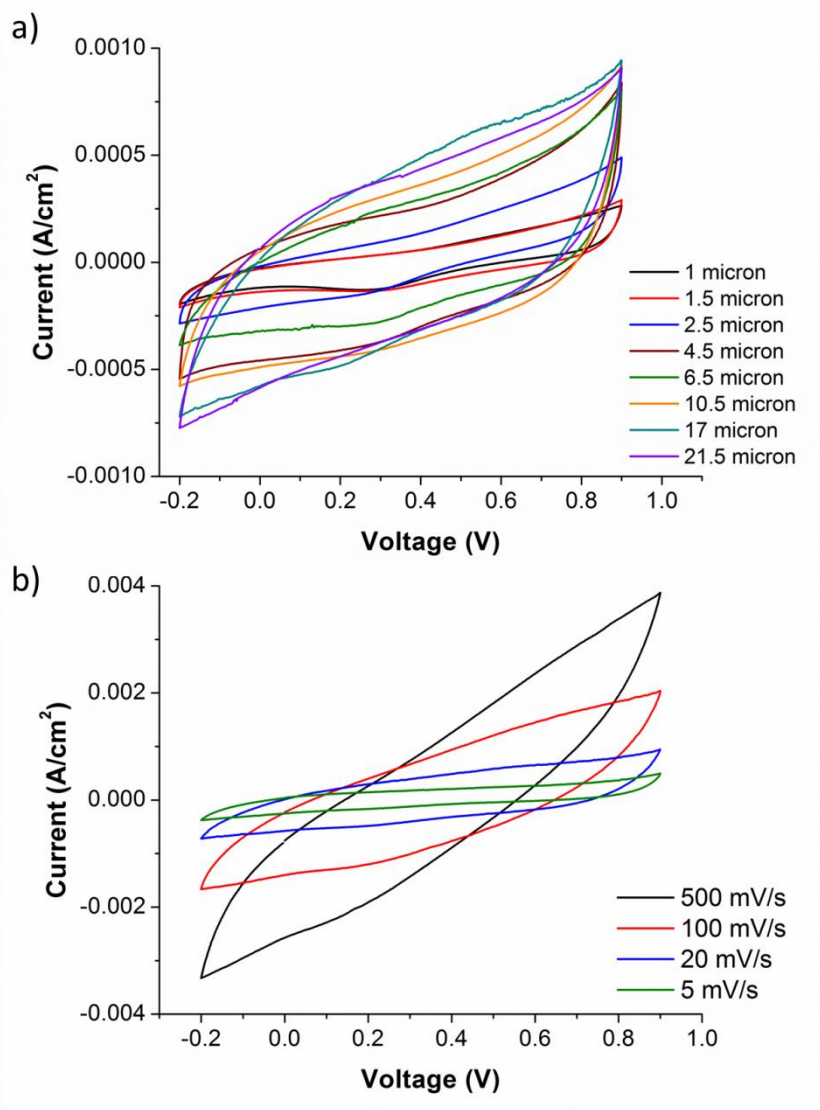

Figure 5. 14: 90% SWNT-10% mw rGO electrodes with varied thicknesses. (a) Varied thicknesses 20mV/s. (b) 17 micron thickness with varied scan rate. System is three electrode with a Pt mesh counter (2cm^2) and 1 M aqueous $NaNO_3$.

The effects of an increase in thickness can be seen by the Nyquist and imaginary capacitance plots of Figure 5. 15. In the Nyquist plot of Figure 5. 15a, the width of the high frequency semi-circle that corresponds to the polarisation resistance (R_p) increases with thickness. This is because as the thickness of the film is increased, there is an increase in diffusion length, as well as a change in the porosity of the

electrode that also effects electrolyte diffusion, making it more sluggish [37]. For the 10.5, 17, and 21.5 micron thicknesses R_s also shifts slightly to the right indicating an increase in the series resistance. The change in R_p with thickness is clearly observed in Figure 5. 15b (with inset) where R_p increases from 3.4 Ohm.cm^2 to 117.5 Ohm.cm^2 as electrode thickness increases from 1 micron to 21.5 micron. Coupled to this in the middle frequency portion of the spectrum, there is a slight extenuation of the Warburg diffusion region which also indicates sluggish electrolyte diffusion [38, 39]. At low frequencies, the imaginary part of the impedance increases indicating capacitive behaviour [40]. It can also be seen that in this low frequency part, there is a deviation from the parallel vertical line due to: (i) Distributed distribution of pore sizes that induces a non-ideal capacitance response; and (ii) Carboxyl redox reactions due to the plasma treatment which contributes some pseudo capacitance [38, 41]. In Figure 5. 15c. there is a shift to the left of the imaginary capacitance peak versus frequency (and hence a decrease in time constant) resulting in lower charging / discharging time of the electrical double layer [42]. The increase in time constant with increasing thickness can be seen in Figure 5. 15d. Here, there is a general increase in τ(s) as the thickness varies from 1 micron to 4.5 micron. Once the thickness exceeds 4.5 microns, there is a sharp increase in τ(s) until a plateau is reached at 10.5 microns. The plateau is due to the fact that the thickness, coupled with the porosity structure is such that ion diffusion pathway is fully exhausted and the rate of charge / discharge cannot get any slower [39, 43].

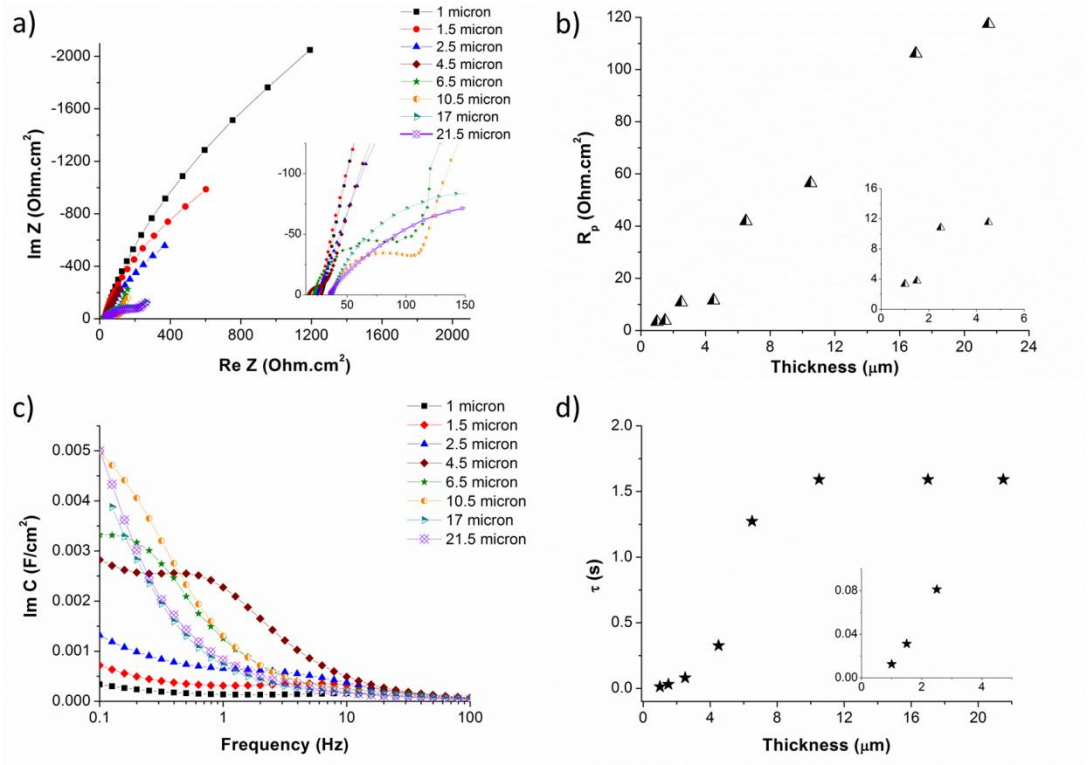

Figure 5. 15: 90% SWNT-10% mw rGO electrodes with varied thicknesses. (a) Nyquist plot. (b) R_p as a function of thickness. (c) Imaginary capacitance versus frequency. (d) τ(s) as a function of thickness.

5.3.3. Supercapacitor device testing of SWNT-mw rGOcomposite.

5.3.3.1 90% SWNT- 10% mw rGO optimisation.

The 90% SWNT – 10% mw rGO was selected as the best ratio to fabricate a device as the three electrode tests of varying weight ratios has shown the 90% SWNT – 10% mw rGO composite electrode with a plasma treatment time of 20 minutes attained the highest specific capacitance of 306 F/g and 123 F/g as scan rates of 20 mV/s and 500 mV/s respectively. In this section the device study is in two parts; (i) Optimising the 90% SWNT – 10% mw rGO supercapacitor with a film thickness of 17

micron by looking at the heat treatment of the electrode to remove / evaporate excess CHP and the use of 1 M $NaNO_3$ and 1 M H_2SO_4. (ii) Once annealing and electrolyte optimised, a device study with varying applied currents and long term testing.

In Figure 5. 16, device testing has taken place using the Swagelok test cell (see section 5.2.4) under different annealing and electrolyte conditions in order to optimise the device performance. In Figure 5. 16a, the comparison of the CV curves clearly shows that the largest current (green line) is obtained for device electrodes that have been annealed at 310^{o}C for 6 hours and cycled in 1 M H_2SO_4. A large redox peak is observable between 0.3 V and 0.55 V due to redox behaviour associated with the interaction of functional groups of the composite material and the sulphuric acid [44, 45]. When considering the Nyquist plot of Figure 5. 16b, it can be seen that the size of the semi-circle (charge transfer resistance R_p) decreases when the electrodes are annealed prior to device testing. There is further reduction in R_p when sulphuric acid is used as the electrolyte. The series resistance R_s (intercept of the Nyquist plot with the x-axis) also shifts to the left to 0.12 Ohm.cm^2 indicating better contact resistance and lower internal resistance of the electrode [46, 47].

The manifestation of two semi-circles is also apparent when using sulphuric acid due to enhanced pseudocapacitive effects that can be represented by two characteristic processes [44]. The first process is typical double layer capacitance

due to ion-rearrangement in response to the alternating voltage signal. The second is thought to occur as a result of charge imbalance at the electrode / electrolyte interface as a result of the redox behaviour. Here, electrolyte ions are being attracted / repelled at the interface to balance the charge. In Figure 5. 16c, each device was compared using galvanostatic charge / discharge testing (GCD) in order to evaluate long term cycling. It can clearly be seen that for all devices as the current is varied from 0.05 A/g to 1.0 A/g there is a decrease in specific capacitance. The 310^0C annealed electrode cycled in 1 M H_2SO_4 has the largest specific capacitance of 80 mF/cm^2 at 0.05 A/g with a stable response of 61 mF/cm^2 at 1.0 A/g. When the current was switched back to 0.05 A/g (cycle 1100-1200) the capacity retention was 98%. All other treated electrodes performed significantly less with a rapid decrease in the performance of the as-fabricated electrode in 1 M $NaNO_3$. The effects of annealing are that it is able to minimise the amount of residual CHP in the electrode, which will increase the active surface area and improve the conductivity within the materials structure. Coupled to this, sulphuric acid enhances the redox behaviour as it is thought that H^+ or OH^- must be involved in the electrochemical reactions according to the strong dependence of pseudocapacitance on the H^+ concentration [45].

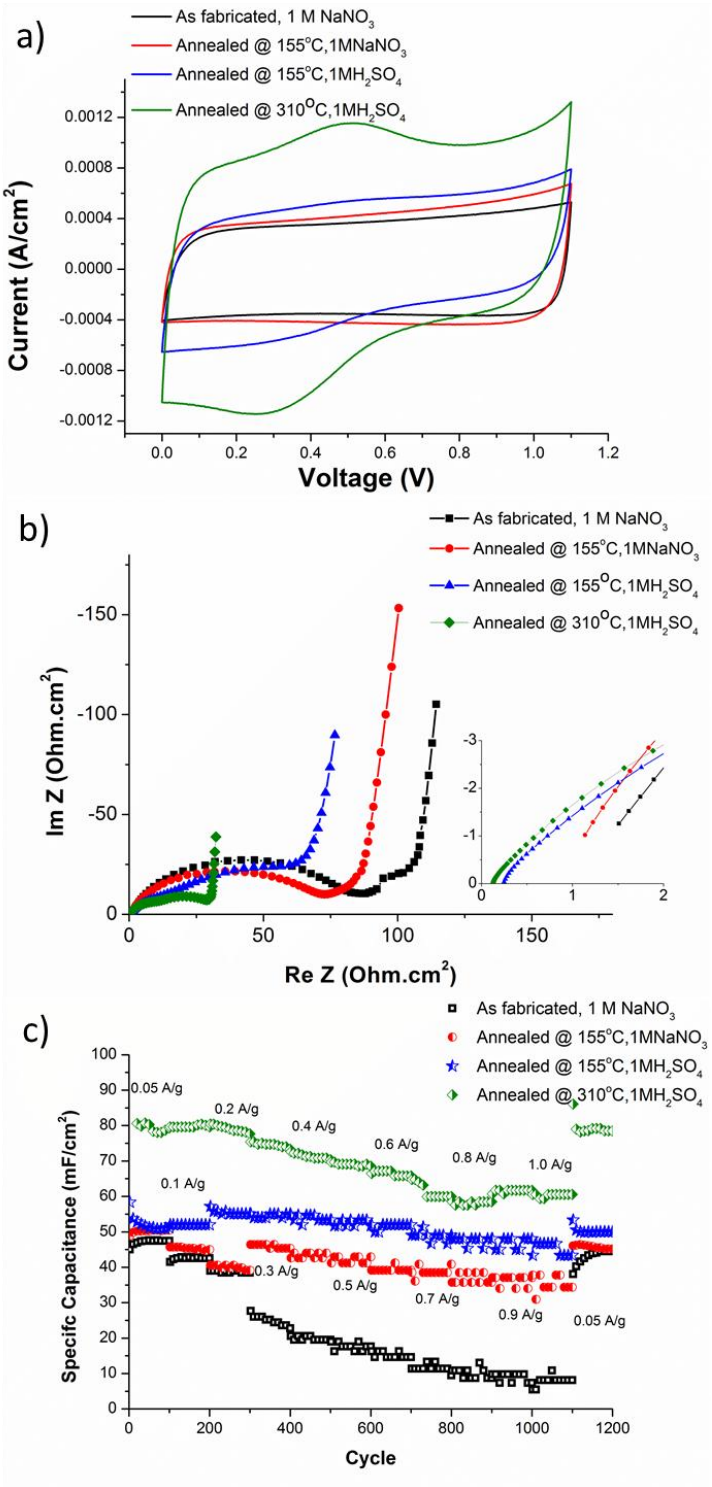

Figure 5. 16: 90% SWNT-10% mw rGO supercapacitor with each electrode at a thickness of 17 micron. Devices have been optimised by annealing utilising different electrolytes.(a) CV, (b) Nyquist plot comparison, (c) GCD comparison up to 1.0 A/g.

In Figure 5. 17a, GCD curves show a symmetrical behaviour, but with a slight curvature at low current rates of 0.1 A/g and 0.2 A/g indicating redox behavior [41]. In Figure 5. 17b, the device has been pushed from 0.05 A/g (cycle 1-100) to 1.0 A/g (cycle 1001-1100) then back to 0.05 A/g (1101-1200). Succeeding this, the current density was increased to 4.0 A/g (cycle 1701-1800) and finally back to 0.05 A/g (cycle 1801-1900) to show the reversibility of the device. After pushing the device to 1.0 A/g, 98% capacity retention was restored when the current was switched back to 0.05 A/g. When the device was pushed to 4.0 A/g then back to 0.05 A/g, the capacity retention was still 83%. The fact that the capacity is recoverable from varying applied currents is a good sign of stability. In the ragone plot of Figure 5. 17c, it can be seen that the 90% SWNT – 10% mw rGO displays a high energy of 6 Wh/kg and a maximum power density 1.9 MW/kg respectively. Equations for energy and power density are outlined in Chapter 2, Section 2.2 where the ESR was determined from the intercept of the Nyquist plot and is only 0.13 Ohm.cm^2. In comparison, commercially available supercapacitors range from 10 µF-470 mF (Murata© polymer and electric double layer capacitors) [48, 49] to 3000 F (Maxwell Technologies© ultracapacitor) [50]. These where the energy and power density range can range from 0.1-10 Wh/kg to 1-100 kW/kg [47, 51].

Long term stability testing (Figure 5. 17d) over 10 000 cycles (≈ 13 days) at 1.0 A/g shows and extremely stable and reversible response of the electrode during the charge / discharge process, with the capacity retention of 95% at cycle 10 000. The

initial increase in capacitance is due to an initial activation where full wetting and volume expansion / contraction equilibrates the system [52].

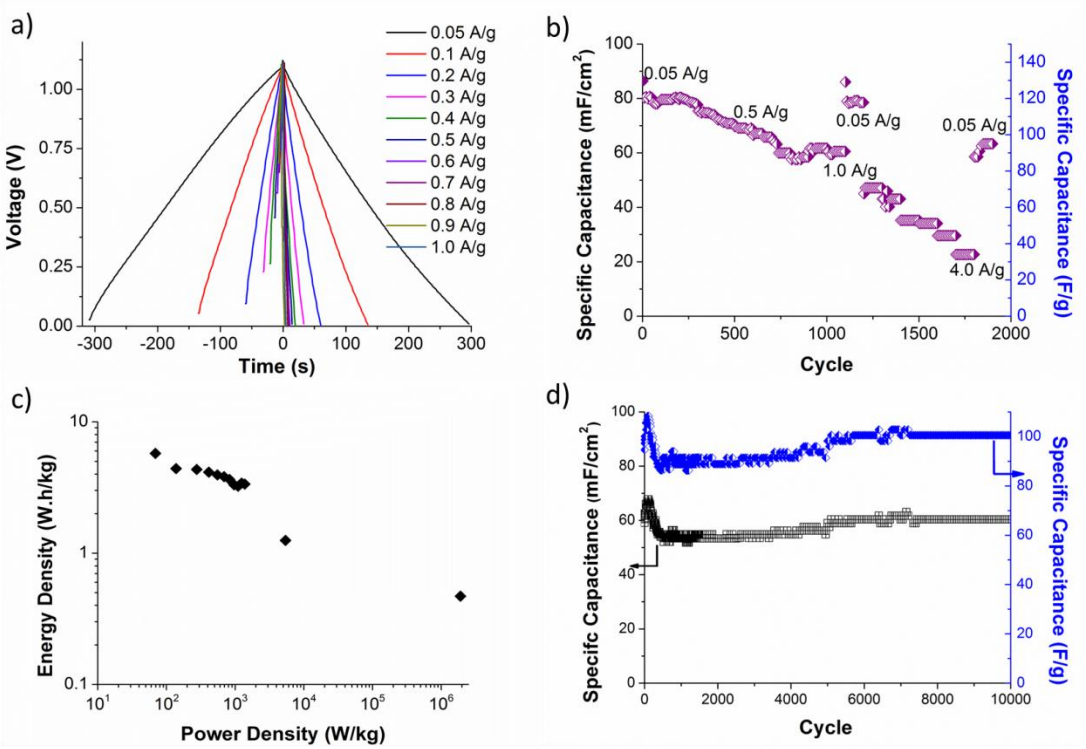

Figure 5. 17: 90% SWNT-10% mw rGO supercapacitor. (a) GCD curves. (b) $C_{(sp)}$ versus cycle no. for different current loadings. (c) Ragone plot of power density versus energy density. (d) Long term cyclability at 1.0 A/g using GCD.

This excellent stability can be seen in the Nyquist plot of Figure 5. 18a where EIS has been used to track changes of the electrode during cycling. The Nyquist spectra at cycle 0, 5000, and 10000 show little change in the impedance response indicating a stable and durable electrode material [53]. It can be seen that R_s does not change and remains constant at 0.13 Ohm.cm^2 after 10 000 cycles. After the initial cycle, there are some volume changes and activation of the electrode material due to penetration of the electrolyte ions into the composite structure. Cycles 5000 and 10

000 show a rapid increase in the imaginary part of the impedance at low frequencies which is indicative of capacitive behaviour [38].

From the SEM image of Figure 5. 18b and Figure 5. 18c, it can be seen that there is no observable difference in the physical structure of the 90% SWNT – 10% mw rGO electrode before and after 10 000 cycles of GCD. In both cases mw rGO is covered and separated by SWNTs. However, it is apparent that after GCD in Figure 5. 18c, the electrode is denser due to the cell configuration that presses both electrodes and separator between the stainless steel plates. Overall the electrode is stable and robust thus maintaining its integrity as it undergoes the charge / discharge process which is extremely important in real world applications where consistency and reliability must be guaranteed.

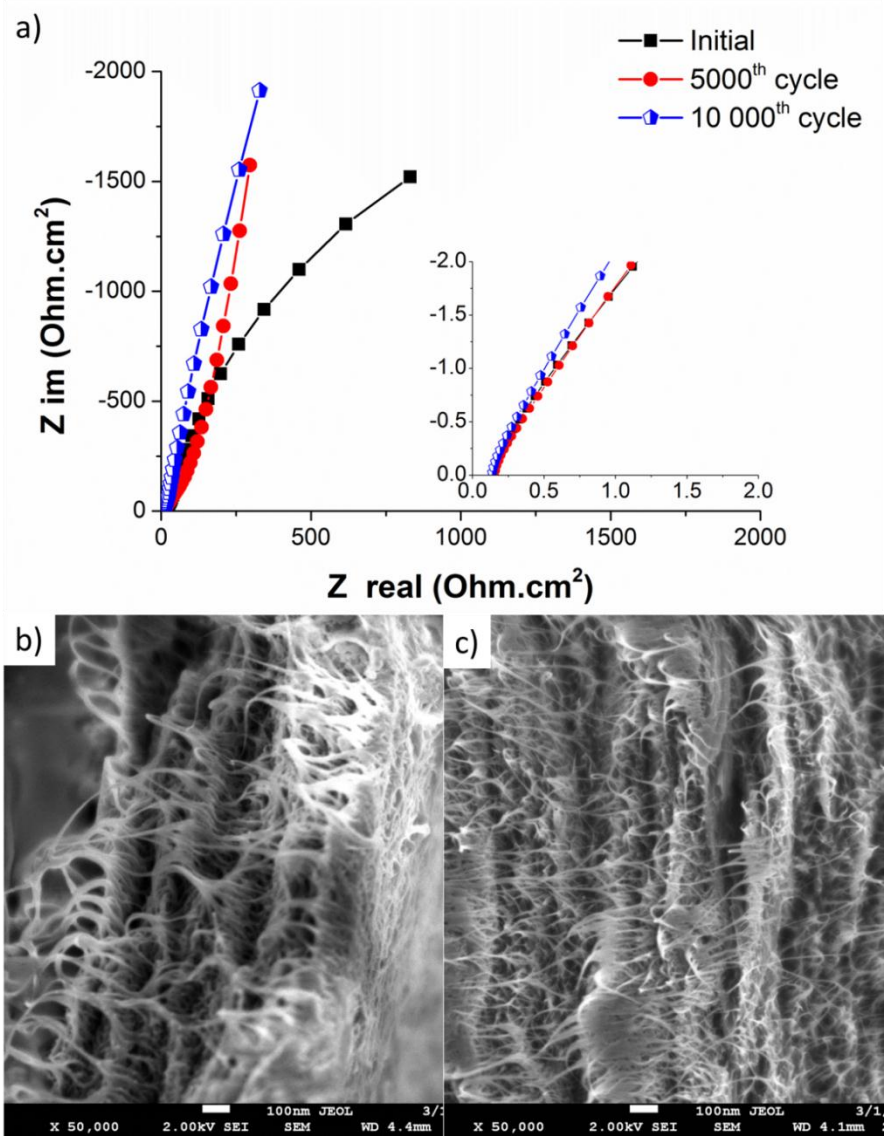

Figure 5. 18: (a) Nyquist plot prior to and after 5000 and 10 000 cycles. (b) and (c) SEM images of electrodes before and after 10 000 cycles of GCD.

5.4. Conclusion.

In summary, a composite material comprising of SWNTs and mw rGO has been successfully synthesised and fabricated into a composite electrode material. The composite was successfully optimised as an electrode material for the use in a supercapacitor. SEM showed a structure whereby SWNTs were better dispersed as

they were able to coat mw rGO sheets thus preventing restacking and maximising utilisable electroactive surface area. Raman spectroscopy showed that the ratio of the D/G band slightly increased after plasma treatment due to the addition of functional groups. While the D band peak of the composite also broadened as the weight ratio of mw rGO increased due to the large D/G ratio of pure mw rGO.

The optimum ratio for the electrode which maximises capacitance (≈300 F/g) was calculated to be 90% SWNT – 10% mw rGO. 20 minutes plasma treatment time maximised the wettability of the electrode surface with contact angle measurements showing that there was a significant decrease in the contact angle ($\approx 55^0$ to $<1^0$) after plasma treatment. It was found that a thickness of 17 micron was optimum in order to insure that the capacitance per unit weight was maximised. Electrode annealing involved heating the electrode at 155^oC for 8 hours in a vacuum oven followed by a further 8 hours at 310^0C on a hot plate (fume hood) in order to insure the removal of any residual CHP. Device fabrication was completed using a Swagelok© test cell with 1 M H_2SO_4 as the electrolyte of choice. Varying charge / discharge rates showed a device that could handle up to 4.0 A/g with the excellent switching capability between 0.05 A/g and 4.0 A/g. Long term testing of the device showed excellent stability over 10 000 cycles with 95% capacity retention. EIS over the course of long term testing showed little change indicating a stable and robust electrode.

5.5. References.

1. Woo, S., Y.-R. Kim, T. D. Chung, Y. Piao, and H. Kim, *Synthesis of a graphene - carbon nanotube composite and its electrochemical sensing of hydrogen peroxide.* Electrochimica Acta, 2012. 59(1): p. 509-514.
2. Buglione, L. and M. Pumera, *Graphene/carbon nanotube composites not exhibiting synergic effect for supercapacitors: The resulting capacitance being average of capacitance of individual components.* Electrochemistry Communications, 2012. 17(1): p. 45-47.
3. Cheng, Q., J. Tang, J. Ma, H. Zhang, N. Shinya, and L.-C. Qin, *Graphene and carbon nanotube composite electrodes for supercapacitors with ultra-high energy density.* Physical Chemistry Chemical Physics, 2011. 13(39): p. 17615-17624.
4. Jae Young Kim, Ji-Wook Jang, Duck Hyun Youn, Jae Yul Kim, Eun Sun Kim, and J. S. Lee, *Graphene–carbon nanotube composite as an effective conducting scaffold to enhance the photoelectrochemical water oxidation activity of a hematite film.* The Royal Society of Chemistry, 2012.
5. Y. Lan, Y. Wang, and Z. F. Ren, *Physics and applications of aligned carbon nanotubes.* Advances in Physics, 2011. 60(4): p. 553-678.
6. Lee, S. H., C. E. Tracy, Y. Yan, J. R. Pitts, and S. K. Deb, *Solid-state nanocomposite electrochromic pseudocapacitors.* Electrochemical and Solid-State Letters, 2005. 8(4): p. A188-A190.
7. Zilli, D., S. Blacher, A. L. Cukierman, J. P. Pirard, and C. J. Gommes, *Formation mechanism of Y-junctions in arrays of multi-walled carbon nanotubes.*

Colloids and Surfaces A: Physicochemical and Engineering Aspects, 2008. 327(1-3): p. 140-143.

8. Meyyappan, M., *Carbon Nanotubes: Science and Applications* 2005, Boca Raton: CRC Press.

9. Bose, S., T. Kuila, A. K. Mishra, R. Rajasekar, N. H. Kim, and J. H. Lee, *Carbon-based nanostructured materials and their composites as supercapacitor electrodes.* Journal of Materials Chemistry, 2012. 22(3): p. 767-784.

10. Li, Q., J. M. Anderson, Y. Chen, and L. Zhai, *Structural evolution of multi-walled carbon nanotube/MnO2 composites as supercapacitor electrodes.* Electrochimica Acta, 2011. 59(0): p. 548-557.

11. Zhao, M.-Q., Q. Zhang, J.-Q. Huang, G.-L. Tian, T.-C. Chen, W.-Z. Qian, and F. Wei, *Towards high purity graphene/single-walled carbon nanotube hybrids with improved electrochemical capacitive performance.* Carbon, 2012. 54(0): p. 403-411.

12. Wan, N., L.-t. Sun, S.-n. Ding, T. Xu, X.-h. Hu, J. Sun, and H.-c. Bi, *Synthesis of graphene–CNT hybrids via joule heating: Structural characterization and electrical transport.* Carbon, 2013. 53(0): p. 260-268.

13. Wimalasiri, Y. and L. Zou, *Carbon nanotube/graphene composite for enhanced capacitive deionization performance.* Carbon, (0).

14. *Hettich RCF / RPM Calculator*. 2013 [cited 26/04/13]; Available from: http://www.hettweb.com/mobile-app.

15. Demarconnay, L., E. Raymundo-Pinero, and F. Béguin, *A symmetric carbon/carbon supercapacitor operating at 1.6 V by using a neutral aqueous solution.* Electrochemistry Communications, 2010. 12(10): p. 1275-1278.

16. Malak-Polaczyk, A., C. Vix-Guterl, and E. Frackowiak, *Carbon/Layered Double Hydroxide (LDH) Composites for Supercapacitor Application* Energy & Fuels, 2010. 24(6): p. 3346-3351.

17. Lee, S. H., D. H. Lee, W. J. Lee, and S. O. Kim, *Tailored Assembly of Carbon Nanotubes and Graphene.* Advanced Functional Materials, 2011. 21(8): p. 1338-1354.

18. Dresselhaus, M. S., G. Dresselhaus, R. Saito, and A. Jorio, *Raman spectroscopy of carbon nanotubes.* Physics Reports, 2005. 409(2): p. 47-99.

19. Salzmann, C. G., S. A. Llewellyn, G. Tobias, M. A. H. Ward, Y. Huh, and M. L. H. Green, *The Role of Carboxylated Carbonaceous Fragments in the Functionalization and Spectroscopy of a Single-Walled Carbon-Nanotube Material.* Advanced Materials, 2007. 19(6): p. 883-887.

20. Lota, G., J. Tyczkowski, R. Kapica, K. Lota, and E. Frackowiak, *Carbon materials modified by plasma treatment as electrodes for supercapacitors.* Journal of Power Sources, 2010. 195(22): p. 7535-7539.

21. S H Shiau, C W Liu, C Gau, and B. T. Dai, *Growth of a single-wall carbon nanotube film and its patterning as an n-type field effect transistor device using an integrated circuit compatible process.* Nanotechnology, 2008. 19(10): p. 105303.

22. Yang, S.-Y., K.-H. Chang, H.-W. Tien, Y.-F. Lee, S.-M. Li, Y.-S. Wang, J.-Y. Wang, C.-C. M. Ma, and C.-C. Hu, *Design and tailoring of a hierarchical graphene-carbon nanotube architecture for supercapacitors.* Journal of Materials Chemistry, 2011. 21(7): p. 2374-2380.

23. Zhu, Y., M. D. Stoller, W. Cai, A. Velamakanni, R. D. Piner, D. Chen, and R. S. Ruoff, *Exfoliation of Graphite Oxide in Propylene Carbonate and Thermal Reduction of the Resulting Graphene Oxide Platelets.* ACS Nano, 2010. 4(2): p. 1227-1233.

24. Zhou, O., R. M. Fleming, D. W. Murphy, C. H. Chen, R. C. Haddon, A. P. Ramirez, and S. H. Glarum, *Defects in carbon nanostructures.* Science, 1994. 263(5154): p. 1744-1747.

25. Chau, T. T., W. J. Bruckard, P. T. L. Koh, and A. V. Nguyen, *A review of factors that affect contact angle and implications for flotation practice.* Advances in Colloid and Interface Science, 2009. 150(2): p. 106-115.

26. Lam, C. N. C., R. Wu, D. Li, M. L. Hair, and A. W. Neumann, *Study of the advancing and receding contact angles: liquid sorption as a cause of contact angle hysteresis.* Advances in Colloid and Interface Science, 2002. 96(1-3): p. 169-191.

27. Dong, Z. H., Y. L. Wei, W. Shi, and G. A. Zhang, *Characterisation of doped polypyrrole/manganese oxide nanocomposite for supercapacitor electrodes.* Materials Chemistry and Physics, 2011. 131(1–2): p. 529-534.

28. Rakhi, R. B., W. Chen, D. Cha, and H. N. Alshareef, *High performance supercapacitors using metal oxide anchored graphene nanosheet electrodes.* Journal of Materials Chemistry, 2011. 21(40): p. 16197-16204.

29. Bobacka, J., *Potential Stability of All-Solid-State Ion-Selective Electrodes Using Conducting Polymers as Ion-to-Electron Transducers.* Analytical Chemistry, 1999. 71(21): p. 4932-4937.

30. Portet, C., P. L. Taberna, P. Simon, and E. Flahaut, *Influence of carbon nanotubes addition on carbon-carbon supercapacitor performances in organic electrolyte.* Journal of Power Sources, 2005. 139(1-2): p. 371-378.

31. Jong, H. J., K. Akiko, M. Kenji, and N. Katsuhiko, *Supercapacitor Performance of Hydrous Ruthenium Oxide Electrodes Prepared by Electrophoretic Deposition.* Journal of The Electrochemical Society, 2006. 153(2): p. A321-A328.

32. Cvelbar, U., B. Markoli, I. Poberaj, A. Zalar, L. Kosec, and S. Spaic, *Formation of functional groups on graphite during oxygen plasma treatment.* Applied Surface Science, 2006. 253(4): p. 1861-1865.

33. Mishra, A. K. and S. Ramaprabhu, *Functionalized Graphene-Based Nanocomposites for Supercapacitor Application.* The Journal of Physical Chemistry C, 2011. 115(29): p. 14006-14013.

34. Masarapu, C., H. F. Zeng, K. H. Hung, and B. Wei, *Effect of Temperature on the Capacitance of Carbon Nanotube Supercapacitors.* ACS Nano, 2009. 3(8): p. 2199-2206.

35. Shen, J., A. Liu, Y. Tu, G. Foo, C. Yeo, M. B. Chan-Park, R. Jiang, and Y. Chen, *How carboxylic groups improve the performance of single-walled carbon nanotube electrochemical capacitors?* Energy & Environmental Science, 2011. 4(10): p. 4220-4229.

36. Chen, W., R. B. Rakhi, L. Hu, X. Xie, Y. Cui, and H. N. Alshareef, *High-Performance Nanostructured Supercapacitors on a Sponge.* Nano Letters, 2011. 11(12): p. 5165-5172.

37. Taberna, P. L., P. Simon, and J. F. Fauvarque, *Electrochemical Characteristics and Impedance Spectroscopy Studies of Carbon-Carbon Supercapacitors.* Journal of The Electrochemical Society, 2003. 150(3): p. A292-A300.

38. Wang, G., L. Zhang, and J. Zhang, *A review of electrode materials for electrochemical supercapacitors.* Chemical Society Reviews, 2012. 41(2): p. 797-828.

39. Muralidharan, V. S., *Warburg impedance - Basics revisited.* Anti-Corrosion Methods and Materials, 1997. 44(1): p. 26-29.

40. Stoller, M. D., S. Park, Y. Zhu, J. An, and R. S. Ruoff, *Graphene-Based Ultracapacitors.* Nano Letters, 2008. 8(10): p. 3498-3502.

41. Liu, H., P. He, Z. Li, Y. Liu, and J. Li, *A novel nickel-based mixed rare-earth oxide/activated carbon supercapacitor using room temperature ionic liquid electrolyte.* Electrochimica Acta, 2006. 51(10): p. 1925-1931.

42. Lewandowski, A., A. Olejniczak, M. Galinski, and I. Stepniak, *Performance of carbon-carbon supercapacitors based on organic, aqueous and ionic liquid electrolytes.* Journal of Power Sources, 2010. 195(17): p. 5814-5819.

43. Centi, G. and S. Perathoner, *Carbon nanotubes for sustainable energy applications.* ChemSusChem, 2011. 4(7): p. 913-925.

44. Huang, Z.-D., B. Zhang, R. Liang, Q.-B. Zheng, S. W. Oh, X.-Y. Lin, N. Yousefi, and J.-K. Kim, *Effects of reduction process and carbon nanotube content on the supercapacitive performance of flexible graphene oxide papers.* Carbon, 2012. 50(11): p. 4239-4251.

45. Chen, Q.-L., K.-H. Xue, W. Shen, F.-F. Tao, S.-Y. Yin, and W. Xu, *Fabrication and electrochemical properties of carbon nanotube array electrode for supercapacitors.* Electrochimica Acta, 2004. 49(24): p. 4157-4161.

46. Zhang, J., J. Jiang, H. Li, and X. S. Zhao, *A high-performance asymmetric supercapacitor fabricated with graphene-based electrodes.* Energy and Environmental Science, 2011. 4(10): p. 4009-4015.

47. El-Kady, M. F. and R. B. Kaner, *Scalable fabrication of high-power graphene micro-supercapacitors for flexible and on-chip energy storage.* Nat Commun, 2013. 4: p. 1475.

48. Murata Manufacturing Co. Ltd., *Electric Double Layer Capacitor*. [cited 08/05/13]; Available from: http://www.murata.com/products/edlc/catalog/index.html.

49. Murata Manufacturing Co. Ltd., *Polymer Capacitors*. [cited 08/05/13]; Available from: http://www.murata.com/products/polymer/index.html.

50. Maxwell Technologies, *Ultracapacitor K2 Series*. [cited 08/05/13]; Available from: http://www.maxwell.com/products/ultracapacitors/products/k2-series.

51. Zhai, Y., Y. Dou, D. Zhao, P. F. Fulvio, R. T. Mayes, and S. Dai, *Carbon materials for chemical capacitive energy storage.* Advanced Materials, 2011. 23(42): p. 4828-4850.

52. Naoi, K. and P. Simon, *New Materials and New Configurations for Advanced Electrochemical Capacitors.* Journal of The Electrochemical Society 2008. 17(1): p. 34-37.

53. Li, L., E. Liu, J. Li, Y. Yang, H. Shen, Z. Huang, X. Xiang, and W. Li, *A doped activated carbon prepared from polyaniline for high performance supercapacitors.* Journal of Power Sources, 2010. 195(5): p. 1516-1521.

Chapter 6: Manganosite : microwave exfoliated graphene oxide electrodes for asymmetric supercapacitors.

6. Manganosite : microwave exfoliated graphene oxide electrodes for asymmetric supercapacitors.

6.1. Introduction.

Within the last decade, there has been an increased effort in the development of new hybrid energy storage devices that possess both high energy and high power density which are beneficial for creating more energy efficient storage and delivery [1]. Asymmetric supercapacitors are promising hybrid energy storage devices as they are able to provide a wider operating voltage at higher energy compared to symmetric capacitors [2]. Such supercapacitors are comprised of an anode that is usually an activated carbon, while the cathode is generally a composite consisting of a carbon material and transition metal oxide. Asymmetric supercapacitors make use of the different potential windows in the anode and cathode leading to an increased operational voltage of the aqueous electrolyte in the cell meaning that specific capacitance, energy and power density are maximised [2].

Manganosite consists of Mn^{2+} and O^{2-} molecules forming an octahedral geometry and a cubic crystal structure [3]. It has potential for use in hybrid energy storage devices due to its quasi-reversible electron transfer that provides high pseudo-capacitive energy density [4]. Over the last decade, manganese oxides with different morphologies including rods, nanotubes, and nanowires have been developed and characterised [1, 5, 6]. In this manuscript, we report a hybrid electrode architecture that incorporates MnO particles onto the active surfaces of

an exfoliated GO matrix. For the composite, the microwave exfoliated reduced graphene oxide (mw rGO) nanosheets serve primarily as a high surface area conductive framework providing support for the adherence of MnO particles. Physical characterisation of the composite electrodes has shown the MnO particles to be dispersed throughout the mw rGO matrix. Electrochemical testing of the composite electrodes yielded a material that was stable over a wide range of current densities and had excellent capacity retention.

6.2. Experimental specific to Chapter 6.

6.2.1. Hydrothermal synthesis of manganosite (MnO).

The MnO was prepared using a hydrothermal synthesis method at the Materials Science Research Centre, Faculty of Science, Chiang Mai University. Potassium permanganate ($KMnO_4$, 97% Aldrich, USA) and Manganese sulfate ($MnSO_4$, 97% Sigma, USA) were prepared by dissolving in deionised water as 0.1M and 0.6M, respectively. Mixing was accomplished by drop-wise addition of 100 ml $KMnO_4$ solution into 100 ml of $MnSO_4$ solution while stirring. The mixed solution was transferred into a Teflon-lined stainless steel autoclave. The hydrothermal synthesis was carried out at 140 °C for 12h. After the reaction was complete, the autoclave was cooled down to room temperature. The black product was washed with deionised water and ethanol, filtered and then dried at 60 °C for 24h [7].

6.2.2. Synthesis of microwave exfoliated graphene oxide

The full description of the synthesis of microwave exfoliated graphene oxide is outlined in Chapter 4.

6.2.3. Fabrication of electrodes.

The fabrication of the working electrode was carried out by employing a similar method to that outlined by Yan et. al. [8]. Different mass ratios of MnO and mw rGO in ethanol were probe sonicated for 30 minutes. After 30 minutes, PTFE (10 wt. %) dissolved in ethanol was mixed into the MnO-mw rGO ethanol mixture and sonicated for a further 30 minutes. The resulting solution was then stirred on a hot plate (using a magnetic stirrer) at 60^{o}C for approximately 2 hours until the ethanol had sufficiently evaporated and the heat allowed the PTFE to bind the material to form a slurry. The four weight ratios of MnO to mw rGO that where prepared were; 0% MnO- 100% mw rGO, 60% MnO- 40 % mw rGO, 70% MnO- 30% mw rGO, and 90% MnO- 10 % mw rGO respectively. Each slurry was then spread over a stainless steel mesh using a fine spatula and dried overnight in a vacuum oven at 100^{o}C. Standardised practices for composite electrode preparation of transition metal oxides involve using a conductive additive and binder to provide a supporting scaffold [9, 10]. MnO by itself is a poor conductor (10^{-9} ohm^{-1} cm^{-1}) [11], which is why the mw rGO was added to provide a conductive scaffold and enhance charge storage and delivery. A film of MnO exceeding 90% (w/w) under the same fabrication conditions could not be formed.

6.2.4. Supercapacitor device fabrication.

For device testing, the positive electrode was made as outlined above in Section 6.2.3. The negative electrode was made out of commercially purchased activated carbon (VC-72, Cabot). Firstly, the activated carbon was functionalised by mixing a 70% (w/w) HNO_3 (Univar) and 98% (w/w) H_2SO_4 (Univar) solution in a 3:1 bath and sonicated for 2 hours. The resulting material was then washed with deionised water until a neutral pH was reached. The functionalised activated carbon (FC) was then mixed with a PTFE binder (10% w/w) (Sigma-Aldrich) to form a slurry that was subsequently spread onto a stainless steel current collector. All electrodes had a geometric area of $1cm^2$, with an approximate equal mass loading of 4 mg/cm^2. Devices were constructed by sputter coating two pieces of indium tin oxide (ITO) glass with 100 nm of Pt to help minimise contact resistance. The two electrodes were pressed between the two current collectors with a PVDF separator of thickness 110 microns and 0.22 micron pore size (Millipore© - Durapore®). A clamp was used to hold the system in place (constant force of 156 N), while UV cure glue (Dynman Light Weld) and UV light source (Dynmax Blue Wave 50) was used to seal the cell. Lastly, a small hole was left where 1M $NaNO_3$ in H_2O was added as the electrolyte via vacuum filling, with the hole being sealed thereafter with UV cure glue.

6.3. Discussion of Results.

6.3.1. Physical characterisation of MnO: mw rGO films.

6.3.1.1 Scanning electron microscopy of mw rGO.

The SEM images shown in Figure 6. 1a and Figure 6. 1b are of the raw GO and mw rGO powders whilst the images of Figure 6. 1c and Figure 6. 1d are of GO and mw rGO that have been drop cast onto a TEM grid. From Figure 6. 1, some qualitative observations can be made. Firstly, in Figure 6. 1a, the SEM is of the GO after it has been washed and dried as outlined in Chapter 4, section 4.2.2. It can be seen that its structure is uneven, containing valleys and elevated regions, which reflect vast amounts of sheet stacking. In Figure 6. 1b, after microwave irradiation; the GO expands leading to the development of an accordion type structure that is highly porous, forming an interconnected network with minimal re-stacking [12]. Optical image comparisons are shown in the insets of Figure 6. 1a and Figure 6. 1b. In Figure 6. 1c, the GO that has been drop cast onto a TEM grid, is extremely flat indicating uniform GO sheets. In Figure 6. 1d, the mw rGO was also drop cast onto a TEM grid, with the ensuing images depicting mw rGO sheets that have a crumpled shape. This crumpling effect adds porosity to the system and hence surface area, which could play a key role in the development and preparation of composite electrode materials.

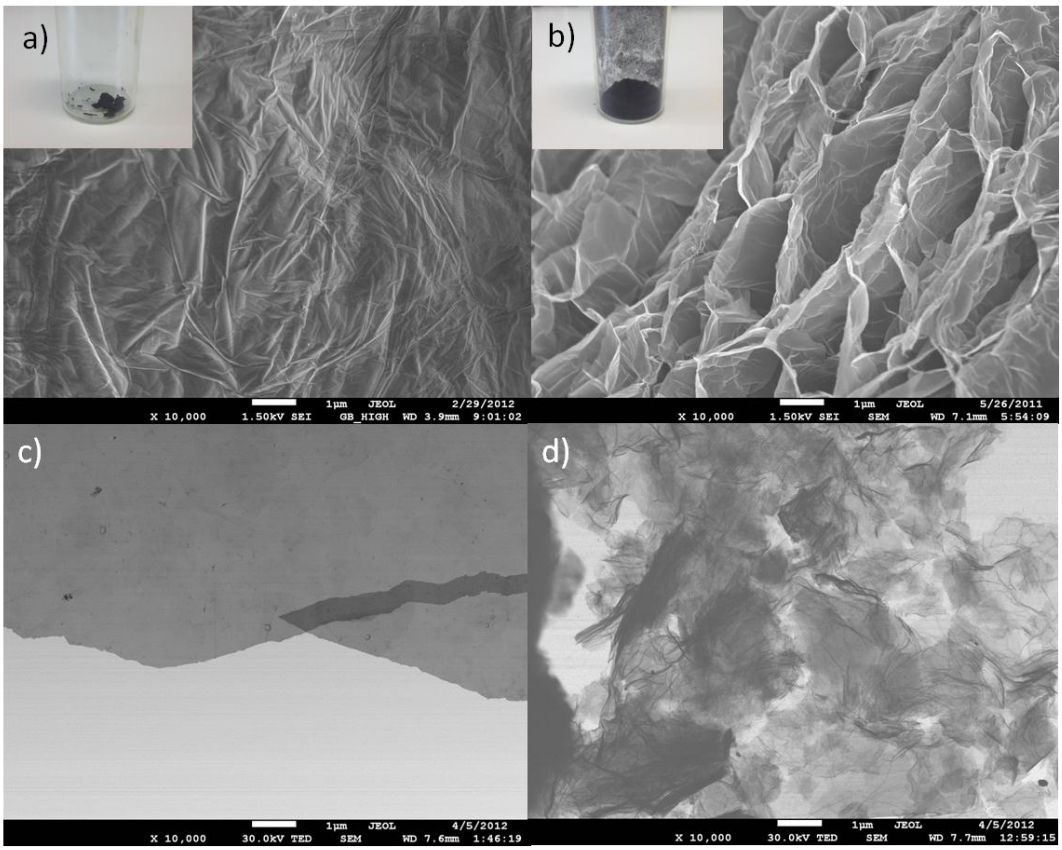

Figure 6. 1: a) SEM image of GO powder after it has been washed and dried as outlined in section 6.3.1.1. Inset shows optical image of the GO sample. b) SEM image of mw rGO powder. Inset shows an optical image of the sample after microwave irradiation on the film. c) TED image of GO after it has been drop cast onto a TEM grid. d) TED image of mw rGO after it has been drop cast onto a TEM grid.

6.3.1.2 Raman Spectroscopy, x-ray diffraction and x-ray photoelectron spectroscopy of mw rGO.

Please refer to Chapter 4, section 4.3 for physical characterisation of GO and mw rGO using Raman spectroscopy, XRD, and XPS.

6.3.1.3 Scanning electron microscopy of MnO – mw rGO composoite.

Manganosites exhibit pseudocapacitive behaviour over small ranges of potentials, through redox processes which contribute electron transfer between the electrode / electrolyte interface. By combining MnO with mw rGO, composites can be formed that combine both Faradaic and non-faradic effects enabling a larger energy density to be obtained, whilst maintaining reasonable power density.

In Figure 6. 2a, the SEM image of the MnO particles after hydrothermal synthesis shows large cube type structures that have a porous nature. When the MnO is imaged at larger magnification (Figure 6. 2b), it can be seen that the particles are comprised of larger spherical platelets and smaller rod-like structures. The MnO particles have a distribution of sizes ranging from 20 nm to 1 μm. To show the distribution of the MnO in the mw rGO matrix, EDS spectra was recorded on a section of the image (Figure 6. 2c and Figure 6. 2d). It is apparent that there is a good distribution of MnO as there is significant overlay of Mn (K_α) lines throughout the composite material, with the lighter regions (approaching white) being more intense. From these qualitative observations, the MnO particles are well mixed throughout the mw rGO matrix

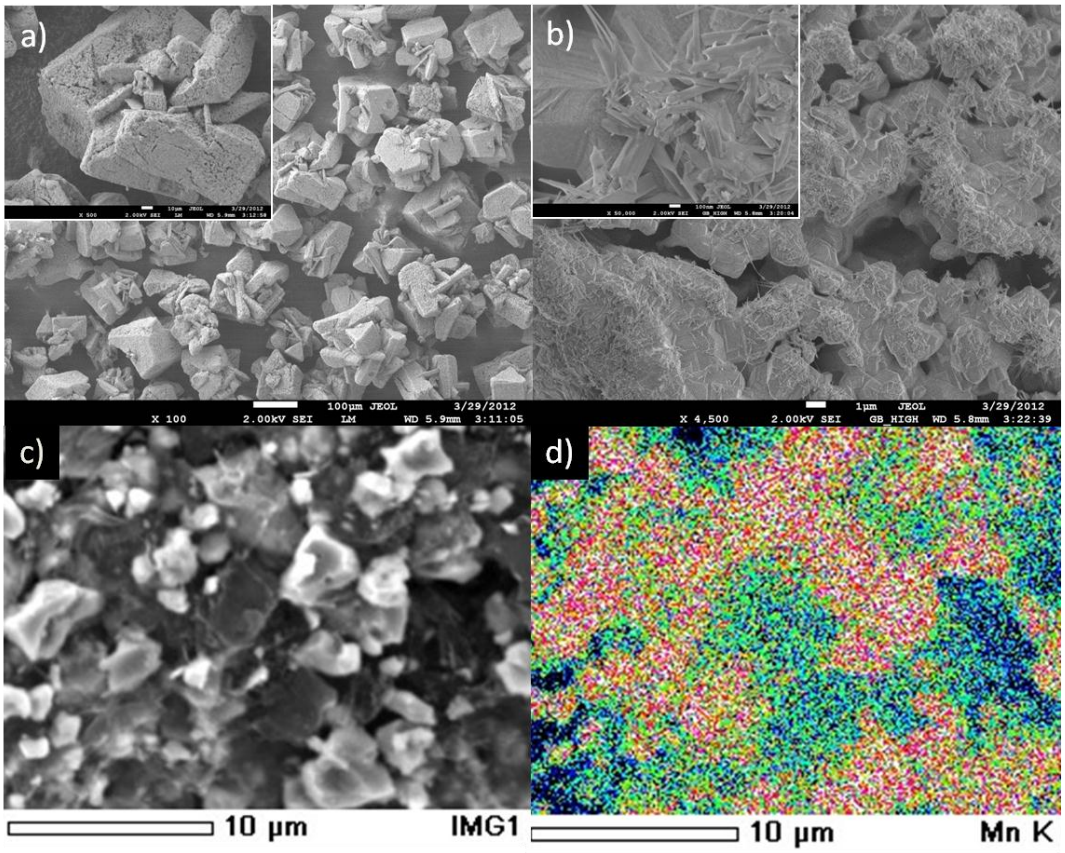

Figure 6. 2: a) SEM image MnO powder after hydrothermal synthesis. (b) SEM image of MnO powder at higher magnification showing spherical platelets and rod shaped structures. (c) SEM image of 90% MnO- 10% mw rGO composite. (d) EDS map of Mn (K_α) showing the uniformity of distribution in the 90% MnO- 10% mw rGO composite.

6.3.1.4 X-ray diffraction of MnO- mw rGO composite.

The 2θ peaks of MnO (Figure 6. 3) at 35°, 41°, 59°, 70°, and 74° correspond to the Manganosite type MnO (JCPDS 00-001-1206). When considering the composite MnO- mw rGO, the carbon (002) peak at 26° along with the 35°, 41°, 59° of MnO are clearly visible. The broad peak of the mw rGO is due to graphene oxide and other amorphous carbons; while the extremely sharp peaks of MnO are due to good crystallinity of the metal oxide [8, 13].

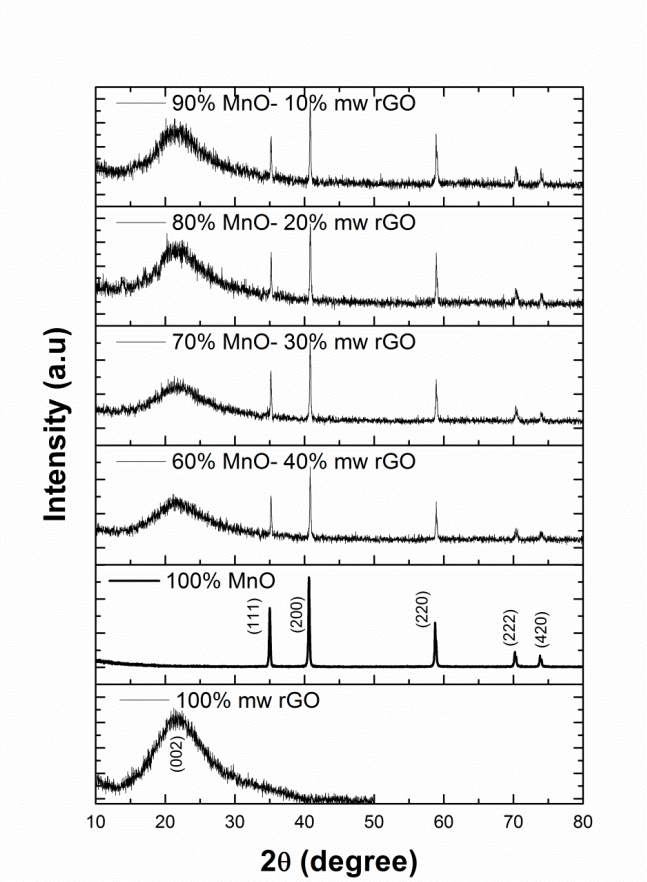

Figure 6. 3: (a) XRD spectra of MnO, mw rGO, and MnO- mw rGO at varying weight ratios.

6.3.2. Electrochemical properties of MnO: mw rGO electrodes using a three electrode system.

6.3.2.1 Cyclic voltammetry of MnO: mw rGO with varied weight composition.

The cyclic voltammograms shown in Figure 6. 4a and Figure 6. 4b depict a comparison of mw rGO, 60% MnO – 40% mw rGO, 70% MnO – 30% mw rGO and 90% MnO – 10% mw rGO composite electrodes on a stainless steel mesh current collector. In all cases, the CV obtained are quasi-rectangular, indicating a pseudo

capacitive type behaviour (mixture of non-Faradaic and Faradaic responses). The slight kink observed between 0.2 V- 0.3 V for the 70% MnO – 30% mw rGO and 0.5 V-0.6 V for 90% MnO – 10% mw rGO are oxidation peaks thought to be due to Faradaic reactions of the MnO and carbon. A proposed quasi reversible reaction that may account for this is described below;

$$MnO + C^{+} + e^{-} \leftrightarrow MnOC$$

CVs above scan rates of 50 mV/s (not shown) started to lose their rectangular shape and distort. This distortion can be attributed to ohmic polarisation ($iR_{uncompensated}$) due to increased current at higher scan rates ($i \sim dc/dx$) as well as an RC time constant that is too large for the higher sweep rates used [14]. The largest current and capacitance by area (Figure 6. 4a) was obtained for the 90% MnO- 10% mw rGO at 42.5 ± 9.2 mF/cm^2, while the 70% MnO- 30% mw rGO was 26.6 ± 1.2 mF/cm^2. Both the 60% MnO- 40% mw rGO and pure mw rGO had values of 18.4 ± 1.1 mF/cm^2 and 19.1 ± 0.3 mF/cm^2 respectively.

The results of current response and capacitance by mass (Figure 6. 4b) behave in a different trend due to the fact that the mw rGO is an extremely light material, while comparatively the MnO is quiet dense. Hence, as the weight ratio of MnO increases the mass of MnO will dominate. The largest current and capacitance by mass was obtained for the 60% MnO- 40% mw rGO at 10.4 ± 0.8 F/g, while the 70% MnO- 30% mw rGO was 7.7 ± 1.0 F/g. Both the 90% MnO- 10% mw rGO and pure mw rGO had values of 4.4 ± 1.0 F/g and 3.8 ± 0.3 F/g respectively.

The capacitance area and by mass weight was calculated at 50 mV/s according to equation 2.2 and 2.3 in Chapter 2. The capacitance calculations were calculated at a larger scan rate of 50 mV/s to show a suitable rate capability.

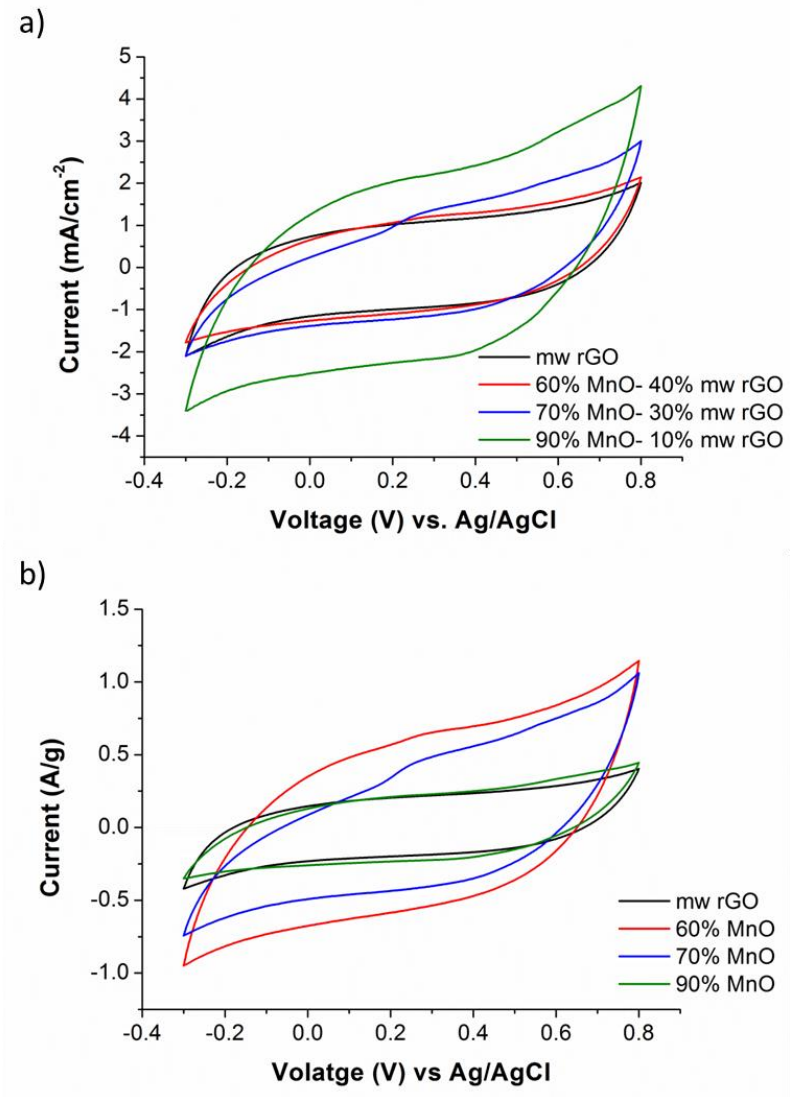

Figure 6. 4: Comparison of CVs for mw rGO, 60% MnO – 40% mw rGO, 70% MnO – 30% mw rGO and 90% MnO – 10% mw rGO composite electrodes. Scan rate is at 50 mV/s. System is three electrode with a Pt mesh counter, and Ag/AgCl reference. Electrolyte used is aqueous 1M $NaNO_3$. Material slurry was cast onto stainless steel mesh using a thin spatula. (a) Current response by area, (b) Current response by mass.

6.3.2.2 Impedance spectroscopy conducted at open circuit potential.

In Figure 6. 5a (experiment conducted at open circuit potential (OCP = 100 mV)) it can be seen that there is systematic behaviour in the variation of the Nyquist plot as the weight percent of MnO is increased. The 90% MnO-10% mw rGO displayed the smallest semi-circle at high frequencies signifying that the kinetics of this system is the fastest with an increase in the semi-circle as the weight percent of MnO decreased. In this system, the semi-circle (R_{ct}) is likely to represent a couple of processes. (i) Electrolyte resistance and double layer capacitance within the pores of the electrode, which is best modelled by a transmission line model; (ii) Charge transfer resistance associated with equation 1 [15, 16].

The low frequency increase in the imaginary impedance looks to be mainly capacitive from double layer charging / discharging, and redox processes as the slope is much steeper than the 45^{o} associated with Warburg diffusion [17] . This result physically speaking is thought to occur due to the MnO particles being large (see Figure 6. 2) which at the high weight ratio of 90% MnO- 10% mw rGO effectively causes the surface of the electrode to be better interconnected and more mesoporous [18]. At high frequencies, the intercept of the real part of impedance (Z') with the x-axis R_s (which represents the resistance of the electrolyte, intrinsic resistance of the substrate and contact resistance) slightly decreases as the weight percent of MnO increased [8]. This reflects the fact that the wettability of the electrode / electrolyte interface is increased [19]. The inset of Figure 6. 5 is an equivalent circuit model which was used to obtain values for R_s and R_{ct}. In the

model R_s represents the ionic resistance of the electrolyte, the contact resistance between the active materials and current collectors, and the intrinsic resistance of the substrates [20]. R_{ct} is the resistance to charge transfer, and *CPE* is a constant phase element which represents the frequency dependence of the charge transfer processes occurring in a porous structure that is filled with electrolyte [21]. W_0 is the Warburg diffusion element corresponding to electrolyte diffusion in the bulk of the electrode [22].

The imaginary part of capacitance versus frequency (Figure 6. 5b) represents the energy dissipation of the complex part of capacitance, characteristic of an irreversible process, which can lead to the hysteresis of the electrochemical process [8, 14, 16, 23]. The relaxation time constant (τ_s) can be evaluated from Figure 6. 5b by finding the peak frequency (f_p) of Im $C(\omega)$, multiplying by 2π and inverting. In Figure 6. 5b, with the experiment conducted at OCP, the 90%MnO-10% mw rGO showed the largest peak frequency. As the weight ratio of MnO is increased, there is a shift of f_p towards higher frequencies (hence lower time constant) due to faster pseudocapacitive effects. The time constant as a function of frequency is shown in the inset of Figure 6. 5b. Refer to Table 6. 1 for R_s and R_{ct} as a function of MnO composition.

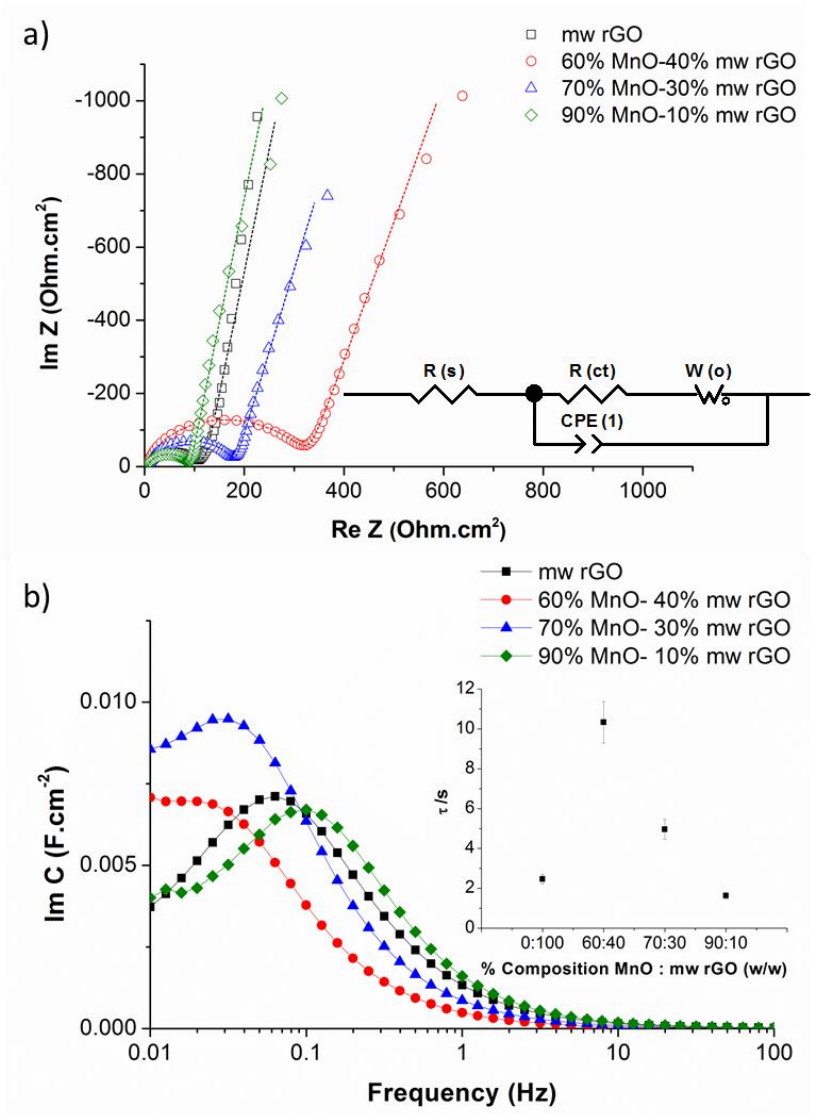

Figure 6. 5: (a) Nyquist plots (with inset) of experimental impedance data (scattering dot) and fitting results (dashed line) for MnO – mw rGO composite electrodes as the mass percentage of MnO is changed. (b) Comparison of the imaginary part of capacitance versus frequency for the MnO – mw rGO composite electrodes. Experiment conducted at open circuit potential. System is three electrode with a Pt mesh counter, and Ag/AgCl Electrolyte used is aqueous 1M $NaNO_3$. Material slurry was cast onto stainless steel mesh using a thin spatula.

Table 6. 1: Comparison of R_s, and R_{ct} as the weight ratio of MnO to mw rGO is increased. Substrate is stainless steel mesh. Values for EIS obtained at open circuit potential.

% Composition of MnO : mw rGO (w/w)	**$R_{(s)}$ (ohm.cm^2)**	**$R_{(ct)}$ (ohm cm^2)**
0:100	8.4 ± 0.5	94.0 ± 5.6
60:40	4.7 ±0.2	293.2 ± 12.5
70:30	7.3 ± 0.2	174.8 ± 4.9
90:10	5.2 ± 0.3	87.6 ± 5.1

6.3.2.3 Impedance spectroscopy conducted at zero voltes versus the reference.

In the Nyquist plot of Figure 6. 6a (experiment conducted at zero volts versus the reference electrode), it can be seen that at low frequencies approaching 0.01 Hz, the imaginary part of impedance rapidly increases and shows very similar behaviour to that of Figure 6. 5a. When we consider the inset of Figure 6. 6a, there are two semi-circles apparent (R_1 and R_2), reflecting two time constants. These two semi-circles are as a result of the multiple interfaces apparent at the electrode / electrolyte interface through new boundaries that are formed during testing [22]. The first interface is thought to be due to double layer capacitance and the Faradaic process of Mn^{2+} being converted to Mn^{+} as mentioned previously. The second interface could possibly be caused by the formation of hausmannite ($Mn^{2+}Mn^{3+}{}_2O_4$) during the impedance spectroscopy and cyclic voltammetry experiments, creating a multi-component system. In Figure 6. 6 the ternary system has been modelled by

an equivalent circuit consisting of R_s that represents the ionic resistance of the electrolyte, the contact resistance between the active materials and current collectors, and the intrinsic resistance of the substrates. R_2 and R_3 are the charge transfer resistances at the interfaces, while CPE_1 and CPE_2 are responsible for the capacitance components of the system generated at each interface [24, 25]. W_0 is the Warburg impedance. The formation of hausmannite ($Mn^{2+}Mn^{3+}{}_2O_4$) during device testing is discussed further down at Figure 6. 9. At high frequencies, the intercept of the real part of impedance (Z') that refers to R_s decreases as the weight percent of MnO increased signifying a decrease in the wettability of the electrode [8, 26]. As the weight ratio of MnO increase, R_1 and R_2 decrease meaning the charge transfer properties / electron transfer kinetics are significantly improved [18, 24]. (The kinetics of the system in terms of the electron transfer rate constant (k^0) is inversely proportional to R; hence the greater the weight percent of MnO, the faster the electron transfer [18]). Physically speaking, it is thought that reduced amount of mw rGO and increased amount of MnO causes better inter-connectivity of the MnO, and less hausmannite (as a percentage of MnO) to be formed which enhanced charge storage and delivery (see Table 6. 2).

The imaginary part of capacitance versus frequency (Figure 6. 5b and Figure 6. 6b) represents the energy dissipation of the complex part of capacitance, characteristic of an irreversible process, which can lead to the hysteresis of the electrochemical process [8, 14, 16, 23]. The relaxation time constant (τ_s) can be evaluated from Figure 6. 5b and Figure 6. 6b by finding the peak frequency (f_p) of $C'(\omega)$, multiplying

by 2π and inverting. In Figure 6. 5b, with the experiment conducted at OCP, the peak frequencies are much lower than in Figure 6. 6b (conducted at 0 V versus reference), with the 90%MnO-mw rGO showing the largest peak frequency. As the weight ratio of MnO is increased, there is a shift of f_p towards higher frequencies (hence lower time constant) due to the driving force at the working electrodes surface (Figure 6. 6b). The time constant as a function of frequency is shown in the inset of Figure 6. 5b and Figure 6. 6b with τ_s being roughly a factor of 4 times less for the experiment conducted at zero volts versus reference than at OCP where there is no DC current flow between the working and the counter electrode. Refer to Table 6. 1 and Table 6. 2 for R_s, R_1 and R_2 as a function of MnO composition.

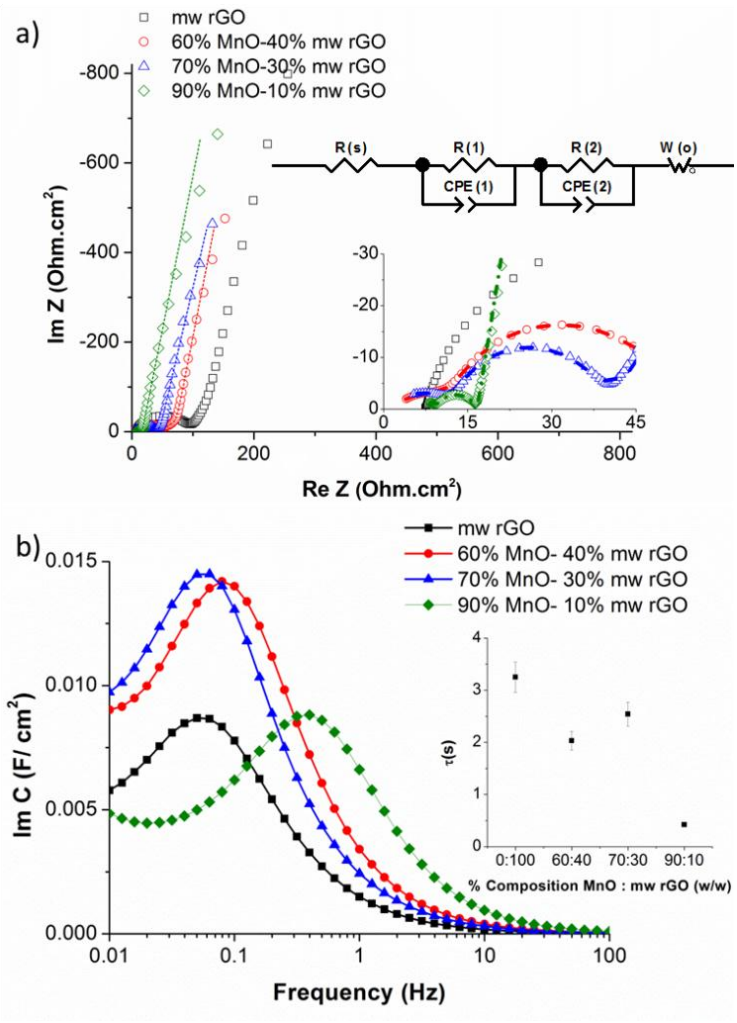

Figure 6. 6: (a) Nyquist plots (with inset) of experimental impedance data (scattering dot) and fitting results (dashed line) for MnO – mw rGO composite electrodes as the mass percentage of MnO is changed. (b) Comparison of the imaginary part of capacitance versus frequency for the MnO – mw rGO composite electrodes. Experiment conducted at zero volts versus the reference electrode. System is three electrode with a Pt mesh counter, and Ag/AgCl Electrolyte used is aqueous 1M $NaNO_3$.Material slurry was cast onto stainless steel mesh using a thin spatula.

Table 6. 2: Comparison of capacitance, R_s, R_p and R_{ct} as the weight ratio of MnO to GO is increased. Substrate is stainless steel mesh. Values for EIS obtained at zero volts versus the reference electrode.

% Composition of MnO : mw rGO (w/w) (w/w)	**$R_{(s)}$ (ohm cm^2)**	**$R_{(1)}$ (ohm cm^2)**	**$R_{(2)}$ (ohm cm^2)**
0:100	7.5 ± 0.1	89.5 ± 0.9	-
60:40	1.5 ± 0.1	11.5 ± 0.2	31.2 ± 0.2
70:30	0.4 ± 0.5	22.5 ± 0.3	12.8 ± 0.7
90:10	2.5 x10^{-6} ± 5 x10^{-8}	10.0 ± 6.3	5.7 ± 0.3

6.3.3. Supercapacitor device testing of 90% MnO: 10% mw rGO.

6.3.3.1 Cyclic voltammetry and galvanostatic charge / discharge.

To investigate device performance of our composite material, an asymmetric supercapacitor device was constructed using the 90% MnO-10% mw rGO as the cathode and functionalised activated carbon (FC) as the anode. Selection of the 90% MnO-10% mw rGO was based on results from the 3-electrode cell comparisons of varying weight ratios of MnO and mw rGO. The 90% MnO- 10% mw rGO displayed the largest current per unit area and superior kinetics due to the enhanced interconnectivity of the MnO and mw rGO resulting in superior charge storage and delivery properties. The cyclic voltammograms of Figure 6. 7a are of the asymmetric 90% MnO- 10% mw rGO // FC device and exhibit rectangular behaviour over a potential window of 1.1 V indicating very good charging and discharging of the device [27, 28]. The rectangular shape is maintained even up to

the high scan rate of 200 mV/s. In Figure 6. 7b and Figure 6. 7c, galvanostatic charge / discharge has been employed in order to simulate and understand real world conditions. The charge / discharge curve (Figure 6. 7b) is very symmetrical, with a slight bend / kink of the charging curve due to the asymmetric nature of the device and the fact that some slower redox processes are occurring due to the MnO [29, 30]. The time difference between charging and discharging gets smaller and smaller as the current is increased from 0.1 A/g to 1.0 A/g; but then nearly goes back to its original time difference when the current is reduced back to 0.1 A/g. This signifies very good reversibility at different current densities which is useful for real world applications as the system is able to handle different current ranges [31]. In Figure 6. 7c, the specific capacitance is computed as a function of cycle number with a step-wise increase in the current every 100 cycles. It can be seen that good stability is achieved at current densities of up to 0.5 A/g. At higher current densities approaching 1.0 A/g, the specific capacitance decreases rapidly. When the system is switched back to its initial conditions (0.1 A/g) at cycles 900-1000, the total charge is only slightly less (approximately 96% of the charge) than cycles 1-100, indicating excellent stability. In Figure 6. 7d, galvanostatic charge / discharge was used to plot energy density versus power density. The maximum calculated [14, 32] energy and power densities were 2.6 W.h/kg and 9024 W/kg respectively. The increase in the energy at low current density is due to the enhanced utilisation of available electroactive surface area. At these low rates, the electrolyte has time to fully wet all of the available surface area.

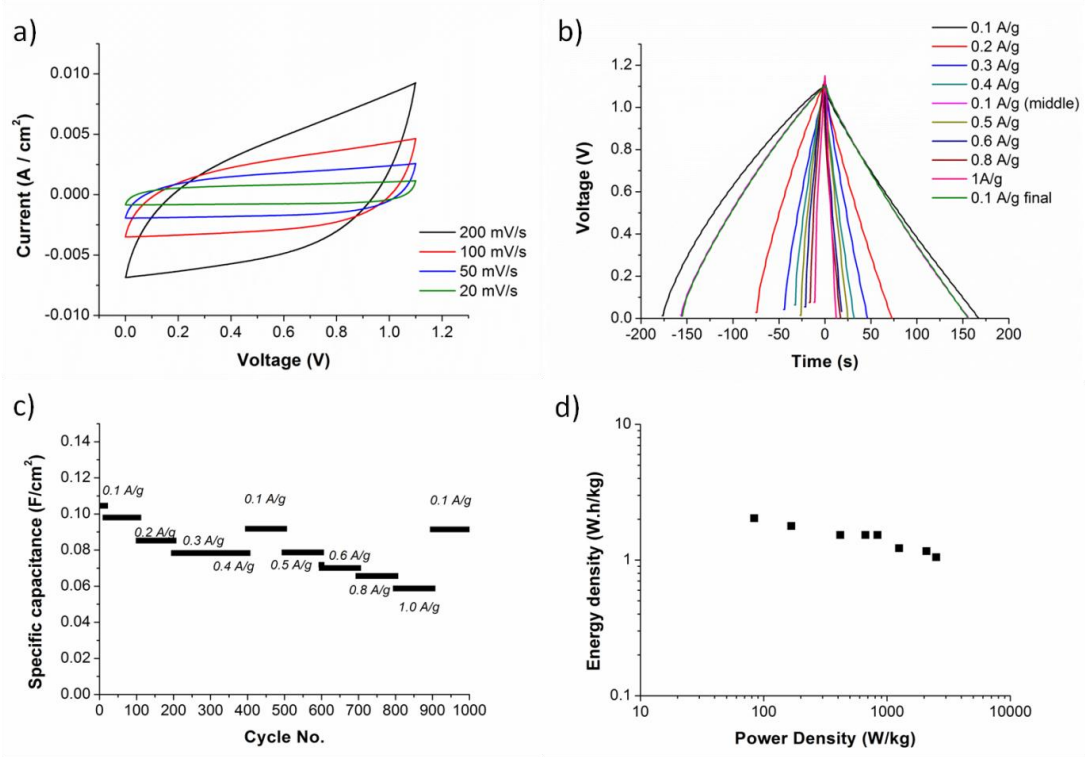

Figure 6. 7: (a) CV of 90% MnO-mw rGO // FC asymmetric supercapacitor at 20 mV/s, 50 mV/s, 100 mV/s, and 200 mV/s. (b) Galvanostatic charge / discharge tests for varying current rates. (c) Specific capacitance over 100 cycles as the current density is increased from 0.1 A/g to 1.0 A/g. (d) Ragone plot. Energy and power density values calculated from galvanostatic charge / discharge.

6.3.3.2 Stability performance.

In Figure 6. 8a, the specific capacitance is plotted against cycle number showing the capacity retention of our asymmetric device. It can be seen that initially there is a decrease in the specific capacitance due to initial activation of the composite material which comprises wetting and changes in volume as the electrolyte is being adsorbed / desorbed into the pores of the material [27, 33]. Once equilibrium is reached the capacitance stabilises. After approximately 1000 cycles, the specific capacitance rises, reaching a maximum between approximately 3100 and 5800

cycles due to enhanced redox behaviour of the MnO. There is a slight fall away in the specific capacitance with a plateau occurring after 9000 cycles due to degradation that is caused by changes in volume and the formation of hausmannite (see Figure 6. 8) [34]. It can be seen that initially the specific capacitance was 0.11 F/cm^2 (51.5 F/g equivalent by mass) and after 15 000 cycles it was 0.09 F/cm^2 (41.7 F/g equivalent by mass) indicating a capacity retention of 82%. Our specific capacitance of 0.11 F/cm^2 also matches the required value of specific capacitance > 0.10 F/cm^2 (peak power demands of pulsed loads) for the devices used in battery-powered electronics [35-38]. Our capacity retention of 82% is comparable to those of other asymmetric supercapacitors such as MnO_2 //AC (96% retention after 1000 cycles) [39]; MnO_2 //CNTs/SnO_2 (92% retention after 100 cycles) [40]; and $LiTi_2(PO_4)_3$ (85% retention after 1000 cycles) [41]. The advantage of our system is the relative abundance and non-toxic nature of graphene and manganese, with the added benefit of no harmful electrolytes being used [42].

In Figure 6. 8b, the Nyquist plot reflects the asymmetric device just as it was made and after 15000 cycles. For the long term galvanostatic charge / discharge, a current density of 0.5 A/g was selected based on Figure 6. 7c where 0.5 A/g was the maximum current density that showed good stability. In the Nyquist plot of Figure 6. 8b, it can be seen that at high frequencies a small semi-circle is observed with the initial part of this semi-circle exhibiting an elongated region. It is thought that there are actually two semi-circles (R_p and R_{ct}) in these regions which are not able to be resolved. The first R_p, is a smaller semi-circle representing predominately non-

Faradaic charge transfer effects and some very small irreversible redox processes from functionalisation of the FC anode during charging / discharging [43]. The second R_{ct}, a larger semi-circle as a result of Faradaic processes arising from MnO [44]. It is apparent however that after 15 000 cycles the size of the semi-circle is much larger due to an increase in R_{ct} with a decrease in the specific capacitance also apparent which is caused by the formation of another manganese compound as discussed below . Accompanied with this, is an increase in R_s from 4.5 Ω to 10.0 Ω. This occurs because as the device continues to be cycled, some degradation of the composite occurs through volume changes and irreversible redox processes that increase the contact resistance and slow down the electron transfer kinetics, thus reducing the effectiveness of charge storage and delivery [20, 45]. At low frequencies for both plots, the imaginary part of capacitance rapidly rises, indicating good pseudo-capacitive behaviour [34].

To further understand the behaviour of this 90% MnO- 10% mw rGO // FC asymmetric device, equivalent circuit modelling (Figure 6. 8b inset) was employed in order to establish values for R_s, R_p, R_{ct}, C_{dl} and C_f before and after long term galvanostatic charge / discharge testing [46, 47]. The model chosen reflects the 2-electrode device where both the FC and the 90% MnO-10% mw rGO must be considered [48]. In the Nyquist plot of Figure 6. 8b, there are thought to be two semi-circles that are not well resolved at the high to middle frequency regime, with pseudocapacitive behaviour extending to the low frequency portion of the spectrum where the imaginary part of capacitance rapidly rises but is not perfectly

vertical. These selected components correspond to two constant phase elements (CPE_{dl} and CPE_f) each accompanied with an associated charge transfer resistance that represent non ideal behaviour of the two electrodes [46, 49]. The Warburg element (W_o) was also selected due to the frequency dependence of the porous capacitance and also counter ion diffusion to the electrode surface that balances the charge while Faradaic processes are taking place [45]. R_s represents the ionic resistance of the electrolyte, the contact resistance between the active materials and current collectors, and the intrinsic resistance of the substrates [20]. Values for R_s, R_p, R_{ct}, C_{dl}, C_f, f_p, and $\tau(s)$ are outlined in Table 6. 3 below.

Table 6. 3: Values for R_s,. R_p, R_{ct}, C_{dl}, and C_f obtained from fitting to model. $\tau(s)$ obtained from imaginary part of capacitance verses frequency.

Cycle	**R_s (ohm.cm^2)**	**R_p (ohm.cm^2)**	**R_{ct} (ohm.cm^2)**	***C_{dl} (F)***	***C_f (F)***	***f_p (Hz)***	***$\tau(s)$***
Initial	4.5	5.9	18.6	0.0014	0.0085	0.32	0.50
15 000th	10.0	18.0	39.5	0.0013	0.0051	0.062	2.57

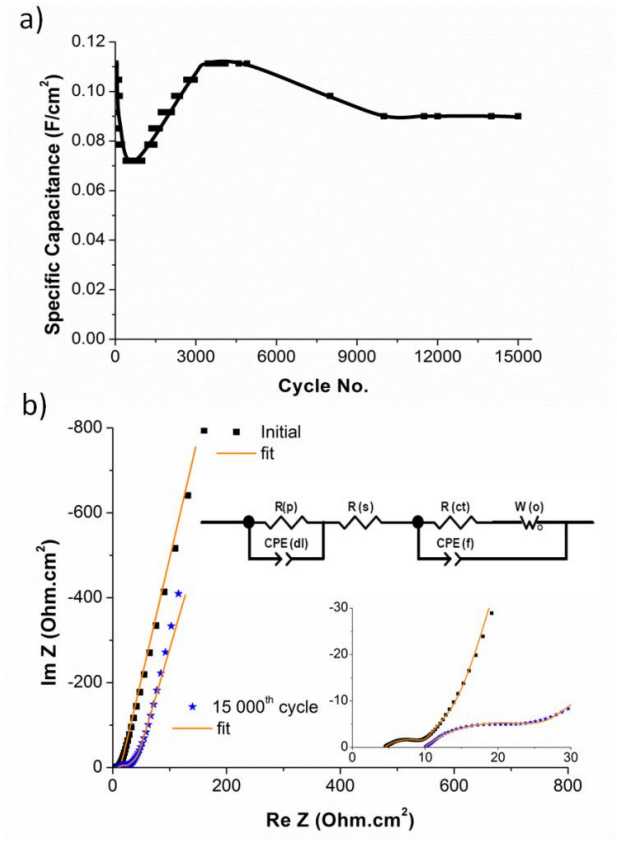

Figure 6. 8: (a) Specific capacitance versus cycle number at a current density of 0.5 A/g. (b) Nyquist plots (with inset) of experimental impedance data (scattering dot) and fitting results. (solid line) for 90% MnO- 10% mw rGO // FC asymmetric device in the frequency range from 100 000 Hz to 0.01 Hz measured before and after 15 000 galvanostatic charge / discharge cycles.

6.3.3.2.1. X-ray diffraction of supercapacitor electrode before and after long term cycling.

Due to the nature of the curve in Figure 6. 8b where there is a change in the specific capacitance profile, XRD was employed after the 15 000th cycle in order to observe any changes in the crystallographic structure of MnO. In Figure 6. 9, an XRD spectra has been taken on the 90% MnO- 10% mw rGO electrode material before and after long term galvanostatic charge / discharge which resulted in a change of the XRD

spectra. It was discovered that after this long term cycling, hausmannite ($Mn^{2+}Mn^{3+}{}_2O_4$) was present in the sample as is shown by the XRD spectra of Figure 6. 9. The ensuing analysis uses Equation 6.1, which describes the percentile volume fraction conversion of manganosite to hausmannite by using the normalised ratios of the relative intensities as described by Bhattacharya et. al. [50].

$$V = \frac{I_{manganosite(hkl)}}{I_{manganosite(hkl)} + I_{hausmannite(hkl)}} \qquad \textit{Equation 6.1}$$

Where V is the volume fraction, $I_{manganosite\ (hkl)}$ and $I_{hausmannite\ (hkl)}$ are the intensities of the respective planes chosen.

After 15 000 cycles, 86% of MnO (cubic) was present whilst the remaining 14% was converted to hausmannite (tetragonal) due to the appearance of main peaks at 2θ = 32.7, 36.2, 44.0, and 60.3 (card no. 00 001 1127) which is a mixture of $Mn^{2+}Mn^{3+}{}_2O_4$. This result shows that the stability of our MnO- mw rGO composite is very good with the decrease in specific capacitance (Figure 6. 8) primarily being as a result of the formation of hausmannite which creates another interface in the system that is not electrochemically active, thus inhibiting charge storage and delivery and contributing to the increased R_s and τ(s) values.

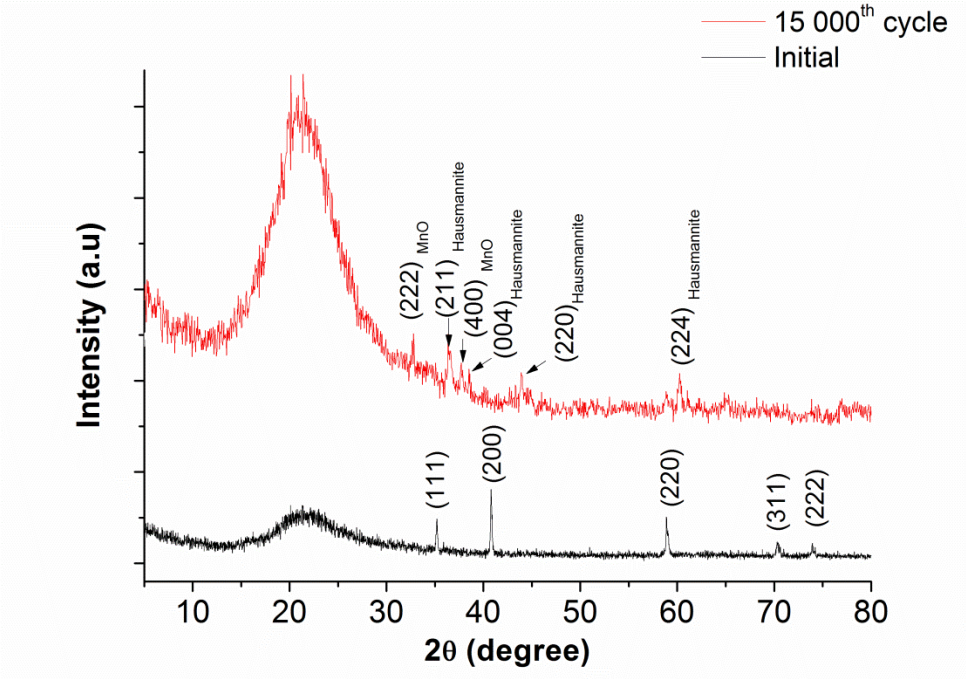

Figure 6. 9: XRD comparison before and after galvanostatic charge / discharge. The current density is 0.5 A/g for 15 000 cycles.

6.4. Conclusions.

In summary, we have successfully synthesised GO through a modified Hummer's method and exfoliated the GO using microwave irradiation. The ensuing SEM and STEM images show significantly altered structure that is highly porous forming an interconnected network with minimal re-stacking of the graphene. The XRD confirms the exfoliation of the GO due to the significant decrease of the sharp peak at $2\theta = 10.2^{o}$; while XPS spectra confirms that reduction of the GO is apparent due to the much sharper C=C at 284.4 eV peak with the relative abundance of C and O increasing to 92.22% and 7.53% respectively. The G/D band ratio of the Raman spectra also increased from 0.8 to 0.9 signifying the GO has somewhat been reduced. The addition of the MnO particles show that they are dispersed

throughout the GO matrix, with the size of the MnO particles varying from 20 nm to 1 µm.

A composite material was made of MnO and mw rGO with three electrode testing performed in order to gauge which weight ratio of MnO to mw rGO would provide the best electrochemical response in terms of capacitance and kinetic behaviour. The results concluded that the 90% MnO- 10% mw rGO was the best performing material with 0.107 F/cm^2, the most rectangular CV and smallest charge transfer resistance. This material was then used to make an asymmetric supercapacitor with functionalised activated carbon. Device testing showed that our composite material displayed excellent reversibility when the current density was altered from 0.1 A/g to 1.0 A/g and then back to 0.1 A/g. The long term cyclability tests over 15 000 cycles was also very good with a capacity retention of 82% at 0.5 A/g. XRD showed the amount of MnO remaining in the device was 86% while the remaining 14% was converted to hausmannite after the 15 000th cycle.

6.5. References.

1. Cheng, Q., J. Tang, J. Ma, H. Zhang, N. Shinya, and L.-C. Qin, *Graphene and nanostructured MnO2 composite electrodes for supercapacitors.* Carbon, 2011. 49(9): p. 2917-2925.
2. Chen, P.-C., G. Shen, Y. Shi, H. Chen, and C. Zhou, *Preparation and Characterization of Flexible Asymmetric Supercapacitors Based on*

Transition-Metal-Oxide Nanowire/Single-Walled Carbon Nanotube Hybrid Thin-Film Electrodes. ACS Nano, 2010. 4(8): p. 4403-4411.

3. Brock, S. L., N. Duan, Z. R. Tian, O. Giraldo, H. Zhou, and S. L. Suib, *A Review of Porous Manganese Oxide Materials.* Chemistry of Materials, 1998. 10(10): p. 2619-2628.

4. Chen, Y., Y. Zhang, D. Geng, R. Li, H. Hong, J. Chen, and X. Sun, *One-pot synthesis of MnO2/graphene/carbon nanotube hybrid by chemical method.* Carbon, 2011. 49(13): p. 4434-4442.

5. Chen, S., J. Zhu, X. Wu, Q. Han, and X. Wang, *Graphene Oxide MnO2 Nanocomposites for Supercapacitors.* ACS Nano, 2010. 4(5): p. 2822-2830.

6. Yu, G., L. Hu, M. Vosgueritchian, H. Wang, X. Xie, J. R. McDonough, X. Cui, Y. Cui, and Z. Bao, *Solution-Processed Graphene/MnO2 Nanostructured Textiles for High-Performance Electrochemical Capacitors.* Nano Letters, 2011. 11(7): p. 2905-2911.

7. Wang, N., H. Pang, H. Peng, G. Li, and X. Chen, *Hydrothermal synthesis and electrochemical properties of MnO2 nanostructures.* Crystal Research and Technology, 2009. 44(11): p. 1230-1234.

8. J. Yan, Z. Fan, T. Wei, W. Qian, M. Zhang, and F. Wei, *Fast and reversible surface redox reactions of graphene Mno2 composites.* Carbon, 2010. 48: p. 3825-3833.

9. Chen, C.-M., Q. Zhang, M.-G. Yang, C.-H. Huang, Y.-G. Yang, and M.-Z. Wang, *Structural evolution during annealing of thermally reduced graphene*

nanosheets for application in supercapacitors. Carbon, 2012. 50(10): p. 3572-3584.

10. V. Ruiz, C. Blanco, M. Granda, R. Menendez, and R. Santamaria, Journal of Electroanalytical Chemistry, 2008. 618: p. 17-23.
11. G. Bhide and R. Dani, *Electrical conductivity in oxides of manganese and related compounds.* Physica, 1961. 27(9): p. 821-826.
12. Tryba, B., A. W. Morawski, and M. Inagaki, *Preparation of exfoliated graphite by microwave irradiation.* Carbon, 2005. 43(11): p. 2417-2419.
13. Li, Z., J. Wang, S. Liu, X. Liu, and S. Yang, *Synthesis of hydrothermally reduced graphene/MnO2 composites and their electrochemical properties as supercapacitors.* Journal of Power Sources, 2011. 196(19): p. 8160-8165.
14. Antiohos, D., G. Folkes, P. Sherrell, S. Ashraf, G. G. Wallace, P. Aitchison, A. T. Harris, J. Chen, and A. I. Minett, *Compositional effects of PEDOT-PSS/single walled carbon nanotube films on supercapacitor device performance.* Journal of Materials Chemistry, 2011. 21(40): p. 15987-15994.
15. Zhang, S. W. and G. Z. Chen, *Manganese oxide based materials for supercapacitors.* Energy Materials: Materials Science and Engineering for Energy Systems, 2008. 3(3): p. 186-200.
16. H. Kurig, A. Janes, and E. Lust, *Electrochemical Characteristics of Carbide-Derived Carbon|1-Ethyl-3-methylimidazolium Tetrafluoroborate Supercapacitor Cells.* Journal of The Electrochemical Society, 2010. 157(3): p. A272-A279.

17. Wang, G., L. Zhang, and J. Zhang, *A review of electrode materials for electrochemical supercapacitors.* Chemical Society Reviews, 2012. 41(2): p. 797-828.

18. Pacios, M., M. del Valle, J. Bartroli, and M. J. Esplandiu, *Electrochemical behavior of rigid carbon nanotube composite electrodes.* Journal of Electroanalytical Chemistry, 2008. 619-620: p. 117-124.

19. Bose, S., T. Kuila, A. K. Mishra, R. Rajasekar, N. H. Kim, and J. H. Lee, *Carbon-based nanostructured materials and their composites as supercapacitor electrodes.* Journal of Materials Chemistry, 2012. 22(3): p. 767-784.

20. Yan, J., Z. Fan, T. Wei, W. Qian, M. Zhang, and F. Wei, *Fast and reversible surface redox reaction of graphene MnO2 composites as supercapacitor electrodes.* Carbon, 2010. 48(13): p. 3825-3833.

21. Rubinson, J. F. and Y. P. Kayinamura, *Charge transport in conducting polymers: insights from impedance spectroscopy.* Chemical Society Reviews, 2009. 38(12): p. 3339-3347.

22. Z. Bakenov, M. Nakayama, M. Wakihara, and I. Taniguchi, *Lithium AlPO4 composite polymer battery with nanostructured LiMn2O4 cathode.* J. Solid State Electrochemistry., 2008. 12(3): p. 295-302.

23. Taberna, P. L., P. Simon, and J. F. Fauvarque, *Electrochemical Characteristics and Impedance Spectroscopy Studies of Carbon-Carbon Supercapacitors.* Journal of The Electrochemical Society, 2003. 150(3): p. A292-A300.

24. Zhang, Y., Y. Zhao, A. Yermukhambetova, Z. Bakenov, and P. Chen, *Ternary sulfur/polyacrylonitrile/Mg0.6Ni0.4O composite cathodes for high*

performance lithium/sulfur batteries. Journal of Materials Chemistry A, 2013. 1(2): p. 295-301.

25. Bakenov, Z. and I. Taniguchi, *Physical and electrochemical properties of LiMnPO4/C composite cathode prepared with different conductive carbons.* Journal of Power Sources, 2010. 195(21): p. 7445-7451.

26. Prabaharan, S. R. S., R. Vimala, and Z. Zainal, *Nanostructured mesoporous carbon as electrodes for supercapacitors.* Journal of Power Sources, 2006. 161(1): p. 730-736.

27. Yan, J., J. Liu, Z. Fan, T. Wei, and L. Zhang, *High-performance supercapacitor electrodes based on highly corrugated graphene sheets.* Carbon, 2012. 50(6): p. 2179-2188.

28. Byon, H. R., S. W. Lee, S. Chen, P. T. Hammond, and Y. Shao-Horn, *Thin films of carbon nanotubes and chemically reduced graphenes for electrochemical micro-capacitors.* Carbon, 2010. 49(2): p. 457-467.

29. Chen, C.-Y., C.-Y. Fan, M.-T. Lee, and J.-K. Chang, *Tightly connected MnO2-graphene with tunable energy density and power density for supercapacitor applications.* Journal of Materials Chemistry, 2012. 22: p. 7697-7700.

30. Mishra, A. K. and S. Ramaprabhu, *Functionalized Graphene-Based Nanocomposites for Supercapacitor Application.* The Journal of Physical Chemistry C, 2011. 115(29): p. 14006-14013.

31. Kasap, S. O., *Principles of Electronic Materials & Devices*. 3rd ed 2009, New York: McGraw-Hill.

32. Jong, H. J., K. Akiko, M. Kenji, and N. Katsuhiko, *Supercapacitor Performance of Hydrous Ruthenium Oxide Electrodes Prepared by Electrophoretic Deposition.* Journal of The Electrochemical Society, 2006. 153(2): p. A321-A328.

33. Yuan, C., X. Zhang, L. Su, B. Gao, and L. Shen, *Facile synthesis and self-assembly of hierarchical porous NiO nano/micro spherical superstructures for high performance supercapacitors.* Journal of Materials Chemistry, 2009. 19(32): p. 5772-5777.

34. Shi, W., J. Zhu, D. H. Sim, Y. Y. Tay, Z. Lu, X. Zhang, Y. Sharma, M. Srinivasan, H. Zhang, H. H. Hng, and Q. Yan, *Achieving high specific charge capacitances in Fe3O4/reduced graphene oxide nanocomposites.* Journal of Materials Chemistry, 2010. 21(10): p. 3422-3427.

35. *Cap-XX Australia, Supercapacitor Product Bulletin; G Series*, 2011.

36. Blanton, G. G., Design Considerations and Characterization of Origami Electrochemical Capacitors, 2004. Department of Mechanical Engineering, Massachusetts Institute of Technology

37. Sharma, P. and T. S. Bhatti, *A review on electrochemical double-layer capacitors.* Energy Conversion and Management, 2010. 51(12): p. 2901-2912.

38. *Cap-XX Australia, Supercapacitor Product Bulletin; H Series*, 2011.

39. Wang, H.-Q., Z.-S. Li, Y.-G. Huang, Q.-Y. Li, and X.-Y. Wang, *A novel hybrid supercapacitor based on spherical activated carbon and spherical MnO2 in a*

non-aqueous electrolyte. Journal of Materials Chemistry, 2010. 20(19): p. 3883-3889.

40. Yu, C., C. Masarapu, J. Rong, B. Wei, and H. Jiang, *Stretchable Supercapacitors Based on Buckled Single-Walled Carbon-Nanotube Macrofilms.* Advanced Materials, 2009. 21(47): p. 4793-4797.

41. Luo, J.-Y. and Y.-Y. Xia, *Electrochemical profile of an asymmetric supercapacitor using carbon-coated LiTi2(PO4)3 and active carbon electrodes.* Journal of Power Sources, 2009. 186(1): p. 224-227.

42. Pasta, M., F. La Mantia, L. Hu, H. Deshazer, and Y. Cui, *Aqueous supercapacitors on conductive cotton.* Nano Research, 2010. 3(6): p. 452-458.

43. Pan, H., J. Li, and Y. Feng, *Carbon Nanotubes for Supercapacitor.* Nanoscale Research Letters, 2010. 5(3): p. 654-668.

44. Hsieh, T.-F., C.-C. Chuang, W.-J. Chen, J.-H. Huang, W.-T. Chen, and C.-M. Shu, *Hydrous ruthenium dioxide/multi-walled carbon-nanotube/titanium electrodes for supercapacitors.* Carbon, 2011. 50(5): p. 1740-1747.

45. Fan, Z., J. Yan, T. Wei, L. Zhi, G. Ning, T. Li, and F. Wei, *Asymmetric Supercapacitors Based on Graphene/MnO2 and Activated Carbon Nanofiber Electrodes with High Power and Energy Density.* Advanced Functional Materials, 2011. 21(12): p. 2366-2375.

46. A. J. Bard and L. R. Faulkner, *Electrochemical Methods: Fundamentals and Applications* 2001: John Wiley & Sons, Inc.

47. J. Koryta, J. D., L. Kavan, *Principles of Electrochemistry 2nd Edition* 1993: John Wiley & Sons Inc.

48. Zhang, L. L. and X. S. Zhao, *Carbon-based materials as supercapacitor electrodes.* Chemical Society Reviews, 2009. 38(9): p. 2520-2531.

49. Conway, B. E., *Electrochemical Supercapacitors: Scientific Fundamentals and Technological Applications.* 1999, New York: Kluwer Acedemic / Plenum Publishers.

50. Bhattacharya, A. K., K. K. Mallick, and A. Hartridge, *Phase transition in BiVO4.* Materials Letters, 1997. 30(1): p. 7-13.

Chapter 7: Conclusions and perspectives.

7. General conclusions and perspectives.

7.1. Conclusions.

Carbon based materials such as CNTs and mw rGO were used as a conductive scaffold and support in the development of composite electrodes for the use in energy storage applications. The combination of materials included signle walled nanotubes (SWNTs) with poly(3,4-ethylenedioxythiophene) poly(styrene sulfonate) (PEDOT/PSS); microwave exfoliated graphene oxide (mw rGO) with manganese oxide (MnO), and mw rGO with SWNTs. All composites were made with varying weight ratios and tested electrochemically using a three electrode system in order to determine the optimum weight ratio. Subsequent to this, the best performing ratios were then successfully fabricated into supercapacitor devices and their performance evaluated.

7.2. Poly(3,4-ethylenedioxythiophene) poly(styrenesulfonate) single walled carbon nanotube composite electrodes for supercapacitor device applications.

Free standing PEDOT/PSS : SWNTs have been characterised by scanning electron microscopy, Raman spectroscopy and thermo-gravimetric analysis to understand the physical properties of the films. Films with varying compositions of PEDOT/PSS : SWNTs were compared by electrochemical impedance spectroscopy, cyclic voltammetry and galvanostatic charge/discharge to understand their electrochemical properties. A comparison of the results shows that having single

walled nanotubes dispersed throughout the polymer matrix increase the capacitance by 65% and the energy density by a factor of 3 whilst achieving good capacity retention over 1000 cycles.

7.3. Synthesis of microwave exfoliated graphene oxide.

GO was synthesised using a modified Hummer's methods using commercially available graphite. The GO was exfoliated using a conventional 1200 W microwave oven that induced rapid volume expansion of the GO sheets. This formed a reduced GO material that had porosity and a marked increase in volume. Physical characterisation using SEM, TGA, Raman, XRD, XPS and UV-Vis confirmed the porous structure and reduction of the GO. Electrochemical measurements in aqueous and organic environments showed the mw rGO had the largest capacitance of 33 F/g and 27 F/g respectively signifying that this material is an excellent conductive scaffold for composite electrode materials.

7.4. SWNT-mw rGO composite electrodes.

Composites containing varying weight ratios of SWNT and mw rGO were fabricated using sonication, centrifugation and vacuum filtration into uniform electrodes. Physical characterisation took place via SEM, Raman spectroscopy, and contact angle measurements. Three electrode electrochemical measurements deduced that the 90% SWNT – 10% mw rGO ratio with 20 minutes plasma treatment was the best performing with a specific capacitance of 306 F/g at 20 mV/s and 123 F/g at 500 mV/s. respectively This weight ratio (90% SWNT-10% mw rGO, with 20 minutes

plasma treatment) was then fabricated into a thin supercapacitor device and tested. CVs of the device showed a rectangular behaviour up to scan rates of up to 500 mV/s.. Lastly the current rate could be pushed to 4.0 A/g with stable capacity retention of 95% over 10 000 cycles tested at 1.0 A/g. The EIS analysis before and after long term testing showed a high frequency response and little change in the impedance spectra signifying a stable and robust electrode material.

7.5. Manganosite- microwave exfoliated graphene oxide electrodes for asymmetric supercapacitors.

A composite material consisting of mw rGO and MnO was synthesised in order to explore their potential as an electrode material. The composite material was characterised by SEM, XRD, XPS, and Raman spectroscopy. CV and EIS were used to explore the process occurring at the electrode / electrolyte interface. Long term cyclability and stability was investigated using galvanostatic charge / discharge testing. From the resulting analysis, an asymmetric supercapacitor was constructed with the best composite containing 90% MnO- 10% mw rGO (w/w). The device exhibited a capacitance of 0.11 F/cm^2 (51.5 F/g by mass) and excellent capacity retention of 82% after 15 000 cycles at a current density of 0.5 A/g.

7.6. Future Work.

Throughout the course of this study, it has become apparent that certain material parameters are critical and must be taken into account in order to optimise a materials performance for energy storage applications. These factors include; (i)

surface area, (ii) conductivity, (iii) porosity, and (iv) kinetics. By combining complementary materials into composites, an electrode material can be tailored to optimise these critical factors mentioned above. This improves the synergy of composite materials through enhanced electrochemical performance, thus amplifying the charge storage and delivery properties. The mechanism by which this could be achieved is to create an electrode structure where all the components are simultaneously optimised in-situ (instead of adding each component individually) leading to a fully integrated and coherent assembly.

One way of achieving total incorporation could involve a suspension of GO and CNTs with a metal ion solution containing a reducing agent. The metal ion solution could be reduced in two ways: (i) the suspension would be vacuum filtered and dried producing a layer-cake type material. The material could then exposed to microwave irradiation that would exfoliate the GO while concurrently reducing the GO and metal ions into metal / metal oxide nanoparticles. (ii) The suspension could be heated sufficiently which will lead to the formation of nanoparticles dispersed throughout the solution. Vacuum filtering and microwave irradiation would be used once more to exfoliate and reduce GO.

It is possible that these types of structures would have uniformly distributed metal / metal oxide nanoparticles throughout the SWNT – mw rGO matrix, while it is thought that the exfoliation in the presence of CNTs would allow for a better adherence of the CNTs to the mw rGO. Overall this would enhance the

electrochemical properties of the material significantly as the energy and power density would be maximised.

7.7. Future developments going forward.

With energy consumption as a whole on the increase, coupled with the rapid economic development of countries such as Brazil, China, India, and Russia there will be a concerted effort to improve how energy is utilised. This expansion in industrialisation has already and will continue to lead to a further increase in the price of oil. Coupled to the rise in fossil fuel costs are drivers of an ageing energy infrastructure system and demand for a low-carbon emission economy through the use of renewable energy [1, 2]. To help accommodate all these factors the supply and demand challenge may be addressed by smarter and more efficient energy systems. Energy storage utilisation will continue to play an increasing key role in providing a solution to the energy problem. Energy must be efficiently stored when it is in excess, and released at a time of high demand. This is extremely important for renewables that are not load-following [3].

With these energy challenges and ongoing research and development, including those that have been conducted over the last decade, the awareness of the benefits of electrochemical capacitors is increasing. As the research and development into energy storage and conversion has increased, the applications of electrochemical capacitors has increased with the technology becoming more diverse meaning that systems can better be tailored / targeted for specific

applications ranging from higher energy density to high power densities where fast charge / discharge efficiencies are needed [3]. The most commonly used material for supercapacitors has been activated carbon with new nanostructured materials such as carbon nanotubes, graphene and its derivatives coming to the forefront of the current fundamental research [4]. In this study, the important conclusions observed relating to improved surface area (Chapter 4 and Chapter 5), porosity (Chapter 3 and Chapter 5), and the benefits of pseudocapacitive effects (Chapter 6) clearly demonstrate that the way forward in terms of trying to improve energy density and power density is in the use of nanostructured carbon materials in composite structures coupled with other carbons, and / or conducting polymers / metal oxides in order to take advantage of the electrochemical properties and robustness that these materials provide.

Future developments will most likely see supercapacitors combined with other energy saving technologies (for example batteries, thermo cells, and / or renewable energy devices) that form part of a hybrid energy storage and power delivery system. These will be suitable for large scale and domestic demand strategies as need for energy continues to grow. These future advancements will not only enable better automotive and portable electronics, but they will revolutionise the fields of medicine, defence and consumer goods thus providing a step change in energy storage technologies [5].

7.8. References.

1. Wilson, I. A. G., P. G. McGregor, and P. J. Hall, *Energy storage in the UK electrical network: Estimation of the scale and review of technology options.* Energy Policy, 2010. 38(8): p. 4099-4106.
2. Lin, C.-C., C.-H. Yang, and J. Z. Shyua, *A comparison of innovation policy in the smart grid industry across the pacific: China and the USA.* Energy Policy, 2013(0).
3. Hall, P. J., *Energy storage: The route to liberation from the fossil fuel economy?* Energy Policy, 2008. 36(12): p. 4363-4367.
4. El-Kady, M. F. and R. B. Kaner, *Scalable fabrication of high-power graphene micro-supercapacitors for flexible and on-chip energy storage.* Nat Commun, 2013. 4: p. 1475.
5. Hall, P. J. and E. J. Bain, *Energy-storage technologies and electricity generation.* Energy Policy, 2008. 36(12): p. 4352-4355.